Development of High-Brightness Field-Emission Cathodes for X-ray Free Electron Lasers

---

Dissertation
zur Erlangung der naturwissenschaftlichen Doktorwürde
(Dr. sc. nat.)
vorgelegt der
Mathematisch-naturwissenschaftlichen Fakultät
der
Universität Zürich
von

Patrick Helfenstein
von
Hohenrain LU

Promotionskomitee

Prof. Dr. Hans-Werner Fink
Dr. Soichiro Tsujino
Dr. Conrad Escher
Prof. Dr. Jens Gobrecht

Zürich, 2013

Gutachter:
Prof. Dr. Günter Müller,
Universität Wuppertal

Zusammenfassung

Die vorliegende Arbeit behandelt die Herstellung und die experimentelle Charakterisierung von Feldemitterkathoden mit dem Ziel, eine alternative Elektronenquelle für Beschleunigeranlagen der 4. Generation wie beispielsweise den SwissFEL Freie-Elektronen-Röntgenlaser anbieten zu können. Aufgrund der potentiellen Fähigkeit solcher Feldemitterkathoden Elektronenstrahlen mit hohen Strömen und Stromdichten zu produzieren wird erwartet, dass sie die herkömmlicherweise verwendeten Photokathoden und thermionischen Kathoden ersetzen können.

Die extrem hohen Stromdichten, die für solch einen Röntgenlaser benötigt werden, können nur unter Zuhilfenahme eines geeigneten Kollimationsmechanismus erzeugt werden. Unter den verschiedenen Möglichkeiten ist eine vertikal geschichtete Feldemitterkathodenstruktur von besonderem Interesse. Durch das Anbringen zweier Elektroden, die sowohl voneinander als auch von den Spitzen elektrisch isoliert sind, lässt sich eine elektrostatische Linse erzeugen, die über das Anlegen einer geeigneten Spannung einen kollimierten Elektronenstrahl erzeugt. Diese Linse minimiert die Bandbreite der transversalen Geschwindigkeiten der Elektronen und damit auch die Emittanz, eine wichtige Grösse für die Beurteilung der Strahlqualität. In einer geschichteten Feldemitterkathodenstruktur wird die untere Elektrode üblicherweise zur Extraktion der Elektronen verwendet. Durch die von den nur wenige Nanometer durchmessenden Spitzen erzeugte lokale Feldverstärkung genügt das Anlegen einer vergleichsweise niedrigen Spannung zwischen diesen Spitzen und der Extraktionselektrode zur Erzeugung der benötigten Felder im Bereich von mehreren GV/m. Das Hauptproblem dieser geschichteten Strukturen war der Einfluss des Kollimationsfeldes auf den Emissionsstrom. Die negative Spannung bewirkt eine Verminderung des Extraktionsfeldes, was sich aufgrund der exponentiellen Abhängigkeit stark auf den emittierten Strom auswirkt. Grosse Öffnungen in der Kollimationselektrode reduzieren diesen Einfluss erheblich, wie in der vorliegenden Arbeit gezeigt wird.

Kreisförmige Öffnungen in der Extraktionselektrode werden durch Plasmaätzen einer planaren Schicht aus Photolack erzeugt. Dabei wird die Tatsache ausgenutzt, dass die Elektrode beim Aufbringen die Oberflächenerhebungen der unterliegenden Strukturen reproduziert und deshalb über den Spitzen erhöht ist. Die Benutzung eines fokussierten Strahls von Galliumionen erlaubt die Materialabtragung in genau definierten Regionen der Kollimationselektrode, wodurch Öffnungen mit beliebigen Geometrien erzeugt werden können. Mit diesen Methoden wurden geschichtete Kathodenstrukturen mit bis zu 400 Spitzen hergestellt. Der fokussierte Ionenstrahl bietet ein ausgezeichnetes Instrument für die Herstellung von Prototypen mit einer geringen Anzahl an Spitzen, kann aber aufgrund des langsamen Materialabtrages nur mit viel Zeitaufwand zur Herstellung von Strukturen mit mehreren tausend Spitzen verwendet werden. Dieses Problem wurde durch die Verwendung von Elektronenstrahllithographie gelöst. Durch die selektive Elektronenbestrahlung eines speziellen Lacks wurden damit geschichtete Kathodenstrukturen mit bis zu 40’000 Spitzen hergestellt.

Um das Verhalten der Feldemitterkathoden unter verschiedenen Bedingungen einschätzen zu können, wurde ein numerisches Modell der vorgenannten geschichteten Struktur implementiert, das die realen Strukturen bis ins grösstmögliche Detail reproduziert. Durch die Aufteilung der Berechnungen in mehrere Stufen konnte die Rechenzeit minimiert und gleichzeitig die Genauigkeit erhöht werden. In einem ersten Schritt wird die Feldverteilung an der Spitzenoberfläche berechnet und daraus dann über die Fowler-Nordheim Gleichung der emittierte Strom in Abhängigkeit der angelegten Spannung ermittelt. Diese Werte bilden die Anfangsbedingungen einer dreidimensionalen Simulation der Elektronenbahnen. Zuerst wird die Situation in der Nähe der Emitterspitze mit einem engmaschigen Gitter simuliert und die Werte dann wiederum als Anfangsbedingungen für die Simulation der Verhältnisse in der kompletten Kammer verwendet, in der die Anode 40-50 mm von der Probe entfernt angebracht ist.

Abstract

The work presented here deals with the fabrication and experimental characterization of stacked double-gate field emitter arrays with the goal to provide an alternative electron source for 4th generation accelerator facilities such as the SwissFEL X-ray free electron laser. Such field emitter arrays are expected to be superior to the conventionally employed photocathodes or thermionic cathodes due to their capability of delivering high current electron beams with an extremely high brightness.

Among the multitude of different possible collimation methods, the stacked double gate structure was shown to provide strong reduction in transversal velocity spread, a quantity closely related to the emittance and thus also to the beam brightness. A stacked double-gate field emitter array consists of two aligned electrodes placed above the emitter tips. By applying a potential between the emitter tips and the lower electrode, the strong fields necessary for a sufficient reduction of the tunneling barrier are created at the nanoscale emitter apex. Due to the field enhancement at nanoscale structures, the application of comparatively low voltages is sufficient. The second electrode, the so-called collimation gate, forms the top layer of the field emitter array structure. By applying a negative voltage to it, an electrostatic lens is created that effectively reduces the transverse velocity spread of the emitted electron beam and leads to an increased current density. Because the field created by the collimation gate reduces the field at the emitter apex, the current density increase is limited by the reduction of the emitted current. With large collimation gate apertures, this problem can be diminished and it is possible to maintain high current levels during collimation.

The extraction gate apertures are patterned by a self-aligned polymer etch-back process. For the opening of the large collimation gate apertures, a focused ion beam milling process was developed and employed to fabricate double-gate field emitter arrays with up to 400 emitters. This flexible, mask-less method is ideal for the prototyping of small arrays but lacks the speed necessary for larger devices. A solution was found by selectively exposing a resist placed on top of the collimation gate by means of electron beam lithography. This method was used to produce double-gate field emitter arrays with up to 40,000 emitter tips.

A numerical model was devised to allow the comparison of theoretical expectations to experimental results. In building the model, careful considerations have been undertaken to represent the fabricated structures as close as possible. For optimal results, a multi-step calculation was employed. First the electric field distribution in the vicinity of the emitter apex is calculated and used to derive the emission current governed by the Fowler-Nordheim equation and the active emission area. The resulting values are then used to initialize a particle tracking simulation. Due to the dense meshing required on the emitter apex surface, the trajectories are first calculated close to the point of emission. The results are exported and used for the initialization of a simulation of the full experimental chamber including an anode placed at 40-50 mm distance along the electron beam axis.

Author Contributions

Manuscripts

Section 4.1 Tsujino S., Helfenstein P., Kirk E., Vogel T., Escher C. & Fink H.-W., "Field-Emission Characteristics of Molded Molybdenum Nanotip Arrays With Stacked Collimation Gate Electrodes", *IEEE Electron Device Letters*, **2010**, *31*, 1059-1061

- Participation in planning and execution of the experiment
- Analysis of the experimental data

Section 4.2 Helfenstein P., Kirk E., Jefimovs K., Vogel T., Escher C., Fink H.-W. & Tsujino S., "Highly collimated electron beams from double-gate field emitter arrays with large collimation gate apertures", *Applied Physics Letters*, **2011**, *98*, 061502

- Fabrication of the structures
- Execution of the experiment
- Analysis of the experimental data
- Writing of the manuscript

Section 5.1 Helfenstein P., Jefimovs K., Kirk E., Escher C., Fink H.-W. & Tsujino S., "Fabrication of Metallic Double-Gate Field Emitter Arrays and Their Electron Beam Collimation Characteristics", *Journal of Applied Physics*, **2012**, *112*, 093307

- Fabrication of the structures
- Programming the measurement equipment for the experiment
- Planning of the experiment
- Execution of the experiment
- Analysis of the experimental data including the coding of the algorithms presented in the supplementary information to the manuscript
- Writing of the manuscript

Section ?? Guzenko V. A., Mustonen A., Helfenstein P., Kirk E. & Tsujino S., "High-Density Large-Scale Field Emitter Arrays for X-ray Free Electron Laser Cathodes", submitted to: *Microelectronic Engineering*, **2012**

- Participation in the finding of suitable alignment marks
- Fabrication of the structures
- Planning and execution of the experiment

Section ?? Helfenstein P., Guzenko V. A., Fink, H.-W. & Tsujino S., "Electron beam collimation with a 40,000 tip metallic double-gate field emitter array and in-situ control of nanotip sharpness distribution", *Journal of Applied Physics*, **2013**, *113*, 043306

- Design of structures and photolithography masks
- Fabrication of the structures and sample holder
- Participation in designing & building the measurement chamber
- Programming of the measurement equipment
- Planning and execution of the experiment
- Analysis of the experimental data including the coding of algorithms for the pattern recognition
- Writing of the manuscript

Appendix A Tsujino S., Paraliev M., Helfenstein P., Gough C., "Field emission cathode structure and driving method thereof", Patent application PCT/EP2012/061988, filed: **21. July 2012**

- Participation in the idea finding
- Investigation of the practical feasibility of the new structures
- Testing possible fabrication methods for the new structures
- Participation in the document search for the international search report

Oral Presentations

Annual meeting of the Swiss Physical Society, 21.-22.6.10, Basel, Switzerland
"Electron Beam Properties of Molybdenum Field Emitter Arrays with Stacked Gates"

EMPA PhD Students Symposium, 7.10.10, Dübendorf, Switzerland
"Highly Collimated Electron Beams from Double-Gate Field Emitter Arrays",

Joint annual meeting of the Swiss & Austrian Physical Societies, 15.-17.6.11, Lausanne, Switzerland
"Double-Gate Field Emitter Arrays: Aperture Size Dependence of Electron Beam Collimation Characteristics",

International Vacuum Nanoelectronics Conference 2011, 18.-22.7.11, Wuppertal, Germany
"Aperture Size Dependent Collimation in Double Gate Field Emitter Arrays"

Universität Zürich, 27.10.11, Zurich Switzerland
"SwissFEL - der neue Röntgenlaser am PSI und die Suche nach der optimalen Elektronenquelle" (presentation (in German) within the lecture series "Physik auf der Nanometer Skala")

Workshop on cold cathodes, 3.-4.9.12, Wuppertal, Germany
"Molybdenum Field Emitter Arrays for High Brightness Electron Beams"

Posters

International Vacuum Nanoelectronics Conference 2010, 26.-30.7.10, Palo Alto CA, USA
"Electron Beam Collimation Properties of Molded Molybdenum Field Emitters",

Winter School on Quantum Nanoscience, 27.3.-1.4.11, Crans-Montana, Switzerland
"Double Gate Field Emitter Arrays: A Bright Electron Source?",

International Workshop on Mechanisms of Vacuum Arcs, 27.-30.6.11, Helsinki, Finland
"Double Gate Field Emitter Arrays: A Bright Electron Source?",

Annual Meeting of the Swiss Physical Society, 21.-22.6.12, Zurich, Switzerland
"Electron Beam Properties of Large Double Gate Field Emitter Arrays with an Optimized Collimation Gate Electrode Geometry"

International Vacuum Nanoelectronics Conference 2012, 9.-13.7.12, Jeju, Korea
"Electron Beam Characterization of Double Gate Field Emitter Arrays Fabricated by a Focused Ion Beam Assisted Process"

Contents

List of Abbreviations

F_{acc} acceleration field

G_{col} collimation gate; see figures 3.9 and 3.10

G_{ext} extraction gate; see figures 3.5, 3.6 and 3.7 in section 3.1.2

I_1 1.2 μm thick SiO_2 insulator layer separating the emitters from the extraction gate; see figures 3.5 (a) and 3.7 in section 3.1.2

I_2 second insulation layer separating the extraction gate electrode from the collimation gate electrode; It consists of SiON which etches slower in BOE, thereby reducing the G_{col} undercut, see section 3.2

k_{col} the ratio V_{col}/V_{em}

V_{col} bias voltage applied to the collimation gate G_{col}

V_{em} bias voltage applied to the emitter tip substrate

V_{ext} bias voltage applied to the extraction gate G_{ext}; this is generally set to ground

BOE buffered oxide solution consisting of NH_4F and hydrofluoric acid in water

e-beam electron beam

F-N Fowler-Nordheim; R. H. Fowler & L. Nordheim developed a theoretical model describing field-emission from flat metallic surfaces. The equation relating the externally applied electric field and the emission current-density is called the Fowler-Nordheim equation

FEA field-emitter array

FEL free-electron laser

FEM field emission microscope

FIB focused ion beam

HF hydrofluoric acid

I-V current-voltage

KOH potassium hydroxide

PEC proximity effect correction; exposure of areas surrounding the area of beam impact due to electron scattering in electron beam lithography

PECVD plasma enhanced chemical vapor deposition

SASE self-amplification by spontaneous emission

TWT travelling-wave tube

Chapter 1

Introduction

Contents

This chapter will give an introduction to the work presented hereafter. It begins by stating the motivation for conducting research in the area of double-gate field-emission cathodes. Then, the necessary theory is introduced and an overview of the state-of-the-art is presented. In each chapter, a short introduction to the manuscripts or the unpublished data included therein is given. The different methods used in the fabrication of field-emitter arrays and, in particular, the processes applied to the fabrication of the collimation gate electrodes are presented in detail in chapter 3. Details concerning the numerical simulation of double-gate field-emitters with different geometries are given in chapter 2.

1.1 Motivation

The work leading to this thesis was initiated to experimentally investigate the predicted superior performance of field-emitter array (FEA) cathodes for accelerator applications compared to laser photocathodes or thermionic cathodes. [1–3] The main application these FEA cathodes are intended for is the SwissFEL X-ray free electron laser (FEL) being built at the Paul Scherrer Institute. [4] The SwissFEL will produce ultrashort X-ray pulses with wavelengths in the range of 0.1-7 nm and allow for future extensions of the range to 0.08-30 nm. [5] At the present time, the state-of-the-art laser photocathodes produce electron pulses of 200 pC charge with a normalized emittance below 0.4 mm mrad. [6]

Most FELs currently in operation [7] have a gain of only a few percent per undulator passage due to the electron beam quality and undulator length. Therefore, they require an optical cavity resonator and a synchronized multibunch electron beam [8]. For the very short wavelengths used in the SwissFEL, high-reflectivity mirrors for normal beam incidence are not available, which means that a sufficient gain has to be reached within a single undulator passage. If the peak current of the electron beam is high enough, the synchrotron radiation acts back on the beam, leading to a density modulation that enhances the power and coherence of the radiation. This self-amplification by spontaneous emission (SASE) causes the radiation power to grow exponentially with the distance along the undulator. [9] In section 1.2, a short introduction to free electron lasers is given and the performance of the double-gate FEAs presented in this work is compared to the SwissFEL requirements.

Another possible application of FEAs are microwave power amplifiers such as travelling wave tubes (TWTs) which could profit from an expected increase in power density and frequency when the thermionic cathodes commonly used as electron sources in these devices are replaced by FEAs. [10, 11] FEAs can help simplify the gun design and extend the operation range of such TWTs because of the possibility of direct current modulation without the use of the grid necessary for controlling the electron emission of thermionic cathodes in such devices. [12] The successful integration of a single-gate Spindt FEA into a TWT producing 100 W output power at 5 GHz [13] demonstrates the practical feasibility of FEA-based TWTs.

In the case of FEAs, the requirement of an almost parallel electron beam with a high-current density mandates some form of beam collimation to reduce the uncollimated emission angle of 40-60°. A multitude of different methods can be applied to achieve this collimation with varying performance. An overview of the most common approaches is given in section 1.3. In this work, a collimated electron beam was obtained by using a stacked double-gate structure to individually collimate the emitted beamlets.

1.2 The SwissFEL X-ray Free Electron Laser

The SwissFEL is a 4th generation accelerator facility presently being constructed by the Paul Scherrer Institute. A number of such X-ray free electron lasers are being built across the world (e.g. European XFEL [14]) or are already in operation (e.g. LCLS [15], SACLA [16]). In a free electron laser, coherent photon radiation is produced when a relativistic electron bunch passes through an undulator section, figure 1.1. The alternating transverse magnetic field forces the electron beam on a sinusoidal path and thereby causes the electrons to lose energy in the form of electromagnetic waves (synchrotron radiation). Due to the relativistic energies of the electron bunch, the radiation is emitted almost completely in longitudinal direction. [9] The synchrotron radiation acts back on the electron beam, causing a density modulation (microbunching) which is in-phase with the emitted radiation. This leads to an exponential increase of coherent photons along the undulator. In a FEL, the electrons are not bound in atomic or molecular states and, different from classical lasers, the electron beam itself acts as the gain medium, making FELs more widely tunable than any other type of laser. [17] The chosen wavelength can be selected by varying the electron energy and the magnetic field in the undulator.

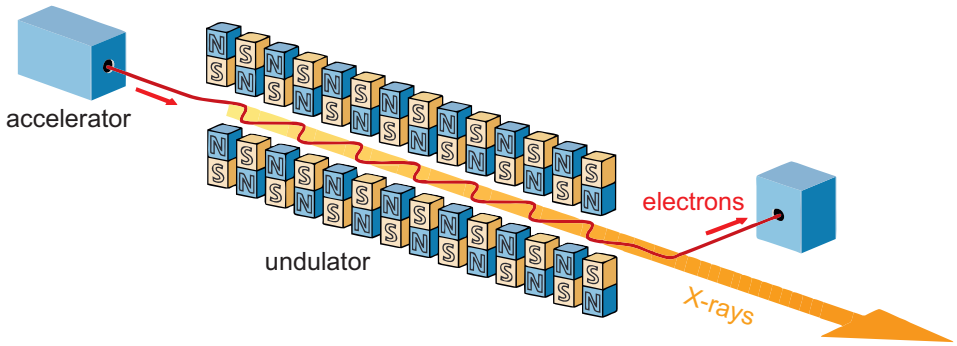

Figure 1.1: Schematic overview of the undulator section where the coherent photon radiation is produced. Image taken from [4]

As shown in table 1.1, the SwissFEL requires an extremely low emittance electron beam. This puts stringent requirements on the electron source as the beam quality is critically dependent on the first few millimeters in the accelerator where the electrons are still at non-relativistic energies. In order for the double-gate FEAs to be considered as an upgrade option to the SwissFEL injector, these requirements have to be fulfilled.

SwissFEL nominal operation modes	**high charge**	**low charge**
Bunch charge	200 pC	10 pC
Gun gradient	100 MV/m	
Beam current (during pulse)	20 A	3 A
Pulse length (flat top, full width)	10 ps	3.3 ps
Normalized rms emittance	0.2 μm	0.09 μm
Pulse repetition rate	100 Hz	

Table 1.1: Overview of baseline specifications for SwissFEL

The normalized rms emittance is given by [18]

$$\epsilon_{n,rms} = \gamma\beta\sqrt{\langle x^2\rangle \langle x'^2\rangle - \langle xx'\rangle^2}, \tag{1.1}$$

where $\gamma = 1/\sqrt{1-\beta^2}$, $\beta = u_z/c_0$ with c_0 the speed of light in vacuum and u_z the longitudinal velocity. x is the source radius and x' the beam divergence angle. The correlation term is equal to zero in this case and the angle can be given in terms of the transverse and longitudinal velocities, leading to

$$\epsilon_{n,rms} = \frac{R_0}{2}\frac{u_t}{c_0}, \tag{1.2}$$

where R_0 is the FEA radius and u_t is the rms transverse velocity. In the experiment, a value of $\sim 2.4\times10^{-4}$ was achieved for u_t/c_0 with a 40,000 tip double gate FEA (see section **??**). The radius of the FEA was 1.14 mm. Inserting these values into equation 1.2 yields a normalized rms emittance of 0.14 μm which is below the value required for the SwissFEL. The particle tracking simulations presented in chapter 2 have shown that the collimation characteristics are preserved when the structure is reduced in size. Assuming a double-gate structure reduced by a factor of ten from the FEAs presented in this work, a circular FEA of 150 nm base length pyramidal emitter tips with a pitch of 1 μm and a radius of 1.14 mm would hold approximately 10^6 emitters. With 10 ps pulsed emission, extracting a current of 20 μA per tip, the total pulse charge amounts to 200 pC as required by the SwissFEL baseline design. The aforementioned value of u_t was obtained at an acceleration field of 60 kV/m and an average tip current of 0.8 nA. The current was deliberately kept low in order to preserve the phosphor screen used in the experiment to image the electron beam. Of course, space-charge effects would become increasingly dominant when going to higher average tip currents in the μA range. However, the particle tracking simulation shows that the space-charge induced degradation of $\epsilon_{n,rms}$ is compensated by the high acceleration gradient of 100 MV/m used in the SwissFEL.

1.3 Overview of the State-of-the-Art

The extremely high-brightness electron beams achievable with field-emission cathodes has enabled the realization of electron microscopes with field-emitter guns capable of atomic resolution [19] and stimulated high current and high current density applications such as free-electron lasers [5, 20] and THz vacuum electronic devices. [21–24] High-brightness electron beams can be extracted from microfabricated emitter tip apexes with radii in the order of a few nanometers down to single-atom emitters [25, 26] by the application of strong electric fields of several GV/m. Because of the field-enhancement occurring at such nanometer-scale structures, the voltages required to create such fields on the emitter apex surface are comparatively low. The fact that this field-enhancement is also present at frequencies of up to almost the visible spectrum has recently triggered intensive studies ranging from fundamental physics such as electron dynamics in strong fields [27] to ultrafast electron beam applications for time-resolved electron diffraction and microscopy, [28] potentially down to the attosecond range. [29]

Experiments and basic research in high current density field-emission were started in the 1950s [30] and with the advent of microfabrication it became possible to arrange multiple emitter tips into arrays [31]. The first single-gate FEAs fabricated consisted of metallic cone shaped emitters evaporated at normal incidence through a shrinking aperture. [32] These Spindt-type FEAs, named after their inventor, operate at very low applied voltages compared to etched wire emitters [33] and have shown current densities of 40 A/cm^2 with a total current of 300 mA for arrays of 50,000 emitters. [34] This is well below the current densities achievable from single emitters [3, 35] and current densities exceeding 2 kA/cm^2 have been reported for FEAs with areas of $\lesssim 10^{-4}$ cm^2. [36] The main obstacle hindering higher current densities in larger FEAs is the inherent non-uniformity of tip apex radii of curvature. One method to increase the emitted current is the irradiation by a near-infrared laser. [37] Using a single-gate molybdenum FEA with 1.2×10^5 emitter tips, the generation of ultra-fast electron bunches with a charge of up to 5 pC was demonstrated using a 50 fs pulsed laser with 800 nm wavelength. [38]

Field-emitters can be fabricated from any material that can be etched, molded, grown or formed into an appropriate shape by other methods. [3] The electrochemical etching used for emitters made from tungsten wires [39] has been known for decades and has been used to test the coating with thin films made from various materials [40–43] in order to reduce the work function. Because of its high chemical and thermal stability, tungsten has been used to fabricate field-emitters of varying tip geometries such as nanowires [44, 45], nanowhiskers [46], nanorods [47] or nanotips [48]. Due to the high availability of silicon fabrication techniques, in addition to FEAs fabricated from single-crystal silicon, [49] the field-emission characteristics of various forms of silicon such as polycrystalline [50, 51], porous [52] and amorphous [53] have been investigated. Next to tungsten, other metallic materials such as molybdenum [54, 55] or cobalt [56] have been used for the fabrication of FEAs. Because it is highly inert to ion bombardment, diamond has been used to fabricate field-emitters by molding and chemical vapor deposition, showing low or negative electron

affinity. [57, 58] Field-emission was also demonstrated with diamond micropowders. [59]

Recently, carbon nanotube (CNT) based field-emitter devices have been presented. [60–63] CNT field-emitter devices have shown very low turn-on fields in the range of a few V/μm [64], which is an order of magnitude smaller than generally needed for metallic field-emitters.

Field-emission has also been demonstrated from composites such as TiN [65], HfN [66], HfC [51, 67] and other more exotic materials such as e.g. from carbon black and carbon black/silica nanoparticles dispersed in photoresist which demonstrated a turn-on field of only 3.5 V/μm. [68]

It has been shown that FEAs can be competitive with state-of-the-art laser photocathodes if the angular spread of individual beams is reduced below $\sim 1^\circ$ while keeping the average current density above ~ 1 kAcm^{-2}. [6, 69] To reach this goal, the intrinsic angular spread of electron beams emitted from FEAs, which is in the order of 60°, has to be reduced by a suitable method while achieving maximum beam brightness enhancement. [70–78]

In addition to the extraction gate electrode an additional focusing electrode, can be added on top of the structure or in-plane. In-plane focusing with a collective focusing electrode [79] is only applicable to FEAs with 10×10 emitters or less, but the incorporation of individual in-plane focusing is expected to deliver improved current-densities. [80] Using stacked double-gate structures, [55, 70, 71, 74, 76–78, 81–86] an increased current density could be achieved, albeit at the cost of strongly reduced emission current due to the influence of the field created by the focusing electrode on the field at the emitter apex. By increasing the thickness of the extraction electrode [72, 87] or by adding additional gate electrodes [88, 89], this current reduction could be mitigated.

Among the different methods proposed, volcano-structured double-gate FEAs [73, 75, 90, 91] and stacked double-gate devices with a collimation gate aperture opening diameter approximately three times larger than that of the extraction electrode [76–78] have shown excellent performance in terms of minimizing the current emission reduction during collimation and achieving increased current-densities.

To extract high current and high current density electron beams from large FEAs with thousands to millions of emitter tips, a very small distribution in emitter tip apex radii of curvature R_{tip} is necessary. Due to the exponential dependency of the emission current on the applied voltage [92, 93], even small variations in R_{tip} significantly influence the total current of the FEA. The presence of adsorbents on the emitter apex can increase the work function locally and atomic protrusions present on the emitter apex can lead to vacuum arcs. Thermal annealing by the extracted field-emission current has been used to clean the emitter tips of contaminants in-situ and can help maintaining a stable emission current level. [94] The variation of apex radius of curvature inherent in most fabrication techniques across large FEAs, however, cannot be amended by this method.

A well established method used originally for the conditioning of electrochemically etched tungsten wires in field-ion microscopy is the sputtering with noble gas ions. [95] After cleaning the W wires by heating them to 2000 K, neon gas was introduced into the chamber with the flow rate adjusted to stabilize the pressure at $\sim 6\times10^{-3}$ Pa. Field-emission was then initiated by applying a voltage between cathode and anode. This voltage was adjusted during the conditioning process to keep the emission current level constant, leading to a constant apex sharpening rate. [96] This method has been applied also to single-gate FEAs, using mixtures of helium, neon and xenon with hydrogen gas. [97] After the glow-discharge treatment, the emission area and current uniformity improved, with Ne showing the best results. Bombardment with Xe resulted in leakage between emitters and gate cathodes which is assumed to be due to the high sputtering yield of Xe. [98] Using pure H gas or a mixture of He and hydrogen gas did not lead to a significant change in the emission characteristics. However, the bombardment with H ions can assist the thermal annealing in removing contaminants. [99] The operation of field-emitter cathodes in vacuum chambers always leads to bombardment of the emitter tips by ionized residual gas atoms. [100] In UHV, the residual gas is mainly composed of hydrogen due to its large outgassing rate from stainless steel. The operation of Si and HfC FEAs under O_2 and Ar residual pressures of 10^{-6} Pa and 10^{-4} Pa showed that after returning to the base pressure of 10^{-7} Pa, the field-emission characteristics prior to the gas exposure could be restored in the case of O_2 but not in the case of Ar. [67]

The noble-gas conditioning method is also interesting for scanning tunneling microscopy and spectroscopy since the properties of the probe tips strongly influence the quality of the obtained data. Using a combination of thermal annealing and noble gas conditioning of W probe tips allows for in-situ conditioning. [101] Recently, the noble gas conditioning was applied to molded molybdenum FEAs with single-gate [102] and double-gate structures (see section **??**). This resulted in improved homogeneity of the emission current across the FEA which is assumed to be caused by homogenization of emitter tip apex radii due to the low-energy ion bombardment. Simulations of ion trajectories have shown that only ions formed near the emitter tips impact on the active emission area. They have energies in the order of 10% of the cathode-anode potential, which was confirmed in experimental damage measurements. [103] These calculations were done for ungated emitters and do not necessarily describe the situation found in single or double-gate FEAs. In the case of double-gate FEAs, calculations using the model presented in chapter 2 have shown that also ions created $\approx 20\,\mu$m away from the emitter apex along the electron trajectory impact on the emission area. This is perhaps due to the electrostatic lense created by the gates at ground potential.

1.4 Field-Emission Theory

Electrons can be extracted from metallic surfaces into vacuum by means of different methods. Through the application of heat, they can gain enough energy to surpass the

potential barrier [104] as is also possible by making use of the photoelectric effect when irradiating a metallic surface with a laser [105]. The third method is a purely quantum mechanical effect, called cold field-emission. By applying strong electrostatic or pulsed fields in the order of several GV/m, the electrons can tunnel through the deformed potential barrier. This is fundamentally different from thermionic emission or photoemission where only those electrons are emitted that have enough energy to pass over the potential barrier. [106–110]

For a sufficient amount of electrons to tunnel through, the barrier width must be very small. This requires extremely high voltages between the electron emitting material and a cathode. In lieu of using high power voltage supplies, the emitter size can be reduced. Field-emitter tips with a radius of curvature of $\sim$5 nm lead to a geometrical field enhancement factor β of $\sim$40. [111] It should be noted that there is no unanimous definition of β which is sometimes expressed in units of inverse length (e.g. in Ref. [10]) to allow the expression of the field F through the applied voltage V by

$$F = \beta V. \tag{1.3}$$

The first approximate theory of field-emission from metallic surfaces was developed almost a century ago by Schottky [112, 113] and was then extended by Fowler & Nordheim [92, 114, 115]. Although their basic ideas are still valid today, the use of a triangular barrier model without taking the image potential into account in their equations led to current-densities that were orders of magnitude lower than measured in experiments. [116] This was later corrected [93, 116, 117] and the theory was extended to field-emission from semiconductors [118,119] and carbon nanotubes. [120,121] There remains, however, a dispute about how to interpret experimental data by Fowler-Nordheim (F-N) theory, as for certain parameters that are currently assumed to be constant in the equations, a dependence on the externally applied electric field or other variables may exist, [122,123] especially at high fields. [124] In the following, the so-called standard F-N theory is introduced and its applicability to the analysis of experimental results is motivated.

The standard F-N theory includes the image potential which rounds off the triangular barrier arising from the application of an external electric field F, fig. 1.2. It uses a number of approximations. Most notably the temperature is assumed to be 0 K and the electrons behave according to the Sommerfeld free-electron model with Fermi-Dirac statistics. The problem is reduced to one dimension by taking the surface to be planar. [110] A relation between F and the resulting emission current density J can be calculated by determining the electron tunneling probability D for electrons approaching the surface. In the absence of F, the electrons are confined to the metal and have kinetic energies below the Fermi surface. The potential barrier B created by the static ion cores has to be lowered in order to increase D which can be calculated using the semi-classical JWKB approximation [125] and is given by [126]

$$D(E,F) = \exp(-G), \tag{1.4}$$

where G is defined by $G \equiv g\int \sqrt{B(x,F)}\,\mathrm{d}x$ where $g = 10.24624\,eV^{-1/2}nm^{-1}$ and x measures the distances in the direction perpendicular to the metal surface. The elementary triangular barrier is then defined by [116]

$$B_{tri}(x,F) = \phi - eFx, \tag{1.5}$$

leading to $G_{tri} = b\phi^{3/2}/F$ with the second Fowler-Nordheim constant $b \equiv 2g/3e \approx 6.830890\ \mathrm{eV}^{-3/2}V\mathrm{nm}^{-1}$. The work function ϕ is defined by the energy necessary to remove an electron from the solid and e denotes the elementary charge equal to $\sim 1.602\times10^{-19}$ C. By using a tunneling exponent correction factor ν and a decay-rate correction factor τ, G can be derived for more general B by

$$G \equiv \nu G_{tri}, \tag{1.6}$$

$$\left(\frac{\partial G}{\partial \phi}\right)_F \equiv \tau\left(\frac{\partial G_{tri}}{\partial \phi}\right)_F, \tag{1.7}$$

With the above assumptions, the current density J is given by [110]

$$J = e\int_0^\infty n(E)D(E,F)\,\mathrm{d}E, \tag{1.8}$$

where n(E) is the number of electrons incident on the barrier per unit area with an energy in the range between E and $E + \mathrm{d}E$ and F denotes the externally applied field.

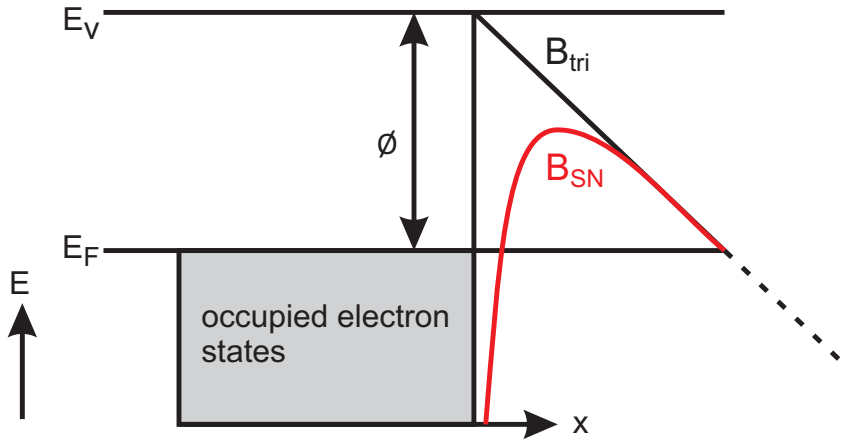

Figure 1.2: Schematic model of field-emission from a flat metallic surface at 0 K. The electrons are confined to the metal and have energies below the Fermi energy E_F. The difference between the vacuum energy E_V and E_F is called the work function ϕ and is the energy necessary to remove an electron from the solid. By applying an external electric field, the barrier is reduced as denoted by B_{sn} when the image potential is considered and B_{tri} if it is neglected

The Schottky-Nordheim barrier is given by [108],

$$B_{SN}(x) = \phi - eFx - e^2/16\pi\epsilon_0 x, \tag{1.9}$$

where the vacuum permittivity ϵ_0 is equal to $\sim 8.8541878 \times 10^{-12}$ Fm^{-1}. The term $e^2/16\pi\epsilon_0 x$ is due to the image potential and rounds of the barrier. Inserting eq. 1.4 using B_{SN} into eq. 1.8 results in [110]

$$J = \frac{aF^2}{\tau_{SN}^2 \phi} \exp\left(-\frac{b\phi^{3/2}}{F} v_{SN}\right), \tag{1.10}$$

where the first Fowler-Nordheim constant a is equal to $e^3/4\hbar \approx 1.541323 \times 10^{-6}$AeVV^{-2}. For B_{SN}, the field F lowers the barrier by the energy [112]

$$\Delta E = \sqrt{\frac{e^3 F}{4\pi\epsilon_0}}. \tag{1.11}$$

Let F_ϕ denote the field at which the barrier is reduced to zero when the local work function is ϕ. Then a scaled barrier field can be defined by [127]

$$f = \frac{F}{F_\phi}. \tag{1.12}$$

In terms of $y = \sqrt{f}$ the correction factors τ_{SN},v_{SN} in equation 1.10 can be written as [128]

$$\begin{aligned} v_{FN}(f) &= (1+y)^{1/2}\left[E(m) - yK(m)\right], \\ \tau_{FN}(f) &= (1+y)^{-1/2}\left[(1+y)E(m) - yK(m)\right], \end{aligned} \tag{1.13}$$

where $m = (1-y)/(1+y)$ and K and E are the complete elliptic integrals of the first and second kind, respectively. [129] The expressions given in eq. 1.13 can be approximated by [127]

$$\begin{aligned} \tau_{FN}(f) &\approx 1 + (1/9)\left[f - (1/2) f ln(f)\right], \\ v_{FN}(f) &\approx 1 - f + qf \log f, \end{aligned} \tag{1.14}$$

with $q \approx 1/6$. Inserting the approximation for $v_{FN}(f)$ into equation 1.10 and noting that $\tau_{FN}(f) \approx 1$ for $0 \leq f \leq 1$ yields the final expression for the current density [123]

$$J = \left[a\phi e^{\eta} F_\phi^{q\eta}\right] F^{2-q\eta} \exp\left(-\frac{b\phi^{3/2}}{F}\right), \tag{1.15}$$

where $\eta = b\phi^{3/2}/F_\phi$. Setting both τ_{FN} and v_{FN} to unity in equation 1.10 results in the so-called elementary Fowler-Nordheim equation.

1.5 Fitting Experimental Data to the Theory

The fitting of experimental current-voltage (I-V) characteristics to equation 1.10 is a widely used practice to demonstrate that the measured current is due to field-emission. Inserting

equation 1.3 into equation 1.10 and multiplying with a notional emission area A to receive the emitted current yields

$$I = \frac{Aa\beta^2 V^2}{\tau_{SN}^2 \phi} \exp\left(-\frac{b\phi^{3/2}}{\beta V} \nu_{SN}\right). \tag{1.16}$$

By defining the fitting parameters $\alpha := Aa\beta^2/\tau_{SN}^2\phi$ and $\gamma := b\phi^{3/2}\nu_{SN}/\beta$, equation 1.16 can be reformed into

$$\log(\frac{I}{V^2}) = \log(\alpha) - \frac{\gamma}{V}. \tag{1.17}$$

Ignoring possible field-dependence in the fitting parameters, plotting the experimental I-V characteristics as $1/V$ versus I/V^2 on a semi logarithmic scale results in a straight line in those cases where the current is due to field-emission.

In principle, the active emission area can be extracted from the ordinate intercept $\log(\alpha)$ if β and ϕ are known. The values of τ_{FN} and ν_{FN} are either taken from tables [106,130,131] or some approximation is used [54,127,132,133] of which the best is that given in equation 1.14, [134] displaying a relative deviation of 0.33% from the exact solution [135] over the whole range $0 \leq f \leq 1$. It was shown, that even without the knowledge of β and ϕ an orders of magnitude estimate of A is possible by measuring I,V and $\mathrm{d}I/\mathrm{d}V$. [132] When emitter tips with apex radii in the nanometer range are used, the experimental behaviour deviates from the straight line plot of equation 1.17 [30, 136, 137]. This deviation can be ascribed to space-charge induced field lowering at the emission site [30] or differences between the actual shape of the potential barrier and the approximate potential barrier B_{SN} used in standard F-N theory. [138]

In this work, a somewhat different approach has been taken in order to monitor the relative change of the emission area and β during the noble gas conditioning presented in chapter 6. Using again two fitting parameters

$$\begin{aligned} A_{FN} &= N_{tip} S_{tip} \frac{ab^2\phi^2}{\tau_{SN}} \exp(\eta), \\ B_{FN} &= b\phi^{3/2}\beta^{-1}, \end{aligned} \tag{1.18}$$

where S_{tip} is the emission area of a single emitter - assumed to be constant across the FEA - and N_{tip} is the number of active emitters. Inserting these parameters into equation 1.10 using equation 1.14 with $q = 0$ for ν_{SN}, $\tau_{SN} \approx 1$ and $J = AI$ results in

$$I = A_{FN} \left(\frac{V}{B_{FN}}\right)^2 \exp\left(-\frac{B_{FN}}{V}\right). \tag{1.19}$$

This gives a better approximation to the experimental data. [116] Since τ_{FN} is close to unity for $0 \leq f \leq 1$, the assumption is justified. Setting $q = 0$ results in better agreement with the experimental data. This is motivated by the possibility of a field dependence of S_{tip} which opposes the $-q\eta$ term in equation 1.15. [139]

Chapter 2

Numerical Modeling of Double-Gate Field-Emitter Array Structures

Contents

To be able to compare the experimental results presented in chapters 4, 5 and 6 to theoretical predictions, a numerical model of the fabricated structures was devised. The simulation is run in three steps. First, the field at the emitter tip apex is calculated for a given bias voltage applied between the extraction gate and the FEA substrate using a two dimensional axisymmetric model in COMSOL Multiphysics. [140] With the obtained field values, the total current and the active emission area can be computed by integrating the F-N equation 1.15 over the emitter surface in MATLAB. [141] These values are then fed into a full three dimensional particle tracking simulation of the emission current in CST Particle Studio. [142] After validating the results of the particle tracking, see chapter 6, the model was extended to higher currents and the inclusion of space-charge effects. In light of the final goal of this work, different acceleration gradients of up to 100 MV/m were calculated for varying collimation gate aperture diameters and the model was reduced in size by a factor of ten. It has recently become possible to fabricate such small emitter tips by exchanging the molding method with an electron beam lithography fabrication process. [143] Such high-density FEAs could be capable of producing a two orders of magnitude higher current level than the double-gate FEAs presented in this work with the same current density increase during collimation, if the emission characteristics are not negatively affected by the size reduction and a sufficiently large G_{col} aperture can be incorporated. The goal of the scaled model is to provide a framework for the further development of high-density double-gate FEAs.

2.1 Calculation of the Emission Current and the Active Emission Area

The multi-step modeling approach is advantageous for the commercial software suites used in this work. Since the calculated current levels need to reflect those measured in the experiments, the calculated emission has to be governed by the F-N equation 1.15, necessitating a sub-nanometer mesh for the calculation of the electric field at the emitter apex as shown in figure 2.1 (b). This is done using a two-dimensional axisymmetric model and an adaptive triangular mesh. The model is built as close as possible to the fabricated structures by studying FIB cross-sections of single emitters and TEM micrographs of a typical emitter apex (see figure 4.2). As an approximation reflecting the average apex radius of curvature across a large FEA, a spherical emitter apex with a radius r_{tip} equal to 10 nm was used in this model. Using the finite element method, [144] the values of the electric field are calculated on each mesh point for a range of collimation voltages. Subsequently, the electric field values along the emitter apex surface are exported for the calculation of the total current and the active emission area.

For the calculation of the total current emitted for a given applied voltage, the current density J has to be integrated over the surface of the emitter tip apex $\vec{S}_{tip}$. This spherical surface can be parametrized by

$$\vec{S}_{tip} = r_{tip} \begin{pmatrix} \cos\theta \cos\varphi \\ \cos\theta \sin\varphi \\ \sin\theta \end{pmatrix}, \tag{2.1}$$

where the angles θ and φ are defined as shown in figure 2.1 (a). With this, the total current I_{tip} is given by [145]

$$I_{tip} = \int_{\vec{S}_{tip}} J \, \mathrm{d}\vec{S}_{tip} = \iint_A J(\theta) \left| \frac{\partial \vec{S}_{tip}}{\partial \theta} \times \frac{\partial \vec{S}_{tip}}{\partial \varphi} \right| \mathrm{d}\theta \, \mathrm{d}\varphi. \tag{2.2}$$

By inserting $\vec{S}_{tip}$ and performing the integration over φ from 0 to 2π, this is reduced to

$$I_{tip} = 2\pi \int_0^{\pi/2} J(\theta) r^2 \cos\theta \, \mathrm{d}\theta. \tag{2.3}$$

To allow the calculation of the total current in MATLAB, equation 2.3 needs to be discretized. This is most conveniently done by using the corresponding Riemann sum which is given by

$$I_{tip} \approx \pi r_{tip}^2 \sum_{i=0}^{n} \left[\theta_{i+1} - \theta_i\right] \left(J(\theta_{i+1}) \cos\theta_{i+1} + J(\theta_i) \cos\theta_i\right). \tag{2.4}$$

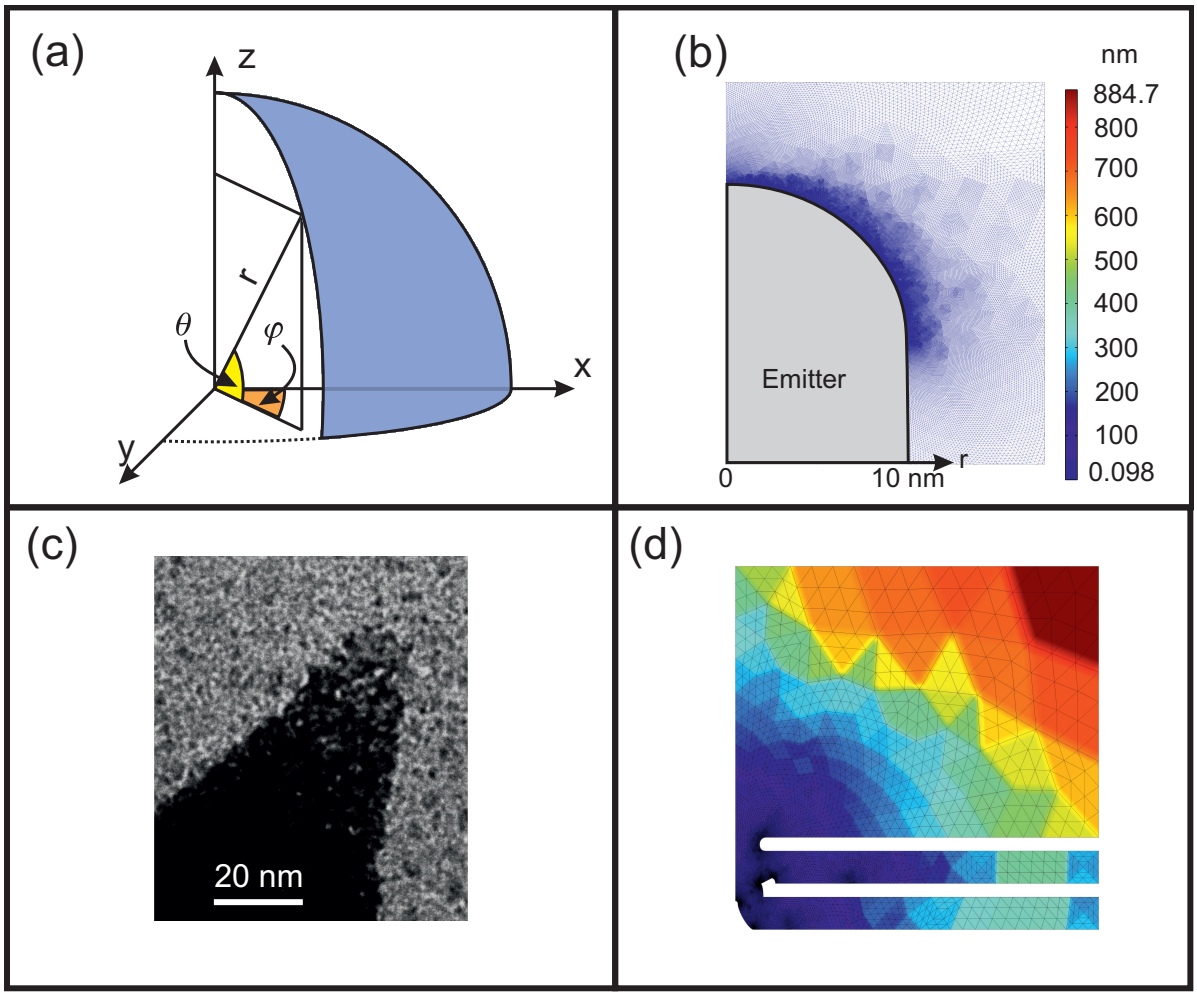

Figure 2.1: (a) Definition of the azimuthal angle φ and the polar angle θ used for integration. (b) Close-up image of the emitter tip apex showing the triangular mesh elements colored by side-length. All mesh elements close to the tip surface have a side length $\lesssim 1$ Å. (c) High-resolution TEM image of a fabricated emitter tip apex for comparison. (d) The full simulation domain of $15 \times 15\,\mu\text{m}^2$ with the mesh size colored according to the legend in (c).

2.2 Full 3-D Simulation of Electron Trajectories

For the simulation of the electron trajectories, a full 3-D model of a single-emitter stacked double-gate structure is used, figure 2.2. Using the finite-differences method, [146] the electric field and the electron trajectories are first calculated in the vicinity of the emitter tip. For that purpose, a virtual anode is placed at a distance of 20 μm along the beam axis. This relatively large distance ensures that the electron trajectories are not influenced by the presence of the virtual anode. During the simulation, the electron trajectories are represented by a predefined number of macro-particles, each representing multiple electrons. The macro-particles have the same charge to mass ratio as a single electron and therefore follow equal trajectories in a given electric field distribution.

The initial positions of these macro-particles lie inside the so-called active emission area A that is defined by the fraction of the emitter tip apex surface encompassing 99% of the total current. A is determined by

$$A = 2\pi r_{tip}^2 \left[1 - \sin(\pi/2 - \theta_{th})\right]. \tag{2.5}$$

For a given t_{tip}, it depends only on θ_{th}, figure 2.2 (c), which can be derived using eq. 2.4. A is covered by an adaptive triangular surface mesh with the center of each triangle defining the initial position of one macro-particle. For the calculation of the electric field and the particle trajectories, the simulation domain is then filled with a hexahedral mesh that has a minimal side length of $\sim$1 nm in the area of the emitter apex $\pm$5 nm in each direction. Due to the specific matrix representation of the discretized Maxwell equations, the finite-differences method was originally limited to a hexahedral mesh. [147] In the meantime, the discretization has been generalized to allow also non-orthogonal meshes that are better suited for the approximation of curved boundaries. [148–150] Unfortunately, the practical implementation of non-orthogonal meshing is very complicated and most finite-differences solvers are still limited to hexahedral meshing. [151] This is also the case for the tracking solver used in this work. However, given a sufficiently dense mesh, the finite-differences method allows for a very accurate reproduction of experimental results. [152]

During the particle tracking simulation, the velocity and position of each macro-particle are recorded upon impact on the virtual anode. These values are then exported and used to initialize a simulation of the full chamber used in the experiment. The imported macro-particles are started at a distance of 20 μm from the chip surface and travel towards the anode that is placed at a distance of 40-50 mm. The results produced with this multi-step simulation approach were in excellent agreement with the experimentally measured evolution of the rms transverse velocity and the rms beam radius for different voltages applied to G_{col} as presented in section **??**.

In figure 2.3, the collimation characteristics of a typical setup are shown. The voltage V_{em} applied between the emitter tips and G_{ext} was set to -72 V, resulting in an emission current of 1.84 pA for the acceleration voltage of 1 kV applied to the anode. The ratio

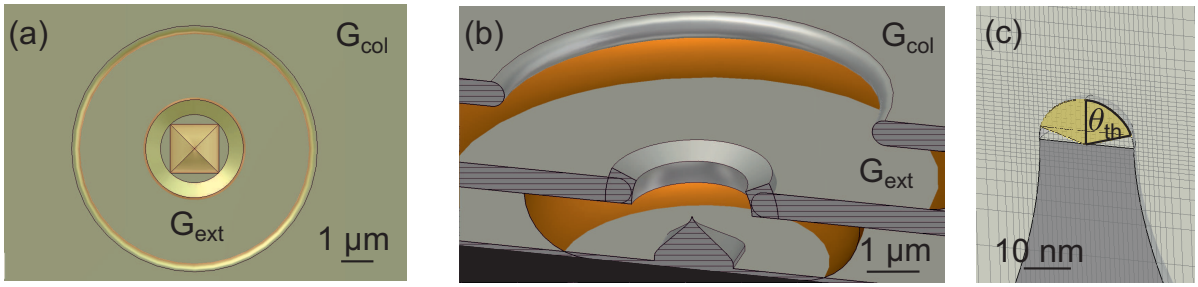

Figure 2.2: (a) Top-view of a full 3-D model of a single-emitter stacked double-gate structure with a G_{col} aperture diameter of 7 μm and a G_{ext} aperture diameter of 2.3 μm. (b) Perspective view of the modeled structure. (c) Close-up view of the emitter tip apex with a 1 nm side length tetrahedral mesh. The active emission area - the area where the macro-particles are started from - is limited by the angle θ_{th} calculated from the electric field.

$k_{col} = V_{col}/V_{em}$, where V_{col} is the voltage applied to G_{col}, was varied between 0 and 0.90 in steps of 0.1 and between 0.91 and 1.05 in steps of 0.01. For $k_{col} = 0$, figure 2.3 (a), the electron beam is uncollimated and displays an emission angle of $\sim 60°$. The increase to $k_{col} = 0.50$, figure 2.3 (c), does not significantly change the emission angle, but the kinetic energy is reduced by ~40%. At $k_{col} = 0.99$, figure 2.3 (e), the electron beam is maximally collimated and nearly parallel. Due to the large G_{col} aperture, the field reduction at the emitter apex is minimal, reducing the current to 50% of its value at $k_{col} = 0$. When k_{col} exceeds 1.0, an increasing part of the macro-particles are deflected to G_{ext} until, finally, at $k_{col} \geq 1.05$ the energy of all particles is reduced so drastically by V_{col}, figure 2.3 (h), that none of them reaches the virtual anode. Instead, they are all caught on G_{ext} which is set to ground potential.

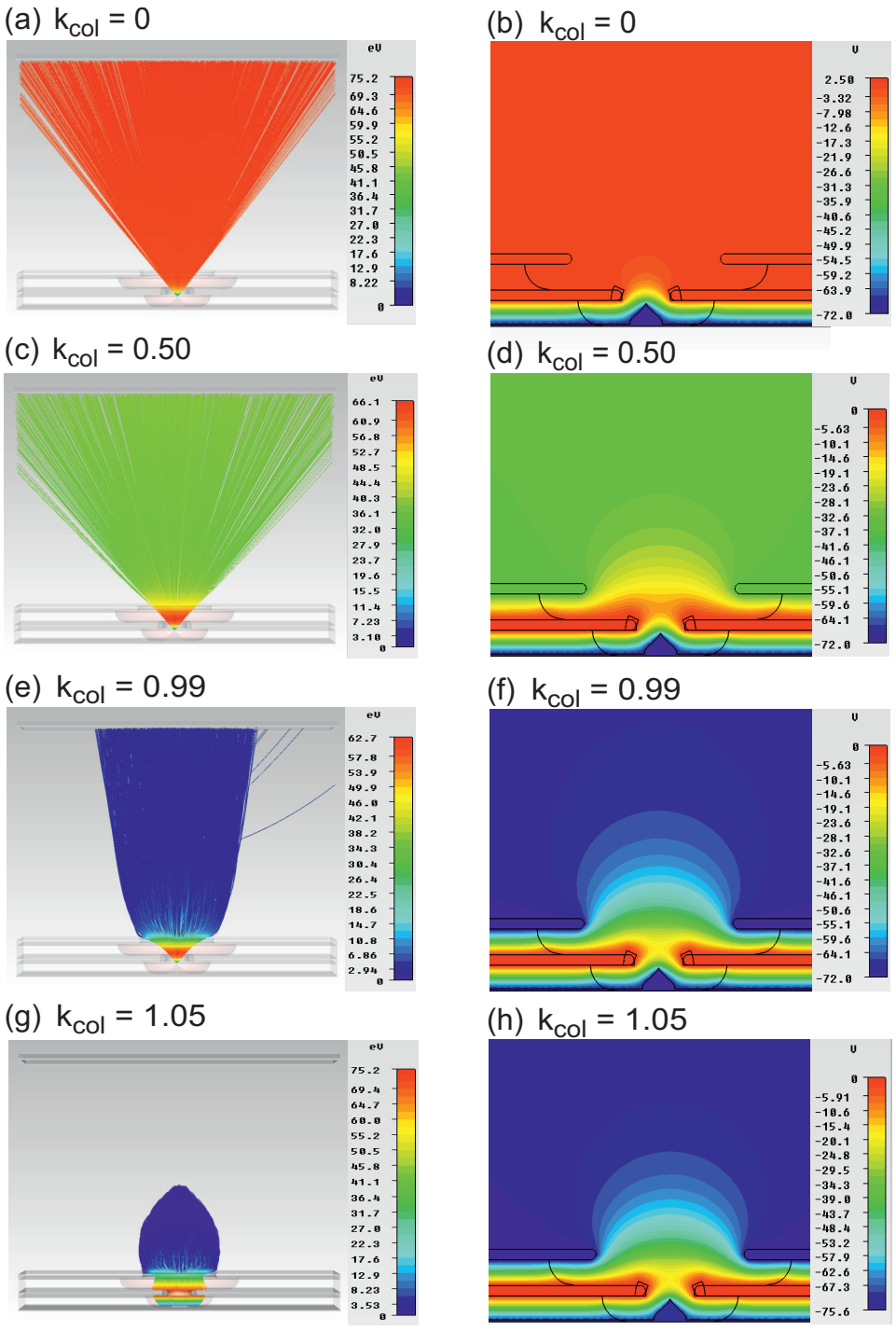

Figure 2.3: In the left column, the particle trajectories in the vicinity of the emitter tips are shown for an emitter bias voltage V_{em} of -72 V at different collimation voltages V_{col}. k_{col} is given by the ratio V_{em}/V_{col}. In the right column, the corresponding potential distributions are presented.

2.3 Results of the Particle Tracking

This section discusses the results achieved by calculating the particle trajectories for the configurations given in table 2.1. All simulations with emitter tips of base length 1.5 μm were simulated with and without the inclusion of space-charge effects. For the high-density emitter tips with a base length of 150 nm, the G_{col} radii were also divided by a factor of ten. The most interesting results are presented in this sections and a full report of the results for all configurations can be found in section D. The G_{ext} radius was set to 1.15 μm for all configurations with emitter tip base length 1.5 μm and 115 nm for those with 150 nm.

G_{col} radius (μm)	F_{acc} (MV/m)	emitter tip base length (μm)
1.0	0.025	0.15
1.5	3	1.5
2.0	30	
2.5	100	
3.0		
3.5		
4.0		

Table 2.1: Overview of the different configurations used in the simulation. For the high-density emitter tips with 150 nm base length, the G_{col} radii given here were also divided by a factor of ten.

To simulate the electron trajectories without the inclusion of space-charge effects, a constant emission voltage V_{em} of -80 V was applied to the emitters. The extraction voltage V_{ext} applied to G_{ext} was set to ground potential and the collimation voltage V_{col} applied to G_{col} was set according to the ratio $k_{col} = V_{col}/V_{em}$. The calculation of the electron trajectories for a predefined range of k_{col} values was then carried out for the G_{col} aperture diameters and acceleration fields F_{acc} listed in table 2.1.

As can be expected, the G_{col} aperture diameter greatly influences the observable electron beam properties. With the smallest simulated diameter of 2 μm, 40% of the emitted current is trapped by G_{col} when F_{acc} is set to 25 kV/m and even at an F_{acc} of 100 MV/m, 30% of the current is trapped. For both of these F_{acc}, the percentage does not decrease significantly when k_{col} is increased from 0 to 0.5. This behaviour is observed to a lesser degree also with larger G_{col} diameters up to 5 μm above which no current is intercepted by G_{col} at any values of k_{col} and F_{acc} (see figure D.2 in the appendix). The collimation gate could, in principle, be employed as a beam blind when the aperture diameter is sufficiently small, thereby achieving a small beam spot size with a small transverse velocity spread. Due to the massive current reduction, however, no current density increase can be achieved in this way and the level of the current reaching the anode is too low for high-brightness applications. The G_{col} aperture diameter also influences the field at the emitter apex when

a high acceleration gradient is applied. For F_{acc} equal to 100 MV/m, the emission current at $k_{col} = 0$ is increased by a factor of $\sim$4.5 from 2.08 nA at a G_{col} aperture diameter of 2 μm to 9.45 nA at a G_{col} diameter of 7 μm. No such influence is found in the case of the lowest F_{acc} of 25 kV/m. The abstract collimation strength of a specific G_{col} aperture diameter can be quantified by the k_{col} value of the inflection point of the plotted curves for the rms transverse velocity u_t and the rms beam radius R_s which marks a cross-over (see figures D.4 and D.5 in the appendix). This inflection point is shifted to higher k_{col} values with increasing G_{col} aperture diameter.

For the stacked double-gate structure, the maximum collimation is found for a G_{col} aperture diameter of 6 μm at $k_{col} = 2.825$ and $F_{acc} = 100$ MV/m. With these parameters, the calculated u_t given as a fraction of the speed of light in vacuum c_0 is equal to 4.71×10^{-5} and R_s is equal to 2.7 μm. Among the simulation configurations calculated in this work, a unique behaviour is found for $F_{acc} = 100$ MV/m in combination with a G_{col} aperture diameter of 4 μm (see figure D.6 in the appendix). In this case, the smallest transverse velocity is achieved with $k_{col} = -0.25$. The values of u_t/c_o and R_s equal to 5.98×10^{-5}, respectively, are nearly as good as in the previous case. However, due to the positive V_{col} applied in the second case, the emission current is maintained high and a ten times higher current-density increase is achieved.

For the electron trajectory calculations including space-charge effects, V_{em} was adjusted for each F_{acc} in order to reach an emission current level of 10 μA. Due to the long calculation times required by the gun iteration, [142] the simulation of the collimation characteristics were limited to the G_{col} aperture diameter of 7 μm. The maximal collimation was achieved with $F_{acc} = 100$ MV/m at a k_{col} of 3.85, resulting in u_t/c_o and R_s values of 1.0×10^{-4} and 6.45 μm, respectively (see figure D.7 in the appendix). The current density at the anode placed at a distance of 40 mm from the emitter structure was equal to 0.5 A/cm^2 and the emission current level was 7 μA. The drop in the emission current level from the 10 μA at $k_{col} = 0$ is due to the influence of V_{col} on the emitter apex field. Assuming completely uniform emission across a 2.28 mm diameter FEA with 40,000 emitter tips, this results in a current density on the anode equal to 0.7 A/cm^2 and a total current of 28 mA.

If the collimation characteristics can be conserved, a higher-density double-gate FEA with an increased number of emitter tips per area can deliver higher current levels and higher current densities. To test the feasibility of this approach, the originally modeled structure was scaled down by a factor of ten except for the emitter tip apex radius of curvature which was left unchanged at 10 nm. The simulation was then carried out for different G_{col} diameters and F_{acc} as listed in table 2.1 and V_{em} was set to -50 V. For the smallest G_{col} aperture diameter, the same behavior as with the large structures can be observed and the current is intercepted by G_{col}. The maximum collimation was observed at $k_{col} = 1.375$ with the largest G_{col} aperture diameter of 0.8 μm at $F_{acc} = 100$ MV/m, yielding u_t/c_o and R_s values equal to 1.6×10^{-4} and 10.3 μm, respectively (see figures D.11 and D.12). These values are comparable to those observed with the larger structures, meaning that the collimation characteristics only depend on the relative dimensions of the

structure. If this is found to hold true in the experiment, a two orders of magnitude higher current density can be achieved compared to the large emitter FEAs for the same array area.

Chapter 3

Device Fabrication

Contents

In this chapter the different fabrication methods used to prepare the double-gate FEAs are presented. The pyramidal shape emitter tips are formed by creating square holes in a silicon wafer and using an anisotropic wet-etching process. The mold is then filled with a sputtered molybdenum film and electro-plated with a nickel substrate. Subsequently, the silicon wafer is etched off completely. FEAs with sizes ranging from single tips up to 1.2×10^6 tips have been fabricated with these methods. To fabricate gated arrays, a SiO_2 insulator is deposited by chemical vapor deposition. The molybdenum extraction gate electrode is sputtered on top of the insulator and patterned by a self-aligned polymer etch-back method. Repeating these fabrication steps, a stacked double-gate structure is created. Because of the required large size ratio between the extraction and collimation gate aperture openings, the use of the self-aligned method is impractical to pattern the collimation gate apertures. For small FEAs of up to 20×20 emitters, a focused ion beam process can be used to mill through the molybdenum electrode and for larger FEAs, an electron beam lithography process was developed including automatic overlay alignment.

3.1 Self-Aligned Fabrication of Single-Gate Field Emitter Arrays

3.1.1 Fabrication of molybdenum field-emitter arrays

To fabricate arrays of molybdenum field-emitter tips, a molding technique invented by Gray and Green [153] is used. It starts by patterning a photoresist mask on a 4 inch Si (100) wafer with square holes of 1.5 μm side length and a pitch of 5 or 10 μm. For the double-gate FEAs, only the 10 μm pitch arrays can be used due to the large collimation gate aperture G_{col} (see section 3.2). The final size and shape of the emitters is the same for both array pitches. Before spin-coating the wafer with photoresist, a 100 nm thick thermal oxide layer is grown to serve as wet-etching mask. The photoresist is patterned by photolithography and the mask is then transferred to the oxide by dry etching in CHF3 plasma using a reactive-ion etcher (RIE, Oxford RIE 100). The exact etching time is recalibrated before each run by etching a dummy wafer and calculating the etch-rate from the remaining oxide thickness measured in a reflectometer (Sentech, FTPadvance). Then, the wafer is immersed into a 20% potassium hydroxide (KOH) solution heated to 70° C. Because the etching of Si in KOH is anisotropic, the slow etching rate along the [111] facets leads to the formation of pyramidal pits in the Si substrate as shown in figure 3.1.

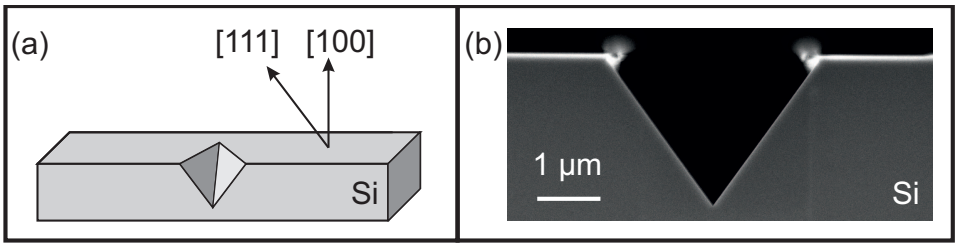

Figure 3.1: (a) Schematic cross-section of the (100) oriented Si wafer. The [111] direction is oriented at an angle of 54.7° to the wafer surface and is etched much slower due to the anisotropic etching properties of Si in KOH, leading to pyramidal pits when the substrate is patterned with square holes. (b) SEM micrograph of the Si wafer after the KOH etching. The bright layer on top is the thermal oxide etching mask.

The pit apex sharpness after the KOH etching is typically in the range of 50-100 nm. Since this sharpness is ultimately transferred to the emitter tips, it is not sufficiently small. This can be amended by thermally oxidizing the mold pits after removing the SiO_2 layer that was used as KOH etching mask. The slower oxide growth at the bottom of the pits due to stress dependent O_2 diffusion [154, 155] sharpens the pit apexes down to a few nanometers. On the downside, this second oxidation step also sharpens the side joints of the [111] facets, figure 3.4 (b), which can potentially cause parasitic emission bombarding the edge of the G_{ext} aperture. Additionally, spikes grow at the topmost edge of the pits which introduce complications in the gate fabrication process described in section 3.1.2 by causing

concave edges at the bottom of the emitters. Adding a third oxidation layer, see figure 3.2, diminishes these problems. [37, 55] After the removal of the second oxide layer, the mold wafer is oxidized yet again, resulting in smooth facet joints of the pyramidal emitter tips while still producing apexes with radii of curvature of a few nanometers, figure 3.4 (a). The final shape of the emitters and the radius of curvature of their apexes depends on the thicknesses of the second and third oxide layers. These are typically chosen to be 200 nm and 600 nm, respectively, which results in apex radii of curvature in the range of ∼5-10 nm, see also section 4.2. These oxide thicknesses are the result of carefully optimizing the smoothness of the facet joints and the emitter apex radii.

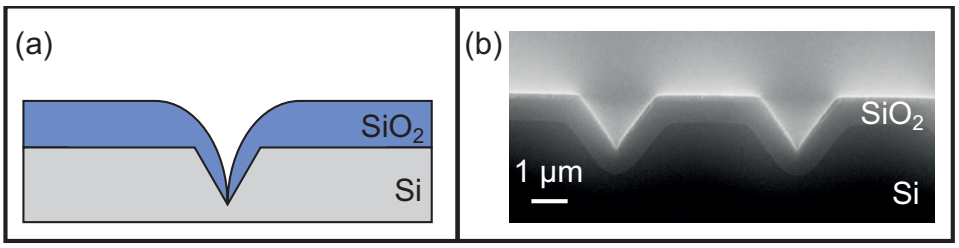

Figure 3.2: (a) Schematic cross-section of the Si mold after thermal oxidation. (b) SEM micrograph of the Si mold after oxidation. Due to the stress dependent O_2. diffusion, the thermal oxide grows slower at the bottom of the pits which leads to sharper emitters.

The process continues by metalizing the oxidized Si mold wafer with a 1 μm thick molybdenum film, figure 3.3, from which the electrons are drawn in the emission experiments. This is done by magnetron sputtering using high-purity ($\geq$ 99.999%) argon gas in a sputter deposition equipment (Nordiko). The flow rate of the argon gas was optimized to deliver a pressure of 1.6×10^2 Pa at a sputtering current of 1.5 A. With these parameters, the stress of the molybdenum film (calibrated by observing the bending of a low-stress Si_3N_4 cantilever upon deposition of the molybdenum film) is minimal. The use of a large sputter target (100×200 mm^2) reduces shadowing within the molded pits across the 4 inch wafer, thus allowing for a uniform metallization of the mold pits at room temperature.

The base pressure of the sputtering chamber is $\sim 2 \times 10^{-4}$ Pa, leading to the incorporation of about 10% O_2 into the film as was measured by X-ray photoelectron spectroscopy. Nevertheless, using high-purity argon gas, the resistivity of the molybdenum film was reduced to $\sim 10\times10^{-6}\,\Omega$cm at room temperature, which is only twice the value exhibited by pure bulk molybdenum. High resolution scanning electron microscopy and X-ray diffraction revealed that the molybdenum film consists of ∼50 nm wide columnar grains oriented perpendicular to the surface of the pits, figure 3.3 (b). Since the growth speed of these grains is not exactly uniform, the surface corrugation eventually shadows the molybdenum flux to the bottom of the pits and a cavity with a diameter in the order of tens of nanometers is left 100-200 nm beneath the emitter apex. It is unknown whether this has any influence on the performance of the FEA. The incorporation of nitrogen gas into the chamber during sputtering results in a smoother surface of the molybdenum film and is especially interesting for the fabrication of FEAs with submicron tips. [156]

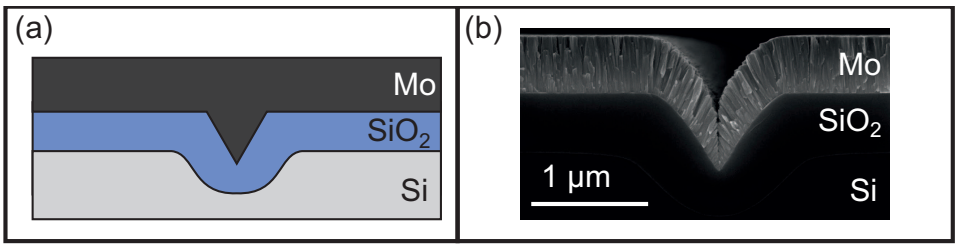

Figure 3.3: (a) Schematic cross-section after the molybdenum sputtering. (b) SEM cross-section after sputtering 500 nm of molybdenum. The thermal oxide layer is used to protect the molybdenum during the subsequent wet-etching to remove the Si wafer.

On the sputtered molybdenum, a 100 nm thick chromium adhesion layer and a 200 nm thick palladium layer are deposited by electron beam evaporation. The palladium functions as a seed layer for the electro-plating of a 400 μm thick nickel layer which serves as substrate after the removal of the Si mold wafer. It has a negligible series resistance of $< 10^{-3}\,\Omega$cm. After the Ni electro-plating, the silicon substrate is completely removed by chemical etching in a heated KOH solution with the same conditions as used for etching the mold pits. The third oxidation layer on the mold protects the surface of the molybdenum layer during the etching. At the end, arrays of pyramidal shaped molybdenum emitters with a base length of $\sim$1.5 μm are obtained. A close-up of a single emitter is shown in figure 3.4 for the case where the third oxidation was carried out, figure 3.4 (a), and also for the case where the molds were filled after the second oxidation step, figure 3.4. Despite the clear difference in the sharpness of the facet joints, the emitter tip apexes in both insets have radii of curvature in the same order. Before the fabrication of the gate electrodes, the FEA wafer is diced into 22×22 mm chips using a diamond blade saw. With the current photolithography mask generation, 12 such chips are patterned on each 4 inch wafer. All further process steps are carried out on these chips. Due to the nature of the Ni growth during electro-plating, the layer thickness varies at the wafer edge which can lead to problems during the overlay alignment in the electron beam lithography step (see also section 3.2.3). For this reason, it is planned to adapt the FEA fabrication process and equipment to 6 inch Si wafers. Details on the parameters used for each fabrication step are given in section B.1

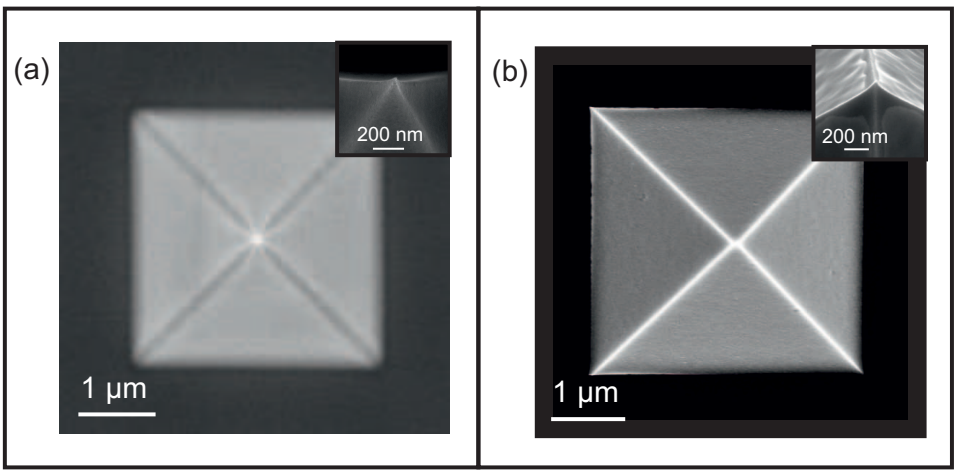

Figure 3.4: (a) Top-view SEM micrograph of an emitter tip from a triple oxidized Si wafer mold with smooth facet joints and sharp apex (inset). (b) Top-view SEM micrograph from a double oxidized Si wafer mold emitter tip with sharp facet joints from which parasitic emission could occur. In the inset, a close-up of the emitter apex is shown.

3.1.2 Extraction gate fabrication

After the sawing, the thick photoresist layer that was spin-coated beforehand is removed in acetone and isopropanol. This step is also important to remove sawing residue from the chip surface that could later lead to short circuits between the emitters and G_{ext}. The third thermal oxidation layer that was used both as etching mask during the KOH etch removal of the Si mold wafer and as protective layer during the sawing is now removed by chemical etching using a buffered oxide etch solution (BOE 7:1; NH_4F and HF in water). Plasma enhanced chemical vapor deposition (PECVD, Oxford PlasmaLab System 80) is then used to deposit a $1.2 \pm 0.05\,\mu$m thick SiO_2 insulator layer (I_1). The SiO_2 deposition rate is calibrated before each fabrication run by measuring the layer thickness deposited on a silicon substrate in a reflectometer. On top of this, 500 ± 20 nm of molybdenum are deposited, forming the G_{ext} layer. This sputter deposition is carried out with the same process parameters as for the mold metalization (see section 3.1.1). The resulting structure is shown in figure 3.5.

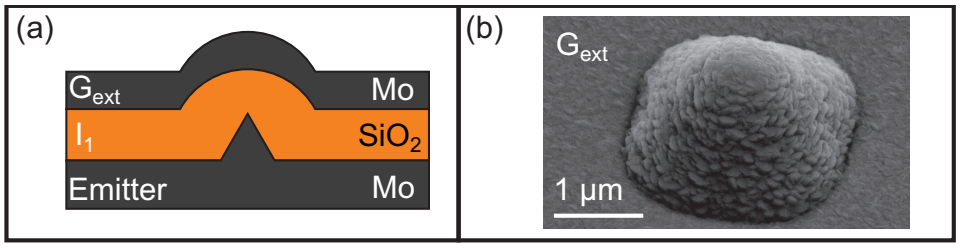

Figure 3.5: (a) Schematic cross-section of an emitter with insulator layer I_1 and the unpatterned extraction gate layer G_{ext}. (b) SEM micrograph showing the G_{ext} layer on top of an emitter tip.

After the deposition of the I_1 and G_{ext} layers, the chip surface exhibits $\sim$ 500 nm tall protrusions on top of the emitters, figure 3.5. These protrusions are utilized in a self-aligned polymer etch-back process to pattern the G_{ext} apertures. First, a $\sim 4\,\mu$m thick photoresist (PR, Microposit S1828) is spin-coated on top of G_{ext} at 2000 rpm and soft-baked at 90° C for 5 min, figure 3.6 (a). Subsequently, the PR-coated FEA is submitted to a low power oxygen plasma (RIE Oxford PlasmaLab System 80) that uniformly thins the PR layer until the molybdenum on top of the emitters is exposed, figures 3.6 (b) and (c). The diameter of the exposed area can be varied between approximately 1 μm and 2.5 μm in diameter by adjusting the time and power of the O_2 plasma etching. With the current parameters of a pressure of 250 mTorr and a power of 50 W, 1.8 μm are reached in approximately 60 min.

The planarity of the spin-coated S1828 is sufficient for the area of a 22×22 mm chip. To have the possibility to process complete wafers at once, Poly methyl methacrylate (PMMA) - a resist commonly used in electron beam lithography - was investigated. [157] Since PMMA is a thermoplastic resist, a reflow effect takes place when it is heated above its glass transition temperature and the planarity of the layer is increased. Using 20% PMMA with a molecular mass of 25 K in Ethyllactate, a 2.6 μm thick layer was spin-coated on a single-gate FEA and baked at 180° for 12 h. The resultant variation in G_{ext} aperture diameter averaged 50 nm across a 22×22 mm chip and is about half the value obtained when using S1828.

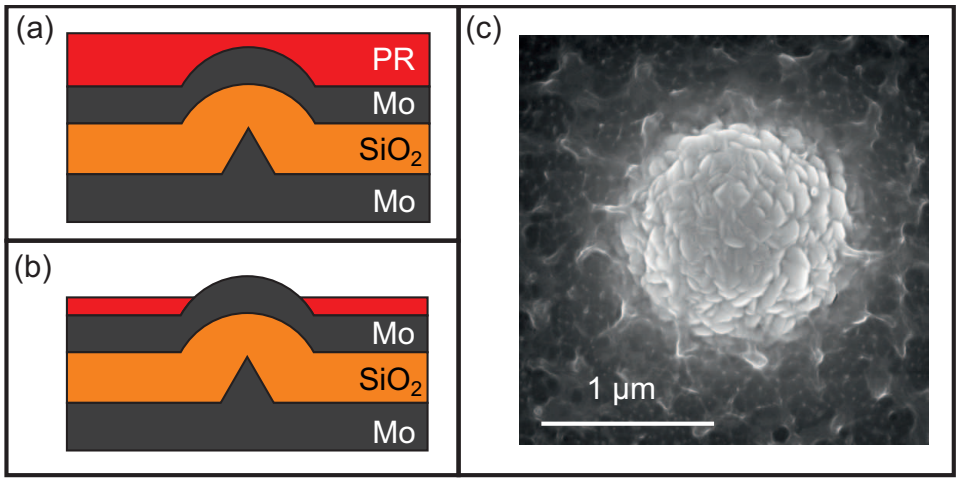

Figure 3.6: (a) Single-gate FEA with unpatterned G_{ext} and photoresist (PR) spin-coated on top. (b) The PR is removed on top of the emitter tips after being exposure to a low-power O_2 plasma. (c) SEM micrograph showing G_{ext} still coated with PR on the flat surface but cleared on the protrusion above the emitter tip.

After the plasma etching, the thinned-down PR is then used as mask for the chemical etching of the G_{ext} apertures in an acid solution (H_3PO_4, CH_3CO_2H, and HNO_3 in 20% water). The resultant structure is shown in figure 3.7 (b). To produce double-gate FEAs, I_1 which covers the emitters at this step is left as protection from ambient air and particles. After the aperture etching, G_{ext} is patterned into its final shape by photolithography and

wet-etching, see also figure 4 in section 5.1. In a completed double-gate FEA, the G_{ext} electrode is buried underneath the collimation gate electrode G_{col} except for the contact pad used for wire bonding, see section 3.2. Details on the parameters used for each fabrication step are given in section B.2.

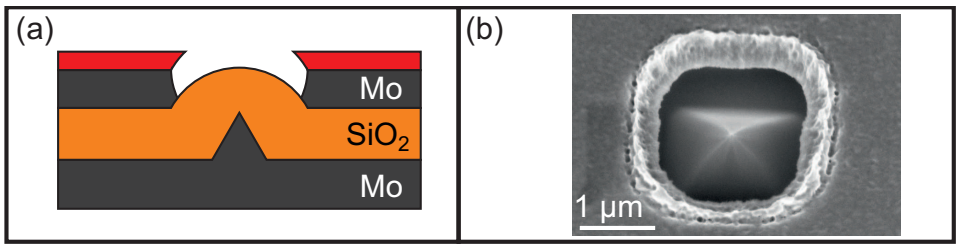

Figure 3.7: (a) After thinning, the PR is used as etching mask (b) Finished single-gate device. When fabricating double-gate FEAs, the SiO_2 insulator remains unetched at this step.

3.2 Fabrication Methods of Double-Gate Field Emitter Arrays

In this section, three methods to fabricate the G_{col} aperture for stacked double gate FEAs are described. After patterning of the G_{ext} electrode, a second insulator layer I_2 of 1.2 μm thickness is deposited on top by PECVD. To reduce the undercut in the final BOE etching step, I_2 consist of SiON which has a slower etch-rate than the SiO_2 used for I_1. Atop of I_2, the 500 nm thick molybdenum G_{col} layer is sputtered with the same conditions as used for the fabrication of G_{ext} and the emitter substrate.

For the G_{col} aperture opening, the self-aligned polymer etch-back method that is employed to fabricate the G_{ext} apertures can also be applied, although the range in achievable aperture diameters is limited to $\lesssim 3.5\,\mu$m. With a focused ion beam (FIB) assisted process, the geometry and size of the G_{col} aperture openings is freely choosable. This method is well suited for rapid prototyping of FEAs with a small number of emitters but impractical for the use on large FEAs due to the required milling time (e.g. ~ 90 s per circular aperture of 6 μm diameter). Using electron beam lithography solves the FIB related problem of long fabrication times by providing a fast alternative to pattern the G_{col} apertures by selectively exposing a resist on top of the structure and also offers complete flexibility in geometry. However, a method of aligning the exposed resist pattern to the underlying structures is necessary.

After the G_{col} apertures have been opened by any of the above methods, the G_{col} electrode is patterned into its final shape by photolithography and wet-etching, see figure 4 in section 5.1. The final step is the removal of the I_1 and I_2 insulator material covering the emitter tips, which is usually done just before inserting the sample into the measurement chamber. In this way, the emitters are protected to minimize their exposure to the ambient air.

3.2.1 Self-aligned polymer etch-back method

The fastest method to pattern the G_{col} apertures is the application of the self-aligned polymer etch-back process that was used for the patterning of the G_{ext} apertures. It allows the processing of arbitrarily large FEAs at once. The achievable aperture diameters are, however, limited to $\lesssim 3.5\,\mu$m and the geometry is defined by the underlying layers. With this method, 40×40 emitter tip FEAs were fabricated with G_{ext} and G_{col} aperture diameters of $1.2\,\mu$m and $3.5\,\mu$m respectively and their electron beam collimation characteristics measured in a field emission microscope (FEM). Due to the large ratio of the G_{ext} and G_{col} aperture diameters, the emission current could be largely upheld during collimation but only a marginal current-density increase was achieved. [76]

3.2.2 Focused ion beam assisted process

As is explained in sections 4.2 and 5.1, the G_{col} apertures need to be approximately 3 times larger in diameter than the G_{ext} apertures to minimize the emission current reduction under collimation conditions. With the self-aligned polymer etch-back process, see also sections 3.1.2 and 3.2.1, this is difficult to achieve in a reproducible way because the required diameter is larger than the protrusions on top of the emitter tips obtained after the deposition of the I_2 and G_{col} layers. Moreover, a circular geometry is preferred for the G_{col} apertures because it collimates the beamlets more evenly than the squarish apertures obtained by the self-aligned process, see figure 1 (b) in section 4.1, resulting in a higher current-density increase.

An alternative method was developed using FIB milling with Ga ions (FEI Strata DB 235). Preliminary experiments showed that direct milling through the G_{col} electrode renders the underlying SiON insulation layer inert to BOE which might be due to the implantation of Ga ions. To circumvent this problem, the G_{col} electrode is only milled to half of its thickness and the rest is subsequently removed by chemical etching. This process requires two sacrificial layers added on top of the FEA: 750 nm of SiO_2 and 100 nm of Mo. In figure 3.8 (a), the milling process is illustrated schematically. The Ga ions (red spheres) bombard the surface and remove atoms with a material dependent rate. The milling is done in an iterative process where the Ga beam is deflected to create a spiraling path from the outside of the circle to the center. When the beam reaches the center it is blanked and the milling is resumed at the initial starting position until the required milling depth is reached. This milling pattern was chosen to minimize the implantation of Ga ions and the deposition of sputtered atoms on the side walls. In figure 3.8 (b)-(e), a series of SEM micrographs show the sample at distinct phases during the milling process of a square pattern (the seemingly rectangular form is due to the tilt of the SEM column): (b) the protrusion on top of an emitter tip is visible before the milling is started. (c) At a depth of 100 nm, the sacrificial Mo layer is almost completely milled through and the square pattern starts to become visible. As mentioned above, circular apertures are advantageous; these square patterns were used to calibrate the milling rate in the sandwiched SiO_2-Mo structure. (d)

After reaching a depth of 200 nm, the redeposited material of the topmost Mo layer is completely removed and the milling continues in the sacrificial SiO_2 layer. (e) When half of the G_{col} electrode is milled, the process is stopped.

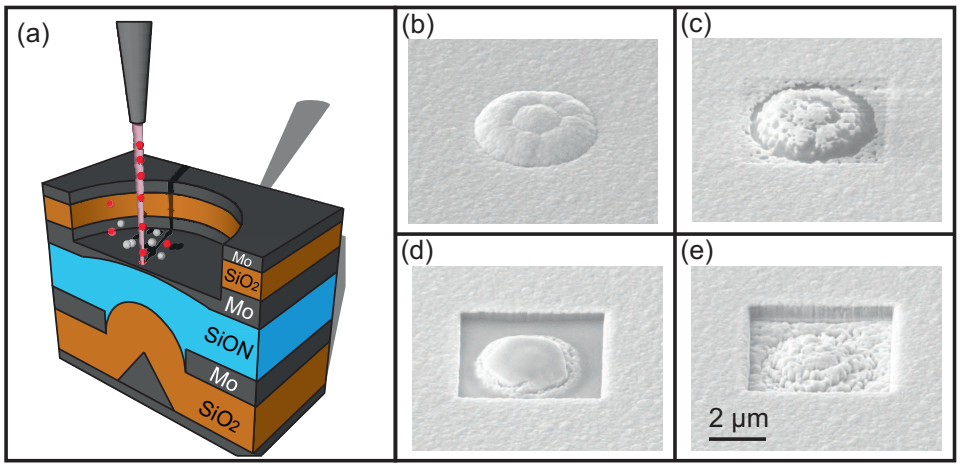

Figure 3.8: (a) Schematic overview of the FIB assisted G_{col} fabrication. When the focused Ga beam (red spheres) impinges on the surface, atoms are sputtered (gray spheres) with a rate depending on the material. The milling is stopped when half of the G_{col} electrode thickness is milled. (b)-(e) SEM micrographs taken during the milling process at depths of 0 nm, 100 nm, 200 nm and 500 nm, respectively. The milling depth is calibrated for Si and does not represent an exact value for the samples used here. Since, compared to pure Si, SiO_2 is milled faster and Mo is milled slower, both sacrificial layer and half of the G_{col} electrode are milled at a nominal depth of $\sim$ 500 nm.

In the next step, the G_{col} aperture opening is completed by chemically etching through the remaining thickness using an acid solution, figure 3.9. The sacrificial SiO_2 layer functions as etching mask and the sacrificial Mo layer is removed. The sacrificial SiO_2 is removed in the final step in BOE together with the insulator material on top of the emitter tips. Because of the sacrificial layers, the G_{col} electrode has to be patterned into its final shape before the FIB milling. The discontinuous layer does not lead to charging during the milling process which is ascribed to the large pattern size (2.5×0.75 mm are used for the 20×20 FEAs, see also figure 4 (d) in section 5.1. This large pattern is also of advantage during the experiment as the bonding wires can be placed at large enough distance of the FEAs to minimize the influence on the electron beam.

No automatic alignment algorithm is used in this process. After switching the device to SEM mode, the milling patterns are aligned manually to the protrusions visible on top of the emitter tips. The use of a pattern generator allows, in principle, for the milling of large FEAs. However, with an FIB milling time of approximately 90 s for each 6 μm diameter aperture with an ion current of 1.5 nA, this amounts to a total FIB milling time for a 20×20 tip FEA of approximately 10 hours without including the time required for stage movements and drift correction. Images of FEAs with G_{col} apertures fabricated by FIB are shown in sections figure 1 in section 4.2 and figure 4 in section 5.1.

This FIB process allows rapid proto-typing of FEAs with different aperture sizes without the

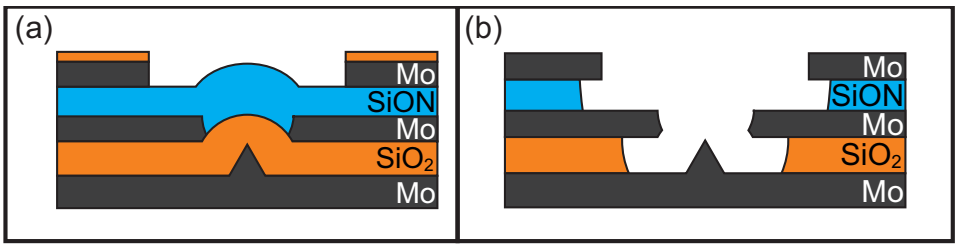

Figure 3.9: (a) After FIB milling, the remainder of the G_{col} aperture is opened by wet-etching using the sacrificial SiO_2 layer as mask. (b) In the final step, the insulator material covering the emitter tips is removed in BOE which also removes the sacrificial SiO_2 layer.

need to modify the preceding fabrication steps in depth. Its high flexibility makes the FIB an ideal tool for exploring the correlation between the gate aperture sizes and the electron beam collimation characteristics. Nevertheless, due to the slow milling speed, the fabrication of large FEAs with thousands of emitter tips is unrealistic. Details on the parameters used for each fabrication step are given in section B.3

3.2.3 Electron beam lithography with automatic overlay alignment

Even though the focused ion beam assisted process is able to produce FEAs with excellent collimation characteristics as shown in sections 4.2 and 5.1, the stringent requirements of the SwissFEL project [4, 5] demand arrays with up to millions of emitter tips to reach the necessary high current. Because of the large ratio of the G_{col} and G_{ext} aperture diameters necessary for the creation of high current-density electron beams, the self-aligned etch-back process, described in section 3.2.1 is not suitable for this task. Therefore, a new method using electron beam (e-beam) lithography was developed.

In electron beam lithography, the electron wavelength is so small that the achievable resolution is no longer defined by diffraction, contrary to conventional optical lithography. It is mainly limited by the scattering of electrons in the resist and substrate and the development of the resist after exposure. [158] These electron scattering effects are commonly referred to as the proximity effect (PEC) and cause exposure of the region surrounding the impact area of the electron beam. [159] With the double-gate FEAs used in this work, the G_{col} apertures had a diameter of $\sim 6\,\mu$m and the array pitch was 10 μm. Although this is nowhere near the resolution limit, a dose variation had to be introduced for PEC. This is determined by using a Monte-Carlo algorithm (PENELOPE, Ref. [160]) to calculate the interaction of the electrons with the FEA substrate during exposure. The pattern to expose is designed in a scripting language (see appendix C for a sample defining various arrays of 4 μm diameter circular apertures) optimized for the input of periodical structures that can then be read and used for exposures by the e-beam software (Layout BEAMER Ref. [161]). This software allows for different exposure strategies to optimize the quality of the exposure and also incorporates the results of the PEC into the calculation of the relative dose. The absolute dose and beam current are defined in a software package

called CJob that transforms the data to the binary format expected by the pattern generator hardware. [162]

Using high-throughput e-beam lithography with 100 keV beam energy (Vistec EBPG5000Plus), a high-sensitivity positive e-beam resist is selectively exposed (ZEP 520A, Zeon Corp.). Prior to the exposure, the resist is spin-coated on top of the FEA at 2000 rpm and soft-baked at 180° C for 180 s resulting in a ∼ 500 nm thick layer, figure 3.10 (a). The I_2 insulator and G_{col} electrode layers are deposited beforehand as described in section 3.2. The subsequent development of the resist is done with a specialized developer (ZED-N50, Zeon Corp.), figure 3.10 (b). Using the patterned resist as etching mask, the G_{col} apertures are opened by wet-etching, figure 3.10 (c). Before the wet-etching, the sample is exposed to oxygen plasma for 100 s to remove resist residues on the exposed and developed surface of the G_{col} layer. In the final step, the I_1 and I_2 insulator material on top of the emitter tips is removed, figure 3.10 (d). With this developed e-beam lithography fabrication method, double-gate FEAs with 4×10^4 emitter tips have been fabricated as shown in figure 1 in section **??**.

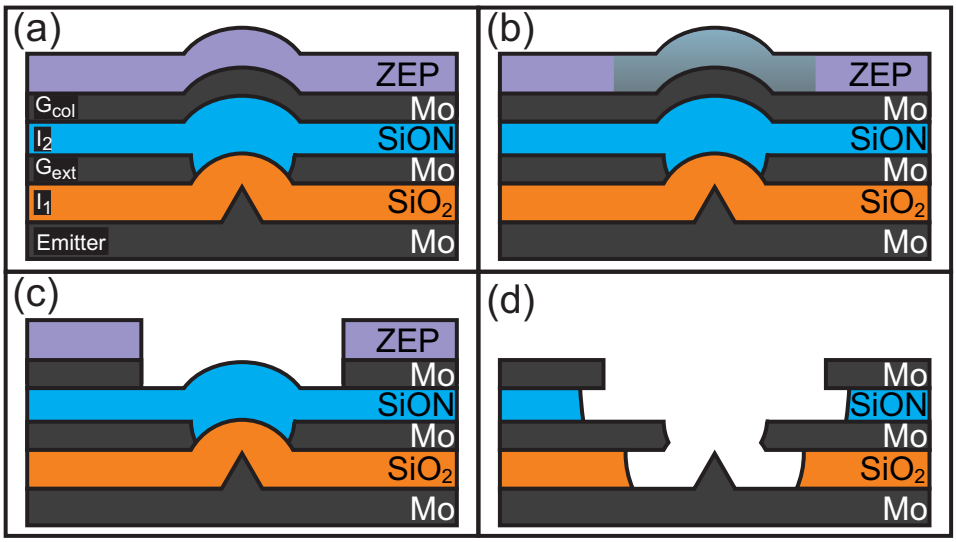

Figure 3.10: Steps to fabricate the G_{col} aperture. (a) Spin coat positive resist on top of collimation gate. (b) Expose resist on top of emitters, using markers for alignment. (c) Develop resist and use it as etching mask for the collimation gate aperture. (d) Removal of the oxide layers covering the tips by wet-etching.

In contrast to the FIB assisted G_{col} fabrication where manual alignment is used, e-beam lithography requires an automatic alignment method using topographical markers. These markers are fabricated simultaneously with the emitter tips during the molding step and consist of truncated pyramids with side lengths of $10 \pm 0.1\,\mu$m on the bottom and $6 \pm 0.1\,\mu$m on the top, figure 3.11 (a). Because of the high electron energy of 100 keV, these markers can be found also when covered by the I_2 and G_{col} layers. It is, favorable to have a continuous conducting layer (G_{col}) on top of the alignment markers because it reduces the number of fabrication steps necessary. The markers are placed in sets of four on all

edges of the 22 × 22 mm chip and also on the edges of each FEA on the substrate. The outermost markers are then used for coarse alignment which is fine-tuned before the exposure of each FEA by using three markers lying closest to it. Using three markers for alignment allows for the correction of the keystone effect (distortion due to a tilted sample relative to the beam axis) next to rotation and stress related changes of the sample size.

Using an optical microscope calibrated to the coordinate system used during the exposure, the approximate coordinates of the alignment markers are noted and passed to the pattern generator as parameters, before starting the exposure. Alignment markers on the sample holder are used to calibrate the coordinate system automatically inside the chamber. The markers for coarse alignment are then searched by moving to the positions given by the user. If the marker is found at once, the position of its center is calculated by using the abrupt change in contrast when passing from the planar top surface to a side wall of the truncated pyramid or vice-versa. If no marker should be found at the expected position, it is searched by a spiraling motion as shown in figure 3.11 (b). The search starts at the marker coordinates input by the user (square S) and moves outward until either the marker is found (square E) or the maximum search area has yielded no result. Details on the parameters used for each fabrication step are given in section B.4.

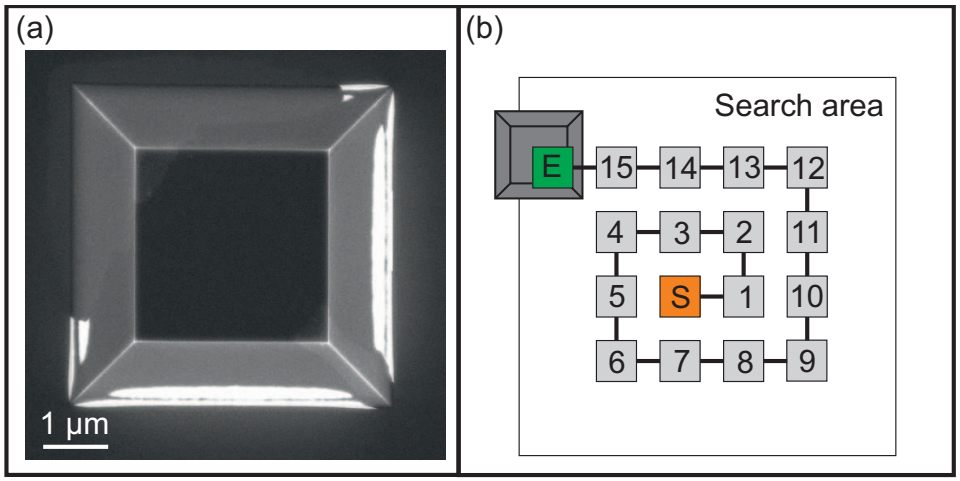

Figure 3.11: (a) SEM micrograph of a molded molybdenum alignment marker fabricated together with the emitter tips. The side length is $10 \pm 0.1\,\mu$m on the bottom and $6 \pm 0.1\,\mu$m on the top. (b) Schematic illustration of the spiral search algorithm applied for the marker search.

Chapter 4

The Influence of the Gate Structure on the Collimation Properties

Contents

In the manuscripts presented in this chapter, the influence of the collimation gate aperture diameter on the performance of the double-gate FEAs in terms of achievable current density increase and beam size reduction is investigated. Measurements carried out with a 40×40 emitter tip FEA with G_{col} aperture openings fabricated by a self-aligned polymer etch-back process have demonstrated that large G_{col} apertures favorably influence the reduction of the emission current under collimation conditions. When the two gate electrodes were set to the same potential, the emission characteristics of the double-gate device were equal to those of a single-gate device fabricated with the same parameters that showed an emission current of $\sim$1 mA with 40×40 emitter tips.

A focused ion beam milling process was then established and used to fabricate double-gate FEAs with a ratio of approximately 3:1 in G_{col} and G_{ext} aperture diameters. With a 2×2 double-gate FEA, a reduction of the emission angle by a factor of 7.1 ± 0.8 with minimal emission current decrease under collimating conditions was demonstrated, resulting in a current density increase of a factor of 13.9 ± 1.0.

IEEE ELECTRON DEVICE LETTERS, VOL. 31, NO. 9, SEPTEMBER 2010 1059

Field-Emission Characteristics of Molded Molybdenum Nanotip Arrays With Stacked Collimation Gate Electrodes

Soichiro Tsujino, *Senior Member, IEEE*, Patrick Helfenstein, Eugenie Kirk, Thomas Vogel, Conrad Escher, and Hans-Werner Fink

***Abstract*—Double-gate field-emission characteristics of metallic field-emitter-array (FEA) cathodes fabricated by molding with stacked collimation gate electrodes with planar end plane are reported. The collimation of field-emission electron beam with minimal reduction of emission current is demonstrated when a negative bias is applied to the collimation gate, whereas when the two electrodes are at the same potential, the emission characteristic of the double-gate device is the same as that of the single-gate device that shows an emission current of ∼1 mA from 40 × 40 tip arrays. Results indicate that the device structure of the fabricated double-gate FEAs is promising for high-brilliance cathode applications.**

***Index Terms*—Collimation, double-gate field-emitter arrays (FEAs), electron emission, high brilliance, metallic emitters, molding.**

I. Introduction

DOUBLE-GATE field-emitter-array (FEA) cathodes having a collimation gate electrode G_c stacked on top of the electron extraction gate electrode $G_{\rm ex}$ have been studied in the past for the purpose of eliminating pixel-to-pixel cross talk in field-emitter displays [1]–[3], for field-ionizer applications [4], and for electron-beam lithography applications [5]–[7]. One other research goal is to achieve the performance requirement with a double-gate FEA for the cathode of a compact free electron laser with subnanometer wavelength, such as Swiss-FEL X-ray free electron laser, as described in [8]. In fact, FEAs can be competitive with the state-of-the-art photocathode [9], [10] when the angular spread $\Delta\theta$ of individual beams is reduced below $\sim 1^\circ$ while keeping the average current density above $\sim$1 kA $\cdot$ cm^{-2}, as demonstrated in single-gate devices [11]. $\Delta\theta$ can be reduced in double-gate FEAs by applying a negative bias V_c to G_c with magnitude comparable to the positive electron extraction bias $V_{\rm ex}$ applied between $G_{\rm ex}$ and emitters, as reported in the literature [1]–[7]. However, since the negative V_c can reduce the electric field $F_{\rm apx}$ at the tip apex and the emission current, the optimization of the device structure minimizing the influence of V_c on $F_{\rm apx}$ is crucial. For the high-brilliance applications in an acceleration gradient on the order of 100 MV/m, device structures with minimal protrusion are preferred to prevent the parasitic breakdown. Our previous approach [12] based on the molded FEAs having the stacked double-gate electrodes showed successful operation of the device, but the emission current decreased substantially by negative V_c. In this letter, we therefore explore the improved field-emission current–voltage characteristics of double-gate FEAs in modified gate aperture geometry.

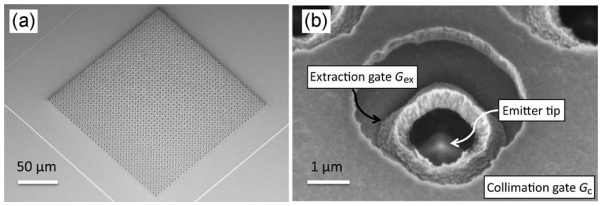

Fig. 1. (a) Scanning electron microscope image of the double-gate FEA cathode with 40 × 40 tips. The emitters are aligned with 5-μm pitch. (b) High-resolution image of one of the emitters from (a). The apex of the molybdenum emitter can be seen as the bright spot inside the extraction gate aperture.

II. Sample and Experiment

We fabricated single-gate FEA devices, namely, SG1 and SG2, and a double-gate FEA, called DG, having 40 × 40 tip array (Fig. 1). SG1 was fabricated using an FEA wafer with an apex diameter $a_{\rm apx}$ of ∼10 nm. SG2 and DG were fabricated using an FEA wafer with $a_{\rm apx}$ of ∼20 nm. In addition, a 4 × 4 tip double-gate FEA was fabricated together with DG. The FEA wafers were fabricated by the molding method [12]–[15] supported by 0.4-mm-thick electroplated nickel. The emitters have 1.5-μm-square base size and ∼1.2-μm height, aligned with 5-μm pitch in the arrays. A $G_{\rm ex}$ layer was 0.5-μm-thick Mo film separated from the arrays by 1.2-μm-thick SiO_2 film deposited by plasma-enhanced chemical vapor deposition. For the double-gate FEAs, a G_c layer of 0.5-μm-thick Mo was added on top of the extraction gate separated by 1.2-μm-thick SiON. The diameter of $G_{\rm ex}$ apertures of SG1 and SG2 was equal to 2.3 ± 0.1 μm. The aperture diameters of DG

Manuscript received May 6, 2010; revised May 25, 2010; accepted May 27, 2010. Date of publication July 19, 2010; date of current version August 25, 2010. This work was supported in part by the SwissFEL Project, Paul Scherrer Institute, and in part by the Swiss National Science Foundation under Grant 200021-125084. The review of this letter was arranged by Editor J. K. O. Sin.

S. Tsujino, P. Helfenstein, E. Kirk, and T. Vogel are with the Laboratory for Micro- and Nanotechnology, Paul Scherrer Institut, 5232 Villigen, Switzerland (e-mail: soichiro.tsujino@psi.ch; patrick.helfenstein@psi.ch; eugenie.kirk@psi.ch; thomas.vogel@psi.ch).

C. Escher and H.-W. Fink are with the Physics Institut, University Zürich, 8057 Zürich, Switzerland (e-mail: escher@physik.uzh.ch; hwfink@physik.uzh.ch).

Color versions of one or more of the figures in this letter are available online at http://ieeexplore.ieee.org.

Digital Object Identifier 10.1109/LED.2010.2052013

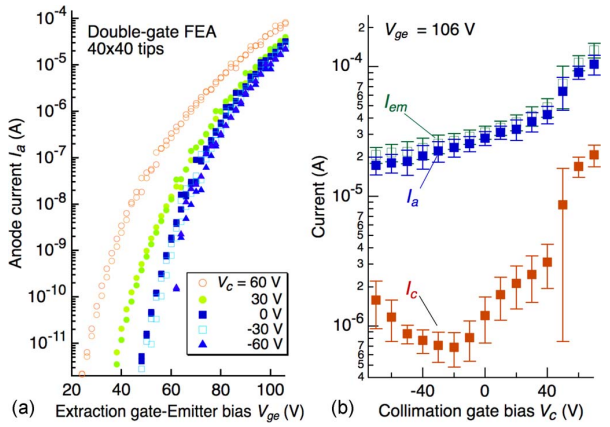

Fig. 2. Field-emission characteristics of the double-gate FEA DG with 40 × 40 emitter tips. (a) Anode current I_a as a function of the bias voltage $V_{\rm ge}$ applied between the extraction gate $G_{\rm ex}$ and the emitter for several collimation gate biases V_c between 60 and −60 V. (b) Variation of I_a, the emitter current $I_{\rm em}$, and the collimation gate current I_c, when V_c was varied between −70 and 70 V when $V_{\rm ge}$ was fixed at 106 V.

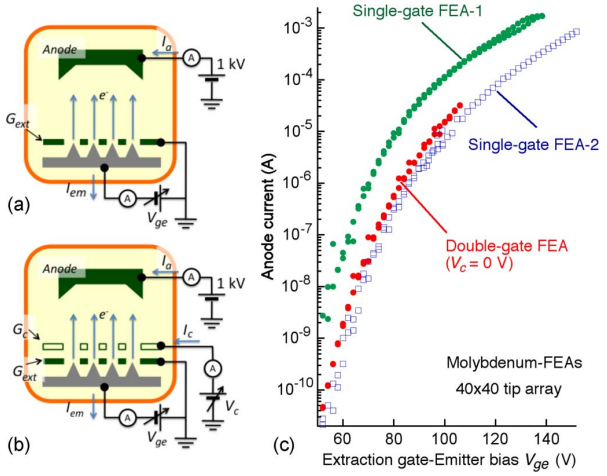

Fig. 3. Schematic diagram of the measurement setup of (a) single-gate FEAs and (b) double-gate FEA. The FEAs and the anode (separated by 10 mm) were mounted in the vacuum chamber (background pressure of $\sim 10^{-9}$ mbar), represented by the enclosed area. (c) Anode current I_a versus extraction gate-emitter bias $V_{\rm ge}$ for two single-gate FEAs, namely, SG1 and SG2, and a double-gate FEA, called DG, with the bias V_c at the collimation gate G_c fixed at 0 V. All the devices have 40 × 40 emitters. SG1 was fabricated using an emitter array with emitter apex diameter of ∼10 nm. SG2 and DG were fabricated using arrays with an emitter apex diameter of ∼20 nm.

were equal to 1.2 ± 0.1 μm for $G_{\rm ex}$ and 3.5 ± 0.1 μm for G_c, respectively. The details of the fabrication procedure were described elsewhere [12].

The field-emission characteristics were measured in the set-ups shown in Fig. 3(a) and (b). The field-emission microscopy experiment was conducted in a separate dedicated system, where the electron beam was amplified by a multichannel plate and imaged by a phosphor screen, Fig. 4(a). The screen assembly was separated from the devices by 30 mm.

III. Results and Discussions

Fig. 2(a) shows the I_a–$V_{\rm ge}$ characteristics of DG for V_c between −60 and 60 V measured in the setup shown in Fig. 3(a) and (b). When we increased V_c negatively, the I_a–$V_{\rm ge}$ characteristic shifts toward the larger $V_{\rm ge}$ direction because of the decrease of $F_{\rm apx}$ with negative V_c. However, the sensitivity of I_a to V_c is five orders of magnitude weaker than that to $V_{\rm ge}$. Fig. 2(b) shows the I_a, the current $I_{\rm em}$ injected to the emitter substrate, and the current I_c through G_c. We observe tendencies that I_c increases faster than I_a and $I_{\rm em}$ for positive V_c and a slight increase of I_c with the decrease of V_c for V_c below −20 V. The former can be ascribed to the increased capture of the field-emission electrons by G_c, while the latter can be ascribed to field emission from the $G_{\rm ex}$ edges to G_c, as observed in [16]. Nevertheless, I_c, as well as the difference between $I_{\rm em}$ and I_a, is less than 5% of I_a for V_c below 0 V; the capture of the field-emission electrons by $G_{\rm ex}$ and G_c is minimal, and the gate leak currents are small.

The observed emission current characteristic fits well to $I_a = AV^{\rm n} \exp(-B/V)$, with n equal to two [17] and with the total effective bias voltage V equal to $(V_{\rm ge} + \gamma V_c)$, where γ is the contribution of V_c to the apex field. From the result of Fig. 2, we evaluated γ to be equal to 0.17 ± 0.014. The evaluation error represents the bound that the rms spread of the quantity $\ln(I_a/V^2)$ is below 4% when V is equal to 60 V for V_c between −70 and +70 V. The observed value of γ is comparable to the theoretical parameter $\gamma^{(\rm th)}$ given by $(1 + D_c/D_{\rm ex})^{-1}$ that is equal to 0.18 ± 0.01, obtained from the device geometry, where $D_{\rm ex}$ and D_c are the distances between the emitter apex and $G_{\rm ex}$ and G_c, respectively. Here, $\gamma^{(\rm th)}$ was derived by assuming that $F_{\rm apx}$ is proportional to $[V_{\rm ge}/D_{\rm ex} + (V_c + V_{\rm ge})/D_c]$. We also note that the previously reported double-gate device [12], which was fabricated from the same emitter array as DG and exhibited a reduction of I_a by a factor of 10^3 for V_c of −70 V, had a factor of ∼3 larger $D_{\rm ex}/D_c$ ratio and γ-value than the present device. This is consistent with the aforementioned analysis.

In Fig. 3(c), we compare the I_a–$V_{\rm ge}$ characteristics of DG with V_c equal to 0 V with two single-gate devices. All three devices have 40 × 40 emitter arrays. We observed that the I_a of the single-gate devices reaches ∼1 mA at a $V_{\rm ge}$ of 130–150 V. The maximum I_a of DG was somewhat lower due to the premature failure of the device, but its I_a–$V_{\rm ge}$ characteristic is same as that of SG2 within ∼5 V of $V_{\rm ge}$. This shows the uniformity of the single- and double-gate fabrication processes over the 40 × 40 tips.

Finally, to study the effect of V_c on the electron-beam collimation, we measured the beam profile in low current regime, Fig. 4, using the double-gate device having 4 × 4 emitters. Similar to the large array device, the decrease of $I_{\rm em}$ for the 4 × 4 emitter array was 20% when V_c was decreased from 0 to −70 V, Fig. 4(d). Fig. 4(b) shows that, when $V_{\rm ge}$ was fixed at 86 V, the beam exhibited the emission angle $\Delta\theta$ of $(20 \pm 3)^\circ$ for V_c larger than −30 V. $\Delta\theta$ was evaluated from the full-width at half-maximum of the intensity distribution of the phosphor screen image and the screen-FEA distance D. This value is consistent with the previous observation for single-gate Spindt-type FEAs [18], [19]. When V_c was further decreased to

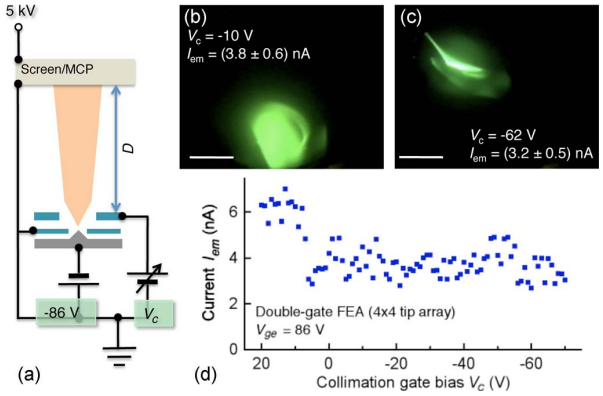

Fig. 4. (a) Schematic diagram of the electron-beam imaging experiment setup for the double-gate FEA with 4×4 emitters with a fixed $V_{\rm ge}$ of 86 V. (b) and (c) show the result for V_c that is equal to -10 and -62 V, respectively, when the distance D between FEA and screen was equal to 30 mm. The bars indicate 10-mm length on the screen. (d) Relation between $I_{\rm em}$ and V_c during the measurement.

-62 V, $\Delta\theta$ was decreased to $(2.3 \pm 0.4)^\circ$ in one direction. The asymmetry and distortion of the collimated beam shape should be improved by careful design of the electrode shape [20] and by elimination of the parasitic field due to the screen assembly, extraction gate, electrical contact assembly of the FEA mount, and aperture shapes in future experiments. A detailed analysis of the observed collimation characteristic and its comparison with theory will be described elsewhere [21].

In summary, we have shown that, by engineering the aperture sizes, it is possible to collimate the field-emission electron beam while minimizing the emission current reduction in double-gate FEAs with stacked G_c with planar end plane. Further optimization of the device structures, such as the gate electrode thicknesses [7], gate insulator thicknesses, and gate aperture sizes, is the next subject of research.

ACKNOWLEDGMENT

The authors would like to thank A. F. Wrulich, J. Gobrecht, and H.-H. Braun for their support and helpful discussions on the FEA applications for FEL; B. Haas, J. Lehmann, and A. Weber for their technical help for the FEA fabrication; and M. Dehler and S. C. Leemann for the discussions on the emittance modeling.

REFERENCES

[1] W. D. Kesling and C. E. Hunt, "Beam focusing for field-emission flat-panel displays," *IEEE Trans. Electron Devices*, vol. 42, no. 2, pp. 340–347, Feb. 1995.

[2] J. Itoh, Y. Tohma, K. Morikawa, S. Kanemaru, and K. Shimizu, "Fabrication of double-gated Si field emitter arrays for focused electron beam generation," *J. Vac. Sci. Technol. B, Microelectron. Process. Phenom.*, vol. 13, no. 5, pp. 1968–1972, Sep. 1995.

[3] L. Dvorson, M. Ding, and A. I. Akinwande, "Analytical electrostatic model of silicon conical field emitters—Part I," *IEEE Trans. Electron Devices*, vol. 48, no. 1, pp. 134–143, Jan. 2001.

[4] L.-Y. Chen, L. F. Velasquez-Garcia, X. Wnag, K. Teo, and A. I. Akinwande, "A micro ionizer for portable mass spectrometers using double-gated isolated vertically aligned carbon nanofiber arrays," in *IEDM Tech. Dig.*, 2007, pp. 843–846.

[5] L. R. Baylor, D. H. Lowndes, M. L. Simpson, C. E. Thomas, M. A. Guillorn, V. I. Merkulov, J. H. Whealton, E. D. Ellis, D. K. Hensley, and A. V. Melechko, "Digital electrostatic electron-beam array lithography," *J. Vac. Sci. Technol. B, Microelectron. Process. Phenom.*, vol. 20, no. 6, pp. 2646–2650, 2002.

[6] Y. Neo, T. Soda, M. Takeda, M. Nagao, T. Yoshida, C. Yasumuro, S. Kanemaru, T. Sakai, K. Hagiwara, N. Saito, T. Aoki, and H. Mimura, "Focusing characteristics of double-gated field-emitter arrays with a lower height of the focusing electrode," *Appl. Phys. Express*, vol. 1, p. 053 001, 2008.

[7] A. Hosono, S. Kawabuchi, S. Horibata, S. Okuda, H. Harada, and M. Takai, "High emission current double-gated field emitter arrays," *J. Vac. Sci. Technol. B, Microelectron. Process. Phenom.*, vol. 17, no. 2, pp. 575–579, Mar. 1999.

[8] B. D. Patterson, R. Abela, H.-H. Braun, U. Flechsig, R. Ganter, Y. Kim, E. Kirk, A. Oppelt, M. Pedrozzi, S. Reiche, L. Rivkin, T. Schmidt, B. Schmitt, V. N. Strocov, S. Tsujino, and A. F. Wrulich, "Coherent science at the SwissFEL X-ray laser," *New J. Phys.*, vol. 12, p. 035012, 2010.

[9] M. Dehler, "Design and modeling of field emitter arrays for a high brilliance electron source," in *Proc. 9th ICAP*, Chamonix, France, Oct. 2–6, 2006, pp. 114–117.

[10] Y. Ding, A. Brachmann, F.-J. Decker, D. Dowell, P. Emma, J. Frisch, S. Gilevich, G. Hays, P. Hering, Z. Huang, R. Iverson, H. Loos, A. Miahnahri, H.-D. Nuhn, D. Ratner, J. Turner, J. Welch, W. White, and J. Wu, "Measurements and simulations of ultralow emittance and ultrashort electron beams in the linac coherent light source," *Phys. Rev. Lett.*, vol. 102, no. 25, p. 254 801, Jun. 2009.

[11] P. R. Schwoebel, C. A. Spindt, and C. E. Holland, "High current, high current density field emitter array cathodes," *J. Vac. Sci. Technol. B, Microelectron. Process. Phenom.*, vol. 23, no. 2, pp. 691–693, Mar. 2005.

[12] E. Kirk, S. Tsujino, T. Vogel, J. Gobrecht, and A. Wrulich, "Fabrication of all-metal field emitter arrays with controlled apex sizes by molding," *J. Vac. Sci. Technol. B, Microelectron. Process. Phenom.*, vol. 27, no. 4, pp. 1813–1820, Jul. 2008.

[13] H. F. Gray and R. F. Greene, "Method of manufacturing a field-emission cathode structure," U.S. Patent 4 307 507, Dec. 29, 1981.

[14] M. Nakamoto, T. Hasegawa, T. Ono, T. Sakai, and N. Sakuma, "Low operation voltage field emitter arrays using low work function materials fabricated by transfer mold techniqu," in *IEDM Tech. Dig.*, Dec. 1996, pp. 297–300.

[15] K. Subramanian, W. P. Kang, J. L. Davidson, R. S. Takalkar, B. K. Choi, M. Howell, and D. V. Kerns, "Enhanced electron field emission from micropatterned pyramidal diamond tips incorporating CH4/H2/N2 plasma-deposited nanodiamond," *Diamond Relat. Mater.*, vol. 15, no. 4–8, pp. 1126–1131, Apr.–Aug. 2006.

[16] M. Nagao, T. Yoshida, S. Kanemaru, Y. Neo, and H. Mimura, "Fabrication of a field emitter array with a built-in Einzel lens," *Jpn. J. Appl. Phys.*, vol. 48, no. 6, p. 06FF K02, 2009.

[17] C. A. Spindt, I. Brodie, and L. Humphrey, "Physical properties of thin-film field emission cathodes with molybdenum cone," *J. Appl. Phys.*, vol. 47, no. 12, pp. 5248–5263, 1976.

[18] P. M. Phillips, C. Hor, L. Malsawma, K. L. Jensen, and E. G. Zaidman, "Design and construction of apparatus for characterization of gated field emitter array electron emission," *Rev. Sci. Instrum.*, ser. 6, vol. 67, pp. 2387–2393, Jun. 1996.

[19] S. C. Leemann, A. Straudel, and A. Wrulich, "Beam characterization for the field-emitter-array cathode-based-low-emittance gun," *Phys. Rev. ST. Accel. Beams*, vol. 10, no. 7, p. 071 302, 2007.

[20] C. Py, J. Itoh, T. Hirano, and S. Kanemaru, "Beam focusing characteristics of silicon microtips with an in-plane lens," *IEEE Trans. Electron Devices*, vol. 44, no. 3, pp. 498–502, Mar. 1997.

[21] P. Helfenstein, E. Kirk, K. Jefimovs, T. Vogel, C. Escher, H.-W. Fink, and S. Tsujino, 2010, unpublished.

APPLIED PHYSICS LETTERS **98**, 061502 (2011)

Highly collimated electron beams from double-gate field emitter arrays with large collimation gate apertures

P. Helfenstein,[1,a)] E. Kirk,[1] K. Jefimovs,[2] T. Vogel,[1] C. Escher,[3] H.-W. Fink,[3] and S. Tsujino[1,b)]
[1]*Laboratory for Micro- and Nanotechnology, Paul Scherrer Institut, CH-5232 Villigen-PSI, Switzerland*
[2]*Electronics/Metrology/Reliability Laboratory, EMPA, Überlandstrasse 129, CH-8600 Dübendorf, Switzerland*
[3]*Physik Institut, University of Zurich, Winterthurerstrasse 190, CH-8057 Zurich, Switzerland*

(Received 4 November 2010; accepted 12 January 2011; published online 9 February 2011)

Electron collimation in field emitter arrays with electron extraction gate and collimation gate electrodes is studied with the goal to develop a high-brightness high current cathode. Using metallic field emitter arrays prepared by the molding method, we fabricated a stacked double-gate device with the two gates differing in diameter by a process utilizing focused-ion beam milling. We measured the field-emission beam characteristics and demonstrated a reduction of the emission angle by a factor of 7.1 ± 0.8 with minimal emission current decrease under collimating conditions, resulting in a current density increase by a factor of 13.9 ± 1.0. © *2011 American Institute of Physics*. [doi:10.1063/1.3551541]

Double-gate field emitter arrays (FEAs) have been studied for high-brightness cathode applications.[1–4] Microwave vacuum electronic devices using single-gate FEAs, which allow for a compact and simplified gun design, have been successfully demonstrated.[5–8] However, a high current density field-emission electron beam with reduced transverse electron velocity spread is a crucial factor in extending the FEA-based vacuum electronic device technology to higher power densities and frequencies in the terahertz gap.[9,10]

In double-gate FEAs, microfabricated field emitters are equipped with an electron extraction gate G_{ext} and a collimation gate G_{col}. By applying a negative bias to G_{col}, the field-emission electron beam can be collimated.[11–19] The reported structures differ in terms of location of G_{col} with respect to G_{ext}, as well as in the number of emitters per single G_{col} aperture. Among these, stacked double-gate devices providing a G_{col} aperture for individual emitters exhibit the smallest electron beam emission angle. Toma *et al.*[17] reported a factor of 15 beam size reduction, but it was accompanied by the decrease of the emission current by a factor of $\sim 10^3$. With volcano-structured double-gated FEAs, electrostatic shielding of the emitter tip from G_{col} in a nonplanar configuration largely prevented current reduction.[19] Although this approach is promising for specific applications such as miniature electron guns for lithography or field-emission displays, device structures with a planar top surface are desirable for applications with high acceleration field strengths such as free electron lasers.[2]

In this letter, we report the fabrication and characterization by field-emission microscope (FEM) of double-gate FEAs with a planar top surface and different gate aperture diameters, which can minimize current reduction at high collimation voltages.[4] By developing a focused-ion beam (FIB)-assisted gate fabrication process and applying it to our molded molybdenum FEAs, we achieve a large reduction in emission angle accompanied by an increased current density.

Our molybdenum FEAs were fabricated by the molding method using silicon (001) wafer substrates.[20] The molybdenum emitters with tip apex diameters of 10–20 nm have a square base with a side length of ~ 1.5 μm and a height of ~ 1.2 μm. The emitter arrays are supported by ~ 400 μm of electroplated nickel. The G_{ext} apertures were fabricated by a self-aligned etch-back and wet-etching process,[20] which leads to square apertures with rounded corners. The achievable extraction gate radii—characterized by the distance from the tip to the closest point of G_{ext}—lie in the range of 1.8–2.5 μm. For the fabrication of the G_{col} apertures, we developed an FIB-assisted process. These were fabricated by FIB milling of a sacrificial mask layer and subsequent wet-etching of the molybdenum G_{col} layer. This enables us to flexibly adjust the G_{col} aperture size and shape. Figure 1 shows scanning electron microscope (SEM) micrographs of the fabricated device. In the experiment described below, we used 2×2 arrays with 10 μm separation between tips and G_{ext} and G_{col} aperture radii of 1.15 ± 0.05 and 3.11 ± 0.05 μm, respectively. After gate aperture fabrication, the G_{col} electrode was patterned into a 1.2 mm diameter circular shape.

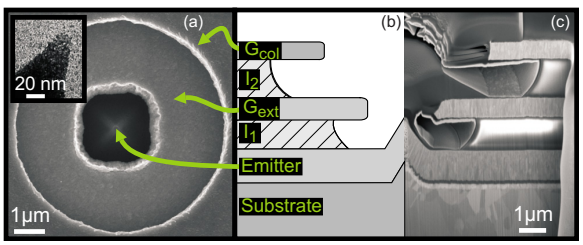

FIG. 1. (Color online) SEM micrographs of a double-gate FEA. (a) Top view and (c) cross-section. (b) Schematic diagram corresponding to the cross-section shown in (c). The shaded layers (I_1 and I_2) are the 1.2 ± 0.1 μm thick SiO_2 insulators. G_{ext} and G_{col} diameters are 2.30 ± 0.05 and 6.22 ± 0.05 μm, respectively. The inlay in (a) shows a transmission electron microscope (TEM) image of the emitter tip apex.

a)Author to whom correspondence should be addressed. Electronic mail: patrick.helfenstein@psi.ch.
b)Electronic mail: soichiro.tsujino@psi.ch.

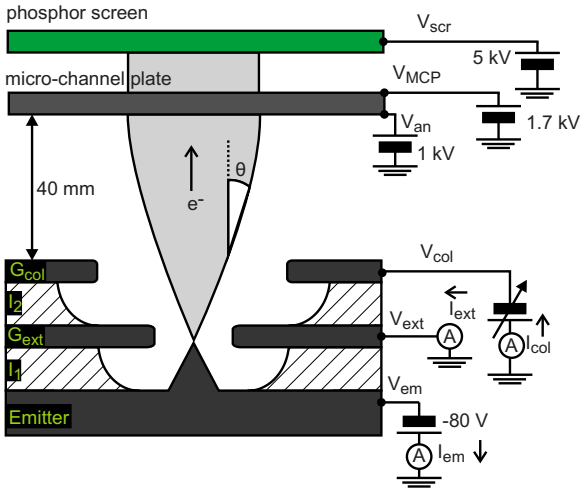

FIG. 2. (Color online) Schematic diagram of the experimental setup. The extracted electron beam is amplified by a microchannel plate biased to 0.7 kV given by ($V_{MCP}-V_{an}$) and detected by the phosphor screen biased at a voltage V_{scr} of 5 kV. The currents I_{em}, I_{ext}, and I_{col} were simultaneously recorded. θ denotes the emission angle of the electron beam at the emitter surface.

The schematic setup of the FEM experiment is depicted in Fig. 2. The FEA chip was mounted on a polyether ether ketone holder and inserted into the FEM chamber which was evacuated to $\sim 5\times 10^{-8}$ mbar. The gate electrodes of up to three double-gate FEAs were wire bonded and connected to electrical feedthroughs. Field emission was initiated by applying negative voltage V_{em} to the emitters while connecting G_{ext} to ground potential. The extracted electron beam was collimated by applying negative voltage V_{col} to G_{col}. We placed the FEA chip at a distance of 40 mm to the microchannel plate (MCP) and the phosphor screen. The emitted electrons were accelerated by a voltage V_{an} of 1 kV applied to the MCP entrance plate, amplified by the MCP, and imaged on the phosphor screen. During the experiment, the current I_{em} injected into the emitter substrate, the current I_{ext} flowing through G_{ext}, and the current I_{col} intercepted by G_{col} were recorded simultaneously with the electron beam image. The net emission current I_{net} that reached the screen assembly was evaluated as ($|I_{em}|-I_{ext}-I_{col}$). At first, the FEA chip was conditioned by scanning V_{em} between 0 and -160 V until I_{net} reached a few microamperes and the current-voltage characteristics stabilized. Subsequently, we applied a constant V_{em} of -80 V with I_{net} between 0.5 and 1 nA to avoid destructive arcing.

In Fig. 3, we show three electron beam images which display the measured reduction in electron beam size and an increase in current density for V_{col} equal to +1, -31, and

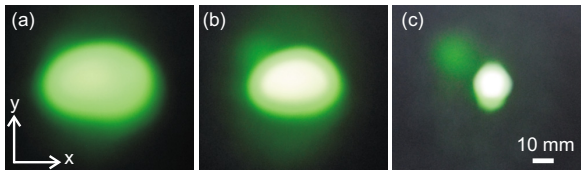

FIG. 3. (Color online) Field-emission microscope images of electron beam at constant extraction bias V_{em} of -80 V at collimation voltages V_{col} of (a) +1, (b) -31, and (c) -61 V.

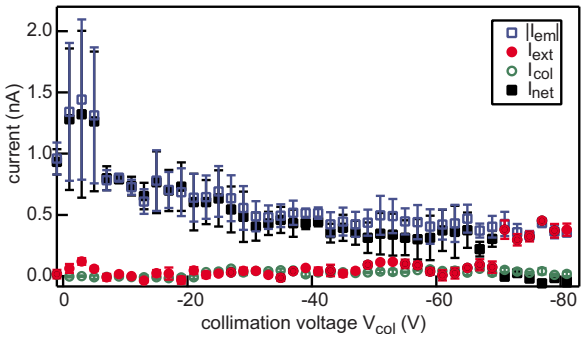

FIG. 4. (Color online) Absolute value of emitter current I_{em} (open squares), net current I_{net} (filled squares), extraction gate current I_{ext} (filled circles), and the collimation gate current I_{col} (open circles) at various V_{col}'s for V_{em} fixed at -80 V.

-61 V, whereas V_{em} was fixed at -80 V. The reduction in electron beam size and the increasing beam brightness with the decrease of V_{col} indicate that the decrease of I_{net} with the decrease of V_{col} is minimal in this voltage range. This is shown by the simultaneously measured current summarized in Fig. 4 for a fixed V_{em} of -80 V. I_{net} was equal to 0.5 ± 0.2 nA for V_{col} between +1 and -65 V, whereas I_{ext} and I_{col} were equal to 0.04 ± 0.03 nA and therefore below $\sim$20% of I_{net}. In Fig. 5(a) we show the variation of the current density on the phosphor screen with the decrease of V_{col}. The current density was evaluated by dividing I_{net} by the beam size for each V_{col}. We found that when V_{col} was decreased from 0 to -69 V, the current density increased by a factor of 13.9 ± 1.0. We note that I_{net} falls to zero for V_{col} beyond -69 V since the electrons are repelled by the potential field of G_{col} and collected by G_{ext} similarly to previous reports.[8–16]

The increased current density at maximal collimation is due to the reduction of the emission angle θ depicted in Fig.

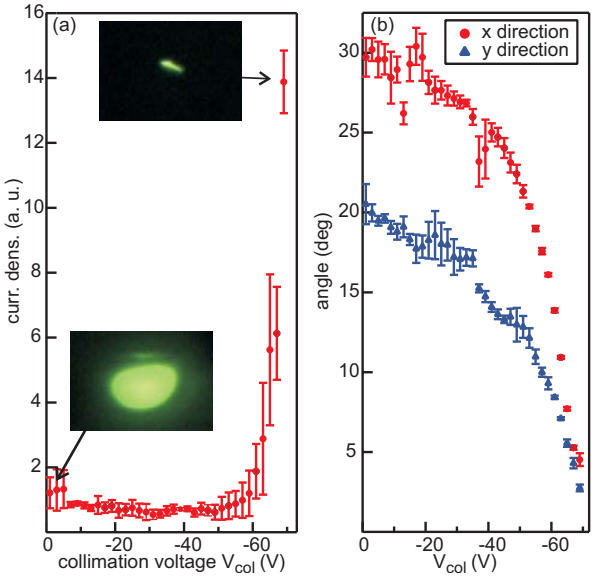

FIG. 5. (Color online) (a) Current density measured on the phosphor screen plotted against V_{col} for fixed V_{em}. The two inlaid pictures show the electron beam at V_{col} of 0 V (bottom) and -69 V (top). (b) The relation between the emission angle θ and V_{col} with the directions as defined in Fig. 3.

2. It is defined as the half width spread of the field-emission electron beam. Using Eq. (1), we evaluated θ at each V_{col} as presented in Fig. 5(b),

$$\frac{D}{L} = \frac{2\tan\theta}{1+\sqrt{1+\frac{V_{an}}{|V_{em}|\cos^2\theta}}}. \quad (1)$$

Herein, the electron beam radius D was obtained from the half width of the half maximum intensity of the phosphor screen image, and L is the distance from the FEA to the MCP and phosphor screen. We found that θ in the x-direction decreased from $29.7° \pm 1.2°$ to $4.5° \pm 0.4°$ when V_{col} was decreased from 0 to -69 V. θ in the y-direction decreased from $20.5° \pm 1.2°$ to $2.7° \pm 0.2°$ at the same time. The reduction factor of θ amounts to (6.6 ± 0.8) and (7.6 ± 0.8) in x- and y-directions, respectively. The asymmetry of the electron beam shape is ascribed to the residual potential distribution of the setup such as the gate contact wires and is partly compensated by the acceleration potential V_{an}.

In summary, using all-metal FEAs combined with self-aligned and FIB-assisted processes, we demonstrated a 14-fold current density increase and a minimal current loss to the extraction gate at large negative collimation voltages. We achieved this by increasing the G_{col} aperture diameter to 6.2 μm through the application of our FIB-assisted process. We thus attained a larger ratio between the two gate-to-tip distances—from emitter tip apex to G_{col} edge and from emitter tip apex to G_{ext} edge—than would have been achievable with the self-aligned process. Also, this larger ratio accounts for the partial shielding of G_{col} from the emitter tip by G_{ext}.[19] Our FIB-assisted process was utilized to produce arrays with well-defined geometric shapes. Further investigations into high tip current operation and upscaling of the emitter array size are needed to realize a high-brightness and high current cathode. Additionally, we expect further improvement in the beam brightness from optimization of the device structure in terms of the gate aperture sizes and the thicknesses of the gate and insulator layers.

The authors would like to thank J. Krbanjevic and E. Minikus for preparing the TEM lamella and taking TEM micrographs. This work was partially supported by the SwissFEL project of the Paul Scherrer Institute and the Swiss National Science Foundation.

[1]M. Dehler, A. Candel, and E. Gjonaj, J. Vac. Sci. Technol. B **24**, 892 (2006).
[2]B. D. Patterson, R. Abela, H. H. Braun, U. Flechsig, R. Ganter, Y. Kim, E. Kirk, A. Oppelt, M. Pedrozzi, S. Reiche, L. Rivkin, T. Schmidt, B. Schmitt, V. N. Strocov, S. Tsujino, and A. F. Wrulich, New J. Phys. **12**, 035012 (2010).
[3]C. M. Tang, M. Goldstein, T. A. Swyden, and J. E. Walsh, Nucl. Instrum. Methods Phys. Res. A **358**, 7 (1995).
[4]S. Tsujino, P. Helfenstein, E. Kirk, T. Vogel, C. Escher, and H. W. Fink, IEEE Electron Device Lett. **31**, 1059 (2010).
[5]H. Makishima, S. Miyano, H. Imura, J. Matsuoka, H. Takemura, and A. Okamoto, Appl. Surf. Sci. **146**, 230 (1999).
[6]D. R. Whaley, B. M. Gannon, V. O. Heinen, K. E. Kreischer, C. E. Holland, and C. A. Spindt, IEEE Trans. Plasma Sci. **30**, 998 (2002).
[7]D. R. Whaley, B. M. Gannon, C. R. Smith, C. M. Armstrong, and C. A. Spindt, IEEE Trans. Plasma Sci. **28**, 727 (2000).
[8]D. R. Whaley, R. Duggal, C. M. Armstrong, C. L. Bellew, C. E. Holland, and C. A. Spindt, IEEE Trans. Electron Devices **56**, 896 (2009).
[9]J. H. Booske, Phys. Plasmas **15**, 055502 (2008).
[10]R. L. Ives, IEEE Trans. Plasma Sci. **32**, 1277 (2004).
[11]L. Dvorson, G. Sha, I. Kymissis, C. Y. Hong, and A. I. Akinwande, IEEE Trans. Electron Devices **50**, 2548 (2003).
[12]A. Hosono, S. Kawabuchi, S. Horibata, S. Okuda, H. Harada, and M. Takai, J. Vac. Sci. Technol. B **17**, 575 (1999).
[13]J. Itoh, Y. Toma, K. Morikawa, S. Kanemaru, and K. Shimizu, J. Vac. Sci. Technol. B **13**, 1968 (1995).
[14]C. Py, M. Gao, S. R. Das, P. Grant, P. Marshall, and L. LeBrun, J. Vac. Sci. Technol. A **18**, 626 (2000).
[15]C. Py, J. Itoh, T. Hirano, and S. Kanemaru, IEEE Trans. Electron Devices **44**, 498 (1997).
[16]Y. Yamaoka, S. Kanemaru, and J. Itoh, Jpn. J. Appl. Phys., Part 1 **35**, 6626 (1996).
[17]Y. Toma, S. Kanemaru, and J. Itoh, J. Vac. Sci. Technol. B **14**, 1902 (1996).
[18]M. Nagao, T. Yoshida, S. Kanemaru, Y. Neo, and H. Mimura, Jpn. J. Appl. Phys. **48**, 06FK02 (2009).
[19]Y. Neo, M. Takeda, T. Soda, M. Nagao, T. Yoshida, S. Kanemaru, T. Sakai, K. Hagiwara, N. Saito, T. Aoki, and H. Mimura, J. Vac. Sci. Technol. B **27**, 701 (2009).
[20]E. Kirk, S. Tsujino, T. Vogel, K. Jefimovs, J. Gobrecht, and A. Wrulich, J. Vac. Sci. Technol. B **27**, 1813 (2009).

Chapter 5

Upscaling of the Array Size by a Focused Ion Beam Assisted Fabrication Process

Contents

In this chapter the scalability of the focused ion beam assisted G_{col} fabrication method is demonstrated by a 20×20 emitter tip double-gate FEA. The measured electron beam characteristics are compared to those obtained with the 2×2 emitter tip double-gate FEA presented in section 4.2 and the reason for the improved current-voltage characteristics of the 20×20 tip array is investigated. To further establish the necessity of large G_{col} apertures to achieve a highly collimated electron beam, the results of the 2×2 emitter tip double-gate FEA are also compared to those of an FEA with small collimation gate apertures, where no current density increase was possible. Finally, the possibility of further improving the beam characteristics of double-gate field emitter arrays and the reduction of the transverse electron velocity spread are discussed.

JOURNAL OF APPLIED PHYSICS **112**, 093307 (2012)

Fabrication of metallic double-gate field emitter arrays and their electron beam collimation characteristics

P. Helfenstein,[1,a)] K. Jefimovs,[2] E. Kirk,[1] C. Escher,[3] H.-W. Fink,[3] and S. Tsujino[1,b)]
[1]*Laboratory for Micro- and Nanotechnology, Paul Scherrer Institut, CH-5232 Villigen-PSI, Switzerland*
[2]*Electronics/Metrology/Reliability Laboratory, EMPA, Überlandstrasse 129, CH-8600 Dübendorf, Switzerland*
[3]*Physik Institut, University of Zurich, Winterthurerstrasse 190, CH-8057 Zurich, Switzerland*

(Received 12 August 2012; accepted 12 October 2012; published online 9 November 2012)

The fabrication of double-gate metallic field emitter arrays with large collimation gate apertures and their field emission beam characteristics are reported. The device fabrication steps, including the molding technique for array fabrication, the electron extraction gate fabrication by the self-aligned resist etch-back method, and the fabrication of the collimation gate electrode using a focused ion beam assisted method are described in detail. The experimental results of 2×2 tip arrays with the proposed double-gate structure demonstrate an order of magnitude enhancement in beam brightness with minimal current loss. A similarly high beam brightness enhancement was achieved with a 20×20 tip array device, showing the scalability of the proposed structure. The observation of improved current-voltage characteristics with the 20×20 tip array is ascribed to the difference in gate aperture shape. The possibility of further improving the beam characteristics of double-gate field emitter arrays and the reduction of the transverse electron velocity spread are discussed. © *2012 American Institute of Physics*. [http://dx.doi.org/10.1063/1.4764925]

I. INTRODUCTION

Research on field emitter arrays (FEAs) has been actively pursued[1–13] with the aim of realizing high current and high current density cathodes, e.g., for compact microwave vacuum electronic amplifiers, such as traveling wave tubes (TWTs)[14–17] and compact free electron lasers.[7,18] FEAs are expected to help simplify the gun design and extend the operation range of such TWTs.[1,15] A recent report on a 5 GHz TWT using a single-gate Spindt FEA with 100 W output[17] demonstrates the practical feasibility of FEA-based TWTs. The possibility to generate high currents with densities above 10–100 A cm^{-2} (Ref. 19) is even more attractive for sub-millimeter and THz vacuum electronic power amplifiers.[20–22]

To take full advantage of FEAs, however, it is crucial to reduce the beam divergence of individual field emission beamlets. In a single-gate FEA, the beam divergence is in the order of 20°–30°. More than a factor of 10 reduction of this divergence could significantly simplify the gun design to inject electrons into micro-machined waveguides for THz devices.[8,9] In addition, FEAs with a normalized transverse emittance below 0.1 mm mrad for a 1 mm diameter FEA and emission current densities of ~1 kA cm^{-2} have a potential to improve the stability and performance of X-ray free-electron lasers significantly.[3,7] Such FEAs are also promising as cathodes for massively parallel electron beam lithography tools.[23]

To reduce the beam divergence and the transverse electron velocity spread, double-gate FEAs equipped with a beam collimation gate electrode G_{col} in addition to the electron extraction gate electrode G_{ext} have been intensely studied.[5,7–9,24–31] This is due to the fact that the emittance of a FEA can be small only when the individual beamlets are maximally collimated,[1] even though the emittance of individual beamlets is small.[33]

In double-gate FEAs, a divergent field emission beam is collimated by applying a negative collimation potential V_{col} to G_{col}. However, since the negative V_{col} reduces the electric field F_{tip} at the emitter tip apexes, the emission current is diminished and a part of the electrons is reflected by the negative G_{col} potential and intercepted by G_{ext}. The main challenge has been lying in minimizing the emission current reduction at the maximum beam brightness.[8,9,26–32]

We have recently shown that stacked double-gate structures with large G_{col} apertures of approximately 3 times the diameter of the G_{ext} apertures improved the emission current characteristics.[9] To fabricate these double-gate FEAs, we have developed a method using focused ion beam (FIB) milling. With this flexible and mask-less method, we realized 2×2 tip double-gate FEAs that exhibited a current density enhancement of a factor of 13.9 ± 1.0 (Ref. 9). The FIB also enables precise alignment of the G_{col} apertures to the underlying G_{ext} apertures and the emitter tips. This is a difficult task with the normally used polymer etch-back method.[5,8,9]

The aims of the present work are to report the fabrication method of our double-gate FEAs in detail, including the FIB assisted G_{col} patterning method and experimentally clarify the impact of the G_{col} aperture diameter on the collimation characteristics. Also, the scalability of the proposed large G_{col} aperture structure is investigated by applying the FIB assisted method to fabricate a 20×20 FEA and test its beam characteristics.

a)patrick.helfenstein@psi.ch.
b)soichiro.tsujino@psi.ch.

II. FOCUSED ION BEAM ASSISTED FABRICATION OF DOUBLE-GATE FEAS

In this section, we describe the fabrication procedure of three double-gate FEAs, two 2×2 double-gate FEAs (FEA1 and FEA2), and one 20×20 double-gate FEA (FEA3) in detail. FEA1 and FEA2 both have G_{ext} apertures with a diameter equal to $\sim 2.0\ \mu$m. Their G_{col} aperture diameters measure $\sim 6.0\ \mu$m for FEA1 [Fig. 4(a)] and $\sim 2.3\ \mu$m for FEA2 [Fig. 4(b)]. The diameter of the G_{ext} and G_{col} apertures of FEA3 [Fig. 4(c)] are nominally the same as FEA1. In Secs. II A and II B, the fabrication procedure of metallic FEAs and the G_{ext} formation procedure that precedes the fabrication of G_{col} are described. In Sec. II C, we detail the FIB assisted method to fabricate G_{col}. Although there are optical and electron-beam lithography tools available for our required precision to fabricate devices with more than tens of thousands of emitters, these require the development of an overlay alignment method that should be adjusted for our specific purposes and device sizes. In contrast, the FIB process described hereafter allows rapid proto-typing of FEAs with different aperture sizes (such as FEA1 and FEA2) without significantly modifying the process conditions. Its high flexibility makes the FIB an ideal tool for exploring the correlation between the gate aperture sizes and the electron beam collimation characteristics.

A. Fabrication of metallic FEAs

The double-gate FEA fabrication starts with the preparation of emitter arrays supported on metallic substrates. The gate electrodes are fabricated on top of the array by the method described in Secs. II B and II C. To fabricate the metallic emitter arrays, the molding technique originally proposed by Gray and Greene[34] is used. The first step is the patterning of pyramidal pits on a 4 in. Si (100) wafer by anisotropic wet-etching [Fig. 1(a)]. As etching mask, we use a 100 nm thick thermal oxide layer, which is patterned with 1.5 μm square hole arrays aligned with a pitch of 5 or 10 μm. The final size and shape of the emitters are the same for both array pitches. To fabricate double-gate FEAs with $\sim 6\ \mu$m diameter G_{col} apertures, we used the 10 μm pitch arrays. The oxide patterning is done by photolithography and dry-etching in CHF_3 plasma using a reactive-ion etcher (RIE, Oxford RIE 100). The subsequent pit etching is done in a 20% potassium hydroxide (KOH) solution heated to 70 °C. Utilizing the slow etching rate of (111) facets, pyramidal pits are thereby formed in the Si substrate.

The sharpness of the bottom of the pits will determine the sharpness of the emitter tips in the end (see below). After the KOH etching, the obtained pit apex sharpness is typically in the order of 50–100 nm and not sufficiently small. To ultimately obtain emitter tips with apex radii of curvature of ~ 5 nm (leading to a field enhancement factor of ~ 40 (Ref. 6)), we add two oxidation steps to sharpen the pits. The first additional oxidation is done after removing the first SiO_2 layer used as KOH etching mask. At this step, the pit apexes are sharpened down to a few nanometers. This is a consequence of the stress dependent diffusion of O_2 during the thermal oxidation.[35,36] This second oxidation also sharpens the side joints of the (111) facets and introduces spikes at the topmost edge of the pits. The sharp facet joints are unfavorable since they may cause parasitic emission bombardment of G_{ext}. The spikes should be eliminated since they introduce complications in the gate fabrication process described below by causing concave edges at the bottom of the emitters. Adding a third oxidation step circumvents these problems.[4] By adjusting the thicknesses of the second and the third oxide layers, we control the final sharpness of the emitter tip apexes. Typically, we choose the second oxidation thickness to be 200 nm, and the third oxidation thickness to be 600 nm. With this combination, we obtain emitters with ~ 5 nm tip apex radii of curvature as shown in Fig. 1(b) and the inset in Fig. 4(a). The oxide thicknesses were calibrated before each fabrication run to achieve the nominal apex sharpness.

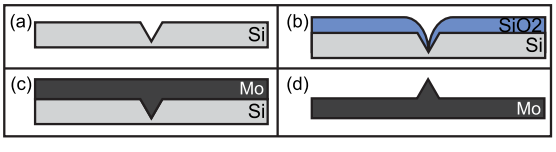

FIG. 1. Process steps used to fabricate the molybdenum field emitter arrays by the molding method. (a) Anisotropic wet-etching of the Si substrate to form pyramidal pits as molds for the emitters. (b) Thermal oxidation of the Si mold substrate is used to tailor the pit shapes and the tip apex sharpness. (c) Metallization of the mold wafer with a 1 μm thick sputtered molybdenum film (the SiO_2 layer is not shown here). (d) A molybdenum field emitter after removing the Si mold substrate.

In the next step, the mold substrate is metalized with a 1 μm thick molybdenum film that will serve as the electron emitting material [Fig. 1(c)]. This is done by magnetron sputtering using high purity Ar gas in a sputter deposition tool (Nordiko). The pressure and the flow rate of the Ar gas were adjusted to minimize the stress of the Mo film. Sputtering allows for a relatively uniform metalization of the mold pits at room temperature. The base pressure of the sputtering tool is 2×10^{-6} mbar, leading to the incorporation of about 10% O_2 into the film. This was confirmed by X-ray photoelectron spectroscopy. Nevertheless, using Ar gas with $\geq$99.999% purity, we were able to lower the room temperature resistivity of the molybdenum film to $\sim 10\ \mu\Omega$ cm, which is only twice the value of pure bulk molybdenum. High resolution scanning electron microscopy (SEM) and x-ray diffraction revealed that the molybdenum film is (110) oriented and consists of ~ 50 nm wide grain columns oriented perpendicular to the surface of the pits. The development of these grains during the deposition introduces a surface corrugation that partially blocks the Mo flux from reaching the bottom of the pits. Consequently, an empty cavity with a width in the order of tens of nm is formed beneath the emitter tip apex. These cavities are visible in the FIB cross-sections shown in Fig. 9.

On the sputtered Mo, a 100 nm thick Cr adhesion layer and a 200 nm thick Pd seed layer are deposited by electron-beam evaporation. A 400 μm thick Ni layer electro-plated on top serves as substrate of the FEA with negligible series resistance ($<10^{-3}\ \Omega$ cm). After the Ni electro-plating, the silicon substrate is completely removed by chemical etching in a heated KOH solution with the same condition as the mold pits etching. The third oxidation layer on the mold protects the emitter surface during the etching. At the end, we obtain arrays of pyramidal shaped molybdenum emitters with a base length of approximately 2 μm. Before the fabrication of

the gate electrodes, we dice the FEA wafers into 22×22 mm chips using a diamond blade saw. All further process steps are carried out on these chips.

B. Fabrication of the electron extraction gate electrode

The fabrication of the electron extraction gate electrode G_{ext} starts with the removal of the SiO_2 layer covering the molybdenum FEAs by chemical etching using a buffered oxide etch solution (BOE 7:1; NH_4F and HF in water). A 1.2 μm thick SiO_2 layer (I_1) is then deposited by plasma enhanced chemical vapor deposition (PECVD, Oxford PlasmaLab System 80). On top of this, a 500 nm thick Mo layer is sputter-deposited (G_{ext}) with the same condition as for the mold metallization. The schematic cross-section of the resulting structure is shown in Fig. 2(a).

After the deposition of the I_1 and G_{ext} layers, the chip surface exhibits ~500 nm tall protrusions on top of the emitters [Fig. 2(a)]. Utilizing these protrusions, we pattern the G_{ext} apertures by using a polymer mask and wet-etching. The etching mask is prepared by a self-aligned etch-back process: A positive photo-resist (PR, Microposit S1828) is spin-coated on top of G_{ext} and soft-baked, resulting in a planarized layer with an average thickness of ~4 μm [Fig. 2(b)]. When submitting the PR-coated FEA chip to low power oxygen plasma, the PR is uniformly thinned, and G_{ext} areas on top of the emitters are selectively exposed [Fig. 2(c)]. By adjusting the time and power of the oxygen plasma etching, the area laid bare on top of the emitters can be controlled between approximately 1.8 μm and 2.5 μm in diameter. Using the patterned PR as etching mask, we etch the G_{ext} apertures using an acid solution (H_3PO_4, CH_3CO_2H, and HNO_3 in 20% water) [Fig. 2(d)]. Afterwards, G_{ext} is further patterned into its final shape [Fig. 4(d)]. In completed double-gate FEAs, the G_{ext} electrodes are buried underneath the G_{col} electrodes with the exception of the contact pads for wire bonding. For the fabrication of double-gate devices, the SiO_2 layer which covers the emitters at this step is left as protection from ambient air and particles.

C. FIB assisted collimation gate aperture fabrication

In the final steps, we fabricate G_{col}. On the FEA chip with the patterned G_{ext}, we deposit a 1.2 μm thick SiON second insulation layer (I_2) by PECVD, followed by a 500 nm thick sputtered Mo layer (G_{col}). The PECVD conditions of the SiON deposition were optimized to reduce the residual stress of the film well below 0.1 GPa. The BOE etching rate of the SiON of I_2 used here is three times slower than that of the SiO_2 of I_1. This difference in etching rates is important to prevent over-etching of I_2 in the last BOE etching step (Fig. 3(d)), necessary to remove the SiON and SiO_2 layers, and to expose the emitter tips.

To minimize the emission current reduction at finite V_{col}, we require the G_{col} apertures to be approximately three times larger than the G_{ext} apertures.[9] This is difficult to achieve in a reproducible way by the self-aligned etch-back process used for G_{ext} because the required diameter is larger than the protrusions on top of the emitter tips obtained after the deposition of the I_2 and G_{col} layers. Therefore, we developed a method using FIB milling with Ga ions (FEI Strata DB 235). We found that the direct milling through the G_{col} electrode makes the underlying SiON layer inert to BOE, perhaps due to Ga ion implantation in the SiON layer. Hence, we add two sacrificial layers (750 nm of SiO_2 and 100 nm of Mo) and use them as mask for the G_{col} etching [Fig. 3(a)]. Using the FIB, we mill through the two sacrificial layers and about one half of the G_{col} layer [Fig. 3(b)]. The remainder of G_{col} is removed by wet-etching afterwards, using the patterned sacrificial SiO_2 layer as the etching mask. The topmost Mo layer, which is needed to avoid charging of the chip surface during the FIB milling, is removed during the wet-etching of G_{col} at the same time [Fig. 3(c)]. The FIB milling time was approximately 90 s per aperture with 6 μm diameter using an ion current of 1.5 nA. This amounts to a total FIB milling time for the 20×20 tip array of approximately 10 h without including the time required for stage movements and drift correction.

Using the patterned gate apertures as mask, we then wet-etch the insulation layers (I_1, I_2) in BOE as depicted in Fig. 3(d). As mentioned above, the undercut in I_2 at this step is minimized owing to the slower SiON etch rate compared to SiO_2. About ~0.5 μm of the I_1 layer thickness is left unetched to minimize the exposure of the emitter tip apexes to ambient air. It is etched off just before inserting the FEA into the experimental chamber. In Fig. 4(a), we show a top-

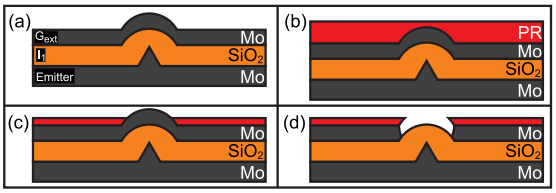

FIG. 2. The process steps applied to fabricate the electron extraction gate electrode by the polymer etch-back method. (a) Deposition of the insulator I_1 and the extraction gate electrode G_{ext} layers. (b) Spin-coating of a PR layer. (c) Oxygen plasma etching of the PR until the metal on top of the emitters is laid bare. (d) Use the patterned PR as wet-etching mask for the extraction gate apertures.

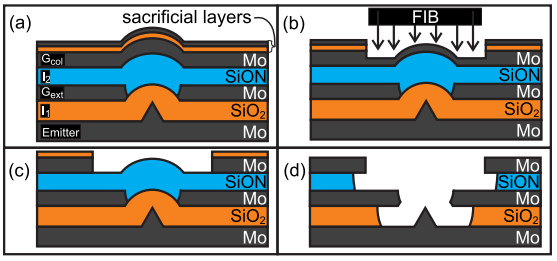

FIG. 3. Process steps to fabricate the collimation gate (G_{col}) by the FIB assisted method. (a) After the fabrication of the G_{ext} aperture, the insulator I_2, the G_{col} layer and the sacrificial layers (SiO_2 (lower), and Mo (upper) are deposited. (b) FIB milling through the sacrificial layers and one half of the G_{col} layer. (c) The G_{col} aperture is finalized by wet-etching. This step also removes the sacrificial Mo layer. (d) BOE etching to remove I_1 and I_2 on top of the emitters using G_{ext} and G_{col} as etching masks. This step also removes the sacrificial SiO_2 layer.

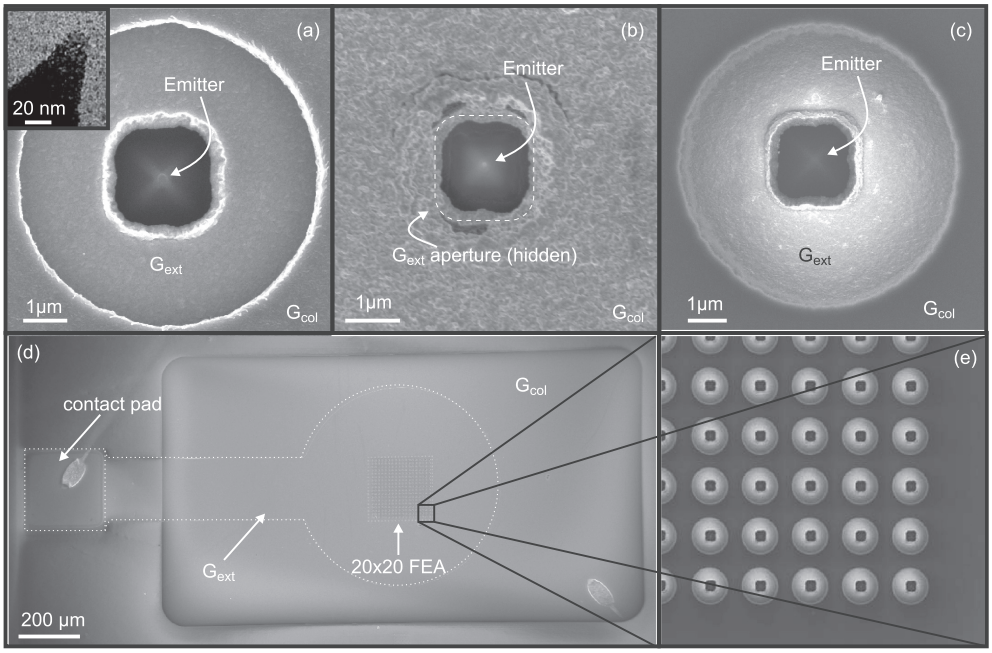

FIG. 4. Top-view SEM micrographs of double-gate FEAs. (a) FEA1 (one of the emitters) with a TEM cross-section of the tip apex (inset). (b) FEA2 (one of the emitters). The dotted line approximately shows the underlying G_{ext} aperture. (c) FEA3 (one of the emitters). (d) Overview of FEA3. The 20×20 emitters are located at the center of the rectangular G_{col} electrode with a size of 2.5×0.75 mm. The G_{ext} electrode is a 500 μm diameter circle with a 0.04 mm^2 rectangular contact pad attached at the end (partially buried underneath G_{col} as indicated by the dotted lines). The oxide on top of the 0.2 mm square contact pad at the end is etched away before the wire bonding.

view SEM image of FEA1 with a G_{ext} diameter of 2.3 ± 0.1 μm and a G_{col} diameter of 6.2 ± 0.1 μm. High-resolution transmission electron microscopy (TEM) imaging of an emitter on the same FEA substrate as FEA1 (inset of Fig. 4(a)) shows that the emitter apex radius of curvature is ~7.5 nm.

Next, the G_{col} electrode of each array is patterned into a rectangular shape of approximately 2.5 mm $\times$ 0.75 mm with rounded corners as shown in Fig. 4(d) for FEA3. The G_{ext} electrode is buried underneath G_{col}. G_{ext} is electrically contacted through the 0.2 mm square via etched into I_2 on top of the G_{ext} contact pad. The comparatively large G_{col} aperture (Fig. 4(a) for FEA1 and Fig. 4(c) for FEA3, and in contrast, Fig. 4(b) for FEA2) provides electro-static shielding of the emitted electrons from the G_{ext} potential or non-uniform electric fields created by the bonding wires and prevents beam distortions. The electrical contact to G_{col} is made by bonding wires to one corner of G_{col} [Fig. 4(d)].

III. EXPERIMENTAL SETUP AND SAMPLE PREPARATION PROCEDURE

A. Field emission microscope

The field emission current-voltage characteristics measurement and the beam imaging were conducted in a field emission microscope schematically shown in Fig. 5. We imaged the electron beam on a metalized P43 phosphor screen after amplifying it with a micro-channel plate (MCP) inserted between the FEA and the phosphor screen. The distance between the MCP front plate and the FEA can be adjusted by a linear translation mechanism and was typically set to 40–50 mm. The electron beam was accelerated by applying a DC potential of 1 kV to the front-plate of the MCP which also functions as the anode in this setup. To amplify the beam, we applied 1.7 kV to the back-plate of the MCP leading to an amplification factor of ~10^3. The

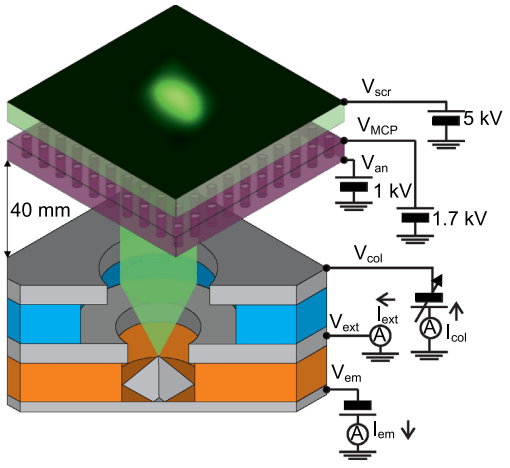

FIG. 5. Schematic diagram of the field emission microscope. The field emission electron beam is amplified by a micro-channel plate biased by (V_{MCP}-V_{an}) and imaged by the phosphor screen (biased at a voltage V_{scr} of 3-5 kV). The currents I_{em}, I_{ext}, and I_{col} were recorded simultaneously while controlling the bias voltages V_{em} and V_{col}. V_{ext} is normally fixed to ground potential.

phosphor screen was biased at 5 kV. A full-color video recorder with 8-bit resolution per color (Canon XL1s) was used to record the phosphor screen images of FEA1 and FEA2. Auto-brightness adjustment was turned off during the experiment to allow for the calculation of the current density from the image brightness. The FEA3 beam images were recorded by a full HD Sony Handycam. The brightness of the images was adjusted by the shutter time, which was kept constant during the whole experiment.

The captured images were subsequently analyzed to evaluate the beam size and the current density. The beam size was extracted by the automatic pattern recognition algorithm described in the supplementary materials.[38]

The FEA chip was mounted on a ceramic (MACOR) holder. To be able to load up to three double-gate FEAs at the same time, we prepared 6 contact terminals for gate electrodes and 1 terminal to be connected with the emitter substrate (via a copper plate underneath the FEA chip) on the holder. These were connected to BNC electrical feedthroughs using Kapton insulated wires. The FEA gate electrodes were wire-bonded by 25 μm thick aluminum wires to Au-plated ceramic bonding pads fixed on the sample holder.

To generate a collimated field emission beam, a negative electron extraction potential V_{em} was applied to the emitter substrate with respect to G_{ext}, thereby initiating electron field emission from the tips. A negative beam collimation potential V_{col} was applied to G_{col} with respect to G_{ext}. G_{ext} was set to ground potential. The current I_{em} injected into the emitter substrate, the G_{ext} current I_{ext}, and the G_{col} current I_{col} were simultaneously measured. The net emission current I_{net} that reached the screen was evaluated by ($|I_{\mathrm{em}}| - I_{\mathrm{ext}} - I_{\mathrm{col}}$). For the FEA3 experiment, it was possible to measure I_{net} directly by inserting a coaxial Faraday cup in front of the FEA chip.

B. FEA preparation procedure

After the BOE etching removal of the remaining SiO_2 layer on top of the emitter tips and wire-bonding to the gate contacts, we quickly loaded the FEA into the field emission microscope chamber and evacuated it with a turbo-molecular pump for 24–48 h while heating the chamber to 140 °C. After this baking, we switched from the turbo-molecular pump to an ion getter pump. The final base pressure was $\sim 5 \times 10^{-9}$ mbar.

At the beginning of the experiment, the field emission current was erratic and fluctuated over several orders of magnitude. It became stable after a conditioning process, in which the FEAs were operated for a prolonged time period. We scanned V_{em} slowly with G_{col} and G_{ext} connected to ground potential while measuring the currents I_{em}, I_{ext}, and I_{col}. V_{em} was scanned between zero volts and a negative maximum with a period of 2–10 cycles/min. For the 2×2 arrays (FEA1 and FEA2), I_{net} was indirectly measured via I_{em}, I_{ext}, and I_{col}. I_{net} of the 20×20 array (FEA3) was directly measured by the Faraday cup. During the initial conditioning phase, the scan range of V_{em} was slowly increased over the course of several days while observing the stability and the increase of the emission current. A more stable and higher emission current is normally obtained by this conditioning. This is likely due to desorption of remaining adsorbents on the tip surface initiated by the emitted current, e.g., via Joule heating. Gentle increase of the scan range of V_{em} may also have helped rounding off atomic protrusions by Joule heating without causing arcs, but the detailed mechanism has not been established yet.[37] After the current-voltage characteristics had stabilized by conditioning, we started the beam imaging experiment.

IV. RESULTS AND DISCUSSIONS

A. The influence of the G_{col} aperture size on the beam collimation characteristics

In Figs. 6(a), 6(c), and 6(e), we present the experimental results of FEA1 with G_{ext} and G_{col} aperture diameters of 2.3 ± 0.1 μm and 6.2 ± 0.1 μm, respectively.[9] Fig. 6(a) shows a set of three phosphor screen images of FEA1 after the conditioning. The images were taken at different V_{col} of +1 V, −31 V, and −61 V from left to right. V_{em} was fixed at −80 V. I_{net} was equal to 0.5–1 nA for these three images. V_{em} and therefore I_{net} were kept low to avoid destructive arcing. The FEA-MCP separation was 40 mm. Reduction of the beam size and simultaneous increase of the beam brightness with the decrease of V_{col} are apparent.

The increased beam brightness indicates a minimal decrease of the emission current with the decrease of the beam size. In fact, as the current-voltage characteristics in Fig. 6(c) show, I_{net} was approximately 0.5 ± 0.2 nA for V_{col} in the range from +1 V to −65 V. The gate currents I_{col} and I_{ext} were less than 20% of I_{net} in the same V_{col} range. As summarized in Fig. 6(e), the average beam radius R_{s} was reduced from 7.2 ± 0.4 mm ($V_{col} = +1$ V) to 1.0 ± 0.2 mm ($V_{col} = -69$ V). Here, we defined R_{s} as the radius of the circle which encloses 80% of the beam area. Combining this with the observed I_{net}, we found that the current density was increased by a factor of 13.9 ± 1.0. When V_{col} was lower than −69 V or, differently put, the ratio k_{col} of V_{col} to V_{em} larger than 0.86, I_{net} fell to zero. We ascribe this to the repulsion of the extracted electrons by the G_{col} potential and their subsequent collection by G_{ext}. This interpretation is consistent with the observation that I_{ext} increased for k_{col} above 0.86 [Fig. 6(c)].[25–30]

We note that, since the acceleration potential V_{an} applied to the MCP front plate is an order of magnitude larger than V_{em}, R_s is proportional to the rms transverse velocity $u_{\|}$. The relation is given by

$$\frac{R_s}{2\sqrt{2\ln|0.2|}L_s} = \frac{u_{\|}}{u_{an}}\left(\sqrt{1+\frac{u_0^2}{u_{an}^2}} - \frac{u_0}{u_{an}}\right), \qquad (1)$$

where L_{s} is the FEA-MCP separation and the velocity u_{an} is given by $\sqrt{2qV_{an}/m}$ (with q the elementary charge and m the electron rest mass). In Eq. (1), we defined the initial longitudinal velocity u_0 as the electron velocity at 1–10 μm off the emitter apex. Even though the classical electron velocity at the emitter apex surface is zero, u_0 is finite because the finite V_{em} accelerates the electrons. For the uncollimated beam at $V_{col} = 0$, u_0 is to a good approximation given by

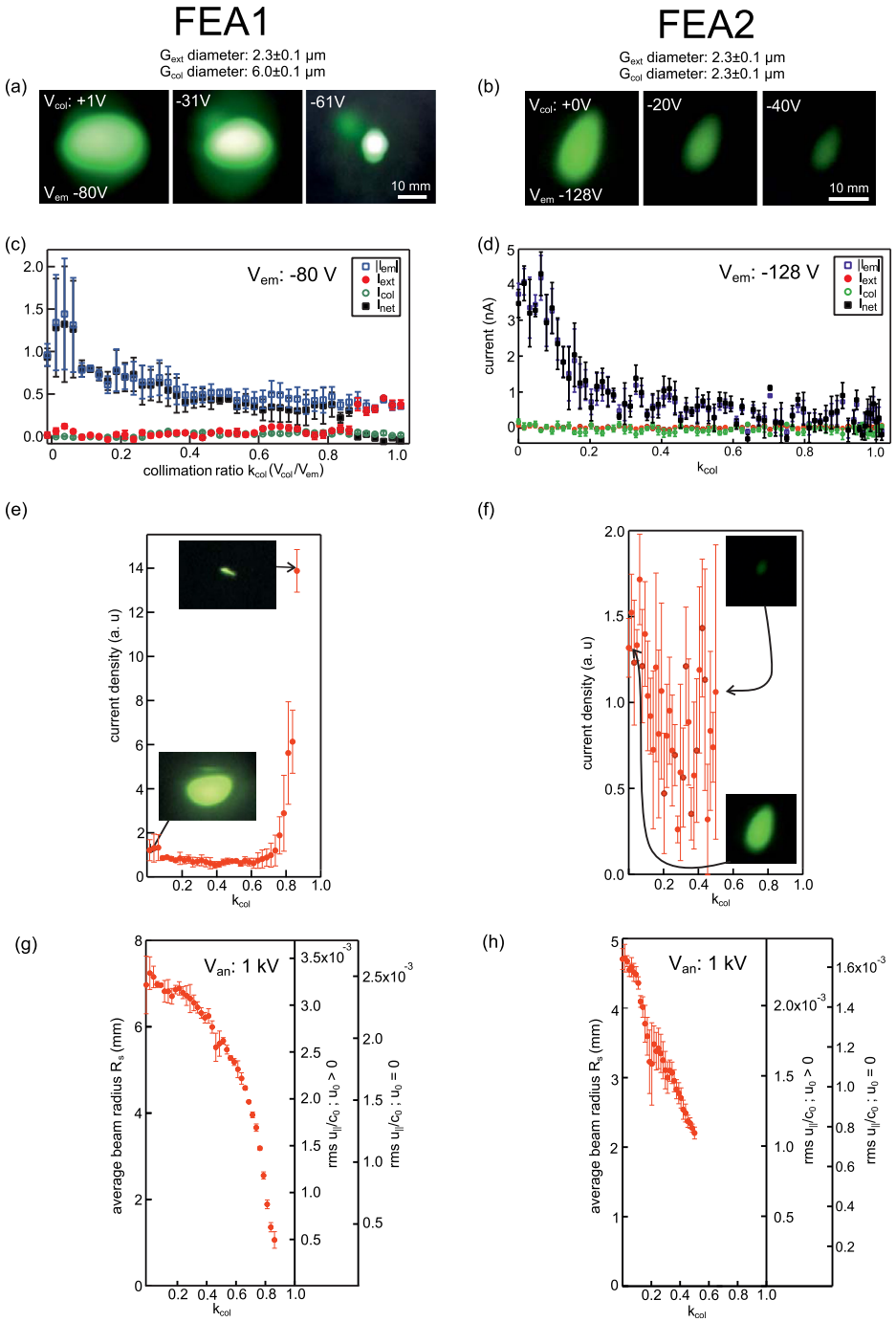

FIG. 6. Summary of the field emission characteristics of FEA1 (G_{col} aperture diameter of $6.2 \pm 0.1\,\mu$m, left panel) and FEA2 (G_{col} aperture diameter of $2.3 \pm 0.1\,\mu$m, right panel) measured with the acceleration voltage V_{an} set to 1 kV. (a) FEA1 beam images with V_{col} of $+1$ V, -31 V, and -61 V. V_{em} was fixed at -80 V. (b) FEA2 beam images with V_{col} of 0, -20, and -40 V. V_{em} was fixed at -128 V. (c) and (d) The current-voltage characteristics of FEA1 and FEA2, where open squares depict the emitter current I_{em}, solid squares the net current I_{net}, filled circles the extraction gate current I_{ext}, and open circles represent the collimation gate current I_{col}. The horizontal axis depicts the ratio k_{col} of V_{col} to V_{em}, where V_{em} was -80 V for FEA1 and -128 V for FEA2, respectively. (e) The relation between the current density and k_{col} of FEA1 (V_{em} of -80 V). The two inset images show the beam at k_{col} of 0 (bottom) and 0.86 (top). (f) The relation between the current density and k_{col} of FEA2 (V_{em} of -128 V). The two inset images show the FEA2 beam at a k_{col} of 0 (bottom) and 0.5 (top). (g) and (h) The relation between the average beam radius R_s (left axis) and k_{col} with $V_{an} = 1$ kV for FEA1 (g, with $V_{em} = -80$ V) and FEA2 (h, with $V_{em} = -128$ V). The right axes show the rms transverse electron velocity evaluated from R_s for the two case $u_0 = 0$ (outermost right axis) and $u_0 > 0$ (inner right axis).

$\sqrt{2q|V_{em}|/m}$ and $u_{||}$ is of the same order of magnitude as u_0. For the collimated beam with V_{col} close to V_{em}, the G_{col} potential decelerates the electrons and u_0 and $u_{||}$ become substantially smaller. Thus, we can safely assume u_0 equal to zero for the evaluation of $u_{||}$ of the maximally collimated beam which makes it insensitive to the actual value of u_0. Additional assumptions to relate R_s and $u_{||}$ by Eq. (1) are discussed in the supplementary material.[38]

In Fig. 6(g), we summarized R_s as a function of k_{col}. The two right vertical axes of Fig. 6(g) indicate the evaluated $u_{||}$ from Eq. (1) for two cases: (i) u_0 equal to $\sqrt{2q|V_{em}|/m}$ and (ii) zero u_0. We found that $u_{||}$ is equal to 3.3×10^{-3} c_0 at zero k_{col} and equal to 3.7×10^{-4} c_0 at the maximum k_{col} of 0.86, where c_0 is the speed of light in vacuum. From these values, we found that $u_{||}$ was reduced by a factor of 8.9 at k_{col} of 0.86.

To experimentally investigate the impact of the large G_{col} aperture of FEA1 on the strong beam collimation, we compare the beam characteristics of FEA1 with FEA2. The most important difference of FEA2 is its small G_{col} aperture diameter of 2.3 ± 0.1 μm, which is approximately equal to the G_{ext} aperture diameter of 2.3 ± 0.1 μm. Figs. 6(b), 6(d), 6(f), and 6(h) summarize the experimental results of FEA2. As shown in Fig. 6(d), the emission current decreased rapidly with the increase of k_{col}. We note that the maximum V_{em} was set to -128 V for FEA2 to increase the emission current and to make the beam image observable at large k_{col}. Nevertheless, the emission current became negligible at k_{col} beyond 0.3. This is in stark contrast to the behavior of FEA1 but similar to the previously reported double-gate FEAs with small G_{col} aperture diameters fabricated by the resist etch-back method.[24] The beam size (and $u_{||}$) decreased (Figs. 6(b) and 6(h)) with the increase of k_{col}. As a consequence of the rapid decrease of the emission current with k_{col}, however, no enhancement of the beam brightness and current density were observed (Figs. 6(b) and 6(f)). We also repeated the same measurements at lower V_{em} values to rule out the possibility that the large V_{em} (-128 V) influenced the results but the behavior was unchanged. The value of $k_{col} > 0.3$ for which I_{em} fell below 10% of its value at $k_{col} = 0$ was also found to be independent of V_{em}.

B. Emission characteristics of a 20×20 double-gate FEA

To test the fabrication method and the collimation characteristics of a FEA with a larger number of emitter tips, we fabricated a 20×20 emitter array (FEA3) [see Figs. 4(c) and 4(e)]. The top-view SEM image in Fig. 4(c) shows a magnified view of one of the emitters of FEA3. FEA3 has G_{ext} aperture diameters of 2.0 ± 0.1 μm and G_{col} aperture diameters of 7.2 ± 0.1 μm. These values are similar to the gate aperture diameters of FEA1. As shown in Fig. 7, the I_{net}-k_{col} relation of FEA3 was similar to that of FEA1. When V_{em} was equal to -60 V, I_{net} decreased monotonously with the increase of k_{col}. I_{ext} started to increase at a k_{col} of 0.95 and reached 50% of I_{em} at a k_{col} of 0.99.

As shown in Figs. 8(a) and 8(b), R_s decreased from ~3.8 mm to ~0.45 mm when k_{col} was increased from 0 to 0.98 (measured at V_{em} of -82 V). As shown in Figs. 8(c) and 8(d), I_{net} at the largest V_{em} decreased from 280 nA to 40 nA with the increase of k_{col} from 0 to 0.98. I_{ext} was negligible at k_{col} of 0 but increased to ~25% of I_{em} at k_{col} of 0.98. Hence, we conclude that the major cause of the I_{net} decrease with the increase of k_{col} is due to the reduction of F_{tip} with the increase of the collimation potential. Combining R_s with the observed I_{net}, we found that the current density enhancement at $k_{col} = 0.98$ was equal to ~13.7.

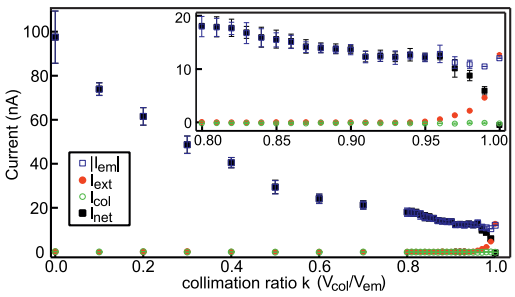

FIG. 7. Current-voltage characteristics of the 20×20 emitter array FEA3. Emitter current I_{em} (open squares), net current I_{net} (solid squares), extraction gate current I_{ext} (filled circles), and the collimation gate current I_{col} (open circles) at various ratios k_{col} ($= V_{col}/V_{em}$) at a V_{em} of -60 V. The inset shows a close up view of the same data for k_{col} between 0.8 and 1.0.

We also evaluated $u_{||}$ at these k_{col} values using Eq. (1). We found $u_{||}$ equal to 2.7×10^{-3} c_0 at $k_{col} = 0$ (with u_0 determined by V_{em} of -82 V) and 2.4×10^{-4} c_0 at $k_{col} = 0.98$ (assuming $u_0 \sim 0$). Therefore, $u_{||}$ was reduced by a factor of ~11.3. This reduction is ~27% higher than in the case of FEA1. Furthermore, the smallest $u_{||}$ of FEA3 at k_{col} equal to 0.98 is 1.9 times smaller than the smallest $u_{||}$ of FEA1 at k_{col} equal to 0.86 (at the maximum current density condition).

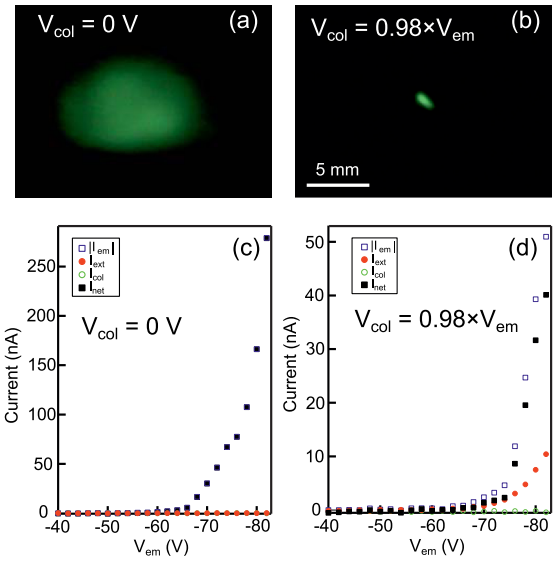

FIG. 8. Beam images of the 20×20 emitter array FEA3 recorded at k_{col} ($=V_{col}/V_{em}$) equal to 0 (a) and k_{col} equal to 0.98 (b); V_{em} was -82 V and the corresponding I_{net} equal to 280 nA in (a) and 40 nA in (b), respectively. (c) and (d) The I-V characteristics of the full V_{em} scan. The images in (a) and (b) were recorded at the maximum V_{em} of (c) and (d), respectively.

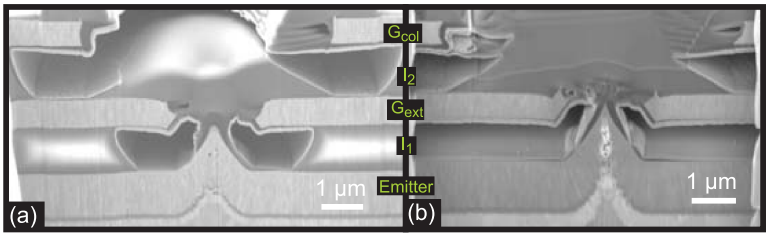

FIG. 9. FIB cross-sections of one of the emitters of (a) FEA1 and (b) FEA3. The comparison of the G_{ext} aperture edge shapes shows that FEA3 has a $\sim 0.2\,\mu$m tall collar blocking the direct line of sight from the emitter tip to G_{col}. No such collar can be found at the G_{ext} edge of FEA1.

We assume that these differences between FEA1 and FEA3 originate from the small difference in the gate aperture shapes as suggested by the top-view SEM images in Fig. 4. To investigate this in detail, we prepared cross-sections of one of the emitters from each of the two FEAs using FIB milling (Fig. 9). The various layers are indicated in the middle of the figure. (The dark carbon layer visible mainly around the tip and G_{ext} was deposited prior to the FIB milling to avoid the collapse of the gate layers.) The comparison of the cross-sections of the two FEAs revealed a $\sim 0.2\,\mu$m tall collar at the G_{ext} edge of FEA3, which is absent for FEA1. This is a consequence of the slightly shorter mask etching and wet-etching times for the G_{ext} aperture patterning of FEA3. The height of the collar is consistent with the top-view SEM images which show a $\sim 0.2\,\mu$m smaller inscribed diameter of G_{ext} of FEA3 compared to that of FEA1 (Figs. 4(a) and 4(c)). Although the height of the collar is less than $\sim 10\%$ of the G_{ext} diameter, combined with the $\sim 1\,\mu$m larger G_{col} aperture diameter, an extra shielding of the emitter apex from G_{col} was introduced, preventing a direct line of sight from the emitter tip apex to G_{col}. Neo *et al.* demonstrated the effectiveness of such shielding recently with volcano-shaped double-gate FEAs (Refs. 28 and 29). We expect even higher current densities and lower rms transverse velocities with double-gate FEAs with a higher G_{ext} collar providing better electro-static shielding of the emitter tip.

V. SUMMARY AND CONCLUSIONS

We presented the fabrication method and the electron beam characteristics of double-gate FEAs with G_{col} aperture diameters approximately three times the size of the G_{ext} apertures and showed that these devices can generate a highly collimated field emission beam with enhanced current density. The comparison of the field emission characteristics of FEA1 and FEA3 with large G_{col} apertures with FEA2 with small G_{col} apertures showed that the large difference in G_{ext} and G_{col} aperture diameter is necessary to achieve significant enhancement of the current density. The scalability of the high-brightness emission current was demonstrated by the successful fabrication and the beam characteristics measurements of the 20×20 emitter array device. In addition, a detailed comparison of the beam characteristics and the gate structures between FEA1 and FEA3 indicated that further improvement of the beam collimation can be achieved by optimizing the G_{ext} aperture. The planar G_{col} surface of our FEAs is likely to be advantageous for the operation in high acceleration electric fields of 10 MV/m and above[10,11] by reducing the probability of parasitic emission from the top surface and subsequent vacuum breakdown.

These results were achieved by the developed FIB assisted G_{col} fabrication method, which we found to be more reliable and stable than the self-aligned resist etch-back method. Yet, the 20×20 tip array appears to be the practical limit in up-scaling the array size because of the required milling time of the available FIB tool. Nevertheless, the capabilities of the FIB such as its flexibility and the mask-less patterning are certainly attractive for studying various device structures with a small number of emitter tips.

We note that although the emission current of the 20×20 FEA was proportionally higher than that of the 2×2 FEA, further increase of the average current to above $4\,\mu$A per tip is expected from our FEAs as demonstrated for single-gate FEAs with 20×20 tip arrays[5] and 10^4 tip arrays.[12] With the 10^4 tip array, this has been achieved with the help of a noble gas conditioning process which can also improve the beam uniformity. The proposed mechanism assumes impact ionization of noble gas molecules close to the current emitting tips and subsequent ion bombardment of these tips. Therefore, we can potentially accelerate the emission homogenization process in double-gate FEAs by applying a positive bias to G_{col} while the FEA is in a noble gas atmosphere. Such noble gas conditioning experiments on double-gate FEAs are currently being conducted.

A detailed comparison of the beam characteristics with the FIB cross-sections of FEA1 and FEA3 indicates the possibility of further performance improvement. Particularly interesting is the fact that we were able to increase k_{col} to 0.98 for FEA3, thereby obtaining a higher maximum current density and smaller transverse velocity than with FEA1. How far k_{col} can be increased in a given device seems to be highly sensitive to the detailed structure of the gate aperture openings and emitter tip apexes. Another important question is the impact of the G_{col} aperture shape and the inhomogeneity of the alignment of G_{col} with the tip (better than $\sim 0.2\,\mu$m precision in the current process) on the emission current quenching at large k_{col}. To investigate these questions and elucidate the performance limitation of double-gate FEAs, further experimental explorations of the device structure and the operation conditions in combination with numerical simulations, which takes into account the actual tip shape and the gate structures, are necessary.

The authors wish to thank J. Krbanjevic for preparing the FIB cross-sections, A. Lücke and K. Vogelsang for their help and advice in using the dicing saw, and J. Lehman and B. Haas for their technical help to fabricate FEAs. This work

was conducted within the SwissFEL project at the Paul Scherrer Institute and was partially supported by the Swiss National Science Foundation No. 200021_125084.

[1]C. M. Tang, M. Goldstein, T. A. Swyden, and J. E. Walsh, Nucl. Instrum. Methods Phys. Res. A **358**, 7 (1995).
[2]M. Dehler, A. Candel, and E. Gjonaj, J. Vac. Sci. Technol. B **24**, 892 (2006).
[3]M. Dehler, in Proceedings of the 9th International Computational Accelerator Physics Conference, ICAP 2006, Chamonix, France, 2-6 Oct 2006.
[4]S. Tsujino, P. Beaud, E. Kirk, T. Vogel, H. Sehr, J. Gobrecht, and A. Wrulich, Appl. Phys. Lett. **92**, 193501 (2008).
[5]E. Kirk, S. Tsujino, T. Vogel, K. Jefimovs, J. Gobrecht, and A. Wrulich, J. Vac. Sci. Technol. B **27**, 1813 (2009).
[6]S. Tsujino, F. le Pimpec, J. Raabe, M. Buess, M. Dehler, E. Kirk, J. Gobrecht, and A. Wrulich, Appl. Phys. Lett. **94**, 093508 (2009).
[7]B. D. Patterson, R. Abela, H. H. Braun, U. Flechsig, R. Ganter, Y. Kim, E. Kirk, A. Oppelt, M. Pedrozzi, S. Reiche, L. Rivkin, T. Schmidt, B. Schmitt, V. N. Strocov, S. Tsujino, and A. F. Wrulich, New J. Phys. **12**, 35012 (2010).
[8]S. Tsujino, P. Helfenstein, E. Kirk, T. Vogel, C. Escher, and H. W. Fink, IEEE Electron Device Lett. **31**, 1059 (2010).
[9]P. Helfenstein, E. Kirk, K. Jefimovs, T. Vogel, C. Escher, H.-W. Fink, and S. Tsujino, Appl. Phys. Lett. **98**, 061502 (2011).
[10]S. Tsujino, M. Paraliev, E. Kirk, T. Vogel, F. Le Pimpec, C. Gough, S. Ivkovic, and H.-H. Braun, J. Vac. Sci. Technol. B **29**, 02B117 (2011).
[11]S. Tsujino, M. Paraliev, E. Kirk, C. Gough, S. Ivkovic, and H.-H. Braun, Phys. Plasmas **18**, 064502 (2011).
[12]S. Tsujino, M. Paraliev, E. Kirk, and H.-H. Braun, Appl. Phys. Lett. **99**, 73101 (2011).
[13]A. Mustonen, P. Beaud, E. Kirk, T. Feurer, and S. Tsujino, Appl. Phys. Lett. **99**, 103504 (2011).
[14]H. Makishima, S. Miyano, H. Imura, J. Matsuoka, H. Takemura, and A. Okamoto, Appl. Surf. Sci. **146**, 230 (1999).
[15]D. R. Whaley, B. M. Gannon, C. R. Smith, C. M. Armstrong, and C. A. Spindt, IEEE Trans. Plasma Sci. **28**, 727 (2000).
[16]D. R. Whaley, B. M. Gannon, V. O. Heinen, K. E. Kreischer, C. E. Holland, and C. A. Spindt, IEEE Trans. Plasma Sci. **30**, 998 (2002).
[17]D. R. Whaley, R. Duggal, C. M. Armstrong, C. L. Bellew, C. E. Holland, and C. A. Spindt, IEEE Trans. Electron Devices **56**, 896 (2009).
[18]C. A. Brau, Nucl. Instrum. Methods Phys. Res. A **407**, 1 (1998).
[19]P. R. Schwoebel, C. A. Spindt, and C. E. Holland, J. Vac. Sci. Technol. B **23**, 691 (2005).
[20]H. Booske, Phys. Plasmas **15**, 055502 (2008).
[21]R. L. Ives, IEEE Trans. Plasma Sci. **32**, 1277 (2004).
[22]J. Tucek, M. Basten, D. Gallagher, K. Kreischer, R. Lai, V. Radisic, and K. Leong, in Proceedings of the IVEC-IVESC, Montrey, CA, 2012.
[23]E. Platzgummer, C. Klein, and H. Loeschner, in Proceedings of Photomask Japan (PMJ), Yokohama, Japan, 2012.
[24]W. D. Kesling and C. E. Hunt, IEEE Trans. Electron Devices **42**, 340 (1995).
[25]J. Itoh, Y. Toma, K. Morikawa, S. Kanemaru, and K. Shimizu, J. Vac. Sci. Technol. B **13**, 1968 (1995).
[26]Y. Yamaoka, S. Kanemaru, and J. Itoh, Jpn. J. Appl. Phys., Part I **35**, 6626 (1996).
[27]C. Py, J. Itoh, T. Hirano, and S. Kanemaru, IEEE Trans. Electron Devices **44**, 498 (1997).
[28]A. Hosono, S. Kawabuchi, S. Horibata, S. Okuda, H. Harada, and M. Takai, J. Vac. Sci. Technol. B **17**, 575 (1999).
[29]C. Py, M. Gao, S. R. Das, P. Grant, P. Marshall, and L. LeBrun, J. Vac. Sci. Technol. A **18**, 626 (2000).
[30]L. Dvorson, G. Sha, I. Kymissis, C. Y. Hong, and A. I. Akinwande, IEEE Trans. Electron Devices **50**, 2548 (2003).
[31]Y. Neo, M. Takeda, T. Soda, M. Nagao, T. Yoshida, S. Kanemaru, T. Sakai, K. Hagiwara, N. Saito, T. Aoki, and H. Mimura, J. Vac. Sci. Technol. B **27**, 701 (2009).
[32]A. Koike, T. Tagami, Y. Takagi, T. Yoshida, M. Nagao, T. Aoki, Y. Neo, and H. Mimura, Appl. Phys. Express **4**, 26701 (2011).
[33]M. R. Scheinfein, W. Qian, and J. C. H. Spence, J. Appl. Phys. **73**, 2057 (1993).
[34]H. F. Gray and R. F. Greene, U.S. patent 4,307,507 (29 December 1981).
[35]H. Umimoto, S. Odanaka, and I. Nakao, IEEE Electron Device Lett. **10**, 330 (1989).
[36]M. Nakamoto, T. Hasegawa, T. Ono, T. Sakai, and N. Sakuma, Tech. Dig. - Int. Electron Devices Meet. **1996**, 297.
[37]C. A. Spindt, I. Brodie, L. Humphrey, and E. R. Westerberg, J. Appl. Phys. **47**, 5248 (1976).
[38]See supplementary material at http://dx.doi.org/10.1063/1.4764925 for details on the image analysis and the derivation of Eq. 1.

SUPPLEMENTARY MATERIALS

Fabrication of Metallic Double-Gate Field Emitter Arrays and Their Electron Beam Collimation Characteristics

P. Helfenstein[1], K. Jefimovs[2], E. Kirk[1], C. Escher[3], H.-W. Fink[3], and S. Tsujino[1]
[1]Laboratory for Micro- and Nanotechnology, Paul Scherrer Institut, CH-5232 Villigen-PSI, Switzerland
[2]Electronics/Metrology/Reliability Laboratory, EMPA, Überlandstrasse 129, CH-8600 Dübendorf, Switzerland
[3]Physik Institut, University of Zurich, Winterthurerstrasse 190, CH-8057 Zurich, Switzerland

In this supplementary document, we give detailed information on how we conducted the field emission experiments with FEA1, FEA2 and FEA3. In section A, the methods to apply and vary the beam extraction and collimation gate potentials are explained. In section B, we describe the method used to evaluate the beam size from the phosphor screen image of the field emission beam. The beam images were captured by a CCD camera (Canon XLS1 for FEA1, FEA2 and Sony Handycam for FEA3) with a rate of 30 frames per second which gives an exposure time of 33 ms per frame. The current-voltage characteristics and the phosphor screen images were recorded simultaneously but asynchronously. The method used for correcting the time shift between the two datasets is presented in section C. The derivation of the relationship between the average beam radius R_s and the rms transverse electron velocity $u_{||}$ is given in section D.

A. The Application of Gate Potentials And Current Measurements

Three source-measure units (Keithley 2400 Multimeter) were used to measure the currents I_{em} flowing through the emitters as well as I_{ext} and I_{col} flowing through G_{ext} and G_{col}, respectively. The potential V_{ext} of G_{ext} was always kept at ground potential. After the conditioning phase, a negative potential V_{col} was applied to G_{col} to collimate the extracted electron beam. The current measurements of the three source-measure units were synchronized by using a hardware trigger signal. For the three FEAs treated in the main document, we applied V_{ext} and V_{col} in different ways:

a) For FEA1, V_{em} was fixed at a constant voltage of -80 V while V_{col} was scanned back and forth between +1 V and -81 V in steps of 2 V.
b) For FEA2, V_{em} was scanned back and forth between 0 V and -128 V in steps of 2 V. For each V_{em} scan, V_{col} was set to a value between 0 V and -130 V. V_{col} was varied in steps of 2 V after each V_{em} scan.

c) For FEA3, V_{em} and V_{col} were scanned simultaneously. The value of V_{em} was varied between 0 V and -60 V with V_{col} being bound to V_{em} by the ratio $k_{col} = V_{col}/V_{em}$. We varied k_{col} in steps of 0.1 from 0 to 0.8 and in finer steps of 0.01 between 0.8 and 1.0.

We found that fixing V_{em} for a prolonged time period resulted in destructive arcs in some cases. To improve the emission stability, it was advantageous to scan both V_{col} and V_{em} simultaneously as was done in b) and c) above. Due to the above mentioned asynchronous data recording, a method to match the current-voltage dataset and the beam image video frames is needed (see section C). The matching of b) and c) were done similarly but it was necessary to adapt the method to the different sequencing of the applied gate potentials. No such reordering was required for a.

B. Extraction of The Electron Beam Diameter From The Phosphor Screen Image

The beam diameter (full width at half maximum) was calculated from the arithmetic mean of the width and the length of the electron beam spot on the phosphor screen. The images captured by the CCD camera in 24 bit RGB format were first converted into an 8 bit grayscale image using the YIQ standard (gray = 0.299*red + 0.587*green + 0.114*blue), Fig. 1 (a). Then the image was binarized using a threshold defined by the grayscale value which is equal to 50% of the brightest value of the grayscale image, Fig. 1 (b). Binarization was necessary to apply the Canny edge detection algorithm[1]. Once the edges were found, the external contour was computed, Fig. 1 (c). Using the contour, a bounding rectangle (Fig. 1 (d)) could be calculated from which we took the arithmetic mean of the width and the length to derive the beam diameter. All image processing was programmed with the aid of the open source library OpenCV for C++ (open source computer vision library, http://opencv.willowgarage.com).

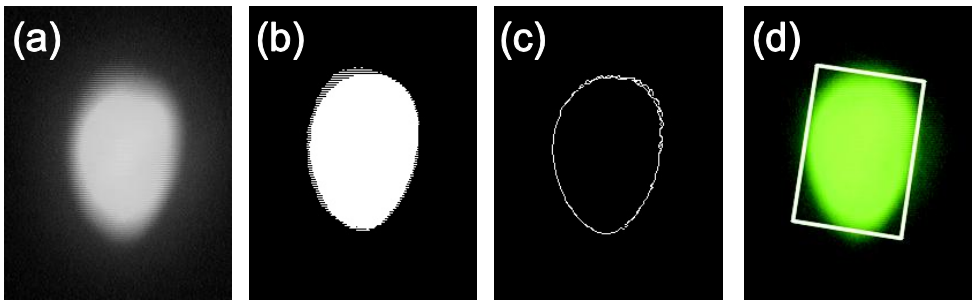

Fig. 1 These figures show the important steps in deducing relevant values from the phosphor screen image. (a) Original spot converted to grayscale (b) binarized grayscale spot (c) contour of the binarized spot calculated by the Canny algorithm (d) original spot with enclosing rotated rectangle drawn from which to deduce width and height of the beam spot.

C. Synchronization of Phosphor Screen Images And Current Measurements

In the experiments reported in the main document, the current-voltage (*I-V*) characteristics and the phosphor screen images were recorded simultaneously but without any means of synchronization. With a frame rate of 30 fps, each frame corresponds to an exposure time of ~33 ms, whereas the step variation of the *I-V* measurements was much faster. To avoid erroneous readings, the *I-V* scan was paused at the maximum V_{em} for 250 ms. Thus, it was ensured that the brightest beam spot was captured on at least 7 frames. In the following, we describe the analysis for a sample measured according to the biasing method b), in which V_{em} was scanned between -42 V and -82 V and V_{col} was kept constant during each V_{em} scan at a value between 0 V and -82 V.

In Fig. 2, we show a complete V_{col} scan. Each "spike" corresponds to a complete V_{em} scan at a fixed value of V_{col}. The inset shows a close up view of a single V_{em} scan where 7 frames were captured at the maximum V_{em}. The beam diameter is calculated based on the average of those 7 frames (see section B on how the diameter of the image from a single frame is derived). This diameter is connected to a single – but presently unknown - V_{col} value at the maximum V_{em} which we call a scan-point. Shown in Fig. 3 are beam diameters for all scan-points of 5 consecutive V_{col} scans.

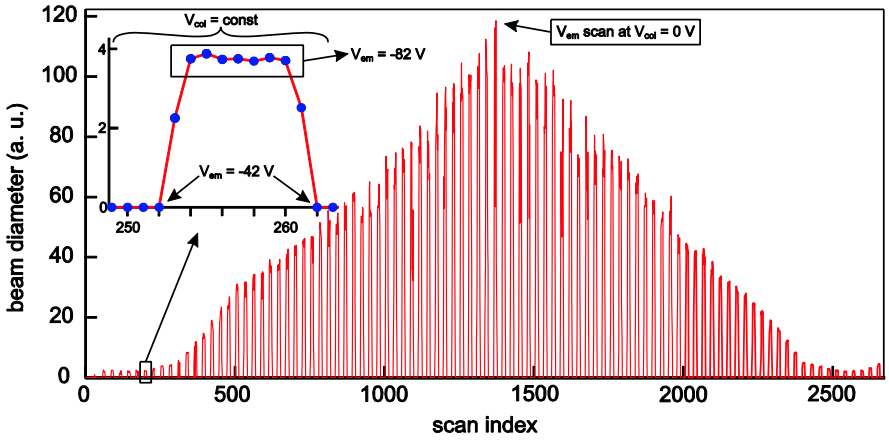

Fig. 2 A complete V_{col} scan from -82 V to 0 V and back again to -82 V in steps of 2 V. Each "spike" corresponds to a V_{em} scan (-42 V to -82 V) as depicted in the inlay. The circles show single phosphor screen images.

Now we need to match this set of beam diameters to the simultaneously measured *I-V* dataset. Using the time stamps of the recorded data, we can make an approximate matching as

shown in Fig. 4 (a). The small time shift was caused by the offset of the clocks of the video camera and the PC controlling the source-measure units.

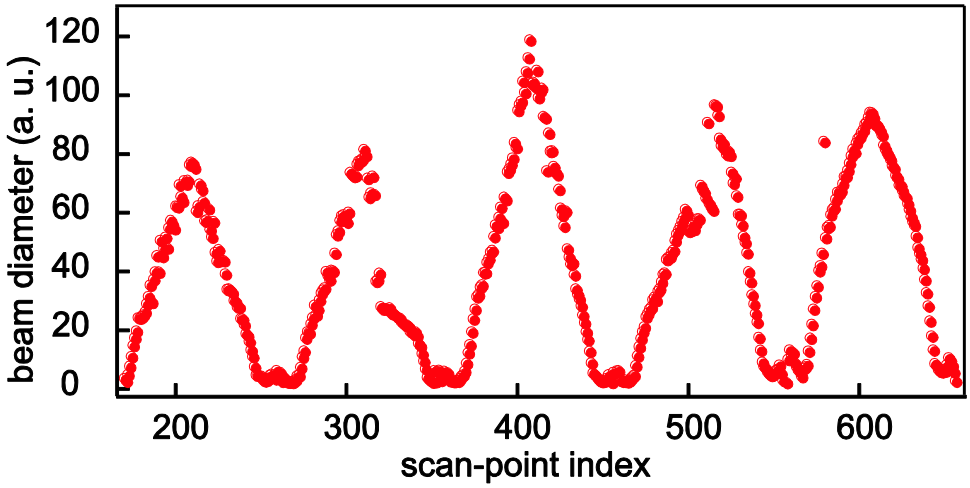

Fig. 3 The extracted beam diameters for all scan-points of five consecutive scans

To correct this shift, we compared the measured current and the integrated beam intensity. By one-dimensional pattern matching (maximizing the cross-correlation of the two datasets), we corrected the unknown time offset. As shown in Fig. 4 (b), the two datasets were aligned perfectly after the cross-correlation. In this way, each scan-point could be matched with the corresponding V_{col} value.

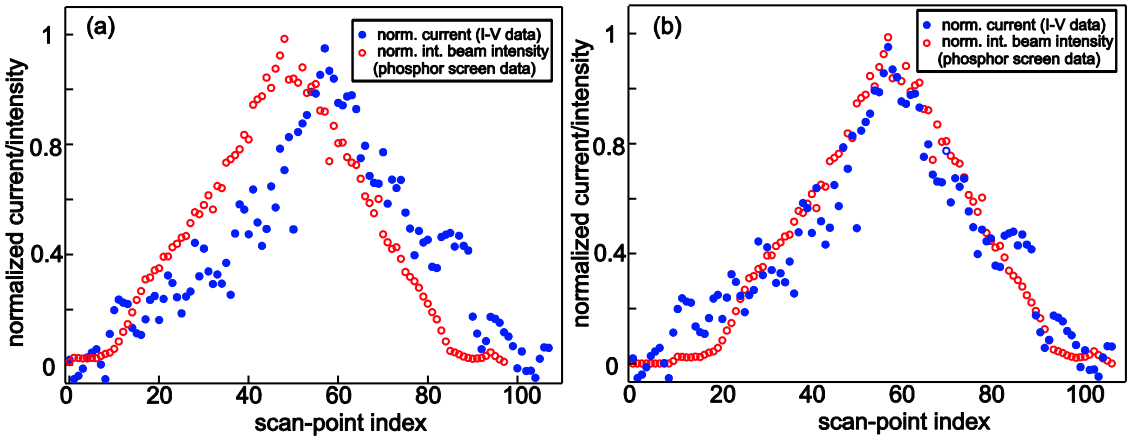

Fig. 4 (a) the normalized curves before cross-correlation show a time-shift (b) after maximizing the cross-correlation, the alignment is improved and a corresponding V_{col} value can be assigned to each beam diameter

D. Derivation of the relationship between R_s and $u_{||}$

First we note that in our measurement setup the transverse velocity of a field emitted electron is conserved after it leaves the gate field of the FEA (1-10 µm above G_{col}, a

negligible distance compared to the cathode-screen distance L_s) until it reaches the screen. Therefore, when the initial rms transverse velocity is $u_{||}$, the average beam radius R_s (defined as the radius of the circle which encloses 80% of the beam area) on the screen is given by

$$R_s = \sqrt{2|\ln(0.2)|}u_{||}T, \quad \text{(S.1)}$$

where T is the average traveling time of the electrons from the cathode to the screen. When the initial longitudinal velocity $u_{||}$ is negligible in comparison to the velocity u_{an} equal to $\sqrt{2qV_{an}/m}$ (determined by the acceleration potential V_{an} applied to the screen), T is equal to $2\,L_s/u_{an}$ and R_s is given by

$$R_s = \sqrt{2|\ln(0.2)|}L_s u_{||}/u_{an}, \quad \text{(S.2)}$$

The equation (S.2) is equal to the equation (1) in the main text in the limit of $u_0/u_{an} << 1$. This case corresponds to the highly collimated beam at k_{col} ~1. Therefore, the evaluation of the minimum $u_{||}$ from the experiment is robust.

The calculation of the traveling time for the uncollimated beam where u_0 cannot be neglected in comparison to u_{an} requires additional assumptions. In this case, the traveling time for electrons with different initial transverse velocities is not constant and can distort the homogeneous transverse velocity distribution. As the experimental conditions correspond to u_0/u_{an} in the order of 0.1 (at most ~0.3), we can safely neglect such effects. Therefore, we can calculate T by solving the equation of motion in the longitudinal direction,

$$\frac{d^2z}{dt^2} = qV_{an}L_s, \quad \text{(S.3)}$$

with the conditions: $\left.\frac{dz}{dt}\right|_{t=0} = u_0$ and $z(T) = L_s$. This results in

$$R_s = \frac{\sqrt{2|\ln(0.2)|}L_s u_{||}}{u_{an}}\left(\sqrt{1+\frac{{u_0}^2}{{u_{an}}^2}} - \frac{u_0}{u_{an}}\right), \quad \text{(S.4)}$$

I. BIBLIOGRAPHY

1 Canny, J., IEEE T. Pattern Anal., **8**(6), 679, 1986.

Chapter 6

Electron Beam Collimation with a 40,000 Tip Metallic Double-Gate Field Emitter Array and In-situ Control of Nanotip Sharpness Distribution

First, the G_{col} aperture fabrication by electron beam lithography is introduced in this chapter. It is shown that this process can easily be extended to the fabrication of the Si wafer mold used to produce the emitter tip arrays as well as the G_{ext} aperture opening by demonstrating the fabrication of high-density single-gate FEAs with up to 10^6 emitter tips. An automatic marker search is used for the overlay alignment of the aperture openings in the electrodes.

The generation of highly collimated electron beams is then demonstrated from a 40,000 emitter tip metallic double-gate field emitter array with large collimation gate apertures fabricated by this electron beam lithography assisted method. Field emission beam measurements are presented, that demonstrate the reduction of the beam envelope down to the array size during collimation. Owing to the optimized gate structure, the concomitant decrease of the emission current was minimal, leading to a net enhancement of the current density. Furthermore, a noble gas conditioning process was successfully applied to the double-gate device to improve the beam uniformity in-situ with orders of magnitude increase of the active emission area. The results show that the proposed double-gate field emission cathodes are promising for high current and high brightness electron beam applications such as free-electron lasers and THz power devices.

Revised Manuscript
Click here to view linked References

High-Density Large-Scale Field Emitter Arrays for X-ray Free Electron Laser Cathodes

Vitaliy A. Guzenko[*]*, Anna Mustonen, Patrick Helfenstein, Eugenie Kirk, Soichiro Tsujino*

Laboratory for Micro- and Nanotechnology, Paul Scherrer Institut, 5232 Villigen PSI, Switzerland

Abstract

High brightness electron sources are of great importance for the operation of the hard X-ray free electron lasers. Field emission cathodes based on the double-gate metallic field emitter arrays (FEAs) can potentially offer higher brightness than the currently used ones. We report on the successful application of electron beam lithography for fabrication of the large-scale single-gate as well as double-gate FEAs. We demonstrate operational high-density single-gate FEAs with sub-micron pitch and total number of tips up to 10^6 as well as large-scale double-gate FEAs with large collimation gate apertures. The details of design, fabrication procedure and successful measurements of the emission current from the single- and double-gate cathodes are presented.

Introduction

Hard-X-ray free electron lasers (FELs) such as the planned SwissFEL X-ray FEL at the Paul Scherrer Institute require high brightness electron sources. Comparing with the state-of-the-art photocathodes [1], field emission cathodes based on double gate metallic field emitter arrays (FEAs) can potentially offer higher brightness by more than a factor of 2. [2-6] Therefore, we explore such FEAs as a possible upgrade option for the SwissFEL cathode. Recently, it has been demonstrated that single-gate FEAs operated in the near infrared laser-induced field emission mode [7-9] are capable of generating ultrafast electron bunches, reaching up to 5 pC with 50 fs excitation pulses. Stable operation of these FEAs with the high acceleration electric field up to 30 MV/m was also shown experimentally. [10, 11] Additionally, reduction of the field emission beam divergence by a factor of 5-10 with stacked double gate FEAs with minimal current loss was shown. [5, 6] The reported results were observed on FEAs fabricated by means of photolithography, which has been a limiting factor for the further improvement of the FEA performance. In particular, it has been difficult to reduce the typical array pitch of 5-10 µm down to the submicron range in order to increase the tip density and thus the total emission current. This could allow us to meet the requirements of SwissFEL for the 200 pC pulse with 10 ps duration while keeping the excitation pulse energy of ~0.1 mJ and nanotip array size about 1mm in diameter. Up-scaling of the number of emitter tips of the double gate FEAs to 10^4 - 10^6 has been hard to achieve so far using optical lithography and focused ion beam milling because of the precision and through-put. However, electron beam lithography is likely to provide the solution to circumvent these problems. The flexibility of electron beam lithography for modifying and optimizing exposure designs allows for fabricating large collimation aperture double-gate FEAs [5, 6] with thousands to millions of emitters. In addition, combining the vacuum nanoelectronic devices with plasmonic structures can enhance the electron yield

[*] Corresponding author. E-mail: vitaliy.guzenko@psi.ch, Tel. +41 56 310 5436, Fax: +41 56 310 2646, Address: Paul Scherrer Institut, ODRA / 116, CH-5232 Villigen PSI, Switzerland.

of laser-induced field emission by orders of magnitude [12, 13], which should boost the FEA performance and make it attractive for SwissFEL as possible upgrade option.

Experimental procedure

Fabrication of the gated FEAs requires several technological steps, that are largely divided into the molding technique for array preparation and the gate fabrication processes on top. [13-17] The major improvement in the fabrication procedure is possible by using an e-beam lithography direct writing tool, particularly Vistec EBPG 5000Plus with the Gaussian shape beam, operated at 100 kV acceleration potential.
The process flow starts with an oxidized 100 mm <001> oriented Si wafer coated by a positive tone resist layer. After the first lithography step (optical or e-beam, depending on the target tip size and density) the pattern is transferred into an SiO_2 layer by reactive ion etching (RIE) and then into the Si wafer by anisotropic wet chemical etching in heated 20% KOH solution. This way, the mold for the arrays of inverted pyramids, the sawing lines, and the registration markers for the following e-beam overlay exposures are created. After thermal oxidation of the wafer, the fabrication of the mold is completed. The last oxidation step is done for fine tuning the mold shape especially that of the pits for the emitter arrays. In the case of photolithographically defined 1.5 µm-base arrays, this step consists of repeated oxidation. [6, 17] In the case of the high-density FEAs defined by e-beam lithography, we typically apply a single oxidation step with the SiO_2 thickness of 400 nm for the emitter tip sharpening. The SiO2 layer also servers as a protection layer for emitters during later demolding step. Next, the mold is sputter coated by Mo and then metallized with Cr and Pd by evaporation. The Pd layer acts as the seed layer for the next electroplating of a low stress Ni support layer with thickness of 400 µm. After demolding, i.e. after complete dissolving of the Si wafer in KOH solution, the all metal nano-tip array wafer is ready for dicing. Subsequent fabrication steps are presently performed with individual chips diced into small pieces, but could be optimized for the whole metallic wafer replica in the future process. In order to manufacture the extractor gate electrode, a layer of SiO_2 is deposited by plasma enhanced chemical vapor deposition (PECVD), sufficiently thick to completely cover the tips, followed by a sputtered layer of Mo, required for the fabrication of the gate electrode. For arrays with 5-10 µm pitches, a self-aligned resist etch-back process has been successfully used in order to open the apertures of the Mo extractor gate electrode. [5, 6, 9, 17] However, this technique is limited to a certain minimum size of the tip. The apertures of the high density FEAs can be reliably defined by means of an e-beam overlay exposure and subsequent etching of Mo and SiO_2 layers. The e-beam-based technique is also the key for the fabrication of the second collimation electrode of the double gate FEA with large collimation gate apertures especially with arrays with a large number of tips. [6, 18]

Results and Discussion

At this point it is worth focusing on the modified fabrication flow, in particular, on the e-beam lithography steps. As mentioned before, applying the direct write e-beam technique instead of photolithography opens up the possibility to decrease remarkably the tip size and thus, the separation between the neighboring tips. In our experiments, the distance between the tips was selected according to simulations of the electrical field enhancement around the tip apex, while illuminating the FEA by Ti:Sapphire laser light with the central wavelength of 800 nm. [12] For the square tip arrangement, the grid parameter was set to

750 nm and for the hexagonal one to 640 nm, an example of which is shown in Fig. 1. In order to reach the target size of the pyramids in the range of 250 nm, the 50 nm smaller squares were exposed with the dose assignment noticeably higher than the dose-to-clear value. Such “undersize -overdose” technique widens the process latitude of the resist development step and consequently of the following pattern transfer into the Si wafer. In this particular case, the exposure dose for the 80 nm thick PMMA 950k layer was 885 $\mu C/cm^2$ and the development time by Methyl isobutyl ketone (MIBK):Isopropyl alcohol (IPA) mixture (3:1) in a spray development step was 90 sec. The SEM image of the tip array shown in Fig. 1 is a part of the hexagonal tip array obtained by this technique. The sawing lines and the set of the registration markers were exposed within the same step. Each tip array was surrounded by a group of markers, which were exposed directly before the exposure of the corresponding tip array and located as close as possible. This ensured that any misalignment between the registration markers and the tip array itself resulting from eventual thermal drift during the exposure is minimized. Since the size of the marker structures exposed in PMMA was $5\times5\ \mu m^2$ and the KOH etching time was optimized for the fabrication of arrays of tips with smaller foot-print, the final registration markers are the truncated-pyramid shape that could successfully be located by an automatic marker search procedure with high precision. The optimization of the marker pattern shape was the important technological key for the successful application of e-beam lithography to this FEA process. This was especially the case since the tips in the sub-micron-pitch arrays were too small for this purpose. Using these so called topographical registration markers has some advantages: Firstly, they are fully compatible with the following mold oxidation steps, which does not tolerate any metals on the wafer surface. Secondly, they facilitate the highest possible overlay precision of the following e-beam exposures, since they were produced together with the tip arrays within the same lithography and etching steps. Thirdly, they are fully compatible with the demolding technique and could be perfectly transferred onto the metallic surface of the chip.

Along with thermal drift, the presence of compressive stress in the electroplated Ni layer, although quite low, is another possible source of pattern distortions. After the dicing of the demolded sample into the square chips for further processing, we found that the compressive stress is partially released. However, breaking the initial circular symmetry of the strain field leads to a non-uniform deformation of the individual chips. Additionally, the difference in the thermal expansion coefficients of the metallic substrate and the SiO_2 insulator layer deposited by PECVD at 300 °C adds deformations and creates additional array distortions (the oxide thickness is ~350 nm in the case of sub-micron pitch arrays. It is 1200 nm-thick for double gate arrays). It is also important not to overlook the fact that electro-plated nickel is weakly magnetic at room temperature, even though added impurities substantially weaken its ferromagnetic property. Therefore, we should be aware of the possibility that spontaneous magnetization may locally influence the trajectory of the electrons and cause random deterioration of the overlay precision.

In order to quantify these effects, we measured the positions of test registration markers on a demonstrator chip by means of e-beam tool and evaluated the displacement from the designed positions in the original mold exposure pattern at different locations. The result is visualized in Fig. 2 as a color map. The direction of the displacement is indicated by arrows. In some regions an offset up to ~30 nm is observed. However, these changes of the lateral dimensions of a chip are evident over the distances of several millimeters. Therefore, in order to minimize the effect of the chip distortion on the quality of the overlay

exposure, the registration markers were placed as close to the tip arrays as possible. The alignment routine was executed prior to exposure of each array on a chip. This allowed us to fabricate functional high density FEAs with an overlay precision between the tip array and the extractor gate electrode better than 30 nm (see Fig. 3). Fig. 4 shows one of the current-voltage characteristics of a high-density single-gate FEA with the diameter of 560 µm recorded after several days of continuous operation, with the gate voltage being swept up and down between 0 and 50 V. The relation between the emission current and the gate bias potential follows the Fowler-Nordheim law (inset of Fig. 4) with the DC emission current up to 25 µA. The FEAs with the larger diameters did not perform all that well yet: disintegration of the device was observed at lower extractor voltages by the short circuiting of some tips and the gate electrode. This appeared to have been caused by some critical fabrication defects that become more probable with scaling up of the array size, such as dust particles or the misalignment between the tip and the aperture of the extractor gate electrode. Further development of extractor gate technology with respect to the e-beam lithography step is under way in order to improve the performance of high density large scale FEAs.

Application of e-beam lithography enabled also remarkable breakthrough in the fabrication of the large scale double gate FEAs. [18] Since the restrictions to the cathode design caused by the self-alignment process were lifted, it became possible to optimize the design of the second collimating electrode, i.e. its aperture diameter and axial positioning, in order to reach the best focusing of electrons while avoiding unacceptable suppression of the emission current. The FEA structures with the 3:1 ratio of the openings of the collimation to the extractor gates demonstrated current density enhancement more than a factor of 10. [5, 6, 18] For an FEA with 1.5 µm-base pyramid emitters and the extractor gate aperture diameter of ~2 µm (fabricated by a self-alignment process) the target diameter of the collimation gate is therefore 6-7 µm. Recent demonstration of such double-gate FEAs were fabricated with the FIB assisted process but limited to 20×20 tips. By using the e-beam process here, we were able to increase the number of the tips. In the Fig. 5, a small part of such large-scale double gate FEA fabricated by means of e-beam lithography and subsequent wet etching steps is shown. The total number of tips per array of 2.3 mm in diameter is to 4×10^4. The required e-beam exposure time for this array was less than 10 minutes. Sets of registration markers of the size of 10×10 μm^2, fabricated according to the procedure described above facilitated reaching the high overlay precision of the collimation gate electrode across the whole array. The functionality of completed devices was tested on an experimental setup equipped with a phosphorescent screen for beam imaging for quantitative characterization of the emission and beam collimation characteristics of the cathode. Application of negative voltage applied to the second gate led to the observation of a clear beam collimation effect as shown in Fig. 6, while the total current emitted by cathode remains quite high (1.5 µA vs. 5 µA without collimation voltage).

Conclusions

We explored the application of an e-beam lithography technique to fabricate the high density single gate FEAs and the large scale double-gate FEAs wth large collimation gate apertures. Key technical steps were clarified, which led to the successful fabrication of the first functional sub-micron pitch single-gate FEAs with dimension up to 2 mm in diameter and emitter densities reaching 3.5×10^6 mm^{-2} was demonstrated and the first 4×10^4 tip double-gate FEAs with more than a factor of 10 collimation capability, which were

successfully tested. Utilizing the e-beam lithography technique enables not only high flexibility in designing individual emitters but also integration of the plasmonic structures into FEAs and thus, boosting the electron yield of the cathode emission.

References

[1] B. D. Patterson, R. Abela, H. H. Braun, U. Flechsig, R. Ganter, Y. Kim, E. Kirk, A. Oppelt, M. Pedrozzi, S. Reiche, L. Rivkin, T. Schmidt, B. Schmitt, V. N. Strocov, S. Tsujino, and A. F. Wrulich, New J. Phys. **12** (2010) 035012.
[2] Hosono, A.; Kawabuchi, S.; Horibata, S.; Okuda, S.; Harada, H., and Takai, M., J. Vac, Sci. Technol. B **17** (1999), 575
[3] L. Dvorson, and A. I. Akinwande, J. Vac. Sci. Technol. B **20** (2002), 53
[4] Neo, Y.; Takeda, M.; Soda, T.; Nagao, M.; Yoshida, T.; Kanemaru, S.; Sakai, T.; Hagiwara, K.; Saito, N.; Aoki, T., and Mimura, H. , J. Vac. Sci. Technol. B **27** (2009), 701
[5] P. Helfenstein, E. Kirk, K. Jefimovs, T. Vogel, C. Escher, H.-W. Fink, and S. Tsujino, Appl. Phys. Lett. **98** (2011) 061502.
[6] P. Helfenstein K. Jefimovs, E.Kirk, C. Escher, H.-W. Fink, and S. Tsujino, J. Appl. Phys. **112** (2012) 093307.
[7] P. Hommelhoff, C. Kealhofer, and M.A. Kasevich, Phys. Rev. Lett. **97** (2006) 247402.
[8] S. Tsujino, P. Beaud, E.Kirk, T. Vogel, H. Sehr, J. Gorbecht, and A. Wrulich, Appl. Phys. Lett. **92** (2008) 193501.
[9] A. Mustonen, P. Beaud, E. Kirk, T. Feurer, S. Tsujino, Appl. Phys. Lett. **99** (2011) 103504.
[10] S. Tsujino, M. Paraliev, E. Kirk, T. Vogel, F. Le Pimpec, C, Gough, S. Ivkovic, and H. H. Braun, J. Vac. Sci. Technol. B **29** (2011) 02B117.
[11] S. Tsujino, M. Paraliev, E. Kirk, C, Gough, S. Ivkovic, and H. H. Braun, Physics of Plasmas **18** (2011) 064502.
[12] A. Mustonen, P. Beaud, E. Kirk, T. Feurer, and S. Tsujino, Scientific Reports **2** (2012) 915.
[13] A. Mustonen, V.A. Guzenko, C. Spreu, T. Feurer, and S. Tsujino, unpublished (2012)
[14] H.F. Gray, and G. J. Campisi, U.S. Patent No. 4.964,946 (23 October 1990)
[15] M. Sokolich, E.A. Adler, R.T. Longo, D.M. Goebel, and R.T. Benton, Tech. Dig. – Int. Electron Devices Meet. 1990, 159
[16] S.M. Zimmermann, D.B. Colavito, and W.T. Babie, Tech. Dig. – Int. Electron Devices Meet. 1990, 163
[17] E. Kirk, S. Tsujino, T. Vogel, H. Sehr, J. Gobrecht, and A. Wrulich, J. Vac. Sci. Technol. B **27** (2009) 1813.
[18] P. Helfenstein, V.A. Guzenko, H.-W. Fink, and S. Tsujino, unpublished (2012).

Figure Captions:

Figure 1. Scanning electron microscope (SEM) image of several Molybdenum tips with the base size of 250 nm, arranged on the hexagonal grid with the period of 640 nm.

Figure 2. Color map of the displacements of the registration marker from expected positions as measured on a demonstrator chip with 20 FEA arrays by means of e-beam lithography tool. The arrows indicate the direction of the marker displacement. Compensation for these distortions had to be done during the overlay exposures of the aperture patterns of the gate electrodes.

Figure 3. A part of a 560 µm large single gate FEA with the tip distance of 750 nm and the overlay precision at any location of arrays better than 40 nm. The inset shows more detailed an individual field emitter.

Figure 4. Emission current vs. gate voltage characteristics of a single gate submicron-pitch FEA with diameter of 560 µm, operated in the DC mode, recorded after several days of operation. The inset shows the corresponding Fowler-Nordheim plot.

Figure 5. Optical microscope overview image of part of a double-gate FEA with the tip distance of 10 µm and a higher magnification SEM micrograph of an individual emitter (inset)

Figure 6. Photographs of the phosphorescent screen exposed to the non-collimated (left) and collimated electron beam emitted by a 2 mm in diameter large double gate FEA. The corresponding emission currents were 5 µA and 1.5 µA, respectively.

Figure1
Click here to download high resolution image

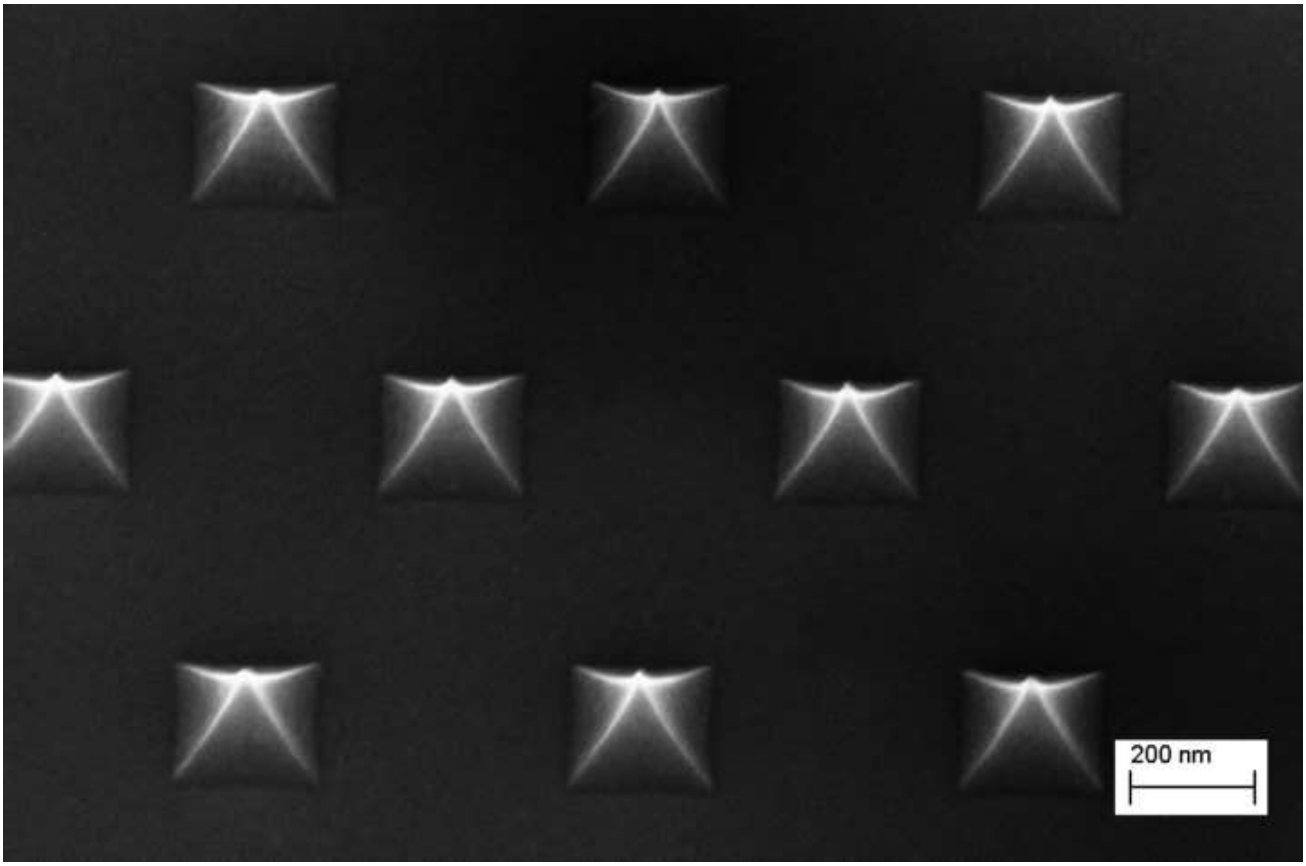

Figure2
Click here to download high resolution image

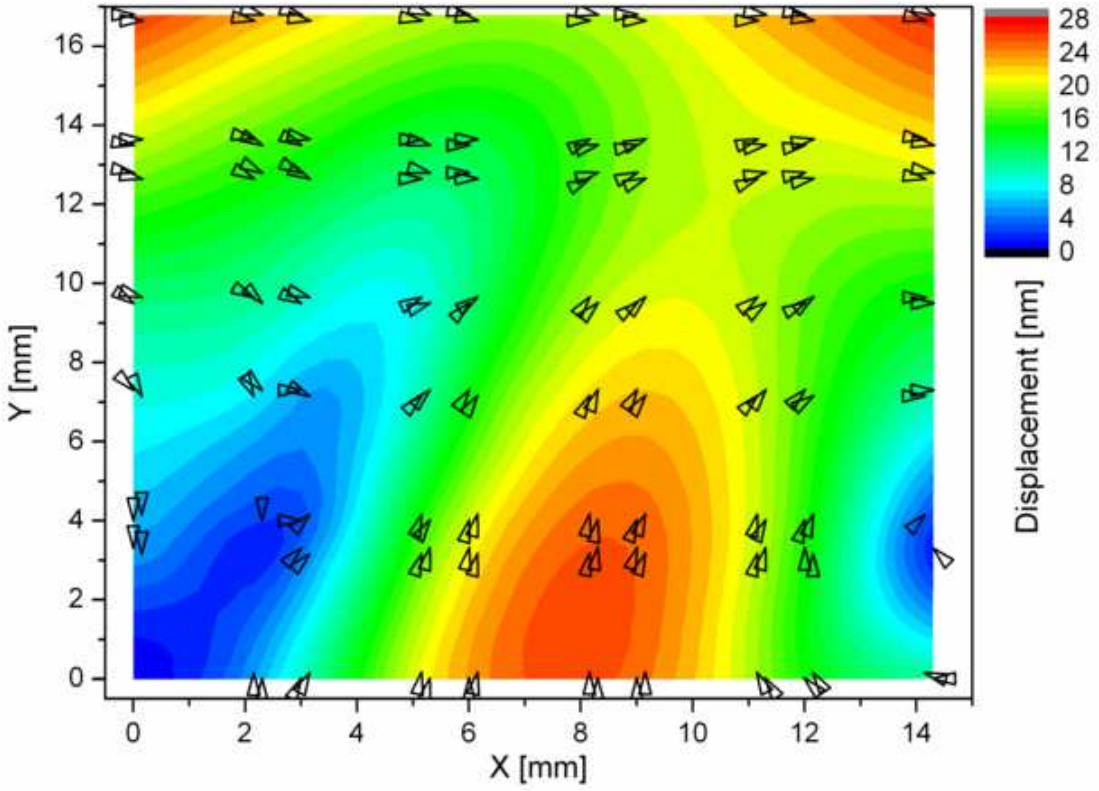

Figure3
Click here to download high resolution image

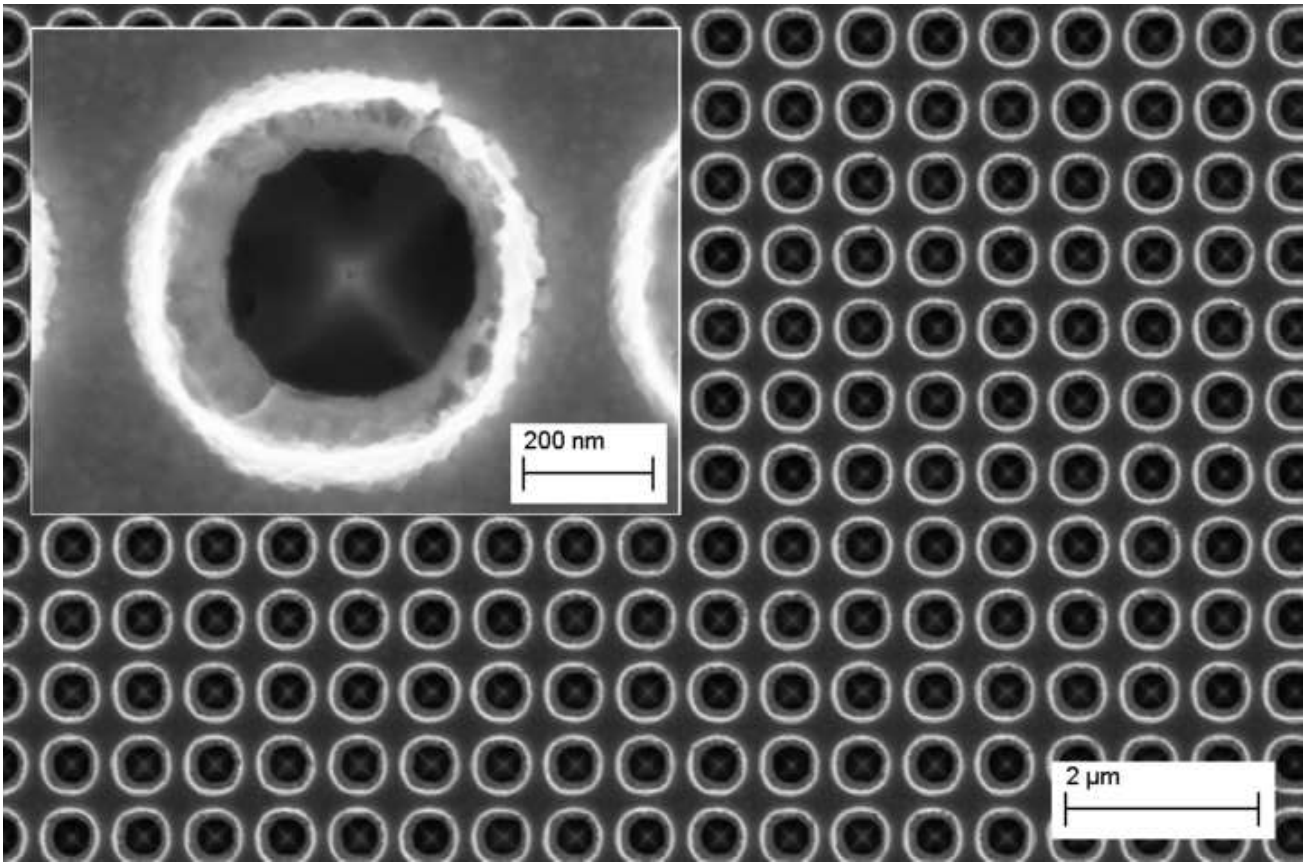

Figure4 (revised)
Click here to download high resolution image

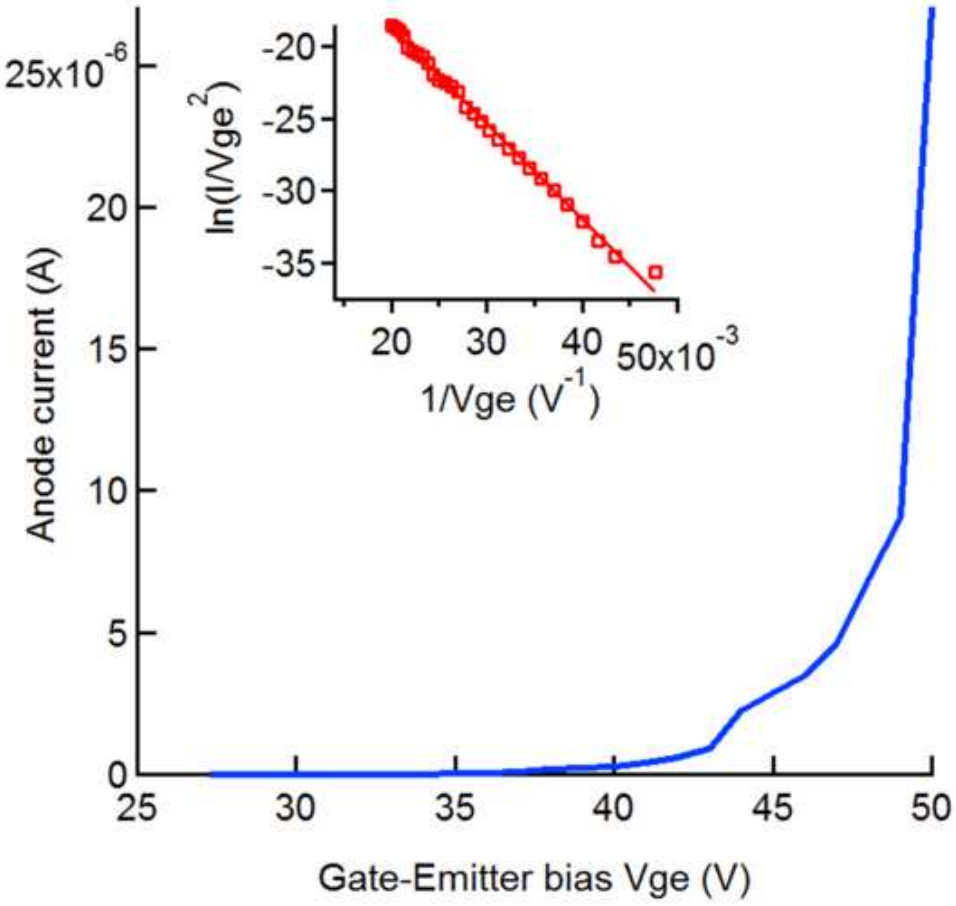

Figure5
Click here to download high resolution image

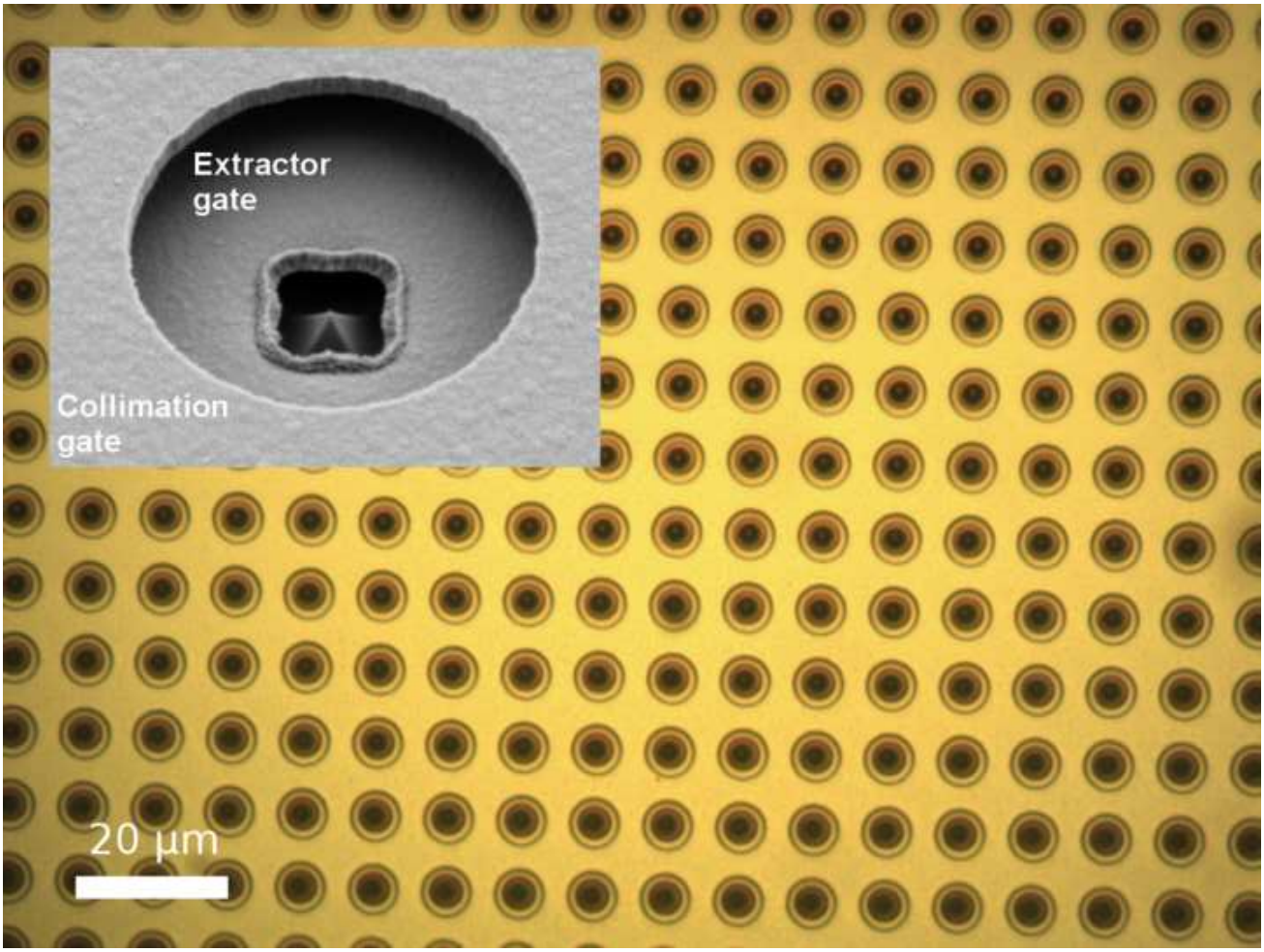

Figure6
Click here to download high resolution image

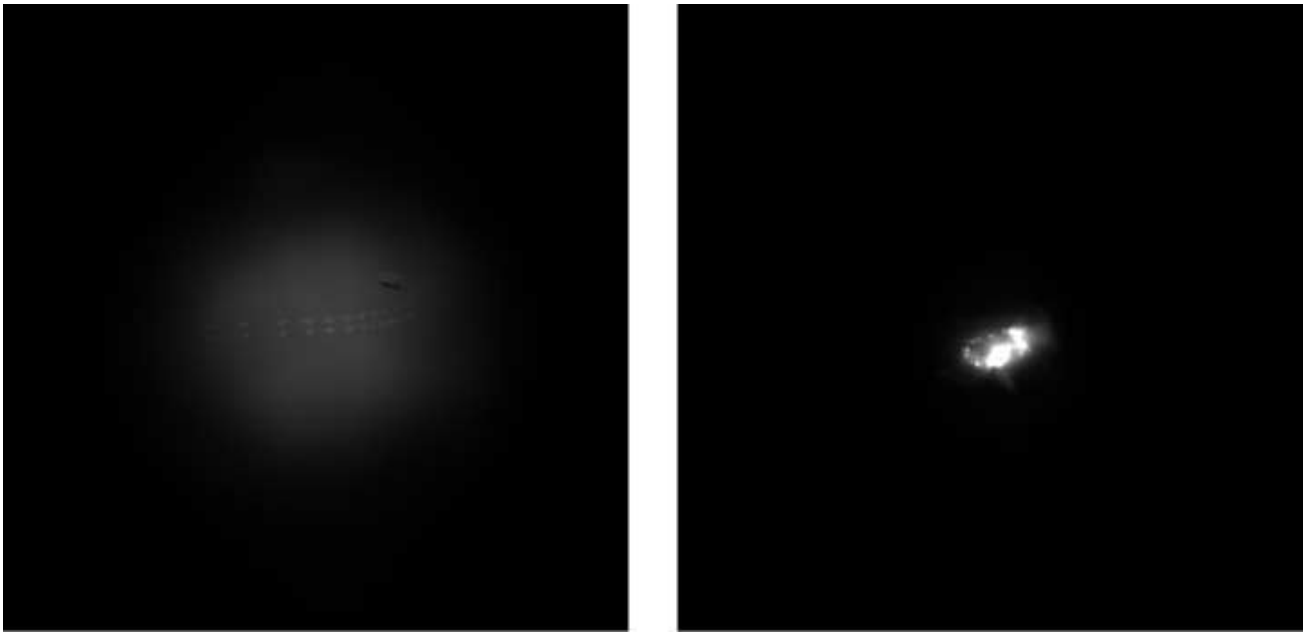

JOURNAL OF APPLIED PHYSICS **113**, 043306 (2013)

Electron beam collimation with a 40 000 tip metallic double-gate field emitter array and in-situ control of nanotip sharpness distribution

P. Helfenstein,[1,a)] V. A. Guzenko,[1] H.-W. Fink,[2] and S. Tsujino[1,b)]
[1]*Laboratory for Micro- and Nanotechnology, Paul Scherrer Institut, CH-5232 Villigen-PSI, Switzerland*
[2]*Physik Institut, University of Zurich, Winterthurerstrasse 190, CH-8057 Zurich, Switzerland*

(Received 10 December 2012; accepted 7 January 2013; published online 24 January 2013)

The generation of highly collimated electron beams from a double-gate field emitter array with 40000 metallic tips and large collimation gate apertures is reported. Field emission beam measurements demonstrated the reduction of the beam envelope down to the array size by applying a negative potential to the on-chip gate electrode for the collimation of individual field emission beamlets. Owing to the optimized gate structure, the concomitant decrease of the emission current was minimal, leading to a net enhancement of the current density. Furthermore, a noble gas conditioning process was successfully applied to the double-gate device to improve the beam uniformity *in-situ* with orders of magnitude increase of the active emission area. The results show that the proposed double-gate field emission cathodes are promising for high current and high brightness electron beam applications such as free-electron lasers and THz power devices. © *2013 American Institute of Physics*. [http://dx.doi.org/10.1063/1.4788998]

I. INTRODUCTION

The extremely high brightness of field emission electron beams has enabled the realization of electron microscopes with single-atom resolution[1] and has stimulated high current and high current density applications such as free-electron lasers[2,3] and THz vacuum electronic devices.[4–7] Field emitters can produce high brightness electron beams via quantum tunneling by applying a strong electric field in the order of GV/m to solid surfaces. Such fields can be created by a comparatively low potential with the help of the field enhancement at the nanometer-scale tip apexes. The recognition that the electric field enhancement occurs not only at dc but also at high frequencies up to nearly optical frequencies has recently triggered intensive studies ranging from fundamental physics such as electron dynamics in strong fields[8] to ultrafast electron beam applications for time-resolved electron diffraction and microscopy,[9] potentially down to the attosecond range.[10]

Field emitter arrays (FEAs) with on-chip electron extraction gate electrodes G_{ext}, which combine the electron emission of thousands to millions of nanotips, have been explored for high current generation with a wide variety of materials.[7,11–14] To generate high brightness beams with a small transverse electron velocity spread, however, it is crucial to add an on-chip gate electrode G_{col} for the collimation of individual field emission beamlets. These so-called double-gate FEAs have been proposed as high current and high brightness cathodes[15,16] and have been actively studied.[17–26] One of the critical obstacles for the realization of high performance double-gate FEAs is the reduction of the emission current during the beam collimation. Recent developments show that this can be circumvented by devising the gate aperture shapes as demonstrated with volcano-shaped FEAs[23] and stacked double-gate device with large G_{col} apertures.[24–26]

For the practical application of FEAs it is important to prepare an array with uniform nanotip apex distribution. Due to the exponential sensitivity of the field emission current on the electric field at the emitter apexes, even a small non-uniformity of the emitter tip apex radius of curvature r_{tip} results in a highly non-uniform beam across the array and limits the total current, making the requirement for the r_{tip} uniformity stringent.[22] In the case of single-gate FEAs, the r_{tip} distribution of as-fabricated FEAs can be improved by an application of high potential switching pulses and blunting the emitter tips by joule heating[27] but at the expense of risking failure by vacuum arcs. Another promising method is the bombardment of ions generated by glow-discharge[28] or by electron impact ionization using the field emission current.[29–32] In particular, an improvement of the beam uniformity by *in-situ* noble gas conditioning for single-gate molybdenum FEAs was demonstrated recently.[32] However, no study has been reported for the beam uniformity control of double-gate FEAs.

In this work, we study the beam collimation characteristics and *in-situ* control of the r_{tip} distribution of a 40 000 tip double-gate FEAs with large G_{col} apertures. The experimental results demonstrated a substantial reduction of the transverse electron beam spread by G_{col} and an improvement of the beam uniformity by the noble-gas conditioning process.

II. EXPERIMENT & METHODS

A. Double-gate FEA fabrication

The double-gate FEA of pyramidal-shaped molybdenum nanotips with r_{tip} of ~10 nm, Figure 1, was fabricated by a combination of molding for the preparation of the emitter arrays, the self-aligned polymer etch-back method for the G_{ext} fabrication, and an electron beam (e-beam) lithography

[a)]Electronic mail: patrick.helfenstein@psi.ch.
[b)]Electronic mail: soichiro.tsujino@psi.ch.

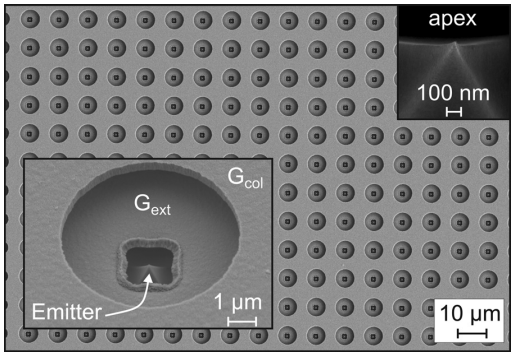

FIG. 1. SEM image of a part of the double-gate FEA with 4×10^4 molybdenum emitter tips. The insets show a close up of a single emitter with extraction (G_{ext}) and collimation gate (G_{col}) aperture openings (left bottom) and the tip-apex (right top).

process for the G_{col} fabrication.[25,26,33–35] The 4×10^4 emitter tips were aligned with 10 μm pitch in a circular area measuring 2.26 mm in diameter. The gate electrodes consisted of 0.5 μm thick molybdenum films. The FEA and G_{ext} were separated by a 1.2 μm thick SiO_2 layer, whereas G_{col} and G_{ext} were separated by a 1.2 μm thick SiON layer.[26] To pattern the apertures of G_{col}, a process using focused ion beam milling was formally developed for arrays up to 20×20 tips.[25,26] This maskless and flexible method is ideal for prototyping small arrays but difficult to apply to larger FEAs because of the required milling time of ~90 s per aperture. With the newly developed e-beam process, we successfully prepared the 4×10^4 tip FEA having a G_{col} aperture diameter of 6.5 ± 0.1 μm, which is a factor of 3 larger than that of the G_{ext} apertures (2.0 ± 0.1 μm).[35] Patterning the gate apertures with this ratio was difficult with the polymer-etch back method but critically important to achieve a high current density enhancement with a small transverse electron velocity spread.[24–26]

B. Field emission experiment

The experiment was conducted in a field emission microscope, Figure 2, equipped with an electron beam imaging screen (metalized P43 phosphor) and a retractable Faraday cup. The FEA was placed 50 mm from the screen. A CCD camera was used to record the beam images which were subsequently analyzed to evaluate the rms beam radius R_s and the rms transverse velocity u_t.[26] We simultaneously measured the current I_{em} through the FEA and the gate currents I_{ext} and I_{col}, Figure 2. The net current I_{net} reaching the screen was evaluated from the relation ($|I_{em}| - I_{ext} - I_{col}$). The field emission beam was accelerated by a potential of 3 kV applied to the screen. Alternatively, I_{net} was measured directly by the Faraday cup biased at 300–500 V. The value of I_{net} was the same for the two measurements.

In the beam collimation experiment, we simultaneously varied V_{col} and V_{em} with a fixed ratio k_{col} ($=V_{col}/V_{em}$) and recorded the beam images at the largest V_{em}. The beam was measured at different collimation strengths by scanning k_{col} from 0 to 0.9 in steps of 0.1 and from 0.91 to 1.05 in steps

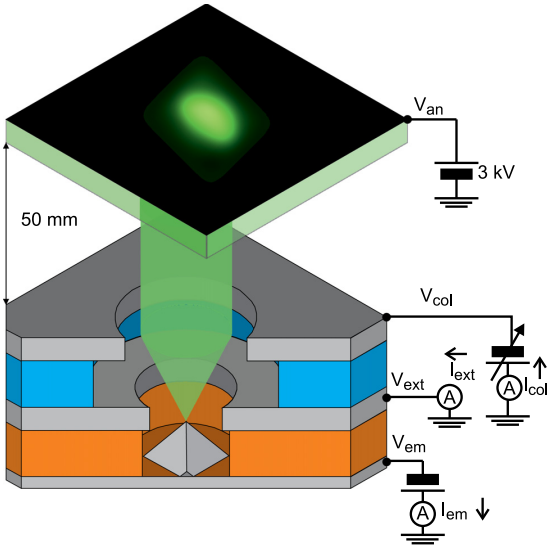

FIG. 2. Schematic illustration of the experimental setup. The double-gate FEA in the field emission microscope generates a collimated electron beam under the potential voltages V_{em}, V_{ext}, and V_{col}. The currents I_{em}, I_{ext}, and I_{col} were simultaneously monitored to evaluate the current I_{net} reaching the screen. Using a retractable Faraday cup (not shown), I_{net} can be measured directly.

of 0.01. To restrict the power consumption of the screen, we limited the maximum I_{net} to ~5 μA.

After inserting the FEA into the field emission microscope, the chamber was evacuated to the base pressure of $\sim 5 \times 10^{-9}$ mbar. Then, the FEA was conditioned by scanning the potential V_{em} applied to the emitter substrate between 0 V and a negative maximum for several days until the emission current level became stable.[26] During this conditioning phase, the gate potentials V_{ext} and V_{col} were set to ground potential. We further conditioned the FEA in a low-pressure Ne gas atmosphere by continuing the V_{em} scan for ~3 h after introducing neon gas at a pressure of $(1–2) \times 10^{-4}$ mbar into the chamber. The relation between the Faraday cup current and V_{em} was continuously recorded and analyzed.

C. Theoretical modeling of the double-gate FEAs

To analyze the experiment, we created a 3D model of a single emitter using commercial tools: CST Particle Studio for the particle tracking simulation and COMSOL Multiphysics for calculating the static electric field at the emitter tip surface. We assumed an r_{tip} of 10 nm and applied the Fowler-Nordheim equation at the emitter surface to calculate the emission current distribution.[36] By subsequently integrating the equation of motion for electrons emitted from the nanotip surfaces, the beam collimation characteristics under the influence of the gate potential field were calculated.

III. EXPERIMENTAL RESULTS

A. Electron beam characteristics

Figures 3–5 show the observed electron beam characteristics of the double-gate FEA. The beam images of Figures

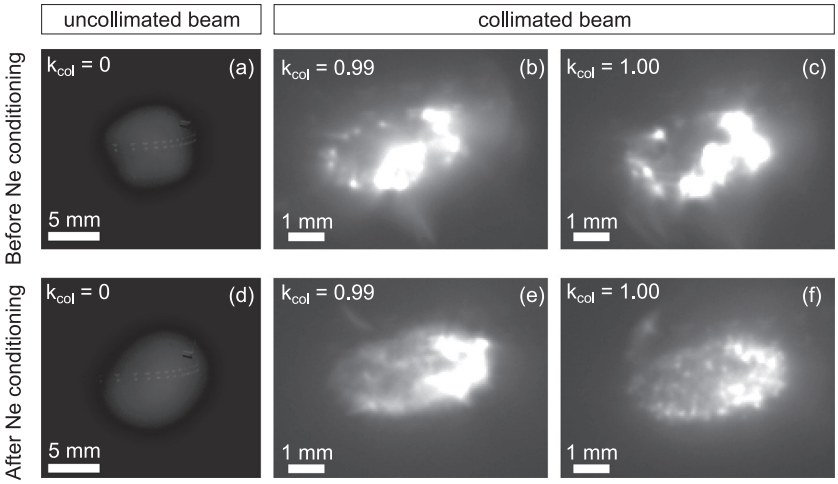

FIG. 3. Images of field emission beams generated by the double-gate FEA with 4×10^4 emitters at different collimation strength denoted by the ratio k_{col} ($=V_{col}/V_{em}$). (a)-(c) were observed before the Ne gas conditioning with V_{em} of -72 V, whereas (d)-(f) were observed after the Ne gas conditioning with V_{em} of -69 V. The maximum current reaching the screen at zero k_{col} was $\sim 5\,\mu$A for both cases. All the beams are displayed with the same intensity scale, highlighting the large beam brightness enhancement at k_{col} of 0.99 and 1.00.

3(a)–3(c) show that the increase of k_{col} from 0 to 0.99 and 1.00 enhanced the beam brightness considerably. Owing to the large G_{col} apertures, more than 30% of the current emitted from the tips was retained at the maximum collimation.[26] This resulted in an enhanced current density with the decrease of $R_s - R_0$, where R_0 equal to 0.57 mm is the rms radius of the FEA. In fact, the I-V characteristics in Figures 5(a) and 5(b) and the variation of $R_s - R_0$ in Figure 4 (open squares) show that increasing k_{col} from 0 to 0.99 resulted in a decrease of I_{net} from $5.5 \pm 0.2\,\mu$A to $1.9 \pm 0.2\,\mu$A, whereas $R_s - R_0$ decreased from 2.9 ± 0.2 mm to 0.1 ± 0.1 mm. Since the beam area decreased more rapidly than I_{net}, this resulted in an enhanced beam brightness. The similarity of this result to the previously reported experiments with FEAs with a smaller number of tips[25,26] demonstrates the capability to upscale the excellent beam characteristics of 4-400 emitters up to 4×10^4 emitters.

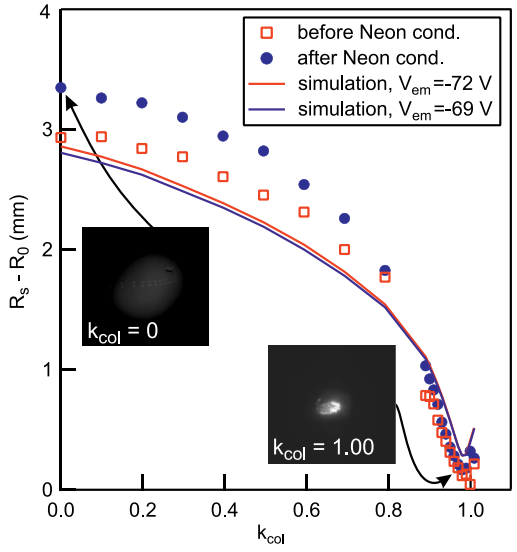

FIG. 4. Variation of R_s with the increase of k_{col} before and after the neon conditioning. The rms radius R_0 equal to 0.57 mm of the FEA was subtracted from R_s for the experiment. The solid lines show the calculated R_s versus k_{col} obtained by the full 3D simulation of a single-emitter at values of V_{em} equal to -72 V and -69 V. The beam images at k_{col} equal to 0 and 1.00 at V_{em} of -69 V obtained after the neon gas conditioning are also displayed.

The beneficial effect of the large G_{col} apertures was also supported by theory. From the single emitter simulation, we calculated the beam characteristics for k_{col} between 0 and 1.05. The simulated I-V characteristics at V_{em} of -72 V and -69 V calculated simultaneously with the beam characteristics are shown in Figures 5(c) and 5(d), respectively. The calculated beam collimation characteristics of the single emitter are shown in Figure 4 for the two V_{em} values (solid lines). (We note that the rms source radius of the single emitter ($\ll$10 nm) is negligible in this scale). The reproduction of the experimental values of the shape of the I-V variation and the beam collimation characteristics as functions of k_{col} are excellent.

The comparison of Figures 3(b) and 3(c) with Figures 3(e) and 3(f) shows that the neon gas conditioning improved the beam uniformity. At approximately the same I_{net} with a slightly smaller V_{em} of -69 V, the beam observed after the gas conditioning exhibited fewer parts with nearly saturated intensity and increased emission around the center of the beam, whereas the $R_s - R_0$ versus k_{col} relation was approximately the same. The I-V characteristics (Figure 5(a)) changed slightly after the neon conditioning (Figure 5(b)). Interestingly, the shape of the I-V characteristics after the gas conditioning (Figure 5(b)) resembles that of simulation more closely. One can ascribe this as a consequence of making the r_{tip} distribution more uniform by the neon gas conditioning. The same shape of the two calculated I-V curves at V_{em} of -72 V and -69 V (Figures 5(c) and 5(d), respectively) shows that the difference of V_{em} in the two experiments is not the source of the different curve shapes.

To quantify the quality of the collimated electron beam, we evaluated the rms transverse velocity u_t evaluated by the following equation[26]

$$\frac{R_s - R_0}{L_s} \approx \frac{2u_t}{u_{an}} \left(\sqrt{1 + \frac{u_0^2}{u_{an}^2}} - \frac{u_0}{u_{an}} \right). \quad (1)$$

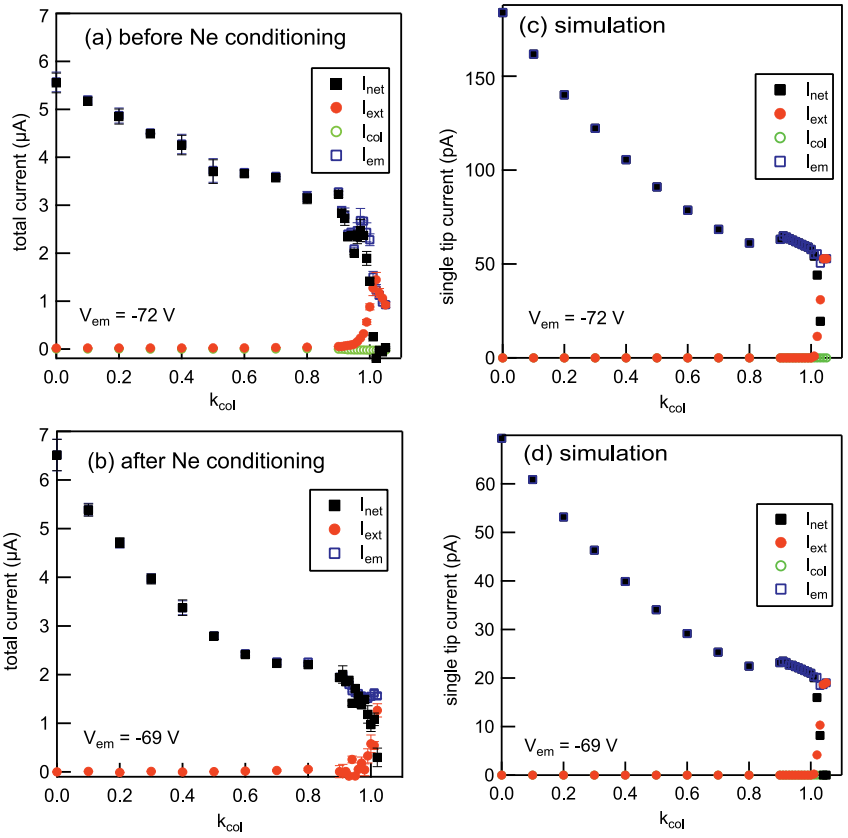

FIG. 5. Current-voltage characteristics of the 40 000 tip FEA measured during the beam collimation experiment of Figure 3, (a) before the neon gas conditioning with V_{em} of −72 V, (b) after the neon gas conditioning with V_{em} of −69 V. The simulated current-voltage characteristics (c) at V_{em} of −72 V and (d) at V_{em} of −69 V were obtained together with the calculation of the $R_s - k_{col}$ relations displayed in Figure 4.

In above equation, L_s of 50 mm is the distance between the FEA and the screen, and u_{an} is the longitudinal velocity at the screen determined by V_{an} of 3 kV as $\sqrt{2q|V_{an}|/m}$ (q being the elementary charge and m is the electron rest mass). u_0 is the initial longitudinal velocity defined at a few microns off the tip surface. At $k_{col} = 0$, it is approximately given by $\sqrt{2q|V_{em}|/m}$. At k_{col} close to unity, u_0 can be safely neglected because the electrons are significantly decelerated by V_{col}. Since V_{an} is an order of magnitude larger than V_{col}, we neglected the effect of V_{col}.

At zero k_{col}, from $R_s - R_0$ of 2.9 ± 0.2 mm and Eq. (1), u_t as a fraction of the speed of light in vacuum c_0 is evaluated to be $(3.7 \pm 0.1) \times 10^{-3}$. At $k_{col} = 0.99$ with $R_s - R_0$ equal to 0.16 ± 0.1 mm, u_t/c_0 is evaluated to be $\sim 2.4 \times 10^{-4}$. The reduction of u_t by a factor of ∼15 is about 1.5 times better than the previous results obtained from FEAs with a smaller number of emitters.[25,26]

We note that a close inspection of the beam images at k_{col} of 0.99 and 1.00 in Figure 3, in particular Figures 3(e) and 3(f), reveals granular spots with a typical rms radius below ∼100 μm. This value is approaching the experimental resolution and is in the same order of magnitude as the calculated single emitter value. The similarity of these images with the granular beam images of as-fabricated single-gate FEAs observed at the acceleration potential of 200 kV using a pulsed diode gun[32,37,38] poses a possibility that individual beamlets were resolved at the large k_{col} values in the present experiment, even though the acceleration potential was only 3 kV and there was no additional focusing element such as a solenoid. This suggests that the actual minimal value of u_t is smaller than the value evaluated above from the beam envelope. Further experiments concerning the direct measurement of the transverse beam emittance and analysis of the model at high k_{col} as a function of high acceleration fields are needed to establish the actual collimation strength.

B. Emission homogenization by noble gas conditioning

Finally, we discuss the impact of the neon gas conditioning on the emission characteristics. Figure 6(a) shows the evolution of the relation between I_{net} and V_{em} during the conditioning. As a result of ∼3 h of the neon gas conditioning, the current at a given V_{em} increased approximately an order of magnitude (from scan a to scan c), with I_{net} reaching 0.14 mA at a V_{em} of −81 V in the end.

We analyzed the I_{net}-V_{em} relation by fitting with the following function

$$I = A_{FN}\left(\frac{|V_{em}|}{B_{FN}}\right)^2 \exp\left(\frac{-B_{FN}}{|V_{em}|}\right). \quad (2)$$

This assumes the Fowler-Nordheim equation for the single-tip current I_{tip} with a constant single-tip emission area S_{tip}

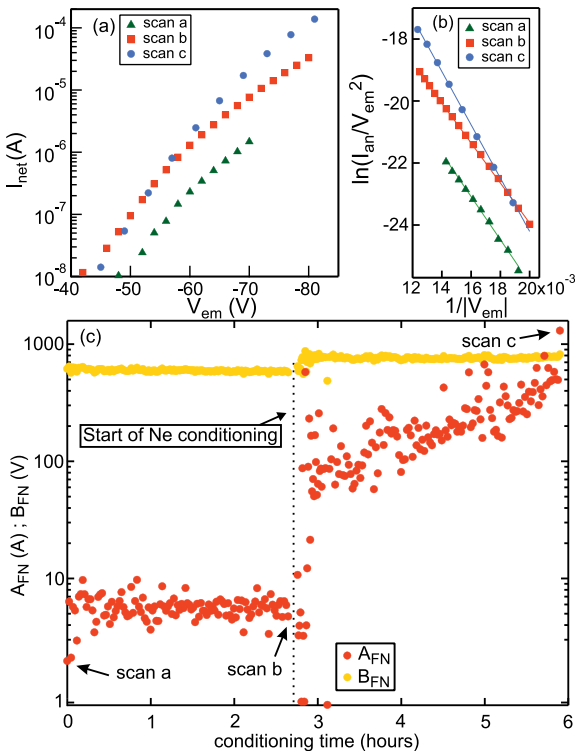

FIG. 6. (a) Evolution of the emission current-voltage characteristics during the conditioning. (b) Fowler-Nordheim plot of the I-Vs shown in (a). (c) The evolution of the Fowler-Nordheim fitting parameters A_{FN} and B_{FN} in UHV and during the neon gas conditioning.

and an electric field F at the emitter tip apex determined by $|V_{em}|$[36,39–41]

$$I_{tip} = S_{tip}\frac{a}{t^2\phi}\exp(bc^2/\sqrt{\phi})F^2\exp\left(-\frac{b\phi^{3/2}}{F}\right), \quad (3)$$

where S_{tip} is the single-tip emission area and F is the electric field at the emitter tip apex. The constants a, b, c are given by $a = 1.541434 \times 10^{-6}$ A eV V^{-2}, $b = 6.830890$ eV$^{-3/2}$ Vnm^{-1}, and $c = 1.199985$ eV V$^{-1/2}$ nm$^{1/2}$. ϕ is the work function (~4.5 eV for molybdenum), and t is approximately equal to 1.[36,42] The fitting parameters A_{FN} and B_{FN} are written as follows

$$A_{FN} = N_{tip}S_{tip}\frac{ab^2\phi^2}{t^2}\exp(bc^2/\sqrt{\phi}), \quad (4)$$

$$B_{FN} = b\phi^{3/2}\beta^{-1}, \quad (5)$$

where N_{tip} is the number of active emitters and β is the field enhancement factor (equal to $F/|V_{em}|$). β is approximately proportional to $(r_{tip})^{-0.5}$ for our pyramidal shaped emitters.[43]

Figure 6(c) summarizes the obtained evolution of A_{FN} and B_{FN}. At the end of the conditioning in UHV and before the neon gas was introduced in the chamber, A_{FN} was equal to 5±2 A and B_{FN} was equal to ~650 V. When the neon gas was introduced into the chamber, B_{FN} increased to ~840 V during the first 10 min and remained approximately unchanged. After the conditioning, A_{FN} increased to ~10^3 A. Referring to Eq. (5), the 30% increase of B_{FN} at the beginning of the neon gas conditioning is ascribed to the increase of ϕ or the decrease of β via an increase of r_{tip}. The decreased fraction of extremely bright spots after the conditioning indicates that the conditioning blunted the sharpest emitters that were already active before, suggesting the increase of r_{tip}. Since A_{FN} decreases with the increase of ϕ (see Eq. (4)), the observed increase of A_{FN} by two orders of magnitude suggests that N_{tip} increased by the same orders of magnitude. These conclusions are compatible with the observed beam uniformity improvement, Figure 3.

The observed effect of the neon conditioning is different from previously reported experiments. In the glow-discharge processing of Spindt single-gate FEAs,[28] the bombardment of neon and hydrogen ions generated by glow-discharge on the FEA decreased B_{FN} but only a small change in A_{FN} resulted. The well-known finishing procedure of etched-wire needle-shape field emitters[44–46] is similar to our method in appearance but different in effect: the irradiation of the neon gas ions created by the impact ionization of the field emitted electrons to the emitter tip results in sharpening of the tip down to a few atoms. In contrast, our observation indicates that the neon gas had blunted the sharp tips while at the same time activating non-emitting tips. We note that the previous report on the noble-gas conditioning of single-gate FEAs for longer time periods increased B_{FN} by more than a factor of 2 together with orders of magnitude increase of A_{FN}. The nature of these different consequences under the different plasma conditions have not been elucidated yet. Since the gas processing is a promising method to improve the beam uniformity and the maximum current, further investigation on the precise physical origin of the observed effect is an urgent task and the subject of intense research.

IV. CONCLUSIONS

In summary, we showed the successful fabrication of a double-gate FEA with 4×10^4 tips with large G_{col} apertures using e-beam lithography and demonstrated its excellent electron beam collimation characteristics. By submitting the FEA to a low pressure neon gas, we were able to increase the active emission area and to obtain a more homogeneous beam. The successful reproduction of the experiment by a full 3D simulation of a single emitter for the beam collimation characteristics and the emission current characteristics was also shown and demonstrates that it is feasible to use the established model for further optimization of the gate structure and to study the beam emission and collimation characteristics under high acceleration electric field.

The collimation of the beam envelope down to the FEA diameter and the hint of resolving individual emitters at low (3 keV) acceleration potential show that the rms transverse velocity was reduced to a significantly low value. To establish this fact with increased resolution on the beam diagnostics, further investigations including the direct beam

emittance measurement using the DC gun test-stand[47,48] and experiments with single-emitters are under way.

ACKNOWLEDGMENTS

The authors acknowledge J. Leemann, K. Vogelsang, and A. Luecke for their help for the FEA fabrication. This work was conducted within the SwissFEL project at the Paul Scherrer Institute and was partially supported by the Swiss National Science Foundation No. 200021_125084.

[1]A. V. Crewe, J. Wall, and J. Langmore, Science **168**, 1338 (1970).
[2]C. Brau, Nucl. Instrum. Methods Phys. Res. **407**, 1 (1998).
[3]B. D. Patterson, R. Abela, H. H. Braun, U. Flechsig, R. Ganter, Y. Kim, E. Kirk, A. Oppelt, M. Pedrozzi, S. Reiche, L. Rivkin, T. Schmidt, B. Schmitt, V. N. Strocov, S. Tsujino, and A. F. Wrulich, New J. Phys. **12**, 035012 (2010).
[4]H. Makishima, S. Miyano, H. Imura, J. Matsuoka, H. Takemura, and A. Okamoto, Appl. Surf. Sci. **146**, 230 (1999).
[5]D. Whaley, R. Duggal, C. Armstrong, C. Bellew, C. Holland, and C. Spindt, IEEE Trans. Electron Devices **56**, 896 (2009).
[6]J. H. Booske, Phys. Plasmas **15**, 055502 (2008).
[7]K. B. K. Teo, E. Minoux, L. Hudanski, F. Peauger, J.-P. Schnell, L. Gangloff, P. Legagneux, D. Dieumegard, G. A. J. Amaratunga, and W. I. Milne, Nature **437**, 968 (2005).
[8]G. Herink, D. R. Solli, M. Gulde, and C. Ropers, Nature **483**, 190 (2012).
[9]A. H. Zewail, Annu. Rev. Phys. Chem. **57**, 65 (2006).
[10]M. Kruger, M. Schenk, and P. Hommelhoff, Nature **475**, 78 (2011).
[11]C. A. Spindt, I. Brodie, L. Humphrey, and E. R. Westerberg, J. Appl. Phys. **47**, 5248 (1976).
[12]P. R. Schwoebel, C. A. Spindt, and C. E. Holland, J. Vac. Sci. Technol. B **23**, 691 (2005).
[13]R. C. Smith and S. R. P. Silva, Appl. Phys. Lett. **94**, 133104 (2009).
[14]C. Li, Y. Zhang, M. T. Cole, S. G. Shivareddy, J. S. Barnard, W. Lei, B. Wang, D. Pribat, G. A. J. Amaratunga, and W. I. Milne, ACS Nano **6**, 3236 (2012).
[15]C. M. Tang, A. C. Ting, and T. Swyden, Nucl. Instrum. Methods Phys. Res. **318**, 353 (1992).
[16]M. Dehler, A. Candel, and E. Gjonaj, J. Vac. Sci. Technol. B **24**, 892 (2006).
[17]J. Itoh, Y. Toma, K. Morikawa, S. Kanemaru, and K. Shimizu, J. Vac. Sci. Technol. B **13**, 1968 (1995).
[18]Y. Yamaoka, S. Kanemaru, and J. Itoh, Jpn. J. Appl. Phys. **35**, 6626 (1996).
[19]C. Py, J. Itoh, T. Hirano, and S. Kanemaru, IEEE Trans. Electron Devices **44**, 498 (1997).
[20]A. Hosono, S. Kawabuchi, S. Horibata, S. Okuda, H. Harada, and M. Takai, J. Vac. Sci. Technol. B **17**, 575 (1999).
[21]C. Py, M. Gao, S. R. Das, P. Grant, P. Marshall, and L. LeBrun, J. Vac. Sci. Technol. A **18**, 626 (2000).
[22]L. Dvorson, G. Sha, I. Kymissis, C. Y. Hong, and A. I. Akinwande, IEEE Trans. Electron Devices **50**, 2548 (2003).
[23]Y. Neo, M. Takeda, T. Soda, M. Nagao, T. Yoshida, S. Kanemaru, T. Sakai, K. Hagiwara, N. Saito, T. Aoki, and H. Mimura, J. Vac. Sci. Technol. B **27**, 701 (2009).
[24]S. Tsujino, P. Helfenstein, E. Kirk, T. Vogel, C. Escher, and H.-W. Fink, IEEE Electron Device Lett. **31**, 1059 (2010).
[25]P. Helfenstein, E. Kirk, K. Jefimovs, T. Vogel, C. Escher, H.-W. Fink, and S. Tsujino, Appl. Phys. Lett. **98**, 061502 (2011).
[26]P. Helfenstein, K. Jefimovs, E. Kirk, T. Vogel, C. Escher, H.-W. Fink, and S. Tsujino, J. Appl. Phys. **112**, 093307 (2012).
[27]P. R. Schwoebel, C. A. Spindt, C. E. Holland, and J. A. Panitz, J. Vac. Sci. Technol. B **19**, 980 (2001).
[28]P. R. Schwoebel and C. A. Spindt, J. Vac. Sci. Technol. B **12**, 2414 (1994).
[29]I. Brodie, Int. J. Electron. **38**, 541 (1975).
[30]C. M. Marrese, "Compatibility of field emission cathode and electric propulsion technologies," Ph.D. thesis (University of Michigan, 1999).
[31]D. Nicolaescu, M. Nagao, T. Sato, V. Filip, S. Kanemaru, and J. Itoh, J. Vac. Sci. Technol. B **23**, 707 (2005).
[32]S. Tsujino, M. Paraliev, E. Kirk, and H.-H. Braun, Appl. Phys. Lett. **99**, 073101 (2011).
[33]E. Kirk, S. Tsujino, T. Vogel, K. Jefimovs, J. Gobrecht, and A. Wrulich, J. Vac. Sci. Technol. B **27**, 1813 (2009).
[34]A. Mustonen, P. Beaud, E. Kirk, T. Feurer, and S. Tsujino, Appl. Phys. Lett. **99**, 103504 (2011).
[35]V. A. Guzenko, A. Mustonen, P. Helfenstein, E. Kirk, and S. Tsujino, Microelectron. Eng. (submitted).
[36]R. G. Forbes and J. H. Deane, Proc. R. Soc. London, Ser. A **463**, 2907 (2007).
[37]S. Tsujino, M. Paraliev, E. Kirk, T. Vogel, F. L. Pimpec, C. Gough, S. Ivkovic, and H.-H. Braun, J. Vac. Sci. Technol. B **29**, 02B117 (2011).
[38]S. Tsujino, M. Paraliev, E. Kirk, C. Gough, S. Ivkovic, and H.-H. Braun, Phys. Plasmas **18**, 064502 (2011).
[39]J. M. Houston, Phys. Rev. **88**, 349 (1952).
[40]R. E. Burgess, H. Kroemer, and J. M. Houston, Phys. Rev. **90**, 515 (1953).
[41]R. G. Forbes, J. Vac. Sci. Technol. B **17**, 526 (1999).
[42]F. R. Abbott and J. E. Henderson, Phys. Rev. **56**, 113 (1939).
[43]S. Tsujino, F. le Pimpec, J. Raabe, M. Buess, M. Dehler, E. Kirk, J. Gobrecht, and A. Wrulich, Appl. Phys. Lett. **94**, 093508 (2009).
[44]A. P. Janssen and J. P. Jones, J. Phys. D **4**, 118 (1971).
[45]R. Smith, J. Phys. D **17**, 1045 (1984).
[46]S. Ernst, S. Wirth, M. Rams, V. Dolocan, and F. Steglich, Sci. Technol. Adv. Mater. **8**, 347 (2007).
[47]S. C. Leemann, A. Streun, and A. F. Wrulich, Phys. Rev. ST Accel. Beams **10**, 071302 (2007).
[48]S. Tsujino, M. Paraliev, P. Helfenstein, and H.-H. Braun, in *Vacuum Nanoelectronics Conference (IVNC), 25th International*, 2012, pp. 1–2.

Chapter 7

Conclusions & Outlook

In this work, double-gate FEAs have been introduced as a possible candidate for upgrading X-ray free electron lasers such as the SwissFEL to shorter wavelengths and improve their beam quality. The devices presented in this work have demonstrated excellent performance in terms of collimation characteristics and it was shown that a large G_{col} aperture diameter is crucial to minimize the emission current reduction under collimation conditions. The current uniformity across a 2.26 mm diameter array with 40'000 emitter tips could be improved significantly by submitting the sample to a low-pressure neon gas atmosphere for the duration of 3 hours.

Using the molding method for the fabrication of pyramidal emitter tips with controlled apex radii of curvature of 5-10 nm and the self-aligned polymer etch-back method for the G_{ext} and G_{col} aperture openings, double-gate FEAs with G_{ext} and G_{col} apertures of $1.2 \pm 0.1 \mu$m and $3.5 \pm 0.1\,\mu$m were fabricated. These aperture diameters represent both the upper and lower limit achievable with the self-aligned method. In the experiment, these devices showed minimal reduction of the emission current during collimation compared to devices with G_{ext} and G_{col} apertures of equal diameter. Nevertheless, a significant current density increase was not achieved with these structures. Due to the limitations in reproducability and aperture geometry imposed by the self-aligned process, a different fabrication method for the G_{col} aperture openings using a focused ion beam assisted process was implemented. This method is ideal for prototyping FEAs with a small number of emitter tips and testing different G_{col} geometries. Using the FIB assisted process, 2×2 emitter tip FEAs were fabricated that showed a heretofore unreached current density increase of a factor of 13.9 ± 0.1 during collimation. These structures had G_{ext} and G_{col} aperture diameters of $2.3 \pm 0.1\,\mu$m and $6.2 \pm 0.1\,\mu$m, respectively. The FIB assisted fabrication process could be up-scaled to 20×20 emitter tip FEAs that showed the same excellent collimation characteristics as exhibited by the smaller FEAs. The only drawback to this method is the large amount of time necessary for the milling of the G_{col} electrode which exceeds 10 hours for the fabrication of a 20×20 FEA.

With the application of electron beam lithography, the rapid fabrication of double-gate FEAs with thousands of emitter tips became possible. Contrary to the FIB assisted method where the alignment of the G_{col} apertures to the underlying emitter tips was done manually, the e-beam is capable of automated marker search. The fabrication of these alignment markers

in the form of truncated pyramids could be integrated into the mold preparation. Using this e-beam process, double-gate FEAs with up to 40,000 emitter tips were fabricated. A slight increase in G_{col} aperture diameter to $6.5 \pm 0.1\,\mu$m while shrinking the G_{ext} diameter to $2.0 \pm 0.1\,\mu$m resulted in diminished leak current to G_{ext} during collimation. As a consequence of this, higher collimation voltages could be applied that led to lower transverse velocities. From the phosphor screen images recorded after the neon gas conditioning, it can be assumed that an almost parallel beam was reached.

To test the influence of variations in device geometry and voltage biasing scheme on the achieved results, a three dimensional model of a single-emitter double-gate structure was created on the basis of high resolution SEM micrographs and TEM cross-sections of a fabricated structure. The simulation of the electron trajectories was then carried out in multiple successive steps. First, a two dimensional projection of the model was used to calculate the electric field on the surface of the emitter tip apex by employing a finite-element solver on a triangular mesh of high-density. A mesh element size of less than 1 Å close to the surface of the emitter apex ensured accurate results. By assuming cylindrical symmetry, the resultant field distribution was subsequently used to calculate the emission current and the active emission area via integrating the current density according to the Fowler-Nordheim equation over the emitter apex surface. These values were then input as initial conditions of a full 3-D model for the particle tracking calculation by a finite-difference algorithm. Due to the high mesh density required on the emitter tip apex and the solver restriction to hexahedral meshes, the particle tracking simulation was split into two parts. First, the simulation was carried out in the vicinity of the emitter tip using a high-density mesh. The position and velocities of each simulated particle were recorded upon impact on a virtual anode placed at a distance of 20 μm from the emitter structure along the electron beam axis. Placing the virtual anode at this distance ensured that it would not influence the particle trajectories. The recorded particle properties were then used to initialize the simulation of the full experimental chamber where the anode was placed 40-50 mm away from the structure with a mesh of lower density. With the application of an iterative particle tracking algorithm, it was also possible to calculate the influence of space-charge effects on the electron trajectories.

The results of the particle tracking simulation stand in excellent agreement with the experimental data. In light of the intended application of the FEAs presented in this work, the simulation was extended to higher acceleration gradients of up to 100 MV/m and the influence of the acceleration field on space-charge dependent broadening of the transverse velocity spread was investigated. It could be shown that even for a relatively high tip current of 10 μA, the space-charge broadening can be compensated by the application of a high acceleration gradient and the stacked double-gate structure is still capable of producing an almost parallel beam with an rms transverse velocity of 1.0×10^{-4} expressed as a fraction of the speed of light in vacuum. This is only a factor of 2 worse than the smallest rms transverse velocity achieved, when space-charge effects are neglected.

Exchanging the optical lithography step used in creating the mold masks by an electron

beam lithography fabrication process, the creation of pyramidal emitter tips with submicron base length is possible. This greatly increases the number of tips that can be incorporated in a given FEA area. If the excellent beam collimation characteristics can be maintained for such a scaled down structure, the current density and emission current level could be increased by two orders of magnitude. The particle tracking simulation of a tenfold reduced version of the modelled double-gate structure discussed above results in a minimum rms transverse velocity of 5.98×10^{-5}, again expressed as a fraction of the speed of light in vacuum at an acceleration field of 100 MV/m. It should be noted that due to the properties of the double oxidation method used during the emitter tip fabrication, the emitter tip apex does not scale with with the base length but remains approximately constant. This was taken into account for the down-scaled emitter model.

In the experiment with the 40,000 tip double gate FEA, a minimal transverse velocity u_t - given as a fraction of the speed of light in vacuum - of $\sim 2.4 \times 10^{-4}$ was achieved. With the FEA radius of 1.14 mm, this amounts to a normalized rms emittance of 0.14 μm which is below the 0.2 μm required by the SwissFEL in high charge operation mode. Since the transverse velocity and therefore also the emittance are preserved when the double-gate structure is reduced by a factor of ten, an FEA of the same diameter but with emitter tips of 150 nm base length and a pitch of 1 μm would be capable of producing the required pulse charge of 200 pC if a 10 ps voltage pulse is applied to extract an average tip current of 20 μA. This average tip current level is three orders of magnitude higher than in the 40,00 tip FEA experiment, and space-charge effects would lead to a broadening of the emitted beam. However, the acceleration gradient applied in the experiment was only 60 kV/m. It was shown in the particle tracking simulation, that by applying a higher acceleration gradient of 100 MV/m the space-charge broadening is compensated, meaning that the emittance could be preserved for the down-scaled FEA even at very high average tip currents.

In the future, the implementation of the conceptual design of an alternative double-gate FEA structure treated in the appendix could further increase the emitted current level by allowing for ps pulsed biasing of the emitter and G_{col}. Instead of necessitating separate contacting for each applied bias voltage, the voltage difference between V_{col} and V_{em} is achieved by overlaying a long voltage pulse by a shorter one. Due to the higher capacitance between G_{col} and G_{ext} compared to that between the emitter substrate and G_{ext}, the shorter pulse only affects the emitter substrate leading to the emission of a collimated pulsed electron beam. As has been shown by the simulation and also in the experiment, a k_{col} value above one or negative might be advantageous for higher emission current levels especially at higher acceleration fields. Adapting the design of the alternative structure as shown in figure 17 in appendix A realizes the application of such k_{col} values.

To further characterize the fabricated devices, a direct measurement of the emittance is mandatory and already planned for the near future. Since this measurement will be carried out with an acceleration gradient of 3 MV/m, it will also allow the verification of the space-charge simulation by experimental data. As shown by the particle tracking results,

a high-density double-gate FEA with emitter tips of submicron base length could lead to higher current densities and current levels. The fabrication steps for single-gate devices has already been established and will be extended to the fabrication of double-gate structures. The main focus in future experiments will lie on increased current levels by means of voltage pulsing and laser induced field-emission while maintaining the collimation characteristics shown for the double-gate FEAs presented in this work

Acknowledgements

First and foremost, I would like to thank my supervisor Dr. Soichiro Tsujino for giving me the opportunity to do these studies and work in his research group in this interesting field. He was a great help in setting up the experiments and giving advice on how to improve the quality of the measurements and the fabricated structures. He expressed great patience and profound knowledge in the many extended discussions we had and never ceased to think of new ways to increase the performance of our devices. For agreeing to be the responsible faculty member for this thesis, I want to thank Prof. Dr. Hans-Werner Fink. He was always helpful and offered great advice concerning the conditioning of FEAs. I also want to express my gratitude to Dr. Eugenie Kirk who introduced me to the clean-room and the various equipment used for the FEA fabrication. She has a great talent to teach people how to use technical equipment and is extremely knowledgeable in the subject of microfabrication from which I could profit immensely during my time at PSI. I am also grateful to Dr. Konstantins Jefimovs for helping me with the FIB milling and spending a considerable amount of thought into optimizing the milling strategies. I would further like to express my thanks to Dr. Conrad Escher, first for agreeing to co-supervise this thesis and second for introducing me to the FIM chamber and being an immense help during the experiments carried out in Zurich. For agreeing to be a co-superviser, I also thank Prof. Dr. Jens Gobrecht whom I've come to know as a very friendly and helpful person.

Furthermore, I would like to thank Bianca Haas and Jana Lehmann for the fabrication of the FEA molds, Julijana Krbanjevic for preparing the excellent cross-sections with the FIB, Eugenia Minikus for the TEM images, Konrad Vogelsang and Arnold Lücke for their patience with my many questions related to the dicing saw and their willingness to often set up the saw on extremely short notice, Stefan Stutz for priceless morsels of technical advice and his unrivaled talent to motivate me to join the lunch-time running group, Thomas Neiger for all his help with computer related problems, Eugen Deckardt for the introductions to various clean-room equipment, Rolf Schelldorfer for the many discussions related to UHV technology and Anja Weber for the SEM introduction and helpful advice in using the machine.

Finally, I want to express my profound gratitude to my girlfriend Alina who stood by my side during these sometimes stressful times and never complained when I stayed until late into the night because the experiment was running well or a deadline was approaching. My time at PSI was sometimes tough but most of all, it was an invaluable experience during which I learned a great amount of new things. For this and the good times we had, I thank all the LMN staff.

Appendix A

Concept of a Simplified Double-Gate Structure for ps Pulsing & High Acceleration Gradients

The following patent application comprises a number of ideas that form the design of a simplified double-gate FEA structure that can produce short electron pulses of high-brightness. By adding a resistive connection between the emitter tips and the collimation electrode, both can be biased by a single source. The voltage difference is created by overlaying a DC voltage or long pulse with a short pulse. Due to the resistive connection, the emitter tips will be biased at a higher negative voltage than G_{col} and a collimated electron bunch is emitted. In this mode, the extraction gate is constantly grounded and k_{col} restricted to values below one and can be varied by the material and geometry of the resistive connection.

As the experimental results in section **??** and the particle tracking simulation in section 2.3 have shown, the highest collimation might likely be reached at k_{col} values higher than one when the acceleration gradient is in the order of a few MV/m or above. An alternative device structure is presented, where sequential voltage pulses are applied between the substrate that is insulated from the emitter tips and the extraction gate. G_{col} is connected to the substrate by a resistive connection and the emitters are connected to G_{ext} by a different resistive connection. By chosing the resistive materials and geometries for the different connections accordingly, a k_{col} value above 1 as well as negative values can be achieved.

Field emission cathode structure and driving method thereof

The present invention relates to field-emitter cathode structures and their driving methods to produce short high brightness electron beam.

In the following specification of the present invention, the pertinent prior art comprises the following documentation:

References Cited

E. Kirk, S. Tsujino, T. Vogel, J. Gobrecht, and A. Wrulich, *Fabrication of all-metal field emitter arrays with controlled apex sizes by molding*, J. Vac. Sci. Technol. B, Microelectron. Process. Phenom., vol. 27, no. 4, pp. 1813–1820, Jul. 2008.

E. Kirk, S. Tsujino, *Method to produce a field-emitter array with controlled apex sharpness*, WO 2009/156242 A1, 30 December 2009.

S. Tsujino, P. Helfenstein, E. Kirk, T. Vogel, C. Escher, and H. W. Fink, IEEE Electron Device Letters, 31 (9), 1059 (2010).

P. Helfenstein, E. Kirk, K. Jefimovs, T. Vogel, C. Escher, H.-W. Fink, and S. Tsujino, Highly collimated electron beams from double-gate field emitter arrays with large collimation gate apertures, Appl. Phys. Lett. **98**, 061502 (2011).

Background of the invention

The present invention relates to field-emitter cathode structures and their driving methods to produce short high brightness electron beam.

Advantages of a field emitter array cathode equipped with an electron extraction gate electrode are known over the thermionic cathodes widely used in microwave vacuum electronic amplifiers and oscillators, including low power dissipation, fast switching capability, and capability of high current and high current density performance. However, the electron beam emitted from such a single-gate field emitter array cathode has a large transverse electron velocity spread, which requires a special electron gun structure comprising a multiple electrostatic lens structure as described in one prior art in US6,683,414 B2, issued January 27, 2004 to Whaley. This problem can be solved in a field-emitter array structure comprising an array of double-gate field emitter units. Each field emitter unit has a field emitter tip in an electron extraction cavity which is equipped with an electron extraction gate electrode and an electrostatic lens structure stacked on top of the electron extraction gate in the direction of the electron propagation as described in one prior art in U.S. Patent No. 5,955,849.

A collimated electron beam can be generated from a double-gate field-emitter array cathode by applying a negative voltage V_{em} to the field emitter array with respect to the electron extraction gate electrode and applying a negative voltage V_{col} to the collimation electrode with respect to the electron extraction gate electrode at the same time. To maximize the reduction of the electron beam emission angle, it is crucial to have the ratio k_{col} defined by V_{col} / V_{em} close to 1. In a double-gate field-emitter array cathode with the collimation gate aperture diameter larger than the diameter of the electron extraction gate electrode aperture, the reduction of the electrical current with increase of k_{col} can be minimized and the emission angle can be reduced by a factor of 5 to 10 when k_{col} is increased from 0 to 0.86 as reported in the reference [P. Helfenstein, E. Kirk, K. Jefimovs, T. Vogel, C. Escher, H. W. Fink, and S. Tsujino, Appl. Phys. Lett. **98**,

061502 (2011)] when the field emitter cathode was operated in an environment in which an external acceleration electric field F_{acc} provided by applying an electric field between the field emitter cathode and an electrode in the direction of the beam propagation is much smaller than 1 MV/m. In a double-gate field-emitter array cathode with the collimation electrode aperture diameter larger than the diameter of the electron extraction gate electrode aperture in an environment with F_{acc} in the order of and higher than 1 MV/m , the reduction of the electrical current with increase of k_{col} from 0 to 1.0 and above can be minimized and the emission angle can be reduced by more than a factor of 5 to 10.

However, the requirement of two separate voltages for the electron extraction and the collimation electrodes which should be applied via three separate electrical contacts increases the complexity of the cathode driver and limits the applicability of such a device compared to a thermionic cathode, for example, which requires only two terminals. In one prior art JP P2000-123715A issued to Makishima et al. on April 28, 2000, a double-gate field-emitter array cathode structure that can be driven as a two-terminal cathode is disclosed. In this structure, the collimation electrode is electrically connected to the electron extraction gate electrode by a resistor R_1 and the same collimation gate electrode is electrically connected to the field emitter array with a resistor R_2. Consequently, by applying a potential V_{em} to the field emitter array, the collimation electrode potential is equal to $R_2V_{em}/(R_1+R_2)$ without requiring an additional bias source and an additional electrical contact to the collimation gate electrode.

However, this structure uses a fixed k_{col}-value, which poses two problems. Firstly, power dissipation in the resistive divider could compromise the low-power-consumption performance of the field-emitter cathode and the reliability of the device. A resistive divider with high resistance can reduce the heat

dissipation but limits maximum switching frequency due to increased *RC* constant of the device. Secondly, since the beam collimation and emitted current are sensitive to the collimation gate voltage and the aperture size, fixed k_{col} limits the possibility to operate the field emitter in the optimal condition and to maximize the brightness of the emitter electron beam.

Brief description of the Invention

Accordingly, it is an object of the invention to provide a double-gate field emitter cathode structure that can be operated as a two-terminal device for producing a collimated electron beam in an environment with low acceleration electric field suitable for small spot short pulse x-ray sources, and other applications.

It is further an object of the invention to provide a double-gate field emitter cathode structure that can be operated as a two-terminal device in an environment with high acceleration electric field for producing a collimated electron beam suitable for small spot short pulse x-ray sources, free-electron lasers, electron deflection amplifiers and sensors, microwave amplifiers, and other applications.

It is yet another an object of the invention to provide a double-gate field emitter cathode structure that produces short electron pulses below 1 ns with adjustable collimation capability.

These objectives are achieved according to the present invention by a field emitter device producing an electron beam, comprising one or several field emission cathode units, one or several resistor units, contact electrode units, and a substrate; wherein the field emission cathode unit comprises:

(a) a field emitter of a pyramidal-, a cone-, or a wire-shape, of a conducting material;

(b) an electron extraction gate electrode, which is supported above the field emitter by an insulator layer, wherein, to extract an electron beam from the field emitter through an aperture, a negative potential difference is established to the field emitter with respect to the electron extraction gate electrode;

(c) a collimation electrode, which is supported on top of the electron extraction gate electrode by a second insulator layer, which collimates the electron beam by establishing a negative potential at said collimation electrode with respect to the said electron extraction gate electrode, wherein the aperture diameter of the collimation electrode is larger than the aperture diameter of the electron extraction gate electrode;said contact electrode unit comprises:

(d) a first contact electrode which electrically connects the electron extraction gate electrodes of the field emitter,

(e) a second contact electrode which electrically connects the collimation electrodes of the field emitter; and said resistor unit comprising:

(f) a resistor which electrically connects the substrate and the collimation electrode;

(g) a substrate having a substance surface, wherein the substrate electrically connects the field emitter and provides the electrical connection to external driving voltages to said field emitter; said substrate also providing a mechanical support of said field emission cathode units, the resistor units and the contact electrode units.

In yet an another embodiment, a field emitter device producing an electron beam, comprising one or several field emission cathode units, one or several resistor units, contact electrode units, and

a substrate; wherein the field emission cathode unit comprises said (a)-(c); said contact units comprise;

(d') a first contact electrode which electrically connects the field emitter;

(e') a second contact electrode which electrically connects the electron extraction gate electrodes of the field emitter;

(f') a third contact electrode which electrically connects the collimation gate electtodes of the field emitter; said resistor units comprising;

(g') a first resistor unit which electrically connects the electron extraction gate electrodes to the field emitter;

(h') a second resistor unit which electrically connects the collimation electrodes to the substrate;

(i') a substrate having a substance surface, wherein the substrate mechanically supports the field emitters units, contact electrodes, resistor units, wherein a third electrical insulator is inserted between the substrate and the field emitters; wherein said substrates provides the electrical connection to external driving voltages.

This field-emitter array cathode structure with two stacked control electrodes and their driving means to produce short electron pulses safeguards that a sequence of electric stimuli applied to the field emitter array generates an electron beam with precisely controlled emission angle, allowing for the production of short collimated electron pulses with high electron beam brightness.

Further preferred examples of the present invention are listed in the remaining depending claims.

The nature of the invention will best be understood when described in connection with the accompanying drawings, in which:

FIG. 1 is a perspective view, on a greatly enlarged scale of a prior art double-gate field emitter array device.

FIG. 2 is a schematic cross-sectional view, of the said prior art double-gate field emitter array device in FIG. 1 along the line A-A′.

FIG. 3 is an example of an electron gun using a prior art double-gate field emitter array device as the electron emitter.

FIG. 4 is an electrical equivalent circuit diagram of a prior art double-gate field emitter array device connected to driving voltage sources.

FIG. 5 is a typical dc field emission characteristic of a double-gate field emitter array device operated in an environment with a low acceleration electric field much smaller than 1 MV/m.

FIG. 6 is an example of an experimentally observed field emission characteristic of a prior art double-gate field emitter array device in an environment with a low acceleration electric field much smaller than 1 MV/m.

FIG. 7 is an example of an experimentally observed collimation characteristic of the field emission electron beam emitted from a prior art double-gate field emitter array device in an environment with a low acceleration electric field much smaller than 1 MV/m.

FIG. 8 is a perspective view, on a greatly enlarged scale of the invention.

FIG.9 is a schematic cross-sectional view, of the invention in FIG. 8 along the line A-A′.

FIG. 10 is a perspective view, on a greatly enlarged scale of the invention with yet an other geometry as compared to FIG. 8 and FIG. 10.

FIG. 11 is a schematic cross-sectional view, of the invention in FIG. 10 along the line A-A'.

FIG. 12 is an example of an electron gun using the double-gate field emitter array device of FIG. 10 as a pulsed electron emitter.

FIG. 13 is an example of an electron gun using the double-gate field emitter array device of FIG. 8 as a pulsed electron emitter.

FIG. 14 is an electrical equivalent circuit of the invention of FIG. 8 connected to driving voltage sources.

FIG. 15 shows electrical waveforms of the driving voltage, the terminal voltages, and the emission pulse of the invented double-gate field emitter array device of FIG. 8 driven by a proposed voltage sequence to produce a collimated electron pulse.

FIG. 16 shows electrical waveforms of the driving voltage, the terminal voltages, and the emission pulse of the invented double-gate field emitter array device of FIG. 8 driven by another proposed voltage sequence for producing a collimated electron pulse with the duration below 1 ns.

FIG. 17 is an electrical equivalent circuit of the invention of FIG. 10 connected to driving voltage sources.

FIG. 18 shows electrical waveforms of the driving voltage, the terminal voltages, and the emission pulse of the invented double-gate field emitter array device of FIG. 10 driven by a proposed

voltage sequence for producing a collimated electron pulse with the duration below 1 ns.

Description of the preferred embodiment

The invention can be best described with reference to Figures 1 to 18.

Referring to the drawing FIG.1 and FIG. 2 of a prior art, a double-gate field emitter array device 110 comprises of an array of single unit of the field emitter 107; 101 designates one of the electron emitting field emitter tips of suitable conducting material, for example, molybdenum; the field emitter tips are supported by a substrate 102 (*Em*) of conducting material; an insulator layer 103 which has cavities for individual emitter tips 101; 103 supports the electron extraction gate layer 104 (G_{ex}) of a conducting material on top of the field emitter array. The electron extraction gate layer 104 has aperture holes for individual emitter tips 101; an insulator layer 105 which has cavities for the transport of electron beam emitted from individual emitter tips 101; the insulator layer 105 supports the electron collimation gate layer 106 (G_{col}) of a conducting material which has aperture holes for the collimation of the field emission electron beamlets emitted from individual emitter tips 101.

Referring to the FIG. 3 of a schematic cross-sectional view of an axially symmetric electron gun using the prior art double-gate field emitter array cathode 110. The cross-section is taken through the plane that contains the gun axis; 201 is the electrical contact to the field emitter array via the substrate 102; an insulator layer 202 supports the cathode 110; 203 is the electrical contact to the electron extraction gate layer G_{ex}; 204 is the electrical contact to electron collimation gate layer G_{col}; 205 is the voltage source to apply a negative acceleration voltage

V_K which accelerates the field emission electron beam; 206 is an electron beam collector.

Referring to the FIG. 4 of an electrical equivalent circuit of a prior art double-gate field emitter cathode connected by driving voltages V_{em} and V_{col}, respectively applied, between *Em* and G_{ex}, and between G_{col}, and G_{ex}, the left area enclosed by the dashed line is an electrical equivalent circuit of the field emitter driver, the central area enclosed by the dashed line represents the prior art double-gate field emitter array cathode 110, and the right area enclosed by the dashed line represents the space transporting and collecting the electron beam by the beam collector 206. When a positive V_{em} is applied and V_{col} is zero, the relationship between V_{em} and the current I_{em} is given by the left panel of FIG. 5 for a typical pyramidal molybdenum field emitter array cathode 110 fabricated by molding with base size of 1.5 μm square, for example by prior art WO 2009/156242 A1, the emitter apex radius of curvature R_{tip} in the order of ~5 nm, the thickness of 103 and 105 of ~1.2 μm, the thickness of 104 layer and 106 layer equal to 0.5 μm, the diameter D_{ex} of the aperture holes of G_{ex} of ~2 μm, and the inscribed diameter D_{col} of the aperture holes of G_{col} of ~6 μm. The right panel of FIG. 5 shows the relationship between I_a and V_{col} for a molybdenum field emitter array cathode with D_{col}/D_{ex} of ~3 when V_{em} is equal to 71.8 V when the said field emitter array cathode is operated in an environment with F_{acc} much smaller than 1 MV/m. F_{acc} is defined for example by V_K and the distance between the surface of said field emission cathode and said beam collector. The collimation characteristics were calculated with reference to the experimental observations relative to FIG. 6 and FIG. 7. Typically, more than 90 % of I_{em} is transported through the G_{ex}– and the G_{col}–apertures towards the collector as the current I_a. The remnant is collected by G_{ex} as I_{ex} and by G_{col} as I_{col}. I_{col} is negligible. I_a is approximately same as I_{em} when the ratio $k_{col} = V_{col}/V_{em}$ is below 0.85. When k_{col} is above $k_{col}^{(th)} = 0.91$, I_a is ~0

and $I_{ex} \sim I_{em}$, since I_{em} is collected by G_{ex} in this case. When k_{col} is increased from 0 to $k_{col}^{(op)} = 0.86$, the beam divergence angle is 5 to 7 times reduced and the beam brightness is enhanced by more than a factor of 10. However, two separate voltage sources with three separate electrical connections to G_{col}, E_m, and G_{ex} are required to produce the maximally collimated electron beam with this device, which complicates the bias circuit as seen in the example of FIG. 3 and FIG. 4, and limits the applicability of double-gate field emitter arrays.

Referring to FIG. 8 and FIG. 9 of the present invention, the double-gate field-emitter array cathode 820 comprises an array of field emitter units 107; external driving voltages V_b (821) and V_p (822) are electrically connected in series between G_{ex} (104) and *Em* (102) via a transmission line 823 with characteristic impedance Z_s, whereas G_{col} (106) is electrically connected to *Em* (102) by one or several of the resistor unit 811, that consists of a resistor 809.

Referring to FIG. 10 and FIG. 11 of yet an other form of the present invention, the double-gate field-emitter array cathode 1020 comprises an array of field emitter units 107; external driving voltages V_b (1021) and V_p (1022) are electrically connected in series between G_{ex} (104) and the substrate 1013 via a transmission line 1023 with characteristic impedance Z_s. G_{col} (106) is electrically connected to the substrate 1013 by one or several of the resistor unit 1011. The emitter contact layer *Em* (1002) is electrically connected to G_{ex} (104) by one or several of resistor unit 1012. Direct dc electrical connection between *Em* and 1013 is prevented by an insulating layer 1014.

Referring to FIG. 12, an example of an electron gun using a double-gate field emitter array using the cathode 820 is shown. Comparing with the electron gun using the prior art double-gate

field emitter array of FIG. 3, the present invention greatly simplifies the electrical connections to the cathode by eliminating a separate contact 204 to G_{col}.

Referring to FIG. 13, an example of an electron gun using a double-gate field emitter array using the cathode 1020 is shown. Comparing with the electron gun using the prior art double-gate field emitter array of FIG. 3, the present invention greatly simplifies the electrical connections to the cathode by eliminating a separate contact 204 to G_{col}.

Referring to FIG. 14, an electrical equivalent circuit of the double-gate FEA, 820, connected by driving voltages V_b and V_p applied between *Em* and G_{ex}, is shown. The left area enclosed by the dashed line is an electrical equivalent circuit of the field emitter driver, the central area enclosed by the dashed line represents the invented double-gate field emitter array cathode 820, and the right area enclosed by the dashed line represents the space transporting and collecting the electron beam by the beam collector 206. In a typical cathode structure, C_1 and C_2 represent respectively the capacitance of G_{ex} (104) and G_{col} (106). The typical value of C_1 and C_2 is 0.5 nF, corresponding to the electrode diameter of 4 mm and 1.2 μm insulator thickness of 103 and 105, R_b is equal to R_0/N kΩ, where N is the number of resistor units and R_0 is the resistance of the resistor 809 of the resistor unit 811 which electrically connects G_{col} and *Em*. The resulting Impedance Z_s is a sum of the characteristic impedance of the feeding transmission line Z_s' (typically 50 Ω) and the impedance Z_s'' of the contact 201.

Referring to FIG. 15, a typical pulsed field emission characteristic of the double-gate FEA 820 operated in an environment with F_{acc} much smaller than 1 MV/m is illustrated, (a) shows the applied voltage comprising a 200 ns full-width-half-

maximum (FWHM) voltage pulse V_p with 10 V amplitude and a V_b of 62 V DC, (b) shows the waveforms of the potential difference between *Em* and G_{ex} represented by V_{em} and the potential difference between G_{col} and G_{ex} represented by V_{col}, (c) shows the potential ratio $k_{col} = V_{col}/V_{em}$, and (d) shows the amplitude of the collimated electron beam I_a transported to the anode. During the time the pulse voltage V_p is on (t = 0 to 200 ns), $V_{col} = V_b$ but V_{em} is higher than V_{col} by V_p, while satisfying the condition, $k_{col} = k_{col}^{(op)}$ with $k_{col}^{(op)}$ of 0.86, with the amplitude of I_a of 0.1 A.

Referring to FIG. 16, a typical pulsed field emission characteristic of the double-gate FEA 820 operated in an environment with F_{acc} much smaller than 1 MV/m to produce collimated electron pulses with the duration below 1 ns is illustrated, (a) shows the applied voltage between *Em* and G_{ex} comprising a V_b of 62 V DC and a double pulse voltage V_p , which consists of a 0.2 ns FWHM duration positive voltage pulse with a 1600 V amplitude and another negative voltage pulse with the same duration and amplitude, delayed by 0.5 ns from the first positive voltage pulse, (b) shows the waveforms of the potential difference between *Em* and G_{ex} represented by V_{em} and the potential difference between G_{col} and G_{ex} represented by V_{col} when Z_s of the transmission line 823 is 50 Ω and the impedance of 201 is neglected, (c) shows the potential ratio $k_{col} = V_{col}/V_{em}$, and (d) shows the amplitude of the collimated electron beam I_a transported to the anode. During the time V_{em} is 10 V higher than V_{col}, the condition k_{col} equal to $k_{col}^{(op)}$ of 0.86 is satisfied and a collimated electron pulse of I_a with the amplitude of 0.1 A and FWHM duration of 0.5 ns is produced.

The finite I_{em} while V_p is off can be partly eliminated by applying V_b also in pulse. The duration of V_b pulse should be longer than the time constant R_bC_2 equal to 5 μs for C_2 of 0.5 nF and R_b of 10 kΩ in order to minimize the transient voltage differences between

G_{col} and *Em* and minimize the power consumption and breakdown probability of the resistor unit 811.

A preferred embodiment of the double-gate FEA 820 is described in the following; a metallic field emitter array (FEA) consisting of molybdenum field emitter tips is fabricated by molding. The FEA is supported by a conducting substrate, for example an electro-plated nickel substrate. G_{ex} is stacked on the FEA separated by an insulator-1 of SiO_2 layer. G_{col} is stacked on the G_{ex} separated by the insulator-2 of SiO_2 or SiON. G_{ex} and G_{col} have apertures for individual emitter tips. G_{ex} and G_{col} are made of suitable conducting material. The resistor of the resistor unit is made of, for example, silicon, germanium, molybdenum nitride, zirconium carbide, or other suitable resistive material. Two examples of device structure parameters are listed in the Table I.

Referring to FIG. 17, an electrical equivalent circuit of the double-gate FEA, 1020, connected by driving voltages V_b (1022) and V_p (1021) applied between 1013 and G_{ex} (104) is shown. The left area enclosed by the dashed line is an electrical equivalent circuit of the field emitter driver, the central area enclosed by the dashed line represents the invented double-gate field emitter array cathode 1020, and the right area enclosed by the dashed line represents the space transporting and collecting the electron beam by the beam collector 206. In a typical cathode structure, C_1 and C_2 represent respectively the capacitance of G_{ex} (104) and G_{col} (106), C_b represents the capacitance between the substrate 1013 and *Em* (1002), R_{ex} represents the resistance between *Em* (1002) and G_{ex} (104), and R_c represents the resistance between G_{col} (106) and the substrate 1013. The typical value of C_1, C_2, and C_b is 0.1 nF, corresponding to the diameter of the field emitter array 1 mm and 1.2 μm insulator thickness of 103, 105, and 1014. R_{ex} is equal to R_0'/N' kΩ, where N' is the number of resistor units (1012) and R_0' is the resistance of the resistor unit 1012 which electrically

connects *Em* (1002) and G_{ex} (104). R_c is equal to R_0''/N'' kΩ, where N'' is the number of resistor units (1011) and R_0'' is the resistance of the resistor unit 1011 which connects electrically G_{col} (106) and the substrate (1013). The resulting Impedance Z_s is a sum of the characteristic impedance of the feeding transmission line Z_s' (typically 50 Ω) and the impedance Z_s'' of the contact 201.

Referring to FIG. 18, a typical pulsed field emission characteristic of the double-gate FEA 1020 operated in an environment with F_{acc} in the order of 1 MV/m or higher to produce collimated electron pulses with the duration below 1 ns is illustrated, (a) shows the applied voltage between the substrate 1013 and G_{ex} (104) comprising a V_b pulse and a double pulse voltage V_p. V_b pulse is of 72.5 V amplitude with FWHM duration of 1 μs and the rise time and the fall time of 0.1 μs applied from the time -1 μs. V_p consists of a 0.14 ns FWHM duration positive voltage pulse with a 2235 V amplitude centered at time 0 μs and an other negative voltage pulse with the same duration and amplitude, delayed by 0.3 ns from the center of the first positive voltage pulse, (b) shows the waveforms of the potential difference between *Em* and G_{ex} represented by V_{em} and the potential difference between G_{col} and G_{ex} represented by V_{col} when Z_s of the transmission line 1023 is 50 Ω and the impedance of 201 is neglected, (c) shows the potential ratio $k_{col} = V_{col}/V_{em}$, and (d) shows the amplitude of the collimated electron beam I_a transported to the beam collector. During the time $|V_{em}|$ is approximately equal to $|V_{col}|$ with k_{col} equal to 1.02 a collimated electron pulse of I_a with the amplitude of 0.1 A and FWHM duration of 0.2 ns is produced. It is apparent that it is also possible to generate emission current with the same order of magnitude with larger beam divergence but in an environment with F_{acc} much smaller than 1 MV/m by decreasing k_{col} by decreasing $|V_{col}|$ to a value smaller than $|V_{em}|$.

A preferred embodiment of the double-gate FEA 1020 is described in the following; a metallic field emitter array (FEA) consisting of molybdenum field emitter tips is fabricated by molding. The FEA is supported by a conducting substrate, for example an electro-plated nickel substrate, a planarized metallic substrate, or a highly conducting semiconductor substrate. G_{ex} is stacked on the FEA separated by an insulator-1 of SiO_2. G_{col} is stacked on the G_{ex} separated by the insulator-2 of SiO_2, SiON, or Si_xN_y. G_{ex} and G_{col} have apertures for individual emitter tips. G_{ex} and G_{col} are made of suitable conducting material. The FEA layer (*Em*) and the substrate are electrically insulated by the insulator-3 of SiO_2, SiON, or Si_xN_y. The resistor of the resistor unit is made of, for example, silicon, germanium, molybdenum nitride, zirconium carbide, or other suitable resistive material. Two examples of device structure parameters are listed in the Table II.

Table I. Design of FEA-1 and FEA-2

	FEA-1	FEA-2
Number of tips	3.1×10^{4}	1.3×10^{6}
Array diameter	1 mm	1 mm
Emitter base size	1.5 μm	0.2 μm
Apex radius of curvature	5-10 nm	5-10 nm
Array pitch	5 μm	0.76 μm
Insulator-1 thickness	1.2 μm	0.3 μm
Insulator-2 thickness	1.2 μm	0.3 μm
G_{ex} thickness	0.5 μm	0.2 μm
D_{ex} (G_{ex} aperture diameter)	1 μm	0.15 μm
G_{ex} diameter	5.2 mm	5.2 mm
G_{col} thickness	0.5 μm	0.2 μm
D_{col} (G_{col} aperture diameter)	3 μm	0.45 μm
G_{col} diameter	3.8 mm	3.8 mm
R_b	1 kΩ	0.25 kΩ

Table II. Design of FEA-3 and FEA-4

	FEA-3	FEA-4
Number of tips	3.1×10^{4}	1.3×10^{6}
Array diameter	1 mm	1 mm
Emitter base size	1.5 μm	0.2 μm
Apex radius of curvature	5-10 nm	5-10 nm
Array pitch	5 μm	0.76 μm
Insulator-1 thickness	1.2 μm	0.3 μm
Insulator-2 thickness	1.2 μm	0.3 μm
Insulator-3 thickness	1.2 μm	0.3 μm
G_{ex} thickness	0.5 μm	0.2 μm
D_{ex} (G_{ex} aperture diameter)	1 μm	0.15 μm
G_{ex} diameter	5.2 mm	5.2 mm
G_{col} thickness	0.5 μm	0.2 μm
D_{col} (G_{col} aperture diameter)	3 μm	0.45 μm
G_{col} diameter	1.2 mm	3.8 mm
R_{ex}	50 Ω	50 Ω
R_{c}	100 Ω	100 Ω

Patent claims

1. A field emitter device producing an electron beam, comprising one or several field emission cathode units, one or several resistor units, contact electrode units, insulator layers, and a substrate; wherein the field emission cathode unit comprises:

(a) a field emitter of a pyramidal-, a cone-, or a wire-shape, of a conducting material;

(b) an electron extraction gate electrode, which is electrically insulated and mechanically supported above the field emitter by an insulator layer, wherein, to extract an electron beam from the field emitter through an aperture, a negative potential difference is established to the field emitter with respect to the electron extraction gate electrode;

(c) a collimation electrode, which is electrically insulated from the electron extraction gate electrode and mechanically supported on top of the electron extraction gate electrode by a second insulator layer, which collimates the electron beam by establishing a negative potential at said collimation electrode with respect to the electron extraction gate electrode, wherein the aperture diameter of the collimation electrode is larger than the aperture diameter of the electron extraction gate electrode;

(d) a first contact electrode which electrically connects the electron extraction gate electrodes of the field emitter,

(e) a second contact electrode which electrically connects the collimation electrodes of the field emitter;

(f) a resistor unit comprising a resistor which electrically connects the substrate and the collimation electrode;

(g) a first insulator layer which electrically insulates the field emitters and the electron extraction gate electrodes, wherein said insulator layer mechanically supports the extraction gate electrodes;

(h) a second insulator layer which electrically insulates the electron extraction gate electrodes and the collimation electrodes, wherein said insulator layer mechanically supports the collimation electrodes;

(i) a substrate having a substance surface, wherein the substrate electrically connects the field emitter, and provides the electrical connection to external driving voltages to said field emitter; said substrate also providing a mechanical support of said field emission cathode units, the resistor units, the contact electrodes, and the insulator layers.

2. The field emitter device according to the claim 1, wherein the material of the field emitter is selected from a group consisting of molybdenum, tungsten, zirconium carbide, molybdenum carbide, hafnium carbide, or molybdenum nitride, and the material for the electrode layers is selected from a group consisting of molybdenum, tungsten, zirconium carbide, molybdenum carbide, hafnium carbide, molybdenum nitride, chromium, copper, gold, silver, or aluminium.

3. The field emitter device according to the claims 1 and 2, being enabled to produce a collimated electron beam by applying between the field emitter and the electron extraction gate electrode

(a) DC voltage

(b) voltage pulse

4. The field emitter device according to the claims 1 and 2, being enabled to produce a collimated electron beam by applying between the field emitter and the electron extraction gate electrode

(a) DC voltage

(b) double voltage pulse

wherein the double voltage pulse consists of two voltage pulses with opposite polarity.

5. The field emitter device according to the claims 1 and 2, being enabled to produce a collimated electron beam by applying between the field emitter and the electron extraction gate electrode

(a) first voltage pulse

(b) second voltage pulse

wherein the duration of the first voltage pulse is longer than the duration of the second voltage pulse and the second voltage pulse is applied during the first voltage pulse.

6. A field emitter device according to the claims 1 and 2, being enabled to produce a collimated electron beam by applying between the field emitter and the electron extraction gate electrode

(a) first voltage pulse

(b) double voltage pulse

wherein the double voltage pulse consists of two voltage pulses with opposite polarity, wherein the duration of and the separation between the two pulses of the double pulse voltage are shorter than the duration of the first pulse voltage and the double voltage pulse is applied during the first voltage pulse.

7. A field emitter device producing an electron beam, comprising one or several field emission cathode units, one or several resistor units, contact electrode units, insulator layers, and a substrate; wherein the field emission cathode unit comprises:

(a) a field emitter of a pyramidal-, a cone-, or a wire-shape, of a conducting material;

(b) an electron extraction gate electrode, which is electrically insulated and mechanically supported above the field emitter by an insulator layer, wherein, to extract an electron beam from the field emitter through an aperture, a negative potential difference is established to the field emitter with respect to the electron extraction gate electrode;

(c) a collimation electrode, which is electrically insulated from the electron extraction gate electrode and mechanically

supported on top of the electron extraction gate electrode by a second insulator layer, which collimates the electron beam by establishing a negative potential at said collimation electrode with respect to the electron extraction gate electrode, wherein the aperture diameter of the collimation electrode is larger than the aperture diameter of the electron extraction gate electrode;

(d) a first contact electrode which electrically connects the electron extraction gate electrodes of the field emitter;

(e) a second contact electrode which electrically connects the collimation electrodes of the field emitter;

(f) a third contact electrode which electrically connects the field emitters;

(g) a first resistor unit comprising a resistor which electrically connects the substrate and the collimation electrode;

(h) a second resistor unit comprising a resistor which electrically connects the electron extraction gate electrodes and the field emitters;

(i) a first insulator layer which electrically insulates the field emitters and the electron extraction gate electrodes, wherein said insulator layer mechanically supports the extraction gate electrodes;

(j) a second insulator layer which electrically insulates the electron extraction gate electrodes and the collimation electrodes, wherein said insulator layer mechanically supports the collimation electrodes;

(k) a third insulator layer which electrically insulates the field emitters from the substrate, wherein said insulator layer mechanically supports the field emitters;

(l) a substrate having a substance surface, wherein it mechanically supports the field emitters, the one or several of resistors, the contact electrodes, and the insulator layers;

wherein said substrates provides the electrical connection to external driving voltages;

8. The field emitter device according to any of the claim 7, wherein the material of the field emitter is selected from a group consisting of molybdenum, tungsten, zirconium carbide, molybdenum carbide, hafnium carbide, or molybdenum nitride, and the material for the electrode layers is selected from a group consisting of molybdenum, tungsten, zirconium carbide, molybdenum carbide, hafnium carbide, molybdenum nitride, chromium, copper, gold, silver, or aluminium.

9. The field emitter device according to the claims 7 and 8, being enabled to produce a collimated electron beam by applying between the field emitter and the electron extraction gate electrode

(a) first voltage pulse

(b) second voltage pulse

wherein the duration of the first voltage pulse is longer than the duration of the second voltage pulse and the second voltage pulse is applied during the first voltage pulse.

10. A field emitter device according to the claims 7 and 8, being enabled to produce a collimated electron beam by applying between the field emitter and the electron extraction gate electrode

(a) first voltage pulse

(b) double voltage pulse

wherein the double voltage pulse consists of two voltage pulses with opposite polarity, wherein the duration of and the separation between the two pulses of the double pulse voltage are shorter than the duration of the first pulse voltage and the double voltage pulse is applied during the first voltage pulse.

Abstract

The present invention describes a field-emitter array cathode structure with two stacked control electrodes and their driving method to produce short electron pulses. A sequence of electric stimuli applied to the field emitter array drives generates an electron beam with precisely controlled emission angle, allowing for the production of short collimated electron pulses with high electron beam brightness.

FIG.1 PRIOR ART

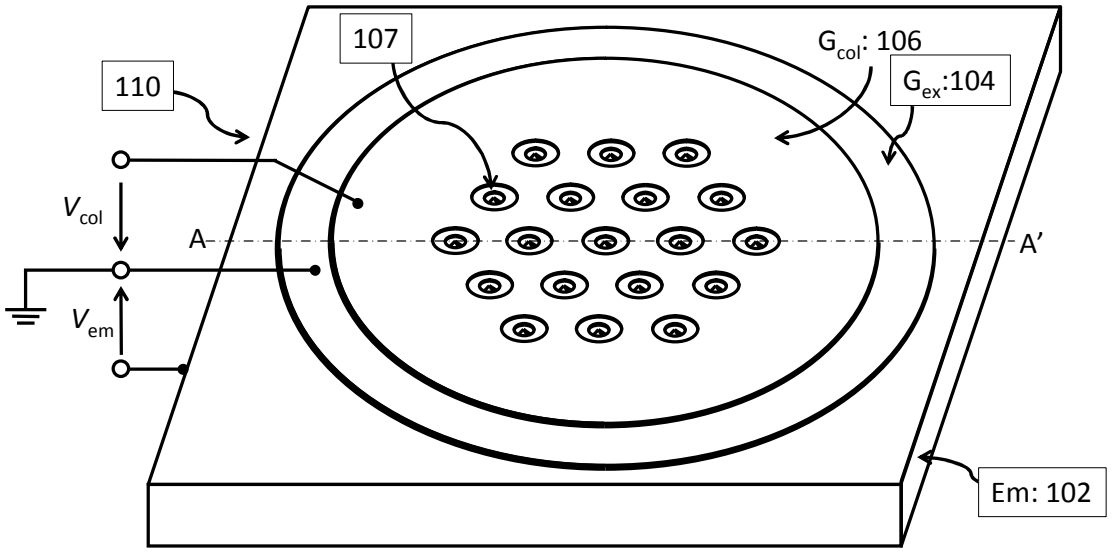

FIG.2 PRIOR ART

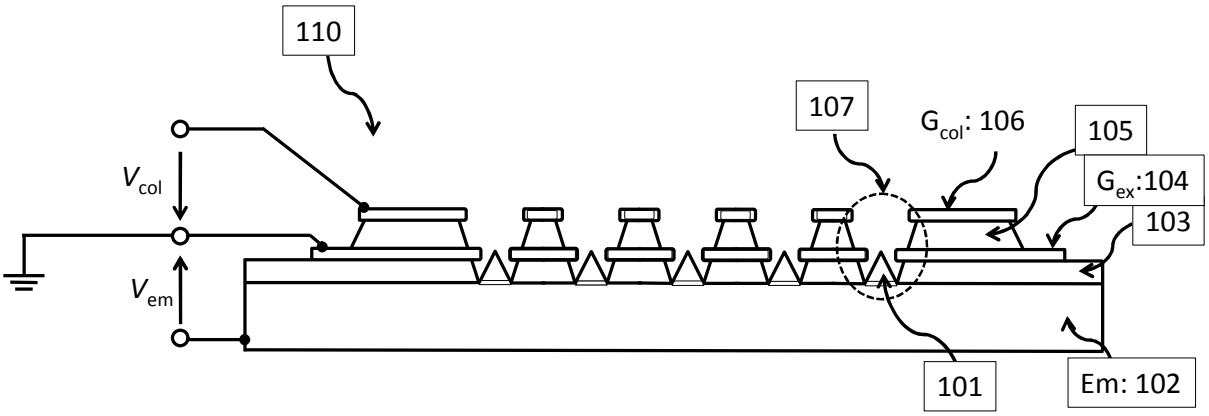

FIG.3

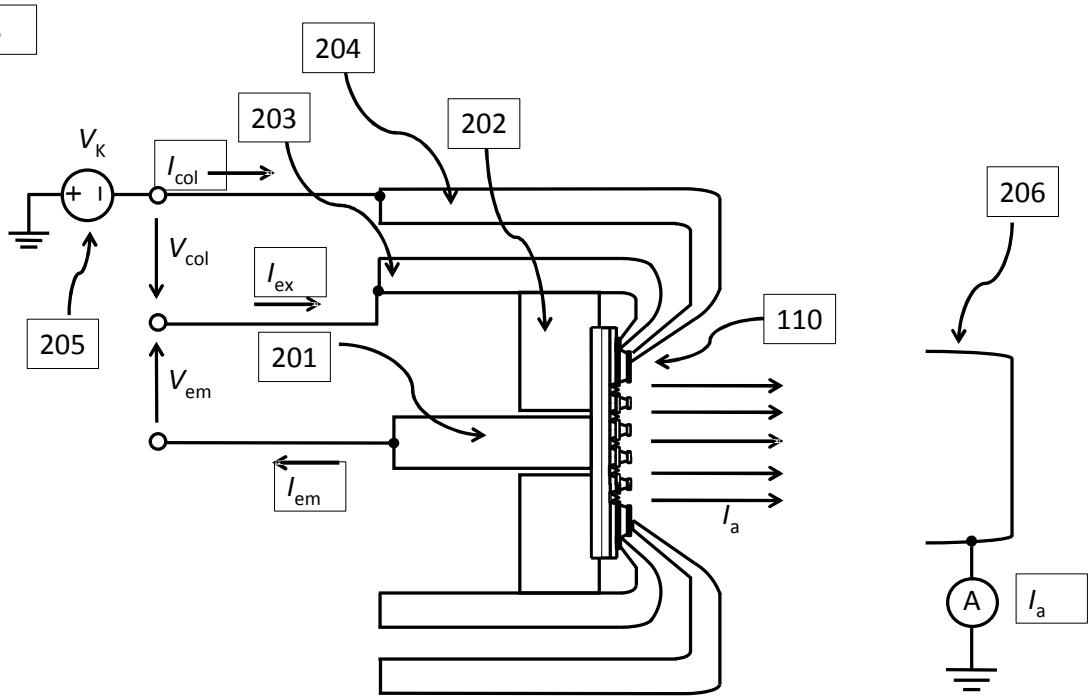

FIG.4

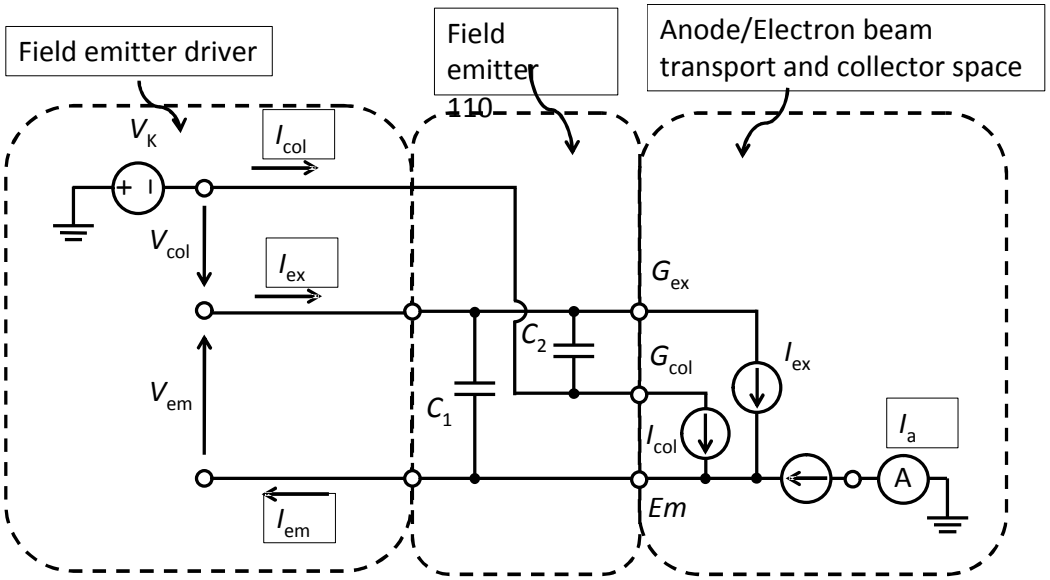
Field emitter driver
Field emitter 110
Anode/Electron beam transport and collector space
V_K
I_{col}
V_{col}
I_{ex}
V_{em}
I_{em}
C_1
C_2
G_{ex}
G_{col}
I_{ex}
I_{col}
I_a
A
Em

FIG.5

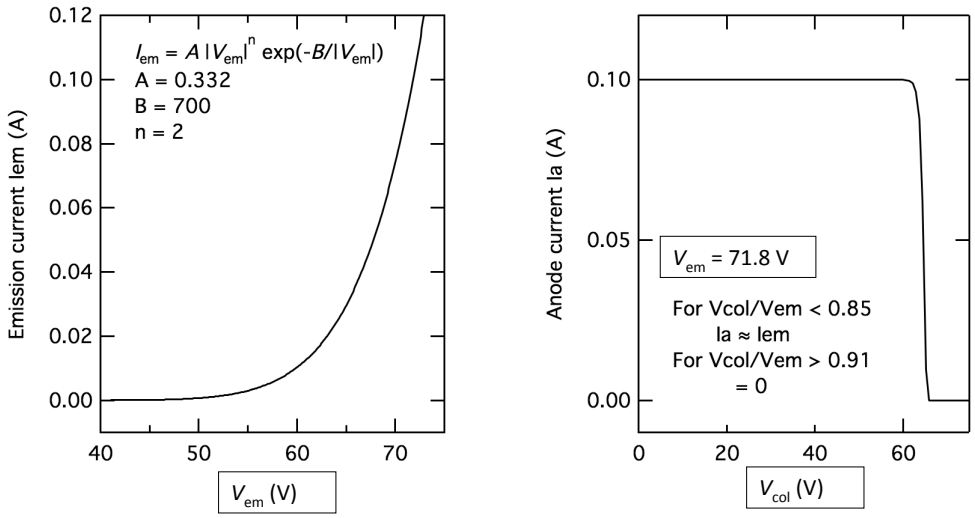
0.12
0.10
0.08
0.06
0.04
0.02
0.00
Emission current Iem (A)
$I_{em} = A\,|V_{em}|^n \exp(-B/|V_{em}|)$
A = 0.332
B = 700
n = 2
40
50
60
70
V_{em} (V)
0.10
0.05
0.00
Anode current Ia (A)
V_{em} = 71.8 V
For Vcol/Vem < 0.85
Ia ≈ Iem
For Vcol/Vem > 0.91
= 0
0
20
40
60
V_{col} (V)

FIG.6

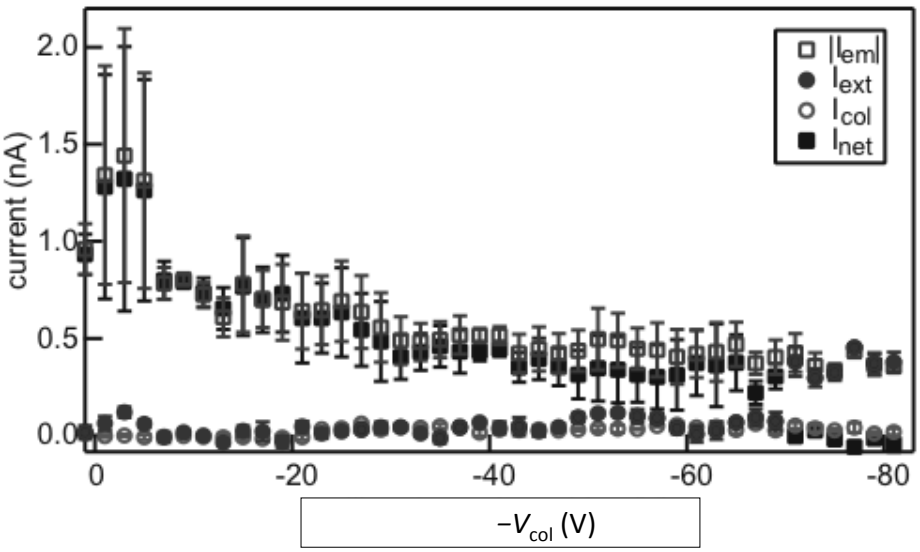

FIG.7

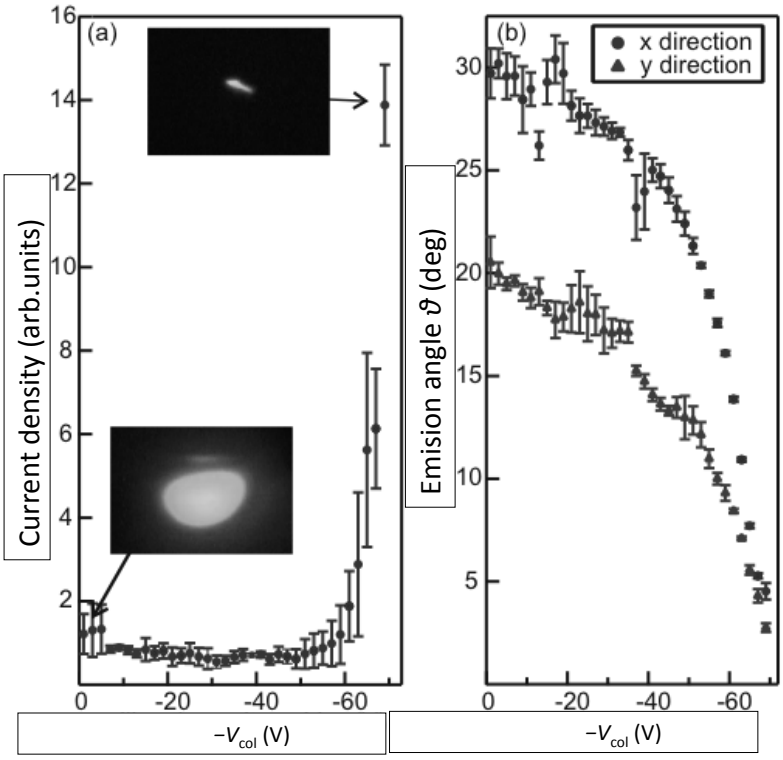
(a)
(b)
x direction
y direction
Current density (arb.units)
Emision angle ϑ (deg)
−V_{col} (V)
−V_{col} (V)
16
14
12
10
8
6
4
2
30
25
20
15
10
5
0
-20
-40
-60

FIG.8

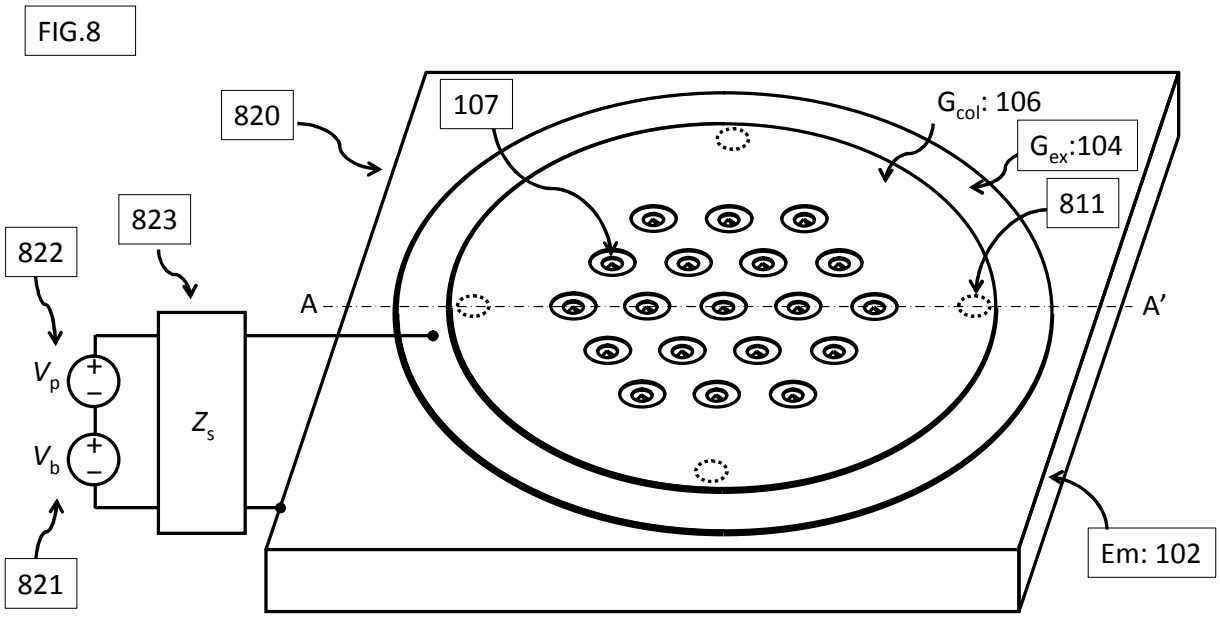

FIG.9

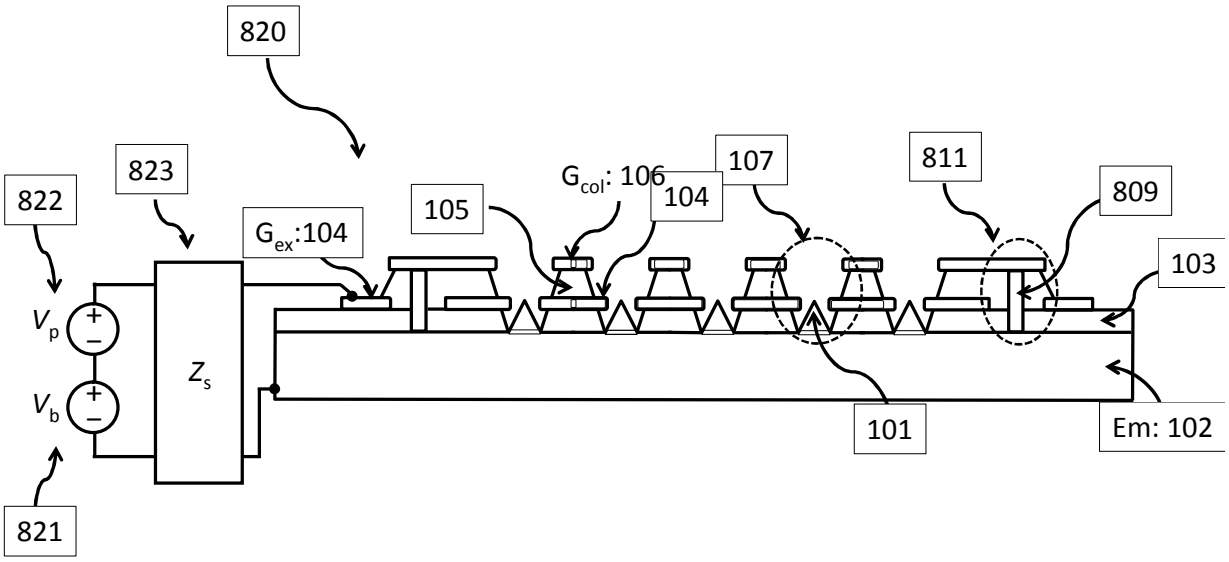
820
823
822
G_{ex}:104
105
G_{col}: 106
104
107
811
809
103
V_p
V_b
Z_s
821
101
Em: 102

FIG.10

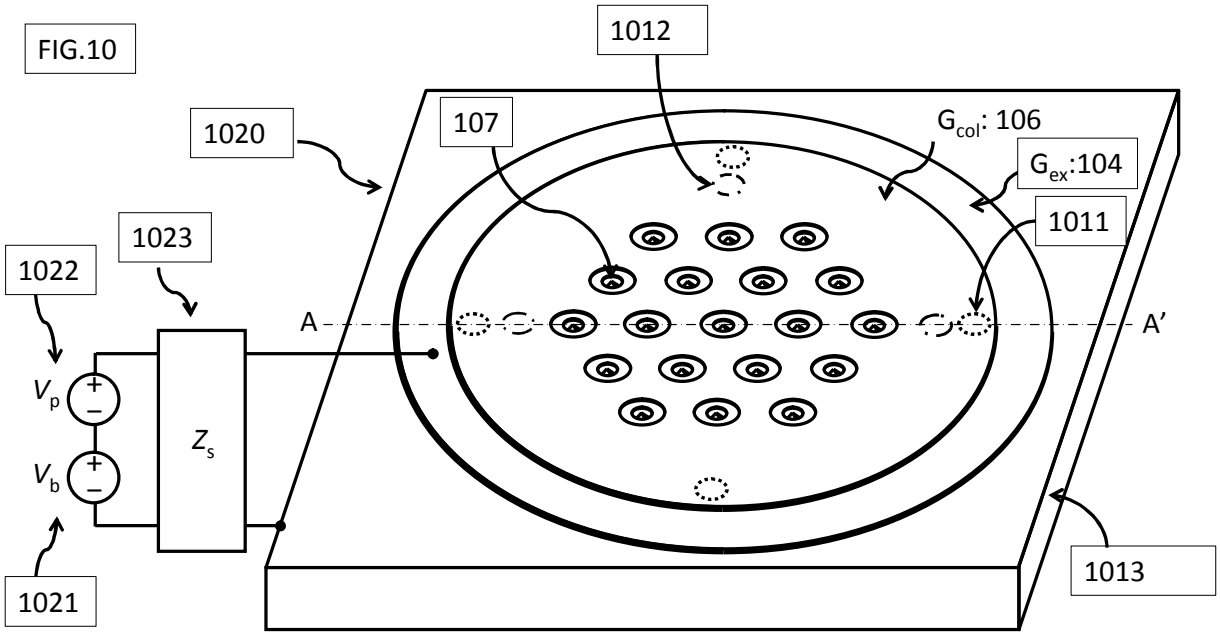
1012
1020
107
G_{col}: 106
G_{ex}:104
1011
1023
1022
A
A'
V_p
V_b
Z_s
1021
1013

FIG.11

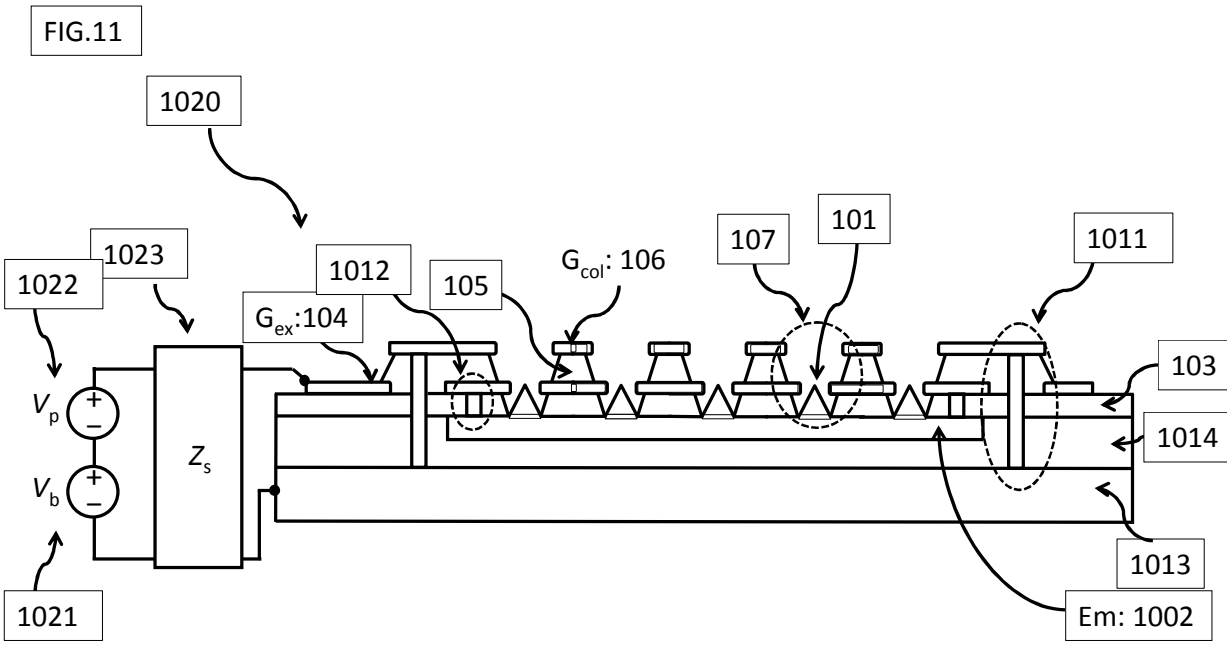
1020
1023
1022
1012
105
G_{col}: 106
107
101
1011
G_{ex}:104
103
1014
V_p
V_b
Z_s
1013
1021
Em: 1002

Appendix B

Fabrication Runsheets

B.1 Fabrication of Ungated Field-Emitter Arrays

Field emitter array with molded Ni substrate

Project No.811120

Verantwortlich: S. Tsujino x2304, P. Helfenstein x2430

Anfangsdatum:	
Enddatum:	

Sample:

Subst: SM 21 [100mm, 380 um-thick, (100), n-type (P) (0.5 - 50Ohm cm), beidseitig poliert, FZ]

Zusammenfassung

1. Wafer oxidieren (Maske für anschliessendes Si ätzen mit KOH)	J. Lehmann
2. Maske belichten (Maske für anschliessendes Si ätzen mit KOH)	J. Lehmann
3. Si ätzen (KOH)	J. Lehmann
4. Oxidation 1	J. Lehmann
5. Oxid 1 ätzen	J. Lehmann
6. Oxidation 2	J. Lehmann

1 Wafer oxidieren

1	**Alle Wafer (inkl. Dummy) reinigen: Standard Caros Reinigung**	

2	**Trockenoxidation [100 +/- 15 nm]**	
	SiO2 Dicke auf Dummy Wafer messen:	

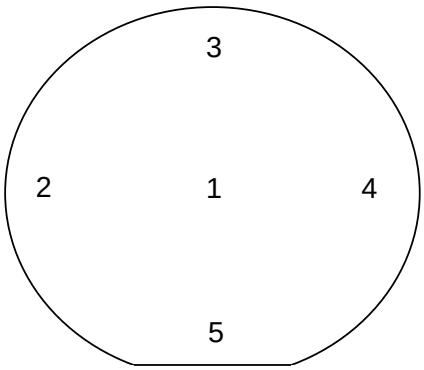

Punkt 1:	
Punkt 2:	
Punkt 3:	
Punkt 4:	
Punkt 5:	
Datum:	
Oxidierte Wafer müssen in N2 gefluteter Box in Reinraum aufbewahrt werden	

2 Maske belichten

	Maske: **"XXX"**	
	Schritte von Dehydration bis Entwicklung müssen **innerhalb eines Tages** ausgeführt werden, das es sonst zu Problemen beim Ätzen kommt	
	Datum:	
	Wafer reinigen falls nötig	
1	**Dehydration**	
a	Ofen: 180 °C für 30 min	

2	**Photolack aufspinnen**	
a	Lack: S1805 (darauf achten, dass Ablaufdatum nicht über-	
	schritten ist. Resist darf nicht älter als 1 Jahr sein)	
b	Spincoaten: Rot: 4000rpm, Beschl: 800rpm/sec, t: 30 sec	
c	Softbake: 110°C, 1 min 30 sec	

3	**Intensität überprüfen**	
	an den 5 angegebenen Punkten überprüfen	
	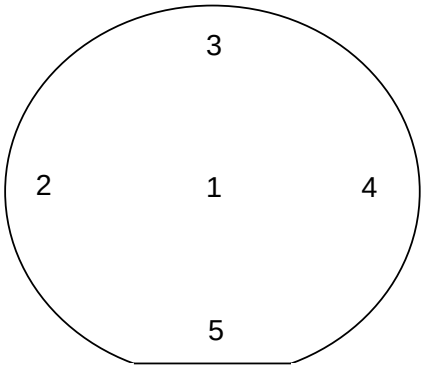	
	Intensität an jedem Punkt muss 18mW betragen	
	(Vergleichswert: CL2, 405nm, 18mW, Datum: 21.1.08)	
	Intensität bei Punkt 1:	
	Intensität bei Punkt 2:	
	Intensität bei Punkt 3:	
	Intensität bei Punkt 4:	
	Intensität bei Punkt 5:	
	Datum:	

4	**Maske belichten: Maske: "XXX"**	
	WXXX	
	WXXX	
	WXXX	
	WXXX	
	WXXX	
	WXXX	
	WXXX	
a	Ausrichten zum Flat	
b	Chuck von MA 6, Vakuum Kontakt	
c	Belichten: ca. 5 sec	
d	Entwickeln: ca. 25 sec, MF-24	
e	Mit DI Wasser spülen und auf Spincoater trocknen	
	Belichtungszeit:	
	Entwicklungszeit:	
	Datum:	
f	Maske reinigen	

5	**Oxid Ätzzeit berechnen:**	
	Parameter für RIE 100: - Gase: CHF3, O2 - Rezept: oxygen plasma cleaning (zum reinigen) - Rezept:vt62_oxide_etch (zum ätzen)	
a	Ätzrate mit Dummy Wafer bestimmen (Vergleichswert: 18nm/min, 22.06.10)	
	Dummy Wafer 3min ätzen in RIE 100	
	Neue Dicke von SiO2 nach Ätzen bestimmen	
	Ätzzeit berechnen:	
	……..…SiO2 / ……..nm/min (Ätzrate) **=……min ……..sec**	
	Beispiel: i.) Dicke vor Ätzen (aus Schritt 1, Wafer oxidieren): 102nm ii.) Dicke nach 3min Ätzen: 48nm iii.) in 3min wurden 54nm geätzt (102nm-48nm=54nm) iv.) Ätzrate=18.0nm/min (54nm/3min=18nm/min) v.) Ätzzeit=5.66min, 5.66min ~ 5 min 40 sec (102nm/18nm/min=5.66 min)	

6	**Oxid ätzen**	
	Reinigen mit Sauerstoffplasma: 20 sec	
	Ätzen: Zeit, die oben berechnet wurde (siehe Beispiel)	
	WXXX	
	WXXX	
	WXXX	
	WXXX	
	WXXX	
	WXXX	
	WXXX	
	WXXX	

7	**Wafer reinigen**	
	Photolack entfernen mit: Remover 1165, Aceton, IPA, DI-Wasser	
	Wafer mit Spincoater trocknen	
	Datum	

3 Si ätzen (KOH)

1	**BOE Dip**	
	BOE (7:1): 5 s	

2	**KOH ätzen**	
	Ätzzeit: 4min 00sec (ergibt Strukturtiefe: 1.06um)	

3	**Strukturen im opt. Mikroskop überprüfen**	
	Datum	

4	**Oxidmaske entfernen**	
	BOE (7:1): 1min 30sec	
	Achtung: falls Oxid (aus Schritt 1) grosse Abweichung von 100nm hat, muss Ätzzeit neu berechnet werden. Das geht so: Oxiddicke/63=Ätzzeit (in Minuten)	
	Ätzzeit:	
	Datum	

4 Oxidation 1

1	**Wafer reinigen**	
a	Caros Reinigung: 5min	
b	BOE (7:1): 20 sec	
c	Caros Reinigung: 5min	
d	BOE (7:1): 10 sec	
e	Caros Reinigung: 5min	
f	BOE (7:1): 10 sec	

2	**Oxidation**	
	Nassoxidation 1: 200 nm	
	falls kein Rezept vorhanden, doppelte Zeit von 100nm nehmen	
	SiO2 Dicke auf Dummy Wafer messen:	
	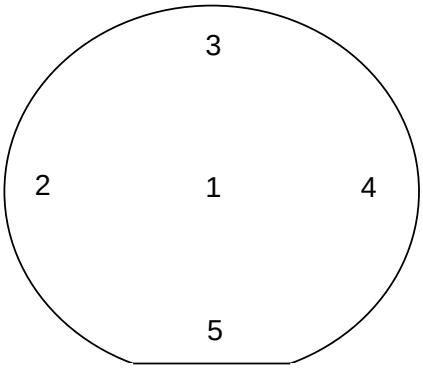	
	Punkt 1:	
	Punkt 2:	
	Punkt 3:	
	Punkt 4:	
	Punkt 5:	
	Datum:	

5 Oxid 1 ätzen

1	**Oxid ätzen**	
	BOE (7:1): 4min 46sec	
	Achtung: falls Oxid (aus Schritt 4) grosse Abweichung von Solldicke hat, muss Ätzzeit neu berechnet werden. Das geht so: Oxiddicke/63=Ätzzeit (in Minuten)	
	Ätzzeit:	
	Datum:	

6 Oxidation 2

1	**Wafer reinigen**	
a	Caros Reinigung: 5min	
b	BOE (7:1): 20 sec	
c	Caros Reinigung: 5min	
d	BOE (7:1): 10 sec	
e	Caros Reinigung: 5min	
f	BOE (7:1): 10 sec	

2	**Oxidation**	
	Nassoxidation 1: 700 nm	
	Kalibration? Zuerst testen mit Rezept für 600nm und Zeit um 20% erhöhen	
	SiO2 Dicke auf Dummy Wafer messen:	
	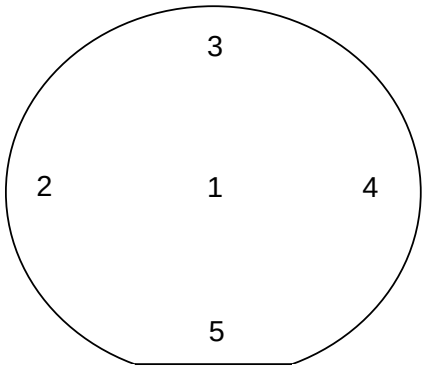	
	Punkt 1:	
	Punkt 2:	
	Punkt 3:	
	Punkt 4:	
	Punkt 5:	
	Datum:	

B.2 Extraction Gate Fabrication Process

Process	Steps	Parameters	Step Time
0. Demolding & Dicing			
	Demold	1.8 l water	
		450g KOH	
		65° C	~24 h
	spincoat Ti-Prime	2000 rpm	60 s
		1000 rpm/s	
		90°C	2 min
	spincoat S1828	2000 rpm	60 s
		1000 rpm/s	
		90°C	5 min
		2000 rpm	60 s
		1000 rpm/s	
		90°C	5 min
	Dice into chips	Prog: Nickel 4-Zoll	1 h
	Resist stripping	Acetone/Isopropanol	5 min.
1. SiO2 Deposition A			
	BOE		8 min 20 sec
	PECVD SiO2 deposition	1200 nm	40.6 nm/m
	Check Si02 thickness		
2. BOE etch Array			
	spincoat PR (S1828)	2000 rpm	60 s
		1000 rpm/s	
	bake	90°C	1 min
	expose		60 s
	develop		45sec. MF26A
	BOE etch		3 min
	Resist stripping	Acetone/Isopropanol	
	BMP	02 plasma	60 sec
2 B. SiO2 Deposition A2			
	PECVD SiO2 deposition	40 nm	
	Check SiO2 thickness		
3. SiON Deposition A			
	PECVD SiON deposition	1200 nm	~2 h
	Check SiON thickness	Reflectometer	
4. Mo Gate Deposition A			
	pump Nordiko	p_base=2E-6 mbar	12 h
	presputter	2.0 mbar	5 min
	sputter	p_Ar=2.0 mbar	45 min/500nm
		sputter current: 1.5 A	
		sputter voltage: ~280 V	
		Rotation: 10	
	target cooling time		10 min
	vent		

5. Resist spinning & thinning Gate 1			
	spincoat PR (S1828)	2000 rpm	60 s
		1000 rpm/s	
	bake	90°C	5 min
	RIE 80		
		PH1828thin	~60 min
	SEM	check apertures	

6. Aperture opening Gate 1			
	paint around edge		
	Al etch		1min 25 sec
	remove PR (acetone/ipa)		

7. Pattern Gate 1 Contacts			
	spincoat PR (S1828)	2000 rpm	60 s
		1000 rpm/s	
	bake	90°C	1 min
	expose		60 s
	develop		
	paint around edge		
	bake	95°C	5 min
	Al etch		2 min
	remove PR (acetone/ipa)		
	BMP (O2 plasma)	Recipe: Helga	5 min

8. Sawing in 9x9 mm pieces			
	spincoat Ti Prime	2000 rpm	60 s
		1000 rpm/s	
	bake	95°C	2 min
	spincoat PR (S1828)	2000 rpm	60 s
		1000 rpm/s	
	bake	95°C	5 min
	spincoat PR (S1828)	2000 rpm	60 s
		1000 rpm/s	
	bake	95°C	5 min
	saw		

B.3 Focused Ion Beam Assisted Collimation Gate Fabrication

Process	Steps	Parameters	Step Time
0. Demolding & Dicing			
	Demold	1.8 l water	
		450g KOH	
		65° C	~24 h
	spincoat Ti-Prime	2000 rpm	60 s
		1000 rpm/s	
		90°C	2 min
	spincoat S1828	2000 rpm	60 s
		1000 rpm/s	
		90°C	5 min
		2000 rpm	60 s
		1000 rpm/s	
		90°C	5 min
	Dice into chips	Prog: Nickel 4-Zoll	1 h
1. SiO2 Deposition			
	BOE		8 min 20 sec
	PECVD SiO2 deposition	1200 nm	55 nm/m
	Check Si02 thickness		
2. Mo Gate Deposition			
	pump Nordiko	p_base=2E-6 mbar	12 h
	presputter	1.1 mbar	5 min
		1.9 mbar	5 min
	sputter	p_Ar=1.9 mbar	45 min/500nm
		sputter current: 1.5 A	
		sputter voltage: 280 V	
		Rotation: 10	
	target cooling time		10 min
	vent		
3. Resist spinning & thinning Gate 1			
	spincoat PR (S1828)	2000 rpm	60 s
		1000 rpm/s	
	bake	90°C	5 min
	RIE		
		PH1828thin	~60 min
	SEM	check apertures	
4. Aperture opening Gate 1			
	paint around edge		
	Al etch		1 min 25 sec
	remove PR (acetone/ipa)		
5. Pattern Gate 1 Contacts			
	spincoat PR (S1828)	2000 rpm	60 s
		1000 rpm/s	
	bake	90°C	1 min
	expose		60 s
	develop		
	paint around edge		
	bake	95°C	5 min
	Al etch		1' 30"
	remove PR (acetone/ipa)		
	BMP (O2 plasma)	Recipe: Helga	5 min

6. SiON Deposition			
	PECVD SiON deposition	1200 nm	11.1nm/min
	Check SiON thickness	1200 nm	

7. Mo Gate Deposition B			
	pump Nordiko	p_base=2E-6	12 h
	presputter	2.0 mbar	40 min
	sputter	p_Ar=2.0 mbar	45 min/500nm
		sputter current: 1.5 A	
		sputter voltage: 300-320 V	
		Rotation: 10	
	target cooling time		10 min
	vent		

8. SiO2 Deposition C (sacrificial FIB Layer)			
	PECVD SiO2	500 nm	
	Check SiO2 thickness		

9. Mo Deposition C (sacrificial FIB layer)			
	pump Nordiko	p_base=4E-6	12 h
	presputter	1.1 mbar	5 min
		1.6 mbar	5 min
	sputter	p_Ar=1.6 mbar	8 min / 100 nm
		sputter current: 1.5 A	
		sputter voltage: 300-320 V	
		Rotation: 10	
	target cooling time		10 min
	vent		

10. FIB Aperture opening			
	FIB aperture opening		

11. Aperture opening (wet-etch)			
	paint around edge		
	Al etch		50 s
	remove PR (acetone/ipa)		
	RIE100 (O2 plasma)		10 min

12. BOE clear tips			
	paint around edge		
	BOE etch		7 min
	remove PR (acetone/ipa)		

13. Pattern Gate 2 Contacts			
	spincoat PR (S1828)	2000 rpm	60 s
		800 rpm/s	
	bake	90°C	1 min
	expose		20 s
	develop		
	paint around edge		
	bake	90°C	5 min
	Al etch		<~2 min
	remove PR (acetone/ipa)		
	RIE100 (O2 plasma)		10 min

14. Pattern Vias			
	spincoat PR (S1828)	2000 rpm	60 s
		800 rpm/s	
	bake	90°C	1 min
	expose	(use inverted hole mask)	20 s
	develop		
	paint around edge		
	bake	90°C	5 min
	dip in DI water		
	BOE etch		4 min
	remove PR (acetone/ipa)		
	RIE100 (O2 plasma)		10 min

B.4 Electron Beam Lithography Assisted Collimation Gate Fabrication

Process	Steps	Parameters	Step Time
0. Demolding & Dicing			
	Demold	1.8 l water	
		450g KOH	
		65° C	~24 h
	spincoat Ti-Prime	2000 rpm	60 s
		1000 rpm/s	
		90°C	2 min
	spincoat S1828	2000 rpm	60 s
		1000 rpm/s	
		90°C	5 min
		2000 rpm	60 s
		1000 rpm/s	
		90°C	5 min
	Dice into chips	Prog: Nickel 4-Zoll	1 h
1. SiO2 Deposition			
	BOE		8 min 20 sec
	PECVD SiO2 deposition	1200 nm	55 nm/m
	Check Si02 thickness		
2. Mo Gate Deposition			
	pump Nordiko	p_base=2E-6 mbar	12 h
	presputter	1.1 mbar	5 min
		1.9 mbar	5 min
	sputter	p_Ar=1.9 mbar	45 min/500nm
		sputter current: 1.5 A	
		sputter voltage: 280 V	
		Rotation: 10	
	target cooling time		10 min
	vent		
3. Resist spinning & thinning Gate 1			
	spincoat PR (S1828)	2000 rpm	60 s
		1000 rpm/s	
	bake	90°C	5 min
	RIE		
		PH1828thin	~60 min
	SEM	check apertures	
4. Aperture opening Gate 1			
	paint around edge		
	Al etch		1 min 25 sec
	remove PR (acetone/ipa)		

5. Pattern Gate 1 Contacts			
	spincoat PR (S1828)	2000 rpm	60 s
		1000 rpm/s	
	bake	90°C	1 min
	expose		60 s
	develop		
	paint around edge		
	bake	95°C	5 min
	Al etch		1' 30''
	remove PR (acetone/ipa)		
	BMP (O2 plasma)	Recipe: Helga	5 min

6. SiON Deposition			
	PECVD SiON deposition	1200 nm	11.1nm/min
	Check SiON thickness	1200 nm	

7. Mo Gate Deposition B			
	pump Nordiko	p_base=2E-6	12 h
	presputter	2.0 mbar	40 min
	sputter	p_Ar=2.0 mbar	45 min/500nm
		sputter current: 1.5 A	
		sputter voltage: 300-320 V	
		Rotation: 10	
	target cooling time		10 min
	vent		

8. Open Gate 2 Alignment Marks	
	No need to open, e-beam will find the alignment much easier if Mo layer is continuous (claim: resist is not charging up this way)

9. ZEP coating			
	spincoat ZEP 520-A	2000 rpm	120 sec
		1000 rpm/s	
	bake	180°C	180 sec

10. E-Beam Exposure			
	expose		
	develop	ZED-N50	5 min
		IPA	
		DI water clean	
	BMP (O2 plasma)	Recipe: Helga	60 sec

11. Aperture Opening			
	Al etch		1min 25 sec
	remove ZEP	ZDMAC	5'
	BMP (O2 plasma)	Recipe: Helga	100 sec

12. BOE clear tips			
	paint around edge	+ bake (95°C, 5')	
	BOE etch	SiOn: 145nm/min	5 min
	remove PR (acetone/IPA)		

13. Pattern Gate 2 Contacts			
	spincoat PR (S1828)	2000 rpm	60 s
		1000 rpm/s	
	bake	90°C	1 min
	expose		60 s
	develop		20 s
	paint around edge		
	bake	95°C	5 min
	Al etch		2'
	remove PR (acetone/ipa)		

14. Pattern Vias			
	spincoat Ti Primer	2000 rpm	60 s
		1000 rpm/s	
	bake	90° C	2 min
	spincoat PR (S1828)	2000 rpm	60 s
		1000 rpm/s	
	bake	90°C	1 min
	expose	(use inverted hole mask)	90 s
	develop		20 s
	paint around edge		
	bake	95°C	5 min
	dip in DI water		
	BOE etch		6 min
	remove PR (acetone/ipa)		

15. Sawing in 9x9 mm pieces			
	spincoat Ti Prime	2000 rpm	60 s
		1000 rpm/s	
	bake	95°C	2 min
	spincoat PR (S1828)	2000 rpm	60 s
		1000 rpm/s	
	bake	95°C	5 min
	spincoat PR (S1828)	2000 rpm	60 s
		1000 rpm/s	
	bake	95°C	5 min
	saw		

Appendix C

Structure Definition Sample for Electron Beam Lithography

```
TEXTLIB 9.0.0
UNIT MICRON
RESOLVE 0.001
BEGLIB

!-------------------------------------------------------------------------------
! Make several different square sizes.
! (0,0) coordinate should be in the center of the square.

STRUCT Square_3um
  LAYER 1
  B (-1.5,-1.5) (1.5,-1.5) (1.5,1.5) (-1.5,1.5) ENDB
ENDSTRUCT

STRUCT Square_5um
  LAYER 2
  B (-2.5,-2.5) (2.5,-2.5) (2.5,2.5) (-2.5,2.5) ENDB
ENDSTRUCT

STRUCT Circle_p10um
  LAYER 3
   C 2.00 0,0 (0 360 24) ENDC
!  B (-0.75,-0.75) (0.75,-0.75) (0.75,0.75) (-0.75,0.75) ENDB
ENDSTRUCT

STRUCT Circle_p5um
  LAYER 4
   C 2.00 0,0 (0 360 24) ENDC
!  B (-0.75,-0.75) (0.75,-0.75) (0.75,0.75) (-0.75,0.75) ENDB
ENDSTRUCT

!-------------------------------------------------------------------------------
! Define the quarters of arrays

! ---------> ARRAY: 10um pitch array (for 1.5mm radius maximum)

STRUCT Quarter_p10um_SqArray
  AREF Circle_p10um (5,5) 150 (10,0) 150 (0,10)
ENDSTRUCT

! ---------> ARRAY: 5um pitch array (for 1.5mm radius maximum)

STRUCT UnitCell_5um
  SREF Circle_p5um (0,0)
```

```
  SREF Circle_p5um (0,5)
  SREF Circle_p5um (5,5)
ENDSTRUCT

STRUCT Quarter_p5um_CrossArray
  AREF UnitCell_5um (5,0) 150 (10,0) 150 (0,10)
  AREF UnitCell_5um (5,0) 150 (10,0) 150 (0,10)
  AREF UnitCell_5um (5,0) 150 (10,0) 150 (0,10)
  AREF UnitCell_5um (5,0) 150 (10,0) 150 (0,10)
ENDSTRUCT

!-------------------------------------------------------------------------------
! Define a full array by rotation of the quarter around the 0,0 origin

STRUCT Full_p5um_CrossArray
  SREF Quarter_p5um_CrossArray (0,0)
  ANGLE 90
  SREF Quarter_p5um_CrossArray (0,0)
  ANGLE 180
  SREF Quarter_p5um_CrossArray (0,0)
  ANGLE 270
  SREF Quarter_p5um_CrossArray (0,0)
ENDSTRUCT

STRUCT Full_p10um_SqArray
  SREF Quarter_p10um_SqArray (0,0)
  ANGLE 90
  SREF Quarter_p10um_SqArray (0,0)
  ANGLE 180
  SREF Quarter_p10um_SqArray (0,0)
  ANGLE 270
  SREF Quarter_p10um_SqArray (0,0)
ENDSTRUCT

!-------------------------------------------------------------------------------
! Define the Circles for extraction

STRUCT Circle_R565um
  LAYER 21
  C 566 (0,0) (0 360 200) ENDC
ENDSTRUCT

STRUCT Circle_R1129um
  LAYER 22
```

```
  C 1129.5 (0,0) (0 360 200) ENDC
ENDSTRUCT

!-------------------------------------------------------------------------------
! Define the Marker Sets
STRUCT MarkerSet
  AREF Square_5um (-3340,-3340) 2 (6680,0) 2 (0,6680)
  AREF Square_5um (-3340,-3190) 2 (6680,0) 2 (0,6380)
  AREF Square_5um (-3190,-3340) 2 (6380,0) 2 (0,6680)
ENDSTRUCT

ENDLIB
```

Appendix D

Additional Particle Tracking Results

The graphs shown in this appendix were created by a particle tracking simulation of modeled double-gate field-emitter structures. Detailed information on the calculation methods and parameters of the simulation are given in chapter 2

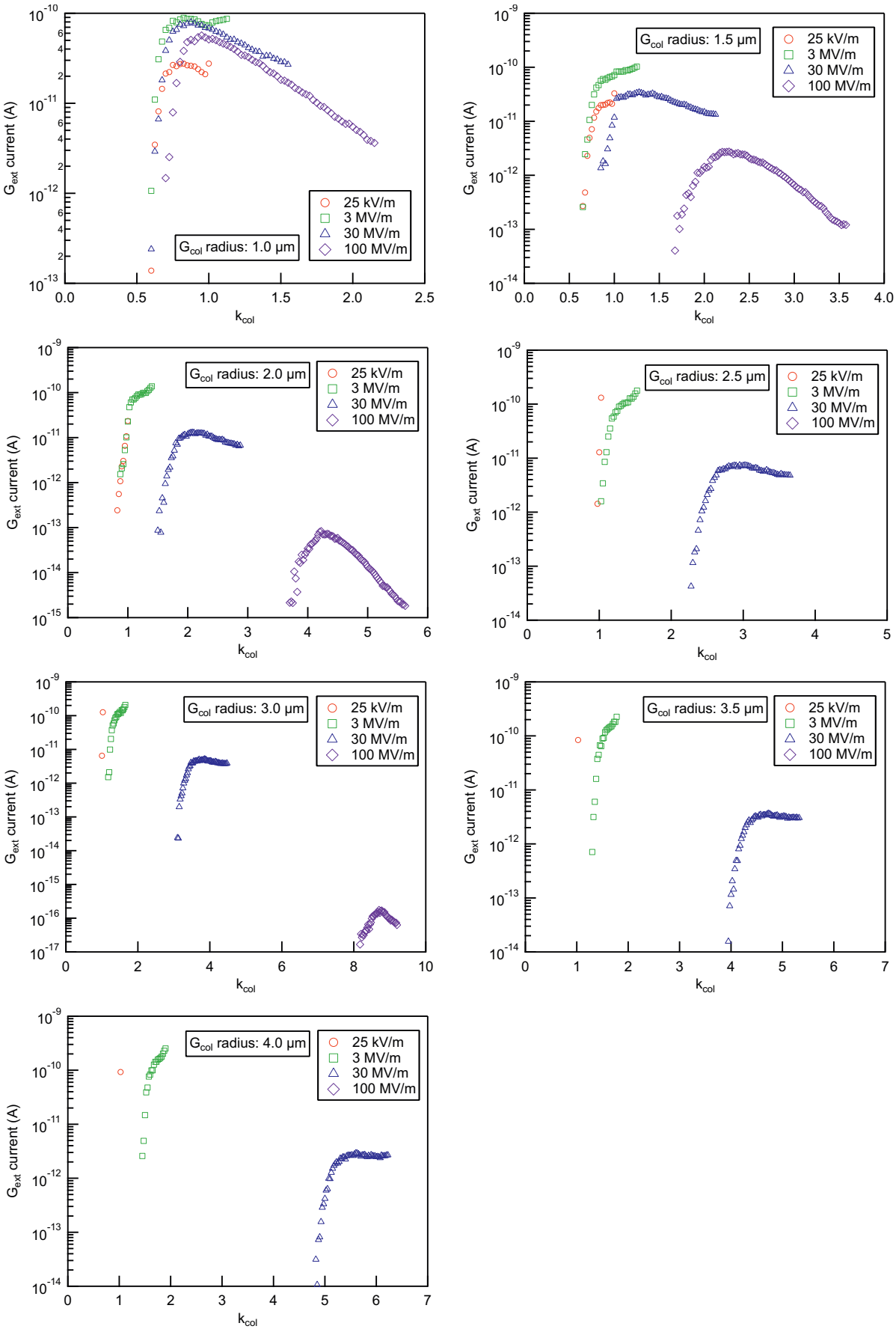

Figure D.1: This figure illustrates the amount of emission current intercepted by the extraction gate G_{ext} for different G_{col} aperture diameters and acceleration fields.

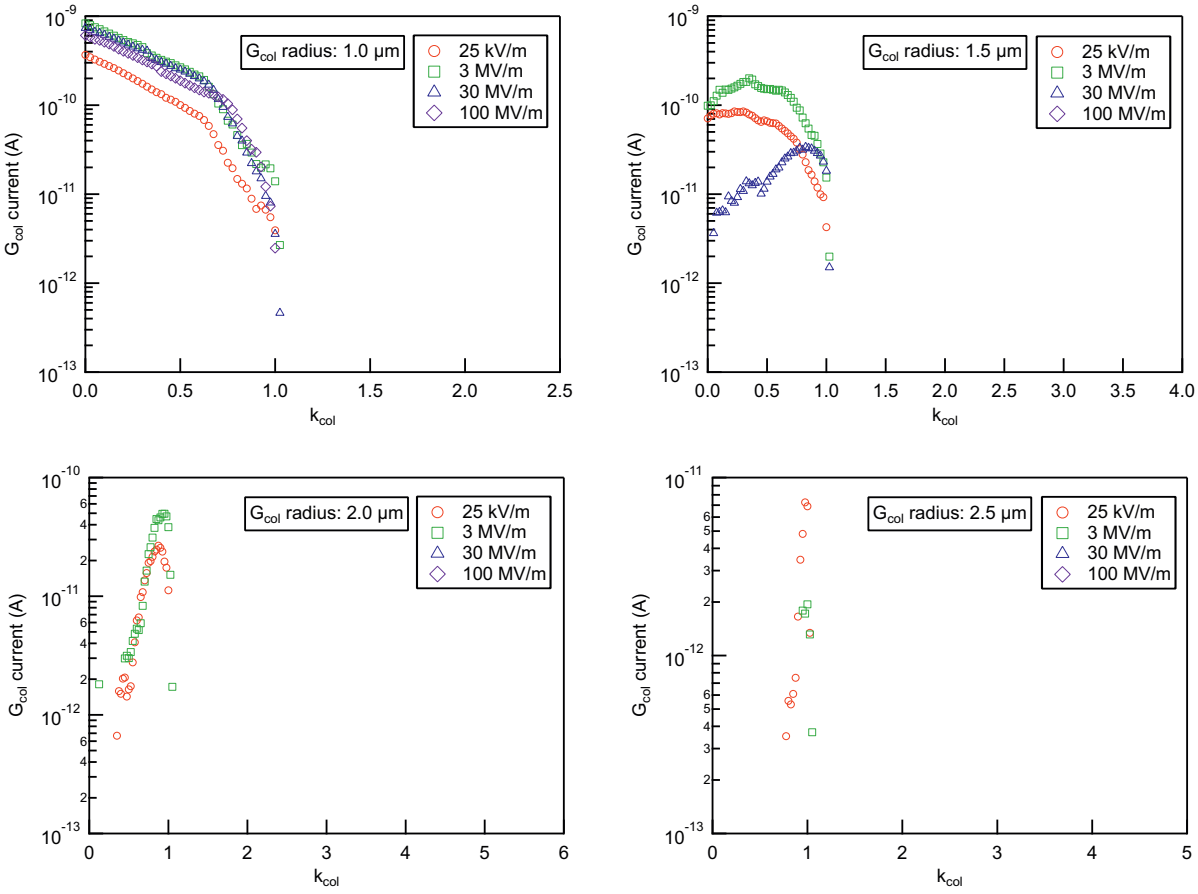

Figure D.2: This figure illustrates the amount of emission current intercepted by the collimation gate G_{col} for different G_{col} aperture diameters and acceleration fields.

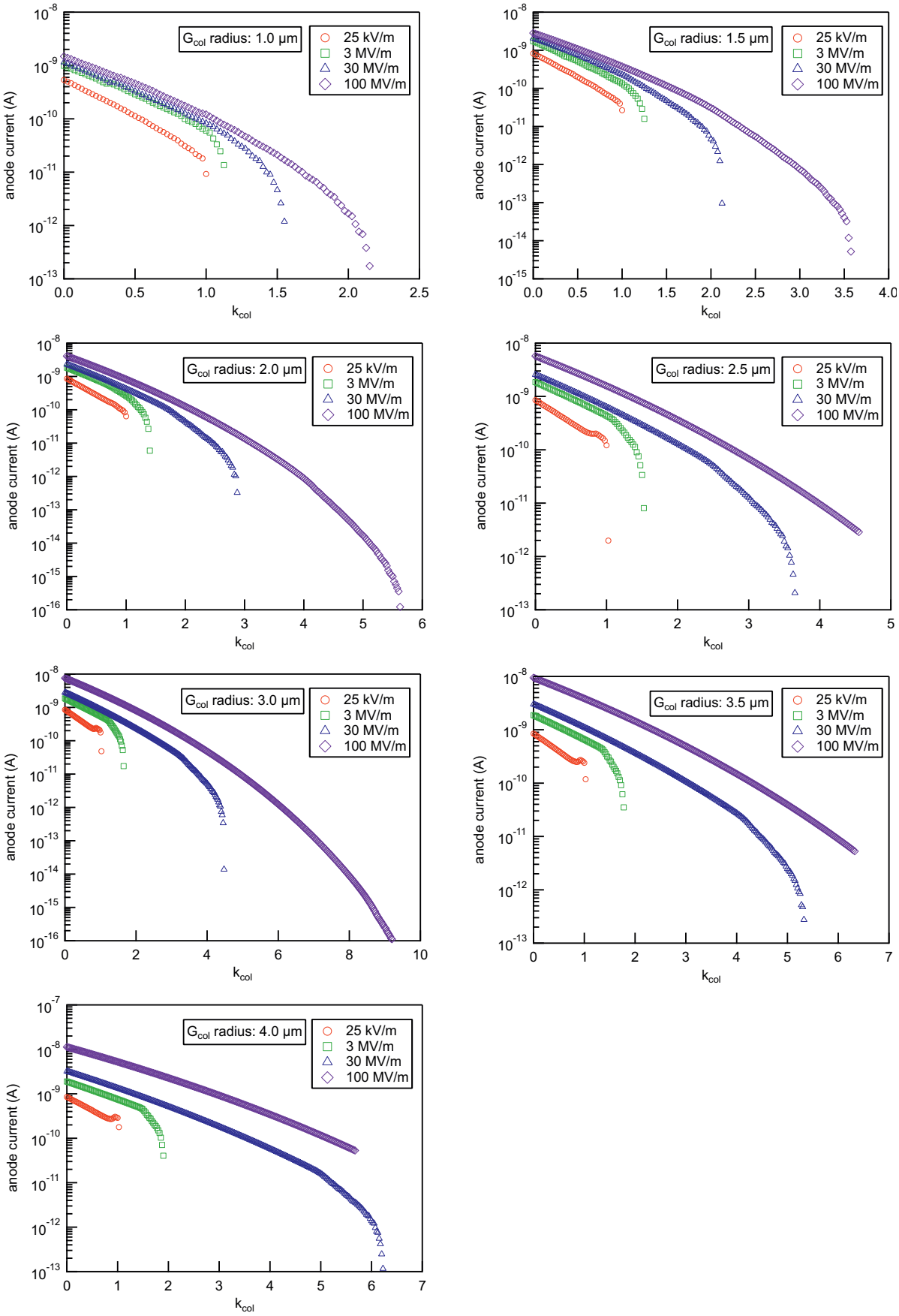

Figure D.3: This figure illustrates the amount of emission current reaching the anode for different G_{col} aperture diameters and acceleration fields.

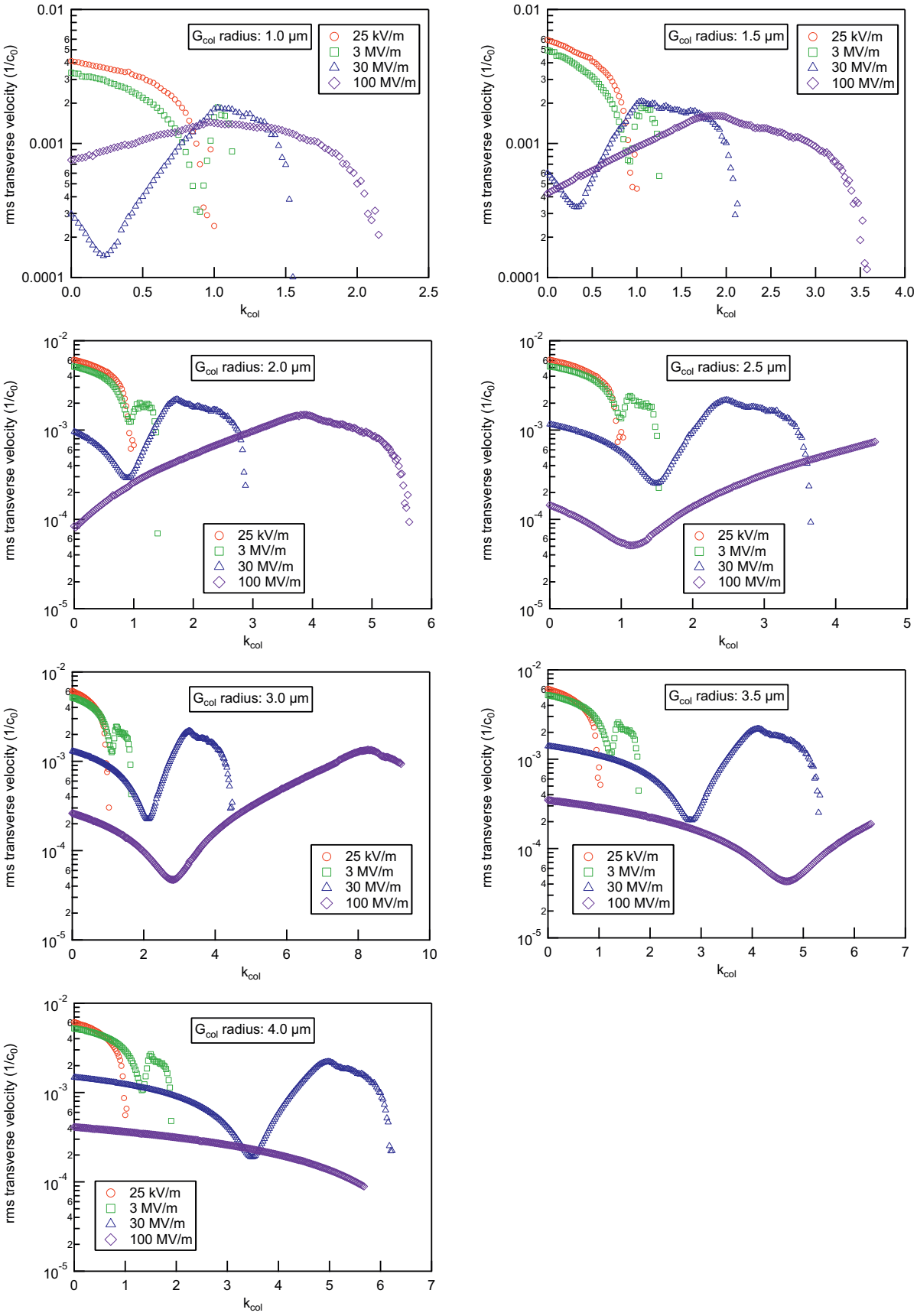

Figure D.4: This figure illustrates the evolution of the rms transverse velocity with k_{col} for different G_{col} aperture diameters and acceleration fields.

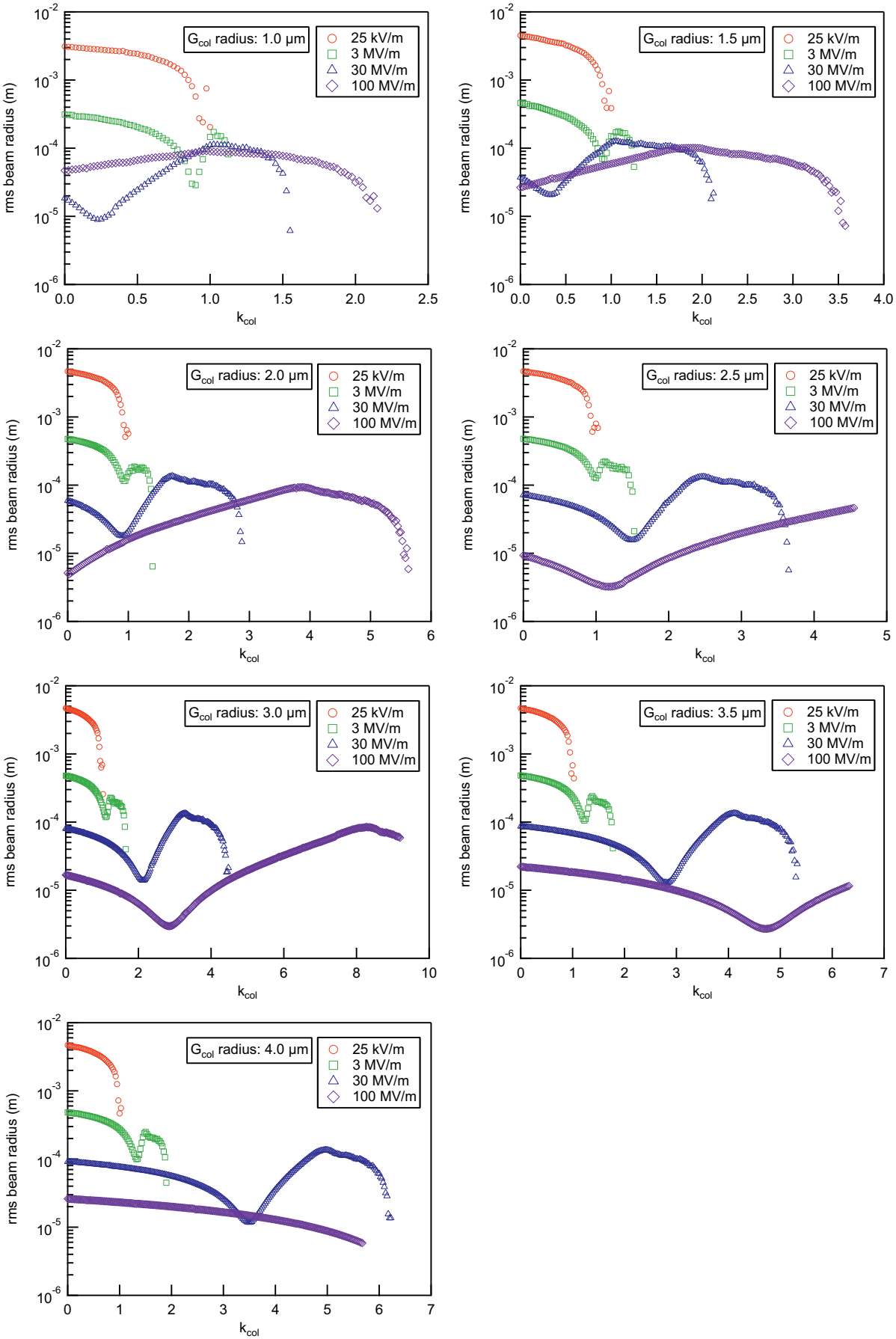

Figure D.5: This figure illustrates the evolution of the rms beam radius with k_{col} for different G_{col} aperture diameters and acceleration fields.

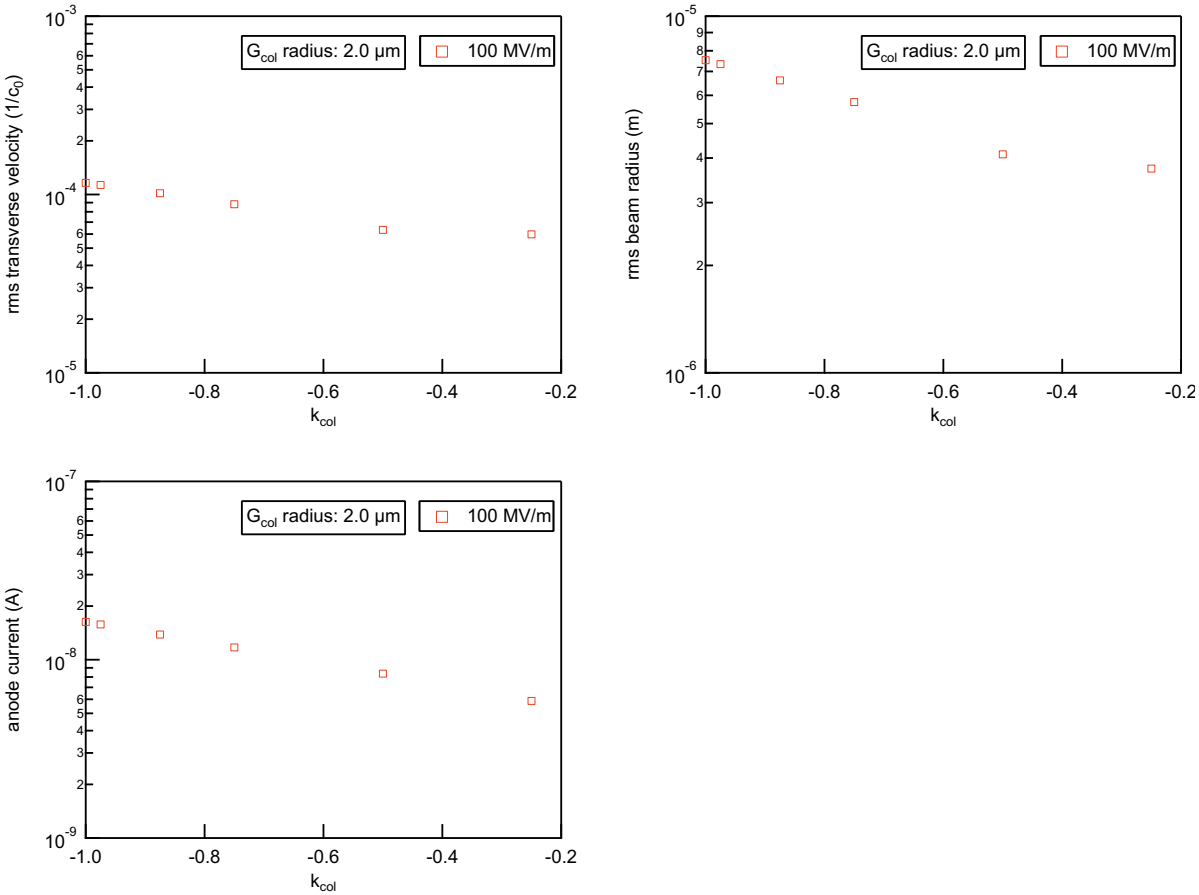

Figure D.6: This figure illustrates a unique behaviour found only for $F_{acc} = 100$ MV/m and a G_{col} aperture diameter of 4 μm where the application of a positive V_{col} leads to a highly collimated beam.

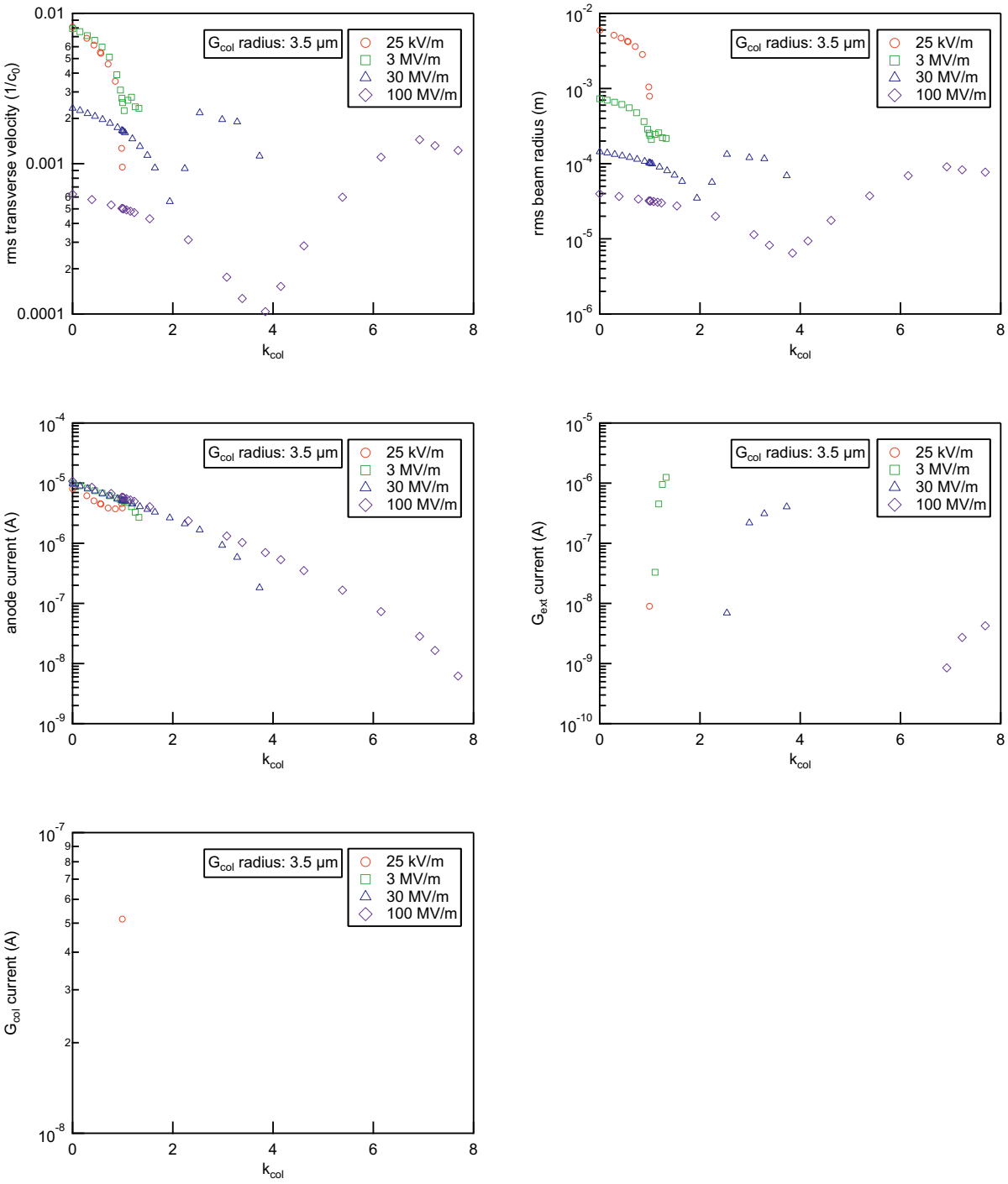

Figure D.7: This figure illustrates the collimation characteristics for a G_{col} aperture diameter of 7 μm when space-charge effects are included in the simulation.

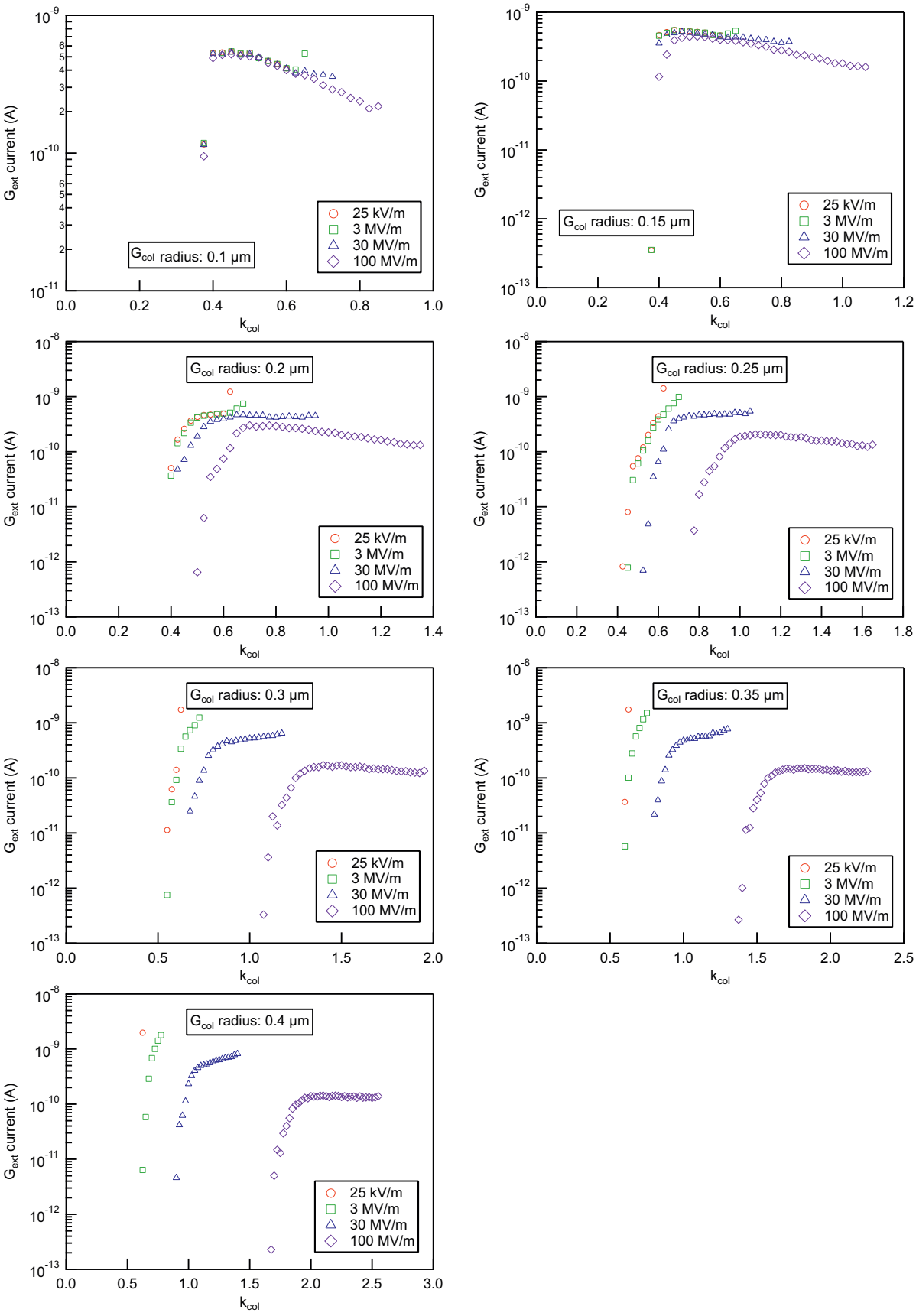

Figure D.8: This figure illustrates the amount of emission current intercepted by the extraction gate G_{ext} for different G_{col} aperture diameters and acceleration fields with a high-density double-gate structure.

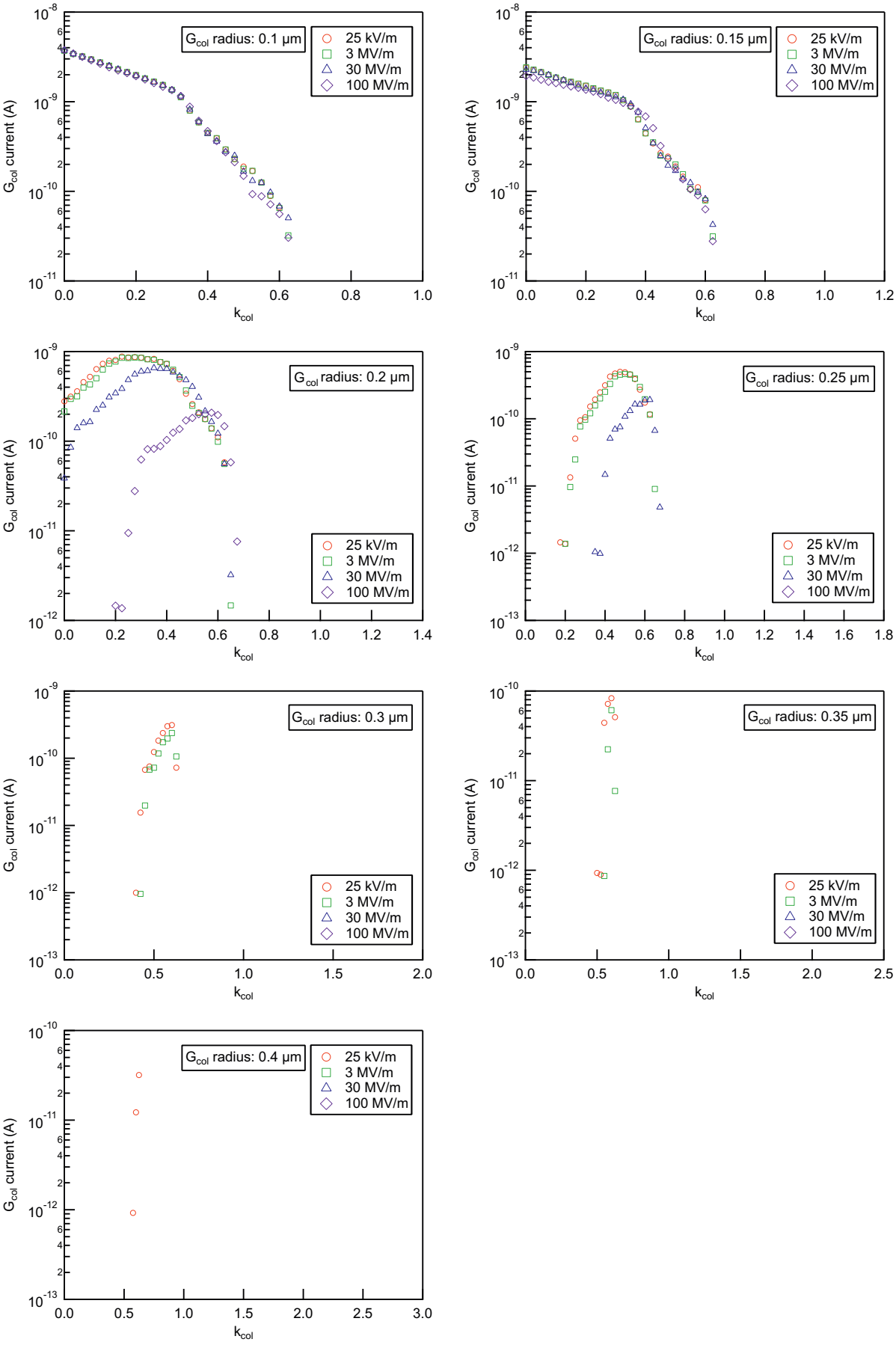

Figure D.9: This figure illustrates the amount of emission current intercepted by the collimation gate G_{ext} for different G_{col} aperture diameters and acceleration fields with a high-density double-gate structure.

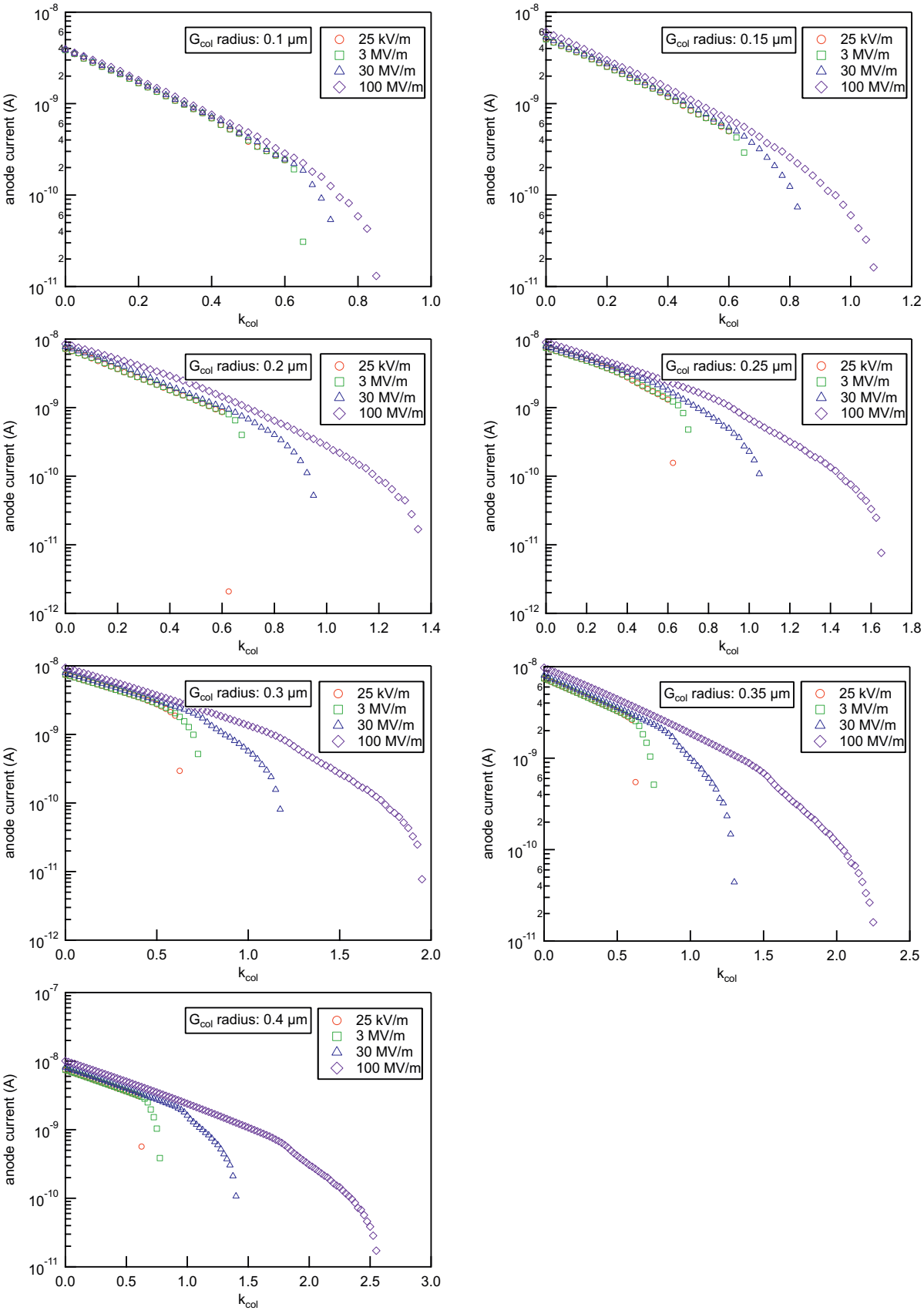

Figure D.10: This figure illustrates the amount of emission current reaching the anode for different G_{col} aperture diameters and acceleration fields with a high-density double-gate structure.

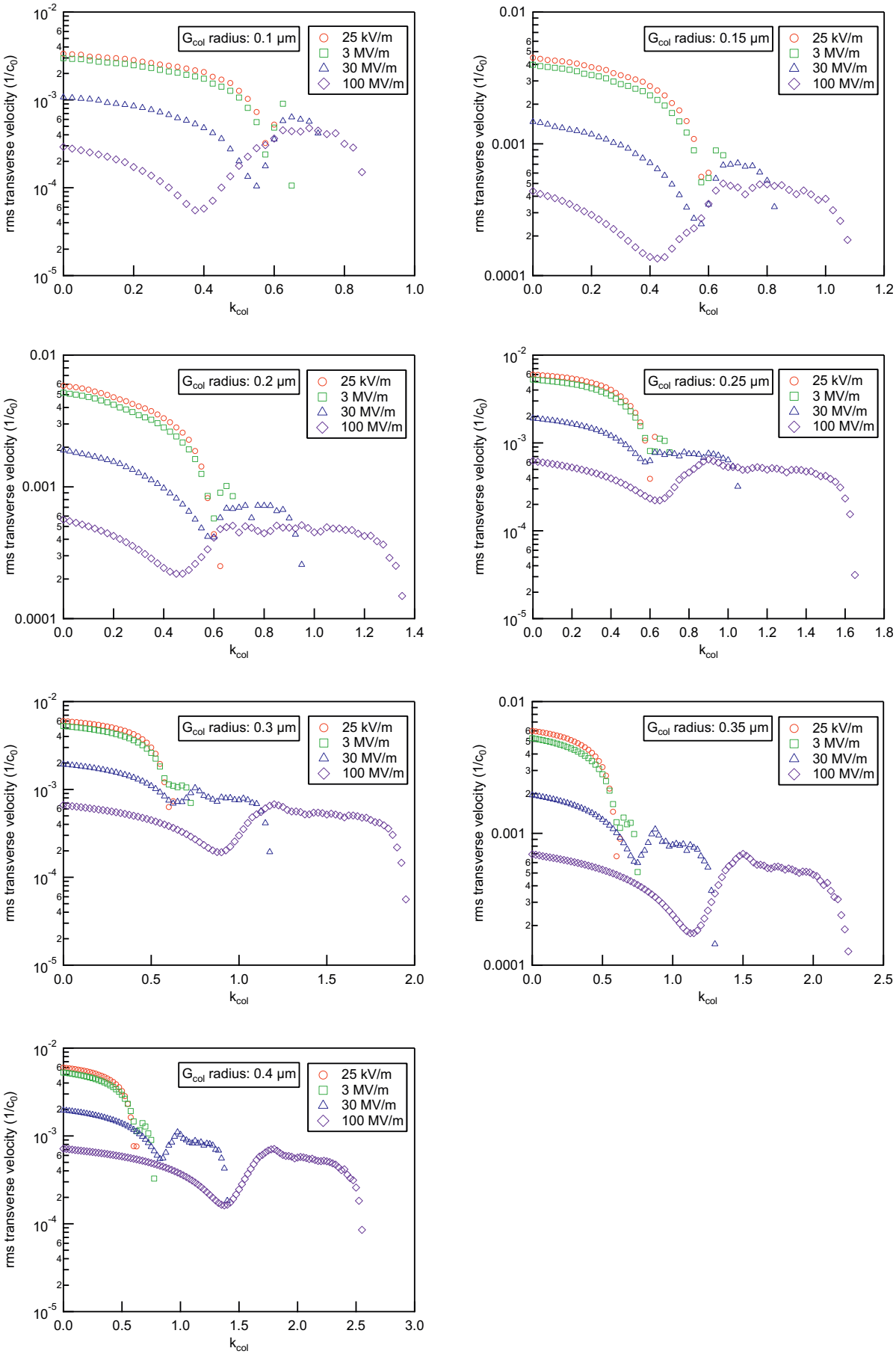

Figure D.11: This figure illustrates the evolution of the rms transverse velocity with k_{col} for different G_{col} aperture diameters and acceleration fields with a high-density double-gate structure.

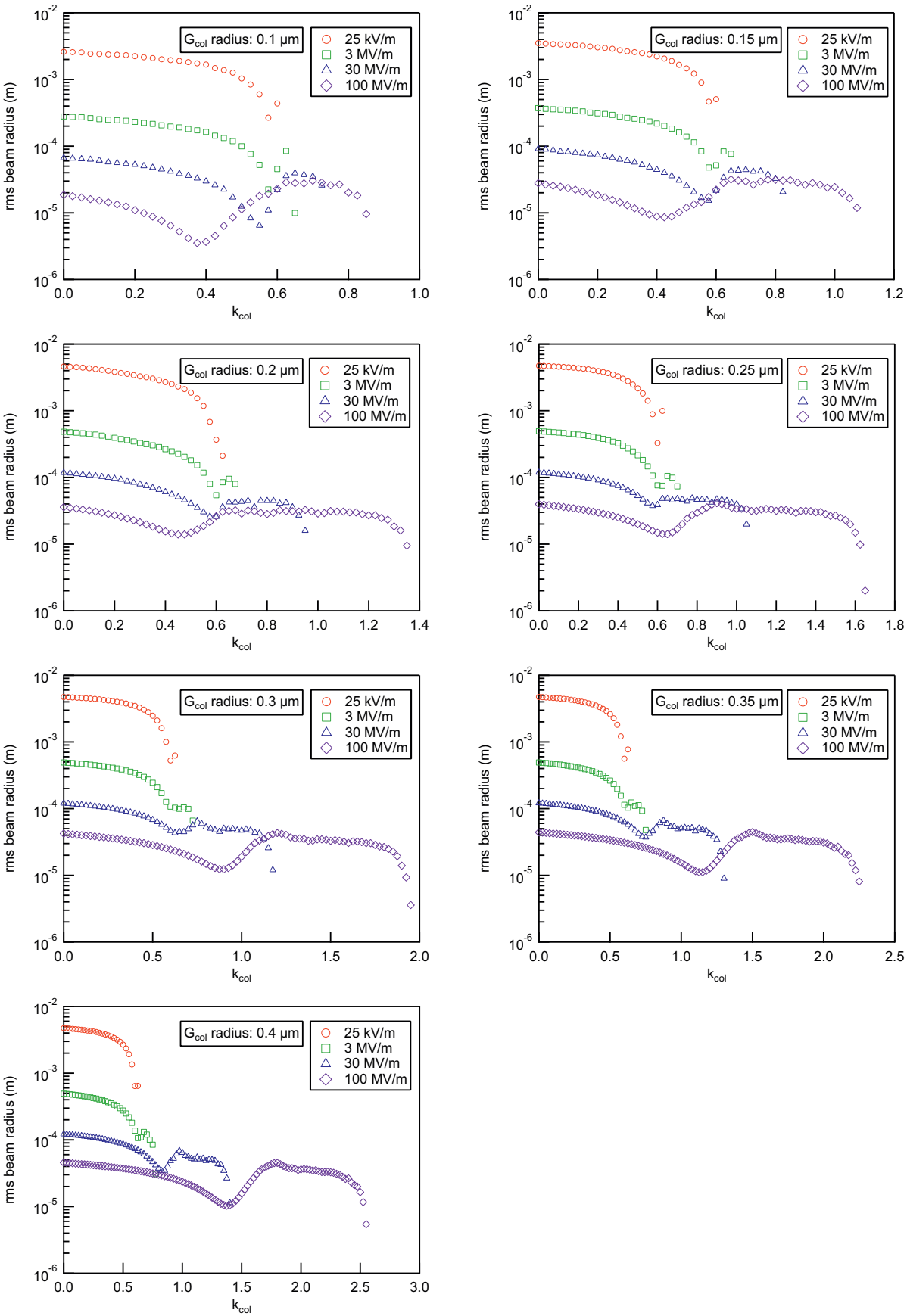

Figure D.12: This figure illustrates the evolution of the rms beam radius with k_{col} for different G_{col} aperture diameters and acceleration fields with a high-density double-gate structure.

Bibliography

[1] C. M. Tang, A. C. Ting, and T. Swyden, "Field-emission arrays - a potentially bright source," *Nuclear Instruments & Methods in Physics Research*, vol. 318, pp. 353–357, 1992.

[2] C. Tang, M. Goldstein, T. Swyden, and J. Walsh, "Free electron micro-lasers," *Nuclear Instruments and Methods in Physics Research A*, vol. 358, no. 1-3, pp. 7–10, 1995. Proceedings of the Sixteenth International Free Electron Laser Conference.

[3] D. Temple, "Recent progress in field emitter array development for high performance applications," *Materials Science & Engineering R-Reports*, vol. 24, pp. 185–239, 1999.

[4] "SwissFEL conceptual design report," April 2012.

[5] B. D. Patterson, R. Abela, H. H. Braun, U. Flechsig, R. Ganter, Y. Kim, E. Kirk, A. Oppelt, M. Pedrozzi, S. Reiche, L. Rivkin, T. Schmidt, B. Schmitt, V. N. Strocov, S. Tsujino, and A. F. Wrulich, "Coherent science at the SwissFEL X-ray laser," *New Journal of Physics*, vol. 12, p. 035012, 2010.

[6] Y. Ding, A. Brachmann, F.-J. Decker, D. Dowell, P. Emma, J. Frisch, S. Gilevich, G. Hays, P. Hering, Z. Huang, R. Iverson, H. Loos, A. Miahnahri, H.-D. Nuhn, D. Ratner, J. Turner, J. Welch, W. White, and J. Wu, "Measurements and simulations of ultralow emittance and ultrashort electron beams in the linac coherent light source," *Physical Review Letters*, vol. 102, p. 254801, 2009.

[7] W. Colson, "Short wavelength free electron lasers in 2000," *Nuclear Instruments and Methods in Physics Research A*, vol. 475, no. 1-3, pp. 397–400, 2001.

[8] J. Andruszkow, B. Aune, V. Ayvazyan, N. Baboi, R. Bakker, V. Balakin, D. Barni, A. Bazhan, M. Bernard, A. Bosotti, J. C. Bourdon, W. Brefeld, R. Brinkmann, S. Buhler, J.-P. Carneiro, M. Castellano, P. Castro, L. Catani, S. Chel, Y. Cho, S. Choroba, E. R. Colby, W. Decking, P. Den Hartog, M. Desmons, M. Dohlus, D. Edwards, H. T. Edwards, B. Faatz, J. Feldhaus, M. Ferrario, M. J. Fitch, K. Flöttmann, M. Fouaidy, A. Gamp, T. Garvey, C. Gerth, M. Geitz, E. Gluskin, V. Gretchko, U. Hahn, W. H. Hartung, D. Hubert, M. Hüning, R. Ischebek, M. Jablonka, J. M. Joly, M. Juillard, T. Junquera, P. Jurkiewicz, A. Kabel, J. Kahl, H. Kaiser, T. Kamps, V. V. Katelev, J. L. Kirchgessner, M. Körfer, L. Kravchuk, G. Kreps, J. Krzywinski, T. Lokajczyk, R. Lange, B. Leblond, M. Leenen, J. Lesrel, M. Liepe, A. Liero, T. Limberg, R. Lorenz, L. H. Hua, L. F. Hai, C. Magne, M. Maslov, G. Materlik, A. Matheisen, J. Menzel, P. Michelato, W.-D. Möller, A. Mosnier, U.-C. Müller, O. Napoly, A. Novokhatski,

M. Omeich, H. S. Padamsee, C. Pagani, F. Peters, B. Petersen, P. Pierini, J. Pflüger, P. Piot, B. Phung Ngoc, L. Plucinski, D. Proch, K. Rehlich, S. Reiche, D. Reschke, I. Reyzl, J. Rosenzweig, J. Rossbach, S. Roth, E. L. Saldin, W. Sandner, Z. Sanok, H. Schlarb, G. Schmidt, P. Schmüser, J. R. Schneider, E. A. Schneidmiller, H.-J. Schreiber, S. Schreiber, P. Schütt, J. Sekutowicz, L. Serafini, D. Sertore, S. Setzer, S. Simrock, B. Sonntag, B. Sparr, F. Stephan, V. A. Sytchev, S. Tazzari, F. Tazzioli, M. Tigner, M. Timm, M. Tonutti, E. Trakhtenberg, R. Treusch, D. Trines, V. Verzilov, T. Vielitz, V. Vogel, G. v. Walter, R. Wanzenberg, T. Weiland, H. Weise, J. Weisend, M. Wendt, M. Werner, M. M. White, I. Will, S. Wolff, M. V. Yurkov, K. Zapfe, P. Zhogolev, and F. Zhou, "First observation of self-amplified spontaneous emission in a free-electron laser at 109 nm wavelength," *Physical Review Letters*, vol. 85, pp. 3825–3829, Oct 2000.

[9] E. L. Saldin, E. A. Schneidmiller, and M. V. Yurkov, *The Physics of Free Electron Lasers*. Springer, 1999.

[10] K. L. Jensen, "Field emitter arrays for plasma and microwave source applications," *Physics of Plasmas*, vol. 6, pp. 2241–2253, 1999.

[11] D. R. Whaley, B. M. Gannon, C. R. Smith, C. M. Armstrong, and C. A. Spindt, "Application of field emitter arrays to microwave power amplifiers," *IEEE Transactions on Plasma Science*, vol. 28, no. 3, pp. 727–747, 2000.

[12] D. R. Whaley, B. M. Gannon, V. O. Heinen, K. E. Kreischer, C. E. Holland, and C. A. Spindt, "Experimental demonstration of an emission-gated traveling-wave tube amplifier," *IEEE Transactions on Plasma Science*, vol. 30, pp. 998–1008, 2002.

[13] D. Whaley, R. Duggal, C. Armstrong, C. Bellew, C. Holland, and C. Spindt, "100 W operation of a cold cathode TWT," *IEEE Transactions on Electron Devices*, vol. 56, no. 5, pp. 896–905, 2009.

[14] European XFEL, http://www.xfel.eu.

[15] LCLS, https://portal.slac.stanford.edu/sites/lcls_public.

[16] SACLA (Spring-8 Angstrom Compact free electron laser, http://xfel.riken.jp/eng.

[17] F. J. Duarte, ed., *Tunable Lasers Handbook*. New York: Academic Press, 1995.

[18] P. M. Lapostolle, "Possible emittance increase through filamentation due to space charge in continuous beams," *IEEE Transactions on Nuclear Science*, vol. 18, no. 3, pp. 1101–1104, 1971.

[19] A. V. Crewe, J. Wall, and J. Langmore, "Visibility of single atoms," *Science*, vol. 168, no. 3937, pp. 1338–1340, 1970.

[20] C. Brau, "High-brightness electron beams - small free-electron lasers," *Nuclear Instruments and Methods in Physics Research*, vol. 407, no. 1-3, pp. 1–7, 1998.

[21] H. Makishima, S. Miyano, H. Imura, J. Matsuoka, H. Takemura, and A. Okamoto, "Design and performance of traveling-wave tubes using field emitter array cathodes," *Applied Surface Science*, vol. 146, pp. 230–233, 1999.

[22] K. B. K. Teo, E. Minoux, L. Hudanski, F. Peauger, J.-P. Schnell, L. Gangloff, P. Legagneux, D. Dieumegard, G. A. J. Amaratunga, and W. I. Milne, "Microwave devices: Carbon nanotubes as cold cathodes," *Nature*, vol. 437, 2005.

[23] R. L. Ives, "Microfabrication of high-frequency vacuum electron devices," *IEEE Transactions on Plasma Science*, vol. 32, pp. 1277–1291, 2004.

[24] J. H. Booske, "Plasma physics and related challenges of millimeter-wave-to-terahertz and high power microwave generation," *Physics of Plasmas*, vol. 15, p. 055502, 2008.

[25] H.-W. Fink, "Point-source for ions and electrons," *Physica Scripta*, vol. 38, no. 2, pp. 260–263, 1988.

[26] V. T. Binh, S. T. Purcell, N. Garcia, and J. Doglioni, "Field-emission electron-spectroscopy of single-atom tips," *Physical Review Letters*, vol. 69, pp. 2527–2530, 1992.

[27] G. Herink, D. R. Solli, M. Gulde, and C. Ropers, "Field-driven photoemission from nanostructures quenches the quiver motion," *Nature*, vol. 483, no. 7338, pp. 190–193, 2012.

[28] A. H. Zewail, "4d ultrafast electron diffraction, crystallography, and microscopy," *Annual Review of Physical Chemistry*, vol. 57, no. 1, pp. 65–103, 2006.

[29] M. Kruger, M. Schenk, and P. Hommelhoff, "Attosecond control of electrons emtted from a nanoscale metal tip," *Nature*, vol. 475, no. 7354, pp. 78–81, 2011.

[30] W. P. Dyke and J. K. Trolan, "Field emission: Large current densities, space charge, and the vacuum arc," *Physical Reviev*, vol. 89, pp. 799–808, Feb 1953.

[31] K. R. Shoulders, "Microelectronics using electron-beam-activated machining techniques," *Advances in Computers 2*, pp. 135–293, 1961.

[32] C. A. Spindt, "A thin-film field-emission cathode," *Journal of Applied Physics*, vol. 39, p. 3504, 1968.

[33] J. He, P. H. Cutler, N. M. Miskovsky, T. E. Feuchtwang, T. E. Sullivan, and M. Chung, "Derivation of the image interaction for nonplanar pointed emitter geometries - application to field-emission IV characteristics," *Surface Science*, vol. 246, pp. 348–364, 1991.

[34] P. R. Schwoebel, C. A. Spindt, and C. E. Holland, "High current, high current density field emitter array cathodes," *Journal of Vacuum Science & Technology B*, vol. 23, pp. 691–693, 2005.

[35] J. Nation, L. Schachter, F. Mako, L. Len, W. Peter, C.-M. Tang, and T. Srinivasan-Rao, "Advances in cold cathode physics and technology," *Proceedings of the IEEE*, vol. 87, no. 5, pp. 865 –889, 1999.

[36] C. A. Spindt, C. E. Holland, P. R. Schwoebel, and I. Brodie, "Field-emitter-array development for microwave applications," *Journal of Vacuum Science & Technology B*, vol. 14, no. 3, pp. 1986–1989, 1996.

[37] S. Tsujino, P. Beaud, E. Kirk, T. Vogel, H. Sehr, J. Gobrecht, and A. Wrulich, "Ultrafast electron emission from metallic nanotip arrays induced by near infrared femtosecond laser pulses," *Applied Physics Letters*, vol. 92, p. 193501, 2008.

[38] A. Mustonen, P. Beaud, E. Kirk, T. Feurer, and S. Tsujino, "Five picocoulomb electron bunch generation by ultrafast laser-induced field emission from metallic nano-tip arrays," *Applied Physics Letters*, vol. 99, no. 10, p. 103504, 2011.

[39] J. H. Daniel, "Field emission from tungsten and thoriated tungsten single crystals," *Physical Review*, vol. 61, pp. 657–667, 1942.

[40] J. B. Taylor and I. Langmuir, "The evaporation of atoms, ions and electrons from caesium films on tungsten," *Physical Review*, vol. 44, pp. 423–458, 1933.

[41] N. Müller, W. Eckstein, W. Heiland, and W. Zinn, "Electron spin polarization in field emission from EuS-coated tungsten tips," *Physical Review Letters*, vol. 29, pp. 1651–1654, 1972.

[42] X. Tianbao, W. Mackie, and P. Davis, "Emission confinement on the (100) planes of etched tungsten field emitters coated with thin-film ZrC," in *Technical Digest of the 17th International Vacuum Nanoelectronics Conference*, pp. 166–167, 2004.

[43] S. Jianping, "Field emission from tungsten carbide on W tips," in *Proceedings of the 2008 International Conference on Advanced Infocomm (ICAIT) Technology*, pp. 81:1–81:4, 2008.

[44] Y.-H. Lee, C.-H. Choi, Y.-T. Jang, E.-K. Kim, B.-K. Ju, N.-K. Min, and J.-H. Ahn, "Tungsten nanowires and their field electron emission properties," *Applied Physics Letters*, vol. 81, no. 4, pp. 745–747, 2002.

[45] J. Zhou, L. Gong, S. Z. Deng, J. Chen, J. C. She, N. S. Xu, R. Yang, and Z. L. Wang, "Growth and field-emission property of tungsten oxide nanotip arrays," *Applied Physics Letters*, vol. 87, no. 22, p. 223108, 2005.

[46] S. Wang, Y. He, X. Fang, J. Zou, Y. Wang, H. Huang, P. M. F. J. Costa, M. Song, B. Huang, C. T. Liu, P. K. Liaw, Y. Bando, and D. Golberg, "Structure and field-emission properties of sub-micrometer-sized tungsten-whisker arrays fabricated by vapor deposition," *Advanced Materials*, vol. 21, no. 23, pp. 2387–2392, 2009.

[47] J. Liu, Z. Zhang, Y. Zhao, X. Su, S. Liu, and E. Wang, "Tuning the field-emission properties of tungsten oxide nanorods," *Small*, vol. 1, no. 3, pp. 310–313, 2005.

[48] K. Sun, J. Y. Lee, B. Li, W. Liu, C. Miao, Y.-H. Xie, X. Wei, and T. P. Russell, "Fabrication and field emission study of atomically sharp high-density tungsten nanotip arrays," *Journal of Applied Physics*, vol. 108, no. 3, p. 036102, 2010.

[49] R. Thomas and H. Nathanson, "Transmissive-mode silicon field emission array photoemitter," *Applied Physics Letters*, vol. 21, no. 8, pp. 387–389, 1972.

[50] E. C. Boswell, S. E. Huq, M. Huang, P. D. Prewett, and P. R. Wilshaw, "Polycrystalline silicon field emitters," *Journal of Vacuum Science & Technology B*, vol. 14, no. 3, pp. 1910–1913, 1996.

[51] M. Nagao, Y. Sacho, T. Sato, T. Matsukawa, S. Kanemaru, and J. Itoh, "Fabrication of polycrystalline silicon field emitter arrays with hafnium carbide coating for thin-film-transistor controlled field emission displays," *Japanese Journal of Applied Physics*, vol. 43, no. 6B, pp. 3919–3922, 2004.

[52] J. R. Jessing, D. L. Parker, and M. H. Weichold, "Porous silicon field emission cathode development," *Journal of Vacuum Science & Technology B*, vol. 14, no. 3, pp. 1899–1901, 1996.

[53] S. Silva, R. Forrest, and J. Shannon, "Electron field emission from amorphous silicon," in *Eleventh International Vacuum Microelectronics Conference*, pp. 285–286, 1998.

[54] C. A. Spindt, I. Brodie, L. Humphrey, and E. R. Westerberg, "Physical-properties of thin-film field-emission cathodes with molybdenum cones," *Journal of Applied Physics*, vol. 47, pp. 5248–5263–, 1976.

[55] E. Kirk, S. Tsujino, T. Vogel, K. Jefimovs, J. Gobrecht, and A. Wrulich, "Fabrication of all-metal field emitter arrays with controlled apex sizes by molding," *Journal of Vacuum Science & Technology B*, vol. 27, pp. 1813–1820, 2009.

[56] L. Vila, P. Vincent, L. Dauginet-De Pra, G. Pirio, E. Minoux, L. Gangloff, S. Demoustier-Champagne, N. Sarazin, E. Ferain, R. Legras, L. Piraux, and P. Legagneux, "Growth and field-emission properties of vertically aligned cobalt nanowire arrays," *Nano Letters*, vol. 4, no. 3, pp. 521–524, 2004.

[57] K. Okano, K. Hoshina, M. Iida, S. Koizumi, and T. Inuzuka, "Fabrication of a diamond field emitter array," *Applied Physics Letters*, vol. 64, no. 20, pp. 2742–2744, 1994.

[58] W. P. Kang, J. L. Davidson, A. Wisitsora-at, Y. M. Wong, R. Takalkar, K. Holmes, and D. V. Kerns, "Diamond vacuum field emission devices," *Diamond & Related Materials*, vol. 13, pp. 1944–1948, 2004.

[59] T. Yoshimoto, H. Yui, and T. Iwata, "Field emission from diamond micropowders with sharp edges," *Journal of Vacuum Science & Technology B*, vol. 28, no. 2, pp. C2B30–C2B33, 2010.

[60] W. A. de Heer, A. Châtelain, and D. Ugarte, "A carbon nanotube field-emission electron source," *Science*, vol. 270, no. 5239, pp. 1179–1180, 1995.

[61] J.-M. Bonard, J.-P. Salvetat, T. Stöckli, W. A. de Heer, L. Forro, and A. Châtelain, "Field emission from single-wall carbon nanotube films," *Applied Physics Letters*, vol. 73, no. 7, pp. 918–920, 1998.

[62] W. I. Milne, K. B. K. Teo, G. A. J. Amaratunga, P. Legagneux, L. Gangloff, J.-P. Schnell, V. Semet, V. Thien Binh, and O. Groening, "Carbon nanotubes as field emission sources," *Journal of Materials Chemistry*, vol. 14, pp. 933–943, 2004.

[63] H. S. Jang, H.-R. Lee, and D.-H. Kim, "Field emission properties of carbon nanotubes with different morphologies," *Thin Solid Films*, vol. 500, pp. 124–128, 2006.

[64] W. B. Choi, D. S. Chung, J. H. Kang, H. Y. Kim, Y. W. Jin, I. T. Han, Y. H. Lee, J. E. Jung, N. S. Lee, G. S. Park, and J. M. Kim, "Fully sealed, high-brightness carbon-nanotube field-emission display," *Applied Physics Letters*, vol. 75, no. 20, pp. 3129–3131, 1999.

[65] M. Nakamoto and J. Moon, "Suitability of low-work-function titanium nitride coated transfer mold field-emitter arrays for harsh environment applications," *Journal of Vacuum Science & Technology B*, vol. 29, no. 2, p. 02B112, 2011.

[66] K. Ikeda, W. Ohue, K. Endo, Y. Gotoh, and H. Tsuji, "Development of a vacuum transistor using hafnium nitride field emitter arrays," *Journal of Vacuum Science & Technology B*, vol. 29, no. 2, p. 02B116, 2011.

[67] D. Nicolaescu, M. Nagao, T. Sato, V. Filip, S. Kanemaru, and J. Itoh, "Emission statistics for Si and HfC emitter arrays after residual gas exposure," *Journal of Vacuum Science & Technology B*, vol. 23, no. 2, pp. 707–717, 2005.

[68] H. Busta, D. Boldridge, R. Myers, E. Edwards, and A. Feinerman, "Field emission from carbon black and carbon black/silica nanoparticles dispersed in photoresist," *Applied Physics Letters*, vol. 83, no. 9, pp. 1779–1781, 2003.

[69] M. Dehler, A. Candel, and E. Gjonaj, "Full scale simulation of a field-emitter arrays based electron source for free-electron lasers," *Journal of Vacuum Science & Technology B*, vol. 24, pp. 892–897, 2006.

[70] J. Itoh, Y. Toma, K. Morikawa, S. Kanemaru, and K. Shimizu, "Fabrication of double-gated Si field emitter arrays for focused electron-beam generation," *Journal of Vacuum Science & Technology B*, vol. 13, pp. 1968–1972, 1995.

[71] Y. Yamaoka, S. Kanemaru, and J. Itoh, "Fabrication of silicon field emitter arrays integrated with beam focusing lens," *Japanese Journal of Applied Physics*, vol. 35, no. 12B (Part 1), pp. 6626–6628, 1996.

[72] A. Hosono, S. Kawabuchi, S. Horibata, S. Okuda, H. Harada, and M. Takai, "High emission current double-gated field emitter arrays," *Journal of Vacuum Science & Technology B*, vol. 17, pp. 575–579, 1999.

[73] C. Py, M. Gao, S. R. Das, P. Grant, P. Marshall, and L. LeBrun, "Double-gated microtip emitters for brighter field-emission displays," *Journal of Vacuum Science & Technology A*, vol. 18, pp. 626–629, 2000.

[74] L. Dvorson, G. Sha, I. Kymissis, C. Y. Hong, and A. I. Akinwande, "Electrical and optical characterization of field emitter tips with integrated vertically stacked focus," *IEEE Transactions on Electron Devices*, vol. 50, pp. 2548–2558, 2003.

[75] Y. Neo, M. Takeda, T. Soda, M. Nagao, T. Yoshida, S. Kanemaru, T. Sakai, K. Hagiwara, N. Saito, T. Aoki, and H. Mimura, "Emission and focusing characteristics of volcano-structured double-gated field emitter arrays," *Journal of Vacuum Science & Technology B*, vol. 27, pp. 701–704, 2009.

[76] S. Tsujino, P. Helfenstein, E. Kirk, T. Vogel, C. Escher, and H.-W. Fink, "Field-emission characteristics of molded molybdenum nanotip arrays with stacked collimation gate electrodes," *IEEE Electron Device Letters*, vol. 31, no. 9, pp. 1059–1061, 2010.

[77] P. Helfenstein, E. Kirk, K. Jefimovs, T. Vogel, C. Escher, H.-W. Fink, and S. Tsujino, "Highly collimated electron beams from double-gate field emitter arrays with large collimation gate apertures," *Applied Physics Letters*, vol. 98, no. 6, p. 061502, 2011.

[78] P. Helfenstein, K. Jefimovs, E. Kirk, T. Vogel, C. Escher, H.-W. Fink, and S. Tsujino, "Fabrication of metallic double-gate field emitter arrays and their electron beam collimation characteristics," *Journal of Applied Physics*, vol. 112, p. 093307, 2012.

[79] C. Py, J. Itoh, T. Hirano, and S. Kanemaru, "Beam focusing characteristics of silicon microtips with an in-plane lens," *IEEE Transactions on Electron Devices*, vol. 44, pp. 498–502, 1997.

[80] W. Kesling and C. Hunt, "Beam focusing for field-emission flat-panel displays," *IEEE Transactions on Electron Devices*, vol. 42, no. 2, pp. 340–347, 1995.

[81] Y. Toma, S. Kanemaru, and J. Itoh, "Electron-beam characteristics of double-gated si field emitter arrays," *Journal of Vacuum Science & Technology B*, vol. 14, pp. 1902–1905, 1996.

[82] L. Dvorson, M. Ding, and A. Akinwande, "Analytical electrostatic model of silicon conical field emitters. ii. extension to devices with focusing electrode," *Electron Devices, IEEE Transactions on*, vol. 48, pp. 144–148, jan 2001.

[83] D. J. Li and J. C. Zhang, "Focusing field emission arrays constructed by self-aligned photolithography," *Journal of Vacuum Science & Technology B*, vol. 19, pp. 1820–1823, 2001.

[84] L. Dvorson and A. I. Akinwande, "Double-gated Spindt emitters with stacked focusing electrode," *Journal of Vacuum Science & Technology B*, vol. 20, pp. 53–59, 2002.

[85] J. H. Choi, A. R. Zoulkarneev, Y. W. Jin, Y. J. Park, D. S. Chung, B. K. Song, I. T. Han, H. W. Lee, S. H. Park, H. S. Kang, H. J. Kim, J. W. Kim, J. E. Jung, J. M. Kim, H. G. Baek, and S. G. Yu, "Carbon nanotube field emitter arrays having an electron beam focusing structure," *Applied Physics Letters*, vol. 84, no. 6, pp. 1022–1024, 2004.

[86] L.-Y. Chen, L. Velasquez-Garcia, X. Wang, K. Teo, and A. Akinwande, "A micro ionizer for portable mass spectrometers using double-gated isolated vertically aligned carbon nanofiber arrays," in *IEEE International Electron Devices Meeting (IEDM)*, pp. 843–846, 2007.

[87] Y. Honda, Y. Takiguchi, N. Egami, M. Nanba, Y. Saishu, K. Nakamura, and M. Taniguchi, "Electrostatic focusing spindt-type field emitter array for an image sensor with a high-gain avalanche rushing amorphous photoconductor target," *Journal of Vacuum Science & Technology B*, vol. 29, no. 4, p. 04E104, 2011.

[88] L. R. Baylor, D. H. Lowndes, M. L. Simpson, C. E. Thomas, M. A. Guillorn, V. I. Merkulov, J. H. Whealton, E. D. Ellis, D. K. Hensley, and A. V. Melechko, "Digital electrostatic electron-beam array lithography," in *Papers from the 46th International Conference on Electron, Ion, and Photon Beam Technology and Nanofabrication*, vol. 20, pp. 2646–2650, 2002.

[89] M. Nagao, T. Yoshida, S. Kanemaru, Y. Neo, and H. Mimura, "Fabrication of a field emitter array with a built-in einzel lens," *Japanese Journal of Applied Physics*, vol. 48, p. 06FK02, 2009.

[90] T. Soda, M. Nagao, C. Yasumuro, S. Kanemaru, T. Sakai, N. Saito, Y. Neo, T. Aoki, and H. Mimura, "Fabrication of volcano-structured double-gate field emitter array by etch-back technique," *Japanese Journal of Applied Physics*, vol. 47, pp. 5252–5255, 2008.

[91] Y. Neo, T. Soda, M. Takeda, M. Nagao, T. Yoshida, C. Yasumuro, S. Kanemaru, T. Sakai, K. Hagiwara, N. Saito, T. Aoki, and H. Mimura, "Focusing characteristics of double-gated field-emitter arrays with a lower height of the focusing electrode," *Applied Physics Express*, vol. 1, no. 5, p. 053001, 2008.

[92] R. H. Fowler and L. Nordheim, "Electron emission in intense electric fields," *Proceedings of the Royal Society of London A*, vol. 119, pp. 173–181, 1928.

[93] E. L. Murphy and R. H. Good, "Thermionic emission, field emission, and the transition region," *Physical Review*, vol. 102, pp. 1464–1473, 1956.

[94] P. R. Schwoebel, C. A. Spindt, C. E. Holland, and J. A. Panitz, "Field emission current cleaning and annealing of microfabricated cold cathodes," *Journal of Vacuum Science & Technology B*, vol. 19, pp. 980–987, 2001.

[95] E. W. Müller, "Beobachtungen über die Feldemission und die Kathodenzerstäubung an thoriertem Wolfram," *Zeitschrift für Physik*, vol. 106, no. 1-2, pp. 132–140, 1937.

[96] A. P. Janssen and J. P. Jones, “The sharpening of field emitter tips by ion sputtering,” *Journal of Physics D*, vol. 4, no. 1, p. 118, 1971.

[97] P. R. Schwoebel and C. A. Spindt, “Glow discharge processing to enhance field-emitter array performance,” *Journal of Vacuum Science & Technology B*, vol. 12, no. 4, pp. 2414 –2421, 1994.

[98] C. H. Weijsenfeld, A. Hoogendoorn, and M. Koedam, “Sputtering of polycrystalline metals by inert gas ions of low energy (100-1000 eV),” *Physica*, vol. 27, pp. 763–764, 1961.

[99] P. R. Schwoebel and C. A. Spindt, “Field-emitter array performance enhancement using hydrogen glow discharges,” *Applied Physics Letters*, vol. 63, no. 1, pp. 33–35, 1993.

[100] I. Brodie, “Bombardment of field-emission cathodes by positive ions formed in the interelectrode region,” *International Journal of Electronics*, vol. 38, no. 4, pp. 541–550, 1975.

[101] S. Ernst, S. Wirth, M. Rams, V. Dolocan, and F. Steglich, “Tip preparation for usage in an ultra-low temperature UHV scanning tunneling microscope,” *Science and Technology of Advanced Materials*, vol. 8, no. 5, p. 347, 2007.

[102] S. Tsujino, M. Paraliev, E. Kirk, and H.-H. Braun, “Homogeneity improvement of field emission beam from metallic nano-tip arrays by noble-gas conditioning,” *Applied Physics Letters*, vol. 99, no. 7, p. 073101, 2011.

[103] R. Smith, “The sputtering of field electron emitters by self-generated positive ions,” *Journal of Physics D*, vol. 17, no. 5, p. 1045, 1984.

[104] E. L. Chaffe, *Theory of Thermionic Vacuum Tubes*. McGraw-Hill, 1933.

[105] M. Cordona and L. Ley, *Photoemission in Solids, Vol. 1*. Springer, 1978.

[106] R. H. Good and E. W. Müller, “Field emission,” in *Handbuch der Physik* (S. Flügge, ed.), Springer, 1956.

[107] W. Dyke and W. Dolan, “Field emission,” in "*Advances in Electronics and Electron Physics*" (L. Marton, ed.), pp. 89–185, Academic Press, 1956.

[108] R. Gomer, *Field emission and field ionization*. Harvard University Press, 1961.

[109] W. Zhu, *Vacuum Microelectronics*. John Wiley & Sons, 2001.

[110] G. N. Fursey, *Field Emission in Vacuum Microelectronics*. Kluwer Academic / Plenum Publishers, 2005.

[111] S. Tsujino, F. le Pimpec, J. Raabe, M. Buess, M. Dehler, E. Kirk, J. Gobrecht, and A. Wrulich, “Static and optical field enhancement in metallic nanotips studied by two-photon photoemission microscopy and spectroscopy excited by picosecond laser pulses,” *Applied Physics Letters*, vol. 94, p. 1779, 2009.

[112] W. Schottky, "Über den Einfluss von Strukturwirkungen, besonders der Thomsonschen Bildkraft, auf die Elektronenemission der Metalle," *Physikalische Zeitschrift*, vol. 15, pp. 872–878, 1914.

[113] W. Schottky, "Über kalte und warme Elektronenentladungen," *Zeitschrift für Physik*, vol. 14, pp. 63–106, 1923.

[114] L. W. Nordheim, "The effect of the image force on the emission and reflexion of electrons by metals," *Proceedings of the Royal Society of London A*, vol. 121, pp. 626–639, 1928.

[115] L. Nordheim, "Die Theorie der Elektronenemission der Metalle," *Physikalische Zeitschrift*, vol. 30, p. 177, 1929.

[116] R. G. Forbes and J. H. Deane, "Reformulation of the standard theory of Fowler-Nordheim tunnelling and cold field electron emission," *Proceedings of the Royal Society A*, vol. 463, pp. 2907–2927, 2007.

[117] K. L. Jensen, "Electron emission theory and its application: Fowler-Nordheim equation and beyond," *Journal of Vacuum Science & Technology B*, vol. 21, no. 4, pp. 1528–1544, 2003.

[118] R. Stratton, "Theory of field emission from semiconductors," *Physical Review*, vol. 125, pp. 67–82, Jan 1962.

[119] A. Modinos, *Field, thermionic, and secondary electron emission spectroscopy*. Plenum Press, 1984.

[120] T. C. Choy, A. H. Harker, and A. M. Stoneham, "Field emission theory for an enhanced surface potential: a model for carbon field emitters," *Journal of Physics*, vol. 16, no. 6, p. 861, 2004.

[121] C. J. Edgcombe and N. de Jonge, "Properties of a field emitter deduced from curvature of its Fowler-Nordheim plot," *Journal of Vacuum Science & Technology B*, vol. 24, no. 2, pp. 869–873, 2006.

[122] R. G. Forbes, "Field emission: New theory for the derivation of emission area from a Fowler-Nordheim plot," *Journal of Vacuum Science & Technology B*, vol. 17, pp. 526–533, 1999.

[123] R. G. Forbes, "Call for experimental test of a revised mathematical form for empirical field emission current-voltage characteristics," *Applied Physics Letters*, vol. 92, p. 193105, 2008.

[124] K. L. Jensen, M. A. Kodis, R. A. Murphy, and E. G. Zaidman, "Space charge effects on the current-voltage characteristics of gated field emitter arrays," *Journal of Applied Physics*, vol. 82, pp. 845–854, 1997.

[125] N. Fröman and P. O. Fröman, *JWKB approximation: contributions to the theory*. North-Holland Publishing Co., 1965.

[126] S. C. Miller and R. H. Good, "A WKB-type approximation to the Schrödinger equation," *Physical Review*, vol. 91, pp. 174–179, Jul 1953.

[127] R. G. Forbes, "Simple good approximations for the special elliptic functions in standard Fowler-Nordheim tunneling theory for a Schottky-Nordheim barrier," *Applied Physics Letters*, vol. 89, p. 113122, 2006.

[128] R. G. Forbes, "Use of a spreadsheet for Fowler-Nordheim equation calculations," *Journal of Vacuum Science & Technology B*, vol. 17, pp. 534–541, 1999.

[129] M. Abramowitz and I. A. Stegun, *Handbook of Mathematical Functions*, vol. 55. Dover, 1965.

[130] J. M. Houston, "The slope of logarithmic plots of the Fowler-Nordheim equation," *Physical Review*, vol. 88, pp. 349–349, 1952.

[131] R. E. Burgess, H. Kroemer, and J. M. Houston, "Corrected values of fowler-nordheim field emission functions $v(y)$ and $s(y)$," *Physical Review*, vol. 90, pp. 515–515, May 1953.

[132] F. M. Charbonnier and E. E. Martin, "A simple method for deriving, from measured I(V) data, information on the geometry of a field emission current source of unknown characteristics," *Journal of Applied Physics*, vol. 33, no. 5, pp. 1897–1898, 1962.

[133] J. Paulini, T. Klein, and G. Simon, "Thermo-field emission and the Nottingham effect," *Journal of Physics D*, vol. 26, no. 8, p. 1310, 1993.

[134] R. Forbes and J. Deane, "Comparison of approximations for the principal Schottky-Nordheim barrier function v(f)," in *22nd International Vacuum Nanoelectronics Conference (IVNC)*, pp. 97 –98, july 2009.

[135] K. L. Jensen and A. K. Ganguly, "Numerical-simulation of field-emission and tunneling - a comparison of the Wigner function and transmission coefficient approaches," *Journal of Applied Physics*, vol. 73, pp. 4409–4427, 1993.

[136] N. S. Xu, J. Chen, and S. Z. Deng, "Physical origin of nonlinearity in the Fowler-Nordheim plot of field-induced emission from amorphous diamond films: Thermionic emission to field emission," *Applied Physics Letters*, vol. 76, no. 17, pp. 246–2465, 2000.

[137] M. Choueib, A. Ayari, P. Vincent, M. Bechelany, D. Cornu, and S. T. Purcell, "Strong deviations from Fowler-Nordheim behavior for field emission from individual sic nanowires due to restricted bulk carrier generation," *Physical Review B*, vol. 79, p. 075421, Feb 2009.

[138] T. J. Lewis, "Theoretical interpretation of field emission experiments," *Physical Review*, vol. 101, pp. 1694–1698, 1956.

[139] F. R. Abbott and J. E. Henderson, "The range and validity of the field current equation," *Physical Review*, vol. 56, pp. 113–118, 1939.

[140] COMSOL Multiphysics, http://ch.comsol.com.

[141] MATLAB, http://mathworks.com.

[142] CST - Computer Simulation Technology, http://www.cst.com.

[143] V. A. Guzenko, A. Mustonen, P. Helfenstein, E. Kirk, and S. Tsujino, "High-density large-scale field emitter arrays for X-ray free electron laser cathodes," *submitted to: Microelectronic Engineering*, 2012.

[144] R. Courant, "Variational methods for the solution of problems of equilibrium and vibrations," *Bulletin of the American Mathematical Society*, vol. 49, pp. 1–23, 1943.

[145] K. Königsberger, *Analysis 1*. Springer, 2003.

[146] K. Yee, "Numerical solution of initial boundary value problems involving Maxwell's equations in isotropic media," *IEEE Transactions on Antennas and Propagation*, vol. 14, no. 3, pp. 302–307, 1966.

[147] T. Weiland, "A discretization model for the solution of Maxwell's equations for six-component fields," *Archiv für Elektronik und Übertragungstechnik*, vol. 31, pp. 116–120, 1977.

[148] R. Holland, "Finite-difference solution of Maxwell's equations in generalized nonorthogonal coordinates," *IEE Transactions on Nuclear Science*, vol. 30, no. 6, pp. 4589–4591, 1983.

[149] U. van Rienen and T. Weiland, "Triangular discretization method for the evaluation of RF fields in waveguides and cylindrically symmetric cavities," *Particle Accelerators*, vol. 20, pp. 239–65, 1987.

[150] R.-B. Wu and T. Itoh, "Hybrid finite-difference time-domain modeling of curved surfaces using tetrahedral edge elements," *IEEE Transactions on Antennas and Propagation*, vol. 45, no. 8, pp. 1302–1309, 1997.

[151] T. Weiland, "Time domain electromagnetic field computation with finite difference methods," *International Journal of Numerical Modelling*, vol. 9, no. 4, pp. 295–319, 1996.

[152] P. Helfenstein, V. A. Guzenko, H.-W. Fink, and S. Tsujino, "Electron beam collimation with a 40,000 tip metallic double-gate field emitter array and in-situ control of nanotip sharpness distribution," *submitted to: Nano Letters*, 2012.

[153] H. F. Gray and R. F. Greene, "Method of manufacturing a field-emission cathode structure," December 1981, US Patent Nr. 4,307,507.

[154] H. Umimoto, "Numerical simulation of stress-dependent oxide growth at convex and concave corners of trench structures," *IEEE Electron Device Letters*, vol. 10, pp. 330–332, 1989.

[155] M. Nakamoto, T. Hasegawa, T. Ono, T. Sakai, and N. Sakuma, "Low operation voltage field emitter arrays using low work function materials fabricated by transfer mold technique," in *Technical Digest Int. Electron Devices Meeting*, pp. 297–300, 1996.

[156] A. Kirk, A. Mustonen, E. Pomjakushina, S. Ritter, J. Gobrecht, and S. Tsujino, "Smoother Mo films for molded FEAs by addition of N_2 to Ar sputter gas," in *24th International Vacuum Nanoelectronics Conference (IVNC)*, pp. 31–32, 2011.

[157] R. Resanovic, "PMMA-Reflow und Oberflächentopografie für die Feld-Emitter-Array (FEA) Prozessherstellung," bachelor's thesis, Hochschule Bremen, 2011.

[158] C. Vieu, F. Carcenac, A. Pepin, Y. Chen, M. Mejias, A. Lebib, L. Manin-Ferlazzo, L. Couraud, and H. Launois, "Electron beam lithography: resolution limits and applications," *Applied Surface Science*, vol. 164, pp. 111–117, 2000.

[159] P. Rai-Choudhury, ed., *Handbook of microlithography, micromachining, and microfabrication*, vol. 1. SPIE Optical Engineering Press, 1997.

[160] J. Baró, J. Sempau, J. Fernández-Varea, and F. Salvat, "PENELOPE: An algorithm for Monte Carlo simulation of the penetration and energy loss of electrons and positrons in matter," *Nuclear Instruments and Methods in Physics Research B*, vol. 100, no. 1, pp. 31–46, 1995.

[161] *Layout BEAMER Manual*. Munich, Germany: GenISys GmbH, 2012.

[162] *CJob Manual*. Jena, Germany: Vistec Lithography B.V., 2012.